Electrons from Charm and Beauty Quarks in Proton-Proton Collisions with ALICE at the LHC and Study of Collective Flow in Low Energy Heavy-Ion Collisions

Ph.D. Thesis

By

SUDHIR PANDURANG RODE

DEPARTMENT OF PHYSICS

INDIAN INSTITUTE OF TECHNOLOGY INDORE

AUGUST 2020

Electrons from Charm and Beauty Quarks in Proton-Proton Collisions with ALICE at the LHC and Study of Collective Flow in Low Energy Heavy-Ion Collisions

A THESIS

Submitted in partial fulfillment of the
requirements for the award of the degree
of
DOCTOR OF PHILOSOPHY

by

SUDHIR PANDURANG RODE

DEPARTMENT OF PHYSICS
INDIAN INSTITUTE OF TECHNOLOGY INDORE
AUGUST 2020

INDIAN INSTITUTE OF TECHNOLOGY INDORE

CANDIDATE'S DECLARATION

I hereby certify that the work which is being presented in the thesis entitled **Electrons from Charm and Beauty Quarks in Proton-Proton Collisions with ALICE at the LHC and Study of Collective Flow in Low Energy Heavy-Ion Collisions** in the partial fulfillment of the requirements for the award of the degree of **DOCTOR OF PHILOSOPHY** and submitted in the **DEPARTMENT OF PHYSICS, Indian Institute of Technology Indore**, is an authentic record of my own work carried out during the time period from **December 2015 to August 2020** under the supervision of **Dr. Ankhi Roy,** Associate Professor, IIT Indore and **Dr. Partha Pratim Bhaduri,** Scientific Officer F, VECC, Kolkata

The matter presented in this thesis has not been submitted by me for the award of any other degree of this or any other institute.

07/08/2020

signature of the student with date
SUDHIR PANDURANG RODE

This is to certify that the above statement made by the candidate is correct to the best of my/our knowledge.

07/08/2020

Signature of Thesis Supervisor #1 with date

Dr. ANKHI ROY

07/08/2020

Signature of Thesis Supervisor #2 with date

Dr. PARTHA PRATIM BHADURI

Mr. SUDHIR PANDURANG RODE has successfully given his/her Ph.D. Oral Examination held on 08/12/2020

Signature of Chairperson (OEB)
Date: 8-12-2020

Signature of External Examiner
Date: 8/12/2020

Signature of Thesis Supervisor
Date: 08/12/2020

Signature of Thesis Co-supervisor
Date: 09/12/2020

Signature of PSPC Member #1
Date:

Signature of PSPC Member #2
Date: 08/12/2020

Signature of Convener, DPGC
Date: **9th DECEMBER 2020**

Signature of Head of Department
Date: 8th December 2020

Dedicated

to

My Family

Acknowledgements

Allow me to express my immense gratitude to all those people who have contributed to this dissertation in some way or the other. First and foremost, this thesis would have been impossible without the constant support and encouragement of my supervisor Dr. Ankhi Roy. Her will to give student full freedom to pursue the research without any extra burden, has a huge impact on my work. Moreover, I would not be able to achieve half of what I have done during my Ph.D. without my co-supervisor Dr. Partha Pratim Bhaduri. His deep understanding of the subject and out-of-the-box thinking led to the completion of this thesis. I am eternally grateful to both of these individuals.

I want to extend my deepest gratitude towards my mentor, Dr. Ralf Averbeck, GSI, Darmstadt, whose guidance and experience have been a game-changer for me. I am eternally grateful to him for his kindness, hospitality when I was at GSI for my research work. Furthermore, I go on and thank, Dr. Andrea Dubla, whose help has been very crucial in the early days of my research and subsequently in the completion of this thesis. I also want to thank other collaborators and colleagues at GSI such as Dr Silvia Masciocchi, Dr Peter Malzacher, Dr Dariusz Miskowiec, Dr Kai Schweda, Dr Ilya Selyuzhenkov, Dr Anton Andronic and other colleagues such as Alberto, Damir, Xiaozhi, Dhevan, Jianhui, Denise, Bogdan, Michael Habib, Michael Ciupek, Sebastian, Camila and Lukas. I thank Karin and Maria for the hospitality and their kind gestures during my visits to GSI. I am extremely grateful to DST-DAAD and Dr. Peter Braun-Munzinger, Scientific director, EMMI for their support via which I was able to make research visits to GSI.

I would like to extend a special thanks to Dr. Amaresh Jaiswal, for his kind collaboration and support in our phenomenological work. I have learnt so much from him during this journey. At VECC, I met some gems of the field like Dr. Subhasis Chattopadhyaay, Dr. Anand Kumar Dubey, Dr. Premomoy Ghosh and Mr. Vikas Singhal. I am also thankful to you for your guidance and support. My sincere thanks to my PSPC members, Prof. Subhendu Rakshit and Dr. Aquil

Khan, Head of DPGC and Head of Discipline of Physics for their time to time support and suggestions. I extend my utmost gratitude towards Director sir, IIT Indore, all the faculties, staff members (Mr. Ujwal Kulkarni, Mr.Vedprakash Thakur, Mr. Nitin Upadhyay, Mr. Prasant Gupta, Mr. Tanmay Harsh Vaishnav), hostel staff (Santosh bhaiyya, Ram bhaiyya, Mr. Digant), housekeeping staff for their support. I acknowledge the sincere efforts of all the staff members of Academic Office (Mr. Tapesh Parihar), Accounts Section, R&D Section (Mr. Sunny Namdev), IT Section and Central Library, Medical staff whose constant support made sure the smooth functioning of my research work. I thank entire IIT Indore family for contributing in this thesis, one way or the other.

I would like to thank whole ALICE collaboration for all the support and privileges provided to me. I am incredibly grateful to the ALICE PWG-HF working group colleagues such as Dr. Deepa Thomas for her time to time suggestions, Dr. Alessandro Grelli, Dr. Andrea Rossi, Dr. Xiaoming Zhang, Dr. Martin Volkl, Dr. Preeti Dhankher, Shreyasi, Erin, Jiyeon and Jonghan. I am thankful to all ALICE-INDIA members for the opportunity to showcase my work in ALICE-INDIA meetings.

My time at GSI was very crucial professionally and during that time I met some fascinating personalities like Kanika ji, Arzoo ji, Diptnil, Ragan, Akash bhaiyya, Rajesh bhaiyya, Rajendra bhaiyya, Soumya bhaiyya and Shaifali. I would like to offer a very special thanks to all you. Rajesh bhaiyya and his family, and Shaifali had always made me feel at home when I was there and I would like to say thank you. You made this journey so much more beautiful. I also thank Ajit and Shaista ji, two of my good friends whose ability to cope with the pressure has always inspired me and I am grateful for your constant support. At VECC, I made very nice friends, Om, Vivek and Apar to whom I would like thank for everything.

This thesis is also reached its completion with the support of my Lab mates Ajay bhaiyya, Ankita didi who has been a major source of inspiration, Sudeep bhaiyya, Saeed, Sumit, Jaswant, Ravindra, Hriday, Prasoon, Ravi and Yoshini. I am extremely thankful to you all. Besides them, there were some good friends

outside lab such as, Rahul, Mritunjay, Manu Shree, Sujata, Siddhartha, Dhurv, Sarvesh, Arnab, Saptarshi, Alok, Pramod, Mrinal, Rajarshi, Sushanta, Dhananjay, Arvind, Aditya bhaiyya, Prakhar bhaiyya to whom I was fortunate to meet and I want to thanks a lot for your kindness. A special thanks to my roommate Priodyuti, whose guidance, late-night conversations and moral support kept me going. I am grateful to my brother like friend, Arijit, who is my go-to person whenever I felt down. I thank Dr. Biplab Ghosh for his encouraging words from time to time. There is special group of friends from Master days, with their constant support this journey was quite the fun. I want to thank Onkar Ramdasi, Umesh Gayake, Arun Jadhav, Sagar Gore, Sudhir Khomane, Sanam Thakur, Sagar Parkhe and others for being there for me all the time. My sincere thanks to all my school teachers and college professors, without their contribution I would not have been here today. I apologize if I have forgotten to acknowledge anybody.

This thesis is a result of the blessings of my parents and family, without their moral support, I would not even be here. I am thankful to my sister, Arti and brother-in-law, Sagar for their constant and never-ending support during my PhD and lots of love to my nephew Atharv. I want to thank all my relatives.

At last, one would like to believe and have faith in some power beyond all the rationalities and our control to guide us on the right path and provide with the required patience and courage to achieve our goal. I would like to seek the blessings from the Almighty and thanks for everything that has been offered to me.

A big thank you.

(Sudhir Pandurang Rode)

Synopsis

Introduction

The strongly interacting deconfined state of quarks and gluons popularly known as quark-gluon plasma (QGP), was expected to have prevailed shortly after the Big-Bang. Strong interactions are explained using a quantum field theory known as Quantum ChromoDynamics (QCD). Since gluons carry "color" charge, this gives rise to self-interactions due to which the QCD coupling constant (α_s) increases with increase in separation between quarks (r) or decrease in the momentum transfer (Q) [7]. Confinement and asymptotic freedom are the properties of QCD. Confinement results in no observation of free quarks and gluons under normal circumstances whereas, at sufficiently high temperature or pressure, the strength of α_s weakens and the quarks and gluons become asymptotically free, i.e. asymptotic freedom. Phase diagram of QCD matter suggests that at sufficiently high temperature and/or density, the nuclear matter undergoes a phase transition from hadronic stage to a phase where the quarks and gluons are no longer confined. One of the major objectives of the relativistic heavy-ion collision research program is to explore the phase structure of such a strongly interacting matter. Regions of temperature and baryon density can be accessed in a particular experiment, depending on the collision energy. Thus, systems with very small net baryon densities but a rather high temperature are formed at top Relativistic Heavy Ion Collider (RHIC) and Large Hadron Collider (LHC) energies. Data collected by the experiments at these two collider facilities have provided conclusive evidence for the formation of strongly coupled QGP [18]. Compared to this, the QCD phase diagram is much less explored in the region of high net baryon densities. Hence, the ongoing Beam Energy Scan (BES) program at RHIC and the upcoming heavy-ion collision experiments at the Nuclotron-based Ion Collider fAcility (NICA) at the Joint Institute for Nuclear Research (Dubna) and at the Facility for Antiproton and Ion Research (FAIR, Germany) aim at probing the moderate temperature and high baryonic chemical potential regime of the QCD phase diagram.

Motivation

As mentioned earlier, QGP is expected to form at high temperature (and low baryon density) as well as at moderate temperature (and very high baryon densities) regime of the QCD phase diagram. This is enough to motivate one to explore the nature of such matter at these conditions of temperature and density. The experiments which perform this study are in huge collaborations and it is not easy to get the opportunity to explore the physics at both these regimes simultaneously. However, running experiments are not the only way to examine the properties of the produced medium; one can perform the phenomenological study by confronting the measurements already performed by the experiments with theoretical models. In this thesis, the attempt has been made to explore the low as well as high energy regimes of the QCD phase diagram. A Large Ion Collider Experiment (ALICE) at the LHC is one of the experiments in the world which is designed to probe such exotic state of QCD matter in heavy-ion collisions at very low baryon density and high temperatures whereas, there are several experiments performed over last four decades to probe the baryon rich matter at low energies at Alternating Gradient Synchrotron (AGS) and Super Proton Synchrotron (SPS) accelerator facilities.

In order to explore the high temperature regime of the QCD phase diagram, the heavy-flavours, i.e. charm and beauty quarks, are a suitable choice for investigating the nature of the quark-gluon plasma. Since their masses are large, they are formed via initial hard scatterings in the early stages of the collision and therefore, can witness whole evolution of the medium. Heavy-flavours can be measured via decay products of open heavy-flavour hadrons (hadrons with single charm or beauty quark) in semi-electronic channels. The electrons originating from both charm and beauty quark decays are measured using different analysis techniques in proton-proton collisions where the possibility of production of QGP is small. These measurements are very important as a baseline for the corresponding study in heavy-ion collisions, where the in-medium modifications of these heavy-flavours due to the presence of medium can be observed. Mass-dependent energy loss of the quarks in the medium can be performed in

heavy-ion collisions and the corresponding reference is provided by measuring electrons coming exclusively from beauty quarks in proton-proton collisions in this thesis. Since these measurements are performed using the detectors and different selection criteria, they are suffered from the systematic uncertainties and it is important to have control over them to achieve a very good precision. The analysis techniques used to perform these measurements have helped to reduce the systematic uncertainties with respect to the published results and other analysis techniques, which is one of the highlights of this thesis. In the low energy regime of the QCD phase diagram, the comparative study of published experimental measurements is performed using different phenomenological models. Moreover, apart from heavy-flavours, there are other observables which can provide some insight into the medium produced in the heavy-ion collisions. Collective flow in central and non-central nuclear collisions is one of such observables which can lead to some information about the dynamics of the medium prevailed. In central collisions, transverse as well as longitudinal flow of the produced particles can reveal information about the collision dynamics at freeze-out surfaces whereas, in non-central collisions, the anisotropic flow of those particles provides insight about the thermalisation of the hydrodynamic driven QCD medium. In the former case, the measurements of light hadrons and heavy strange hadrons from low energy experiments are confronted with the blast-wave description within the non-boost-invariant scenario to study the mass-dependent hierarchy of the kinetic freeze-out parameters such as kinetic freeze-out temperature (T_{kin}) and average transverse velocity (β_T) at different bombarding energies. However, in the latter case, more of a feasibility study using the Ultra-relativistic Quantum Molecular Dynamics (UrQMD) model [66] is done which is essential and can provide important predictions useful for the upcoming experiments at different accelerator facilities such as FAIR and NICA.

Data analysis in high energy nuclear collisions

In this thesis, the data analysis is performed with the data collected by ALICE detector at the LHC. ALICE consists of several sub-detectors which are based

on various detection principles according to the nature of particles and their kinematics. Some of the detectors such as Inner Tracking System (ITS), Time Projection Chamber (TPC), Time Of Flight (TOF) are used for tracking as well as particle identifications in these analyses. These analyses are performed in a special framework of computing Grid resources in ALICE environment.

Electrons from heavy-flavour hadrons in pp collisions

Electrons from charm and beauty quarks are measured using a data-driven technique known as photonic electron tagging method in pp collisions at $\sqrt{s} = 7$ TeV and 13 TeV with normal (0.5 Tesla) and low (0.2 Tesla) magnetic field (B) respectively. Electrons are identified using TPC and TOF detectors based on specific energy loss and time of flight information of the traversing particles, respectively. Moreover, the remaining contamination from hadrons is subtracted statistically by parameterising the TPC signal in different momentum regions. The dominant source of background to heavy-flavour electrons is the electrons originating from the Dalitz decay of light mesons (π^0 and η) and conversion of photons, named as photonic electrons in the text. The electron-positron pairs from all the final state particles of Dalitz decays are used to estimate the contribution from the photonic electrons in each transverse momentum (p_{T}) bin. For this purpose, the pools of the electrons with tighter selection criteria to select the signal and looser selection criteria to allow as much photonic background as possible, are built. Then the invariant mass distributions of like (e^+e^+ or e^-e^-) and unlike (e^+e^-) pairs are obtained by ”tagging” electron (positron) from one pool (inclusive candidates) with the electron (positron) from other pool (associated candidates) and contribution below certain pair invariant mass ($m_{inv} <$ 0.14 GeV/c) is selected in each transverse momentum (p_{T}) bin. However, due to the acceptance and the detector limitations, we are not able to get all the photonic electrons. So, using Monte Carlo (MC) simulations, we estimate the conditional probability (also called as tagging efficiency) that how much of the electrons are being ”tagged” within the acceptance out of total produced and the actual photonic contribution is estimated. Since MC simulations are not able to

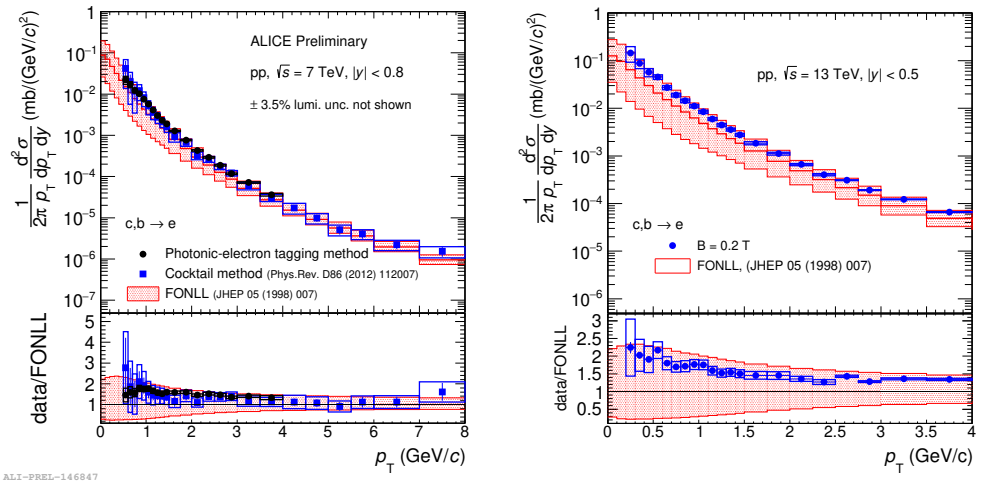

Figure 1. The p_{T}-differential invariant production cross-section (black, circle symbols) of electrons from semileptonic heavy-flavour hadron decays measured at mid-rapidity in pp collisions at $\sqrt{s} = 7$ TeV (left plot) and at $\sqrt{s} = 13$ TeV (right plot) with the FONLL pQCD calculations [48] (upper panel), and the ratio of the data to the FONLL calculation (lower panels of the plots). The cross-section at $\sqrt{s} = 7$ TeV is also compared with the previously published result (blue, square symbols) and shows nice agreement.

reproduce the data well, the transverse momentum distributions of the mothers of photonic electrons are re-weighted using the measured spectra to calculate the proper tagging efficiency. The raw heavy-flavour electron spectrum is obtained by subtracting photonic spectra from the inclusive electron spectrum. This raw spectra is further corrected for detector effects by estimating tracking and particle identification (PID) efficiencies of the detectors.

The final invariant production cross-section is then compared with pQCD (perturbative QCD) calculations, i.e. FONLL (Fixed Order Next-to-Leading Log Resummation). The measured cross-sections at both $\sqrt{s} = 7$ TeV and 13 TeV show nice agreement with those predictions as shown in Figure 3.28. Statistical uncertainties are shown as vertical bars whereas, boxes denote the systematic uncertainties. Moreover, the cross-section at $\sqrt{s} = 7$ TeV is also compared with previously published measurement which was performed using the cocktail method [86] and had sizable systematic uncertainties. The photonic electron tagging method has helped to reduce the systematic uncertainties down by factor 3 at low p_{T} region. The cross-section at $\sqrt{s} = 7$ TeV is measured in transverse momentum range 0.5 to 4.0 GeV/c whereas, the one at $\sqrt{s} = 13$

TeV is measured between 0.2 to 4.0 GeV/c due to the low magnetic field which allows better reconstruction efficiency at low transverse momentum region.

Electrons from beauty hadrons in pp collisions

Furthermore, the energy loss of the particles in the quark-gluon plasma exhibits mass dependence which can be tested by measuring beauty quarks alone. The electrons from beauty quark decays are measured using the DCA (Distance of Closest Approach to the Primary Vertex) fit method in pp collisions at $\sqrt{s} = 5.02$ TeV. In this method, the DCA distributions (or templates) of electrons from different sources are obtained from MC simulations and are fitted to the measured inclusive electron DCA spectrum using the maximum likelihood fit approach. The fit returns four amplitudes for four different electrons sources and the raw yield of electrons from beauty quarks is obtained. The final invariant production cross-section is obtained by correcting raw yield using the tracking and PID efficiencies. However, due to a very small signal to background ratio and low tracking and PID efficiencies, the measurement of beauty electrons at low transverse momentum is difficult. So, the measurement of the cross-section is restricted down to transverse momentum 2 GeV/c up to 8 GeV/c.

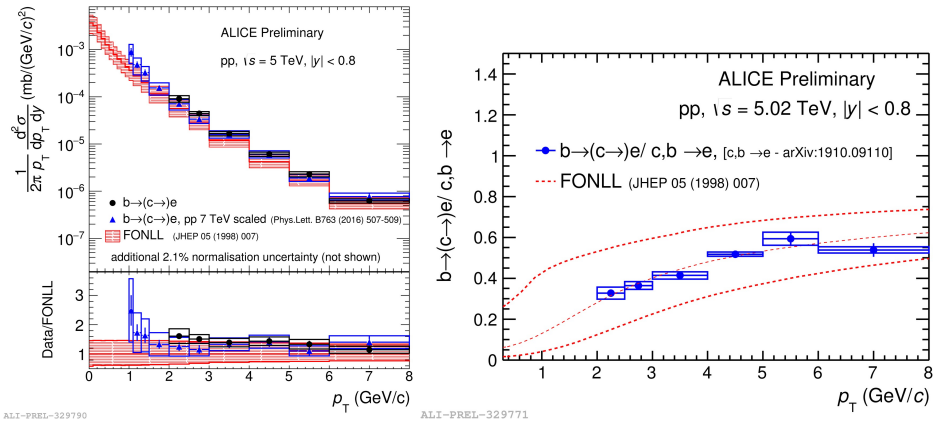

Figure 2. Left: p_{T}-differential cross-section of electrons from beauty hadron decays and its comparison with the FONLL prediction [48] and its comparison with the cross-section obtained from scaling $\sqrt{s} = 7$ TeV cross-section using FONLL. Right: Fraction of electrons of beauty hadron decays to electron from heavy-flavour hadron decays

The measured cross-section is then compared with FONLL predictions

and it shows nice agreement. The cross-section is also compared with measured cross-section at $\sqrt{s} = 7$ TeV [104] scaled to $\sqrt{s} = 5.02$ TeV using the FONLL predictions and are consistent with each other within the uncertainties as shown in Figure 4.23 (left plot). Vertical bars are statistical uncertainties and systematic uncertainties are denoted by boxes. The relative contribution of beauty quarks to the total heavy-flavour electron contribution is obtained, as shown in the Figure 4.23 (right plot). The production cross-section of electrons from heavy-flavour hadron decays in pp collisions at $\sqrt{s} = 5.02$ TeV is used for the estimation of the fraction which is measured by ALICE with good precision [63]. This ratio is compared with the central, upper and lower limit of FONLL predictions. The beauty contribution hints to dominate the total heavy-flavour electron contribution beyond $p_{\mathrm{T}} > 4$ GeV/c.

Collective flow in low energy nuclear collisions

In this section, we attempt to study the collective properties of the produced fireball and the freeze-out conditions of the emitted particles in the low energy heavy-ion collisions which can be used as predictions for the upcoming experiments in different accelerator facilities around the globe. Study of the collective flow, both isotropic and anisotropic, have been one of the interesting domain of the relativistic heavy-ion collisions since the start of the heavy-ion program. In central collisions, the average longitudinal and transverse components of the isotropic collective flow infer about the properties of collision dynamics at the freeze-out surface whereas, in non-central collisions, the anisotropic flow coefficients are sensitive to the underlying nuclear equations of state.

Kinetic freeze-out conditions of light and heavy hadrons

At first, the kinetic freeze-out conditions of light/bulk hadrons ($\pi^{\pm}$, $\mathrm{K}^{\pm}$ and p) are studied in central Au + Au and Pb + Pb collisions, at AGS, SPS and partially at RHIC BES energies, using a non-boost-invariant version of the blast-wave model. Due to its simplicity, blast-wave models have been widely used for a

long time to analyse momentum distribution of the produced hadrons and provide information about the properties of the matter at kinetic freeze-out. The main underlying assumption is that the particles in the system produced in the collisions are locally thermalised (till they are emitted from the medium) and the system expands collectively with a common radial velocity field undergoing an instantaneous common freeze-out. The assumption of underlying boost-invariant longitudinal dynamics is reasonable at RHIC and LHC energies; however, it does not hold good at AGS and SPS energies. Therefore, in order to describe particle production at these energy domains, the assumption of boost-invariance must be relaxed. We have thus employed a variant of the blast-wave model, where the boost-invariance is explicitly broken by introducing a dependence of the transverse size of the fireball on the space-time rapidity (η).

E_{Lab} (AGeV)	Hadrons	η_{max}	$\langle\beta_T\rangle$	T_{kin} (MeV)	χ^2/N_{dof}
20	Strange	1.288 ± 0.021	0.4418 ± 0.0032	93.09 ± 0.19	1.9
	Light	1.882 ± 0.005	0.5177 ± 0.0011	79.77 ± 0.05	6.5
30	Strange	1.728 ± 0.026	0.4501 ± 0.0029	95.84 ± 0.17	2.2
	Light	2.084 ± 0.004	0.5368 ± 0.0011	80.28 ± 0.05	6.7
40	Strange	1.752 ± 0.018	0.4536 ± 0.0026	98.82 ± 0.14	3.7
	Light	2.094 ± 0.004	0.5356 ± 0.0009	81.92 ± 0.04	5.5
80	Strange	1.989 ± 0.021	0.4489 ± 0.0022	106.46 ± 0.12	3.6
	Light	2.391 ± 0.005	0.5347 ± 0.0012	82.68 ± 0.05	3.8
158	Strange	2.031 ± 0.029	0.4688 ± 0.0016	109.24 ± 0.11	3.4
	Light	2.621 ± 0.006	0.538 ± 0.0013	84.11 ± 0.06	4.4

Table 1. Summary of the fit results of heavy strange and light hadrons at different energies from SPS.

The transverse momentum (p_T) spectra for a variety of bulk and rare hadronic species are analysed within the opted non-boost-invariant blast-wave model framework, in the beam energy (E_{lab}) range 20 A - 158 A GeV. Following a linear transverse flow profile, there are three parameters namely T_{kin}, η_{max} and β_T^0 respectively signifying the kinetic freeze-out temperature, width of space-time rapidity and transverse flow gradient which are common for all hadrons at a given energy and extracted from the simultaneous fitting of the p_T spectra of selected hadronic species. To explore the effect of longitudinal dynamics, the

available rapidity spectra are also analysed using the extracted parameters from p_{T} spectra.

Furthermore, identified hadrons over a wide range of masses are analysed under the same framework to study the mass-dependent hierarchy in kinetic freeze-out parameters. For this, along with the results from light hadrons (π^- and $\mathrm{K}^{\pm}$), the p_{T} and rapidity spectra of heavy strange hadrons such as Λ, $\bar{\Lambda}$, ϕ, $\Xi^{\pm}$ and $\Omega^{\pm}$ at different SPS energies and only p_{T} spectra of Charmonia (J/ψ, $\psi^{'}$), due to unavailability of their rapidity spectra at top SPS energy ($\mathrm{E_{lab}} = 158$ AGeV) are analysed using the same model. The fit results for heavy strange and light hadrons at SPS energies are shown in Table 5.3 and displayed in Figure 5.13. Left plot of the Figure 5.13 shows a higher value of T_{kin} for heavy

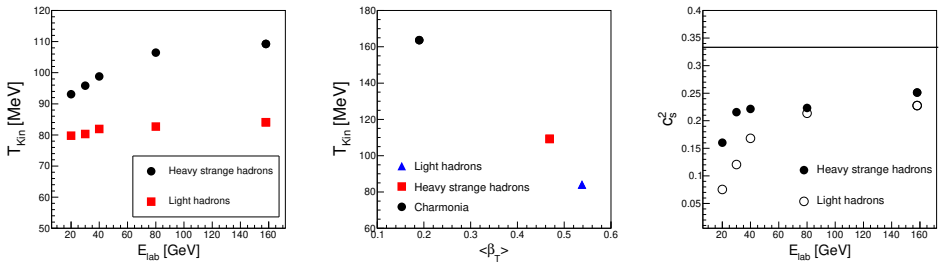

Figure 3. Left: Kinetic freeze-out temperature (T_{kin}) for heavy strange and light hadrons with incident beam energy ($\mathrm{E_{lab}}$). Middle: The (partial) expansion history of the fireball created in central Pb+Pb collisions at $\mathrm{E_{lab}} = 158A$ GeV. The points indicate T_{kin} and mean transverse collective flow velocity ($\langle\beta_T\rangle$) of the system at the time of charm, heavy strange and light hadron kinetic freeze-out. Right: Variation of the speed of sound for heavy strange and light hadrons using a non-conformal solution of Landau hydrodynamical model with beam energy. The horizontal line at $\mathrm{c_s^2} = 1/3$ indicates the ideal gas limit. Errors are within the marker size.

strange hadrons than the light hadrons indicating early kinetic decoupling of the former from the medium at all beam energies. We saw a mass-dependent hierarchy in T_{kin} and $\langle\beta_T\rangle$, as shown in the middle plot of Figure 5.13. Moreover, to take a more deeper look into the longitudinal properties of the medium, the rapidity spectra of heavy strange and light hadrons are analysed using recently developed non-conformal solution of Landau hydrodynamical model [154]. In this model, the speed of sound (c_s) is a common free parameter which is extracted from simultaneous fitting and found to be shown similar mass-dependent

hierarchy for heavy strange and light hadrons as shown in the right plot of Figure 5.13.

Anisotropic flow of charged hadrons

Study of the anisotropic flow coefficients of the bulk particles in the low energy non-central heavy-ion collisions is also performed. We made an attempt to address a long-standing issue of probing the equation-of-state of the strongly-interacting matter, from the measurement of collective flow observables in non-central heavy-ion collisions. We focus on the flow parameters, namely directed flow (v_1), elliptic flow (v_2) and quadrangular flow (v_4) at mid-rapidity in semi-central Au+Au collisions, in the beam energy (E_{lab}) range $6-25A$ GeV, where the future FAIR and NICA accelerators would be operated. The UrQMD transport approach coupled with the ideal hydrodynamic expansion for different nuclear equations of state is employed for this purpose.

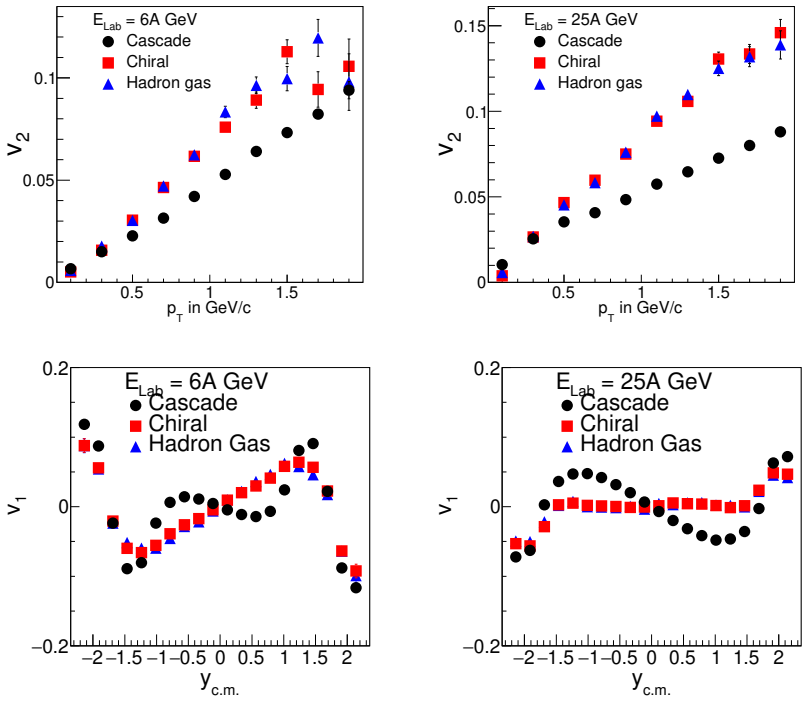

Figure 4. Top: v_2 vs p_T for charged hadrons using UrQMD for different EoS for E_{lab} = 6A and 25A GeV. Bottom: v_1 vs $y_{c.m.}$ for charged hadrons using UrQMD for different EoS for E_{lab} = 6A and 25A GeV

The elliptic flow parameter, v_2 of charged and identified hadrons as a function of transverse momentum and rapidity, is examined and it is noticed that v_2 is always higher in the hydrodynamic scenario when compared with the transport mode of the UrQMD model but fails to differentiate between the partonic and hadronic degrees of freedom as shown in Figure 6.1. This insensitivity can be attributed to the small lifetime of the hydrodynamic phase at such low energy collisions. Constituent quark number scaling of v_2 for all the energies and nuclear EoS is also studied, and reasonably good scaling of v_2 is observed. First harmonic coefficient of the azimuthal distribution, i.e. v_1 is sensitive to the longitudinal dynamics of the medium and hence it is studied as a function of the rapidity ($y_{c.m.}$). The slope of v_1 is observed to be sensitive to the hydrodynamical scenario and able to differentiate the pure transport mode from the hydro mode. However, similar to v_2, v_1 also shows insensitivity to the partonic and hadronic degrees of freedom.

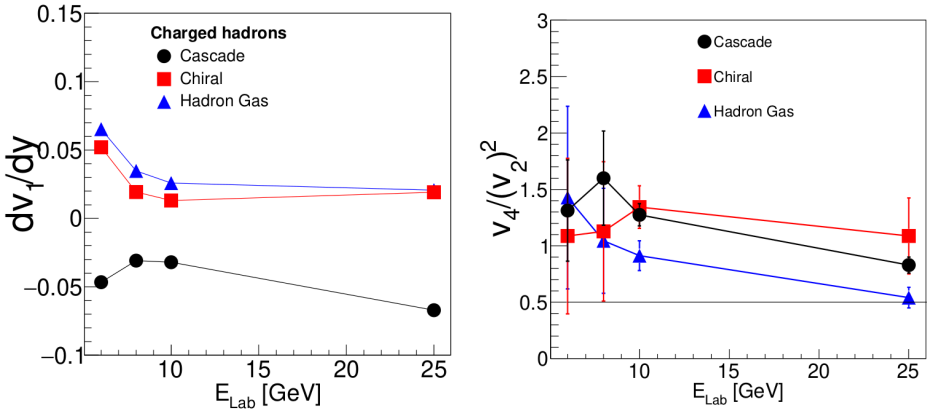

Figure 5. On left, Slope ($\frac{dv_1}{dy}$) at $y_{c.m.} \approx 0$ by fitting with polynomials as a function of beam energy (E_{Lab}) for different EoS at midrapidity. On right, $v_4/(v_2)^2$ as a function of beam energy (E_{Lab}) for different EoS at midrapidity.

Moreover, the beam energy (E_{Lab}) dependence of the slope of the directed flow (dv_1/dy), v_2 and v_4 of charged hadrons is examined for different equations of state. The generation of v_4 is governed by both the intrinsic v_2 and the 4^{th} order moment of collective flow and therefore, the contribution of v_2 to v_4 is simply estimated as $v_4 = 0.5(v_2)^2$, within ideal fluid dynamics and in the absence of any fluctuations. Hence, with the ratio $v_4/(v_2)^2$, one can gain some insights about the dynamics of the collision when studied as a function of beam energy

(E_{Lab}). The ratio is found to be varying between 0.5 to 2 (see right plot of Figure 6.19) but, given the statistical fluctuations, more conclusive remarks can be made upon their reduction.

Conclusions and outlook

In this thesis, an attempt is made to explore the properties of the medium that can be formed in low as well as high energy nuclear collisions. In the context of high energy collisions, the measurements of electrons from charm and beauty quarks in proton-proton collisions are performed using the data provided by ALICE experiment where the matter with very high temperature and almost zero baryonic chemical potential is believed to be produced. For these measurements, different analysis techniques are adopted and the results are compared with the theoretical predictions which show consistency. In the view of ongoing ALICE detector upgrade, the improved primary vertex and impact parameter resolution, together with the improved luminosity of the LHC accelerator complex, will provide a chance to perform the precision measurements. Moreover, the new measurements of the species such as Λ_b baryon and B meson would be possible.

In the later part, the focus is shifted to the other end of the QCD phase diagram, i.e. to study the matter produced in moderate temperature and high net baryon density regime. The mass-dependent hierarchy in the kinetic freeze-out parameters of light hadrons, heavy strange hadrons and charmonia produced in central low energy nuclear collisions are examined in the framework of the non-boost-invariant blast-wave model. Similar hierarchy in the speed of sound of light hadrons and heavy strange hadrons is observed when their rapidity spectra are studied using the non-conformal solution of the Landau hydrodynamical model. For the upcoming experiments at FAIR and NICA accelerator facilities, these measurements would be useful for a better understanding of the freeze-out conditions. Moreover, a simulation study of different anisotropic flow coefficients of charged hadrons in non-central nuclear collision at FAIR energies is performed using the UrQMD model which will also be very crucial once the data from experiments at FAIR and NICA will be available.

PUBLICATIONS

List of Publications:

(Results from papers marked with [*] are included in this thesis.)

1. [*] **S. P. Rode**, P. P. Bhaduri, A. Jaiswal and A. Roy, "Kinetic freeze out conditions in nuclear collisions with 2A - 158A GeV beam energy within a non-boost-invariant blast-wave model", Phys. Rev. C **98**, no. 2, 024907 (2018).

2. [*] **S. P. Rode**, P. P. Bhaduri and A. Roy, "Anisotropic flow of charged and identified hadrons at FAIR energies and its dependence on the nuclear equation of state", Eur. Phys. J. A **55** (2019) 216.

3. [*] **S. P. Rode**, P. P. Bhaduri, A. Jaiswal and A. Roy, "Hierarchy of kinetic freeze out parameters in low energy heavy-ion collisions", Phys. Rev. C **102**, 054912 (2020).

4. [*] Paper Draft: "Inclusive and multiplicity dependent production of heavy-flavour hadron decay electrons in pp and p-Pb collisions", Paper committee: P. Dhankher,S. Acharya, **S. P. Rode**, D. Thomas and A. Dubla, https://alice-publications.web.cern.ch/node/6090, **Manuscript in preparation**

5. [*] **Preliminary Physics Summary:** "Measurements of low-p_{T} electrons from semileptonic heavy-flavour hadron decays at mid-rapidity in pp collisions at $\sqrt{s} = 7$ TeV", **S. P. Rode**, A. Dubla https://cds.cern.ch/record/2317185?ln=en **[2018]**

6. [*] **Analysis Note:** "Electrons from heavy-flavour hadron decays at mid-rapidity and low transverse momenta in pp collisions at $\sqrt{s} = 7$ TeV and $\sqrt{s} = 5.02$ TeV", M. R. Ciupek, A. Dubla, S. Hornung, **S. P. Rode**

https://aliceinfo.cern.ch/Notes/node/782. **[2018]**

7. [*] **GSI Scientific Report:** "Production of electrons from semileptonic heavy-flavour hadron decays in proton-proton and heavy-ion collisions measured with ALICE at the LHC","RESEARCH-NQM-ALICE-6" http://dx.doi.org/10.15120/GSI-2017-01856. **[2018]**

8. [*] **Analysis Note:** "Measurement of beauty decay electron cross-section in pp collisions at mid-rapidity and low transverse momenta in pp collisions at $\sqrt{s} = 5.02$ TeV" **S. P. Rode**
https://aliceinfo.cern.ch/Notes/node/984. **[2019]**

9. [*] **Analysis Note:** "Electrons from heavy-flavour hadron decays at mid-rapidity and low transverse momenta in pp collisions at $\sqrt{s} = 13$ TeV with Low magnetic field (B = 0.2 T)", **S. P. Rode**
https://aliceinfo.cern.ch/Notes/node/1019. **[2019]**

10. **CBM progress report 2016:** "Differential elliptic flow of charged hadrons at FAIR SIS100" **S. P. Rode**, A. Roy , P.P. Bhaduri
http://repository.gsi.de/record/201318. **[2016]**

11. **CBM progress report 2017:** "Inclusion of detector in-efficiency in CBM MuCh simulations", **S. P. Rode**, P.P. Bhaduri, V. Singhal, E. Nandy, S. Chattopadhyay, and A. Roy
http://repository.gsi.de/record/209729. **[2017]**

12. S. Acharya, ..., **S. P. Rode** *et al.* [ALICE Collaboration], "Pion-kaon femtoscopy and the lifetime of the hadronic phase in Pb−Pb collisions at $\sqrt{s_{\rm NN}}$ = 2.76 TeV," [arXiv:2007.08315 [nucl-ex]].

13. S. Acharya, ..., **S. P. Rode** *et al.* [ALICE Collaboration], "Production of ω mesons in pp collisions at $\sqrt{s}$ = 7 TeV," [arXiv:2007.02208 [nucl-ex]].

14. S. Acharya, ..., **S. P. Rode** *et al.* [ALICE Collaboration], "Elliptic and triangular flow of (anti)deuterons in Pb-Pb collisions at $\sqrt{s_{\rm NN}}$ = 5.02 TeV," [arXiv:2005.14639 [nucl-ex]].

15. S. Acharya, ..., **S. P. Rode** *et al.* [ALICE Collaboration], "J/ψ elliptic and triangular flow in Pb-Pb collisions at $\sqrt{s_{\rm NN}}$ = 5.02 TeV," [arXiv:2005.14518 [nucl-ex]].

16. S. Acharya, ..., **S. P. Rode** *et al.* [ALICE Collaboration], "Measurement of isolated photon-hadron correlations in $\sqrt{s_{\rm NN}}$ = 5.02 TeV pp and p-Pb collisions," [arXiv:2005.14637 [nucl-ex]].

17. S. Acharya, ..., **S. P. Rode** *et al.* [ALICE Collaboration], "Constraining the Chiral Magnetic Effect with charge-dependent azimuthal correlations in Pb-Pb collisions at $\sqrt{s_{\rm NN}}$ = 2.76 and 5.02 TeV," [arXiv:2005.14640 [nucl-ex]].

18. S. Acharya, ..., **S. P. Rode** *et al.* [ALICE Collaboration], "Soft-dielectron excess in proton-proton collisions at $\sqrt{s}$ = 13 TeV," [arXiv:2005.14522 [nucl-ex]].

19. S. Acharya, ..., **S. P. Rode** *et al.* [ALICE Collaboration], "Dielectron production in proton-proton and proton-lead collisions at $\sqrt{s_{\rm NN}}$ = 5.02 TeV," [arXiv:2005.11995 [nucl-ex]].

20. S. Acharya, ..., **S. P. Rode** *et al.* [ALICE Collaboration], "A new laboratory to study hadron-hadron interactions," [arXiv:2005.11495 [nucl-ex]].

21. S. Acharya, ..., **S. P. Rode** *et al.* [ALICE Collaboration], "Elliptic flow of electrons from beauty-hadron decays in Pb-Pb collisions at $\sqrt{s_{\rm NN}}$ = 5.02 TeV," [arXiv:2005.11130 [nucl-ex]].

22. S. Acharya, ..., **S. P. Rode** *et al.* [ALICE Collaboration], "Z-boson production in p-Pb collisions at $\sqrt{s_{\rm NN}} = 8.16$ TeV and Pb-Pb collisions at $\sqrt{s_{\rm NN}} = 5.02$ TeV," [arXiv:2005.11126 [nucl-ex]].

23. S. Acharya, ..., **S. P. Rode** *et al.* [ALICE Collaboration], "First measurement of quarkonium polarization in nuclear collisions at the LHC," [arXiv:2005.11128 [nucl-ex]].

24. S. Acharya, ..., **S. P. Rode** *et al.* [ALICE Collaboration], "Transverse-momentum and event-shape dependence of D-meson flow harmonics in Pb-Pb collisions at $\sqrt{s_{NN}} = 5.02$ TeV," [arXiv:2005.11131 [nucl-ex]].

25. S. Acharya, ..., **S. P. Rode** *et al.* [ALICE Collaboration], "Production of light-flavor hadrons in pp collisions at $\sqrt{s}$ = 7 and $\sqrt{s}$ = 13 TeV," [arXiv:2005.11120 [nucl-ex]].

26. S. Acharya, ..., **S. P. Rode** *et al.* [ALICE Collaboration], "Multiplicity dependence of J/ψ production at midrapidity in pp collisions at $\sqrt{s}$ = 13 TeV," [arXiv:2005.11123 [nucl-ex]].

27. S. Acharya, ..., **S. P. Rode** *et al.* [ALICE Collaboration], "Measurement of the low-energy antideuteron inelastic cross section," [arXiv:2005.11122 [nucl-ex]].

28. S. Acharya, ..., **S. P. Rode** *et al.* [ALICE Collaboration], "ΛK femtoscopy in Pb-Pb collisions at $\sqrt{s_{\rm NN}}$ = 2.76 TeV," [arXiv:2005.11124 [nucl-ex]].

29. S. Acharya, ..., **S. P. Rode** *et al.* [ALICE Collaboration], "J/ψ production as a function of charged-particle multiplicity in p-Pb collisions at $\sqrt{s_{\rm NN}} = 8.16$ TeV," [arXiv:2004.12673 [nucl-ex]].

30. S. Acharya, ..., **S. P. Rode** *et al.* [ALICE Collaboration], "Search for a common baryon source in high-multiplicity pp collisions at the LHC," [arXiv:2004.08018 [nucl-ex]].

31. S. Acharya, ..., **S. P. Rode** *et al.* [ALICE Collaboration], "Measurement of nuclear effects on $\psi(2S)$ production in p-Pb collisions at $\sqrt{s_{\rm NN}} = 8.16$ TeV," [arXiv:2003.06053 [nucl-ex]].

32. S. Acharya, ..., **S. P. Rode** *et al.* [ALICE Collaboration], "(Anti-)Deuteron production in pp collisions at $\sqrt{s} = 13$ TeV," [arXiv:2003.03184 [nucl-ex]].

33. S. Acharya, ..., **S. P. Rode** *et al.* [ALICE Collaboration], "Multiplicity dependence of π, K, and p production in pp collisions at $\sqrt{s} = 13$ TeV," [arXiv:2003.02394 [nucl-ex]].

34. S. Acharya, ..., **S. P. Rode** *et al.* [ALICE Collaboration], "Coherent photoproduction of ρ^0 vector mesons in ultra-peripheral Pb-Pb collisions at $\sqrt{s_{\rm NN}}$ = 5.02 TeV," JHEP **06** (2020), 035

35. S. Acharya, ..., **S. P. Rode** *et al.* [ALICE Collaboration], "Linear and non-linear flow modes of charged hadrons in Pb-Pb collisions at $\sqrt{s_{\rm NN}}$ = 5.02 TeV," JHEP **05** (2020), 085

36. S. Acharya, ..., **S. P. Rode** *et al.* [ALICE Collaboration], "Non-linear flow modes of identified particles in Pb-Pb collisions at $\sqrt{s_{\rm NN}}$ = 5.02 TeV," JHEP **06** (2020), 147

37. S. Acharya, ..., **S. P. Rode** *et al.* [ALICE Collaboration], "Investigation of the p-Σ^0 interaction via femtoscopy in pp collisions," Phys. Lett. B **805** (2020), 135419

38. S. Acharya, ..., **S. P. Rode** *et al.* [ALICE Collaboration], "Centrality and transverse momentum dependence of inclusive J/ψ production at midrapidity in Pb-Pb collisions at $\sqrt{s_{\rm NN}}$ = 5.02 TeV," Phys. Lett. B **805** (2020), 135434

39. S. Acharya, ..., **S. P. Rode** *et al.* [ALICE Collaboration], "Evidence of rescattering effect in Pb-Pb collisions at the LHC through production of $\rm K^*(892)^0$ and $\phi(1020)$ mesons," Phys. Lett. B **802** (2020), 135225

40. S. Acharya, ..., **S. P. Rode** *et al.* [ALICE Collaboration], "Longitudinal and azimuthal evolution of two-particle transverse momentum correlations in Pb-Pb collisions at $\sqrt{s_{\rm NN}}$ = 2.76 TeV," Phys. Lett. B **804** (2020), 135375

41. S. Acharya, ..., **S. P. Rode** *et al.* [ALICE Collaboration], "Production of (anti-)^{3}He and (anti-)^{3}H in p-Pb collisions at $\sqrt{s_{\rm NN}}$ = 5.02 TeV," Phys. Rev. C **101** (2020) no.4, 044906

42. S. Acharya, ..., **S. P. Rode** *et al.* [ALICE Collaboration], "Underlying Event properties in pp collisions at $\sqrt{s}$ = 13 TeV," JHEP **04** (2020), 192

43. S. Acharya, ..., **S. P. Rode** *et al.* [ALICE Collaboration], "Measurement of electrons from heavy-flavour hadron decays as a function of multiplicity in p-Pb collisions at $\sqrt{s_{\rm NN}}$ = 5.02 TeV," JHEP **02** (2020), 077

44. S. Acharya, ..., **S. P. Rode** *et al.* [ALICE Collaboration], "Probing the effects of strong electromagnetic fields with charge-dependent directed flow in Pb-Pb collisions at the LHC," Phys. Rev. Lett. **125** (2020) no.2, 022301

45. S. Acharya, ..., **S. P. Rode** *et al.* [ALICE Collaboration], "Jet-hadron correlations measured relative to the second order event plane in Pb-Pb collisions at $\sqrt{s_{\rm NN}}$ = 2.76 TeV," Phys. Rev. C **101** (2020) no.6, 064901

46. S. Acharya, ..., **S. P. Rode** *et al.* [ALICE Collaboration], " production in pPb collisions at $\sqrt{s_{NN}}$=8.16 TeV," Phys. Lett. B **806** (2020), 135486

47. S. Acharya, ..., **S. P. Rode** *et al.* [ALICE Collaboration], "Measurement of spin-orbital angular momentum interactions in relativistic heavy-ion collisions," Phys. Rev. Lett. **125** (2020) no.1, 012301

48. S. Acharya, ..., **S. P. Rode** *et al.* [ALICE Collaboration], "Azimuthal correlations of prompt D mesons with charged particles in pp and p-Pb collisions at $\sqrt{s_{\rm NN}}$ = 5.02 TeV," [arXiv:1910.14403 [nucl-ex]].

49. S. Acharya, ..., **S. P. Rode** *et al.* [ALICE Collaboration], "Multiplicity dependence of K*(892)^0 and ϕ(1020) production in pp collisions at $\sqrt{s}$ =13 TeV," Phys. Lett. B **807** (2020), 135501

50. S. Acharya, ..., **S. P. Rode** *et al.* [ALICE Collaboration], "Global baryon number conservation encoded in net-proton fluctuations measured in Pb-Pb collisions at $\sqrt{s_{\rm NN}}$ = 2.76 TeV," Phys. Lett. B **807** (2020), 135564

51. S. Acharya, ..., **S. P. Rode** *et al.* [ALICE Collaboration], "K$^*(892)^0$ and $\phi(1020)$ production at midrapidity in pp collisions at $\sqrt{s}$ = 8 TeV," [arXiv:1910.14410 [nucl-ex]].

52. S. Acharya, ..., **S. P. Rode** *et al.* [ALICE Collaboration], "Measurement of electrons from semileptonic heavy-flavour hadron decays at midrapidity in pp and Pb-Pb collisions at $\sqrt{s_{\rm NN}}$ = 5.02 TeV," Phys. Lett. B **804** (2020), 135377

53. S. Acharya, ..., **S. P. Rode** *et al.* [ALICE Collaboration], "Measurement of the (anti-)^{3}He elliptic flow in Pb-Pb collisions at $\sqrt{s_{\rm NN}}$ = 5.02 TeV," Phys. Lett. B **805** (2020), 135414

54. S. Acharya, ..., **S. P. Rode** *et al.* [ALICE Collaboration], "Production of charged pions, kaons, and (anti-)protons in Pb-Pb and inelastic pp collisions at $\sqrt{s_{NN}}$ = 5.02 TeV," Phys. Rev. C **101** (2020) no.4, 044907

55. S. Acharya, ..., **S. P. Rode** *et al.* [ALICE Collaboration], "Measurements of inclusive jet spectra in pp and central Pb-Pb collisions at $\sqrt{s_{\rm NN}}$ = 5.02 TeV," Phys. Rev. C **101** (2020) no.3, 034911

56. S. Acharya, ..., **S. P. Rode** *et al.* [ALICE Collaboration], "Studies of J/ψ production at forward rapidity in Pb-Pb collisions at $\sqrt{s_{\rm NN}}$ = 5.02 TeV," JHEP **02** (2020), 041

57. S. Acharya, ..., **S. P. Rode** *et al.* [ALICE Collaboration], "Global polarization of $\Lambda\bar{\Lambda}$ hyperons in Pb-Pb collisions at $\sqrt{s_{NN}}$ = 2.76 and 5.02 TeV," Phys. Rev. C **101** (2020) no.4, 044611

58. S. Acharya, ..., **S. P. Rode** *et al.* [ALICE Collaboration], "Multiplicity dependence of (multi-)strange hadron production in proton-proton collisions at $\sqrt{s}$ = 13 TeV," Eur. Phys. J. C **80** (2020) no.2, 167

59. S. Acharya, ..., **S. P. Rode** *et al.* [ALICE Collaboration], "$^3_\Lambda$H and $^{\bar{3}}_{\bar{\Lambda}}\bar{\rm H}$ lifetime measurement in Pb-Pb collisions at $\sqrt{s_{\rm NN}} = 5.02$ TeV via two-body decay," Phys. Lett. B **797** (2019), 134905

60. S. Acharya, ..., **S. P. Rode** *et al.* [ALICE Collaboration], "Measurement of $\Upsilon(1S)$ elliptic flow at forward rapidity in Pb-Pb collisions at $\sqrt{s_{\rm NN}} =$ 5.02 TeV," Phys. Rev. Lett. **123** (2019) no.19, 192301

61. S. Acharya, ..., **S. P. Rode** *et al.* [ALICE Collaboration], "Measurement of prompt D^0, D^+, D^{*+}, and D_S^+ production in pPb collisions at $\sqrt{s_{NN}}$ = 5.02 TeV," JHEP **12** (2019), 092

62. S. Acharya, ..., **S. P. Rode** *et al.* [ALICE Collaboration], "Multiplicity dependence of light (anti-)nuclei production in p-Pb collisions at $\sqrt{s_{NN}}$ = 5.02 TeV," Phys. Lett. B **800** (2020), 135043

63. S. Acharya, ..., **S. P. Rode** *et al.* [ALICE Collaboration], "Measurement of the inclusive isolated photon production cross section in pp collisions at $\sqrt{s}$ = 7 TeV," Eur. Phys. J. C **79** (2019) no.11, 896

64. S. Acharya, ..., **S. P. Rode** *et al.* [ALICE Collaboration], "Scattering studies with low-energy kaon-proton femtoscopy in proton-proton collisions at the LHC," Phys. Rev. Lett. **124** (2020) no.9, 092301

65. S. Acharya, ..., **S. P. Rode** *et al.* [ALICE Collaboration], "Charged-particle production as a function of multiplicity and transverse spherocity in pp collisions at $\sqrt{s} = 5.02$ and 13 TeV," Eur. Phys. J. C **79** (2019) no.10, 857

66. S. Acharya, ..., **S. P. Rode** *et al.* [ALICE Collaboration], "Study of the Λ-Λ interaction with femtoscopy correlations in pp and p-Pb collisions at the LHC," Phys. Lett. B **797** (2019), 134822

67. S. Acharya, ..., **S. P. Rode** *et al.* [ALICE Collaboration], "Inclusive J/ production at mid-rapidity in pp collisions at $\sqrt{s}$ = 5.02 TeV," JHEP **10** (2019), 084

68. S. Acharya, ..., **S. P. Rode** *et al.* [ALICE Collaboration], "Production of muons from heavy-flavour hadron decays in pp collisions at $\sqrt{s}$ = 5.02 TeV," JHEP **09** (2019), 008

69. S. Acharya, ..., **S. P. Rode** *et al.* [ALICE Collaboration], "Measurement of the production of charm jets tagged with D^0 mesons in pp collisions at $\sqrt{s} = 7$ TeV," JHEP **08** (2019), 133

70. S. Acharya, ..., **S. P. Rode** *et al.* [ALICE Collaboration], "Exploration of jet substructure using iterative declustering in pp and PbPb collisions at LHC energies," Phys. Lett. B **802** (2020), 135227

71. S. Acharya, ..., **S. P. Rode** *et al.* [ALICE Collaboration], "Measurement of charged jet cross section in pp collisions at $\sqrt{s} = 5.02$ TeV," Phys. Rev. D **100** (2019) no.9, 092004

72. S. Acharya, ..., **S. P. Rode** *et al.* [ALICE Collaboration], "Measurement of jet radial profiles in PbPb collisions at $\sqrt{s_{\rm NN}} = 2.76$ TeV," Phys. Lett. B **796** (2019), 204-219

73. S. Acharya, ..., **S. P. Rode** *et al.* [ALICE Collaboration], "First Observation of an Attractive Interaction between a Proton and a Cascade Baryon," Phys. Rev. Lett. **123** (2019) no.11, 112002

74. S. Acharya, ..., **S. P. Rode** *et al.* [ALICE Collaboration], "Coherent J/ψ photoproduction at forward rapidity in ultra-peripheral Pb-Pb collisions at $\sqrt{s_{\rm NN}} = 5.02$ TeV," Phys. Lett. B **798** (2019), 134926

75. S. Acharya, ..., **S. P. Rode** *et al.* [ALICE Collaboration], "One-dimensional charged kaon femtoscopy in p-Pb collisions at $\sqrt{s_{\rm NN}}$ = 5.02 TeV," Phys. Rev. C **100** (2019) no.2, 024002

76. S. Acharya, ..., **S. P. Rode** *et al.* [ALICE Collaboration], "Measurement of strange baryonantibaryon interactions with femtoscopic correlations," Phys. Lett. B **802** (2020), 135223

77. S. Acharya, ..., **S. P. Rode** *et al.* [ALICE Collaboration], "Investigations of Anisotropic Flow Using Multiparticle Azimuthal Correlations in pp, p-Pb, Xe-Xe, and Pb-Pb Collisions at the LHC," Phys. Rev. Lett. **123** (2019) no.14, 142301

78. S. Acharya, ..., **S. P. Rode** *et al.* [ALICE Collaboration], "Multiplicity dependence of (anti-)deuteron production in pp collisions at $\sqrt{s}$ = 7 TeV," Phys. Lett. B **794** (2019), 50-63

79. S. Acharya, ..., **S. P. Rode** *et al.* [ALICE Collaboration], "Calibration of the photon spectrometer PHOS of the ALICE experiment," JINST **14** (2019) no.05, P05025

80. S. Acharya, ..., **S. P. Rode** *et al.* [ALICE Collaboration], "Measurement of D^0 , D^+ , D^{*+} and D_s^+ production in pp collisions at $\sqrt{s} = 5.02$ TeV with ALICE," Eur. Phys. J. C **79** (2019) no.5, 388

81. S. Acharya, ..., **S. P. Rode** *et al.* [ALICE Collaboration], "Event-shape and multiplicity dependence of freeze-out radii in pp collisions at $\sqrt{s}$ = 7 TeV," JHEP **09** (2019), 108

82. S. Acharya, ..., **S. P. Rode** *et al.* [ALICE Collaboration], "Real-time data processing in the ALICE High Level Trigger at the LHC," Comput. Phys. Commun. **242** (2019), 25-48

83. S. Acharya, ..., **S. P. Rode** *et al.* [ALICE Collaboration], "Charged-particle pseudorapidity density at mid-rapidity in p-Pb collisions at $\sqrt{s_{\rm NN}}$ = 8.16 TeV," Eur. Phys. J. C **79** (2019) no.4, 307

84. S. Acharya, ..., **S. P. Rode** *et al.* [ALICE Collaboration], "Study of J/ψ azimuthal anisotropy at forward rapidity in Pb-Pb collisions at $\sqrt{s_{\rm NN}} =$ 5.02 TeV," JHEP **02** (2019), 012

85. S. Acharya, ..., **S. P. Rode** *et al.* [ALICE Collaboration], "Jet fragmentation transverse momentum measurements from di-hadron correlations in $\sqrt{s}$ = 7 TeV pp and $\sqrt{s_{\rm NN}}$ = 5.02 TeV p-Pb collisions," JHEP **03** (2019), 169

86. S. Acharya, ..., **S. P. Rode** *et al.* [ALICE Collaboration], "Λ_c^+ production in Pb-Pb collisions at $\sqrt{s_{\rm NN}} = 5.02$ TeV," Phys. Lett. B **793** (2019), 212-223

87. S. Acharya, ..., **S. P. Rode** *et al.* [ALICE Collaboration], "Event-shape engineering for the D-meson elliptic flow in mid-central Pb-Pb collisions at $\sqrt{s_{\rm NN}} = 5.02$ TeV," JHEP **02** (2019), 150

88. S. Acharya, ..., **S. P. Rode** *et al.* [ALICE Collaboration], "Measuring $K^0_S K^{\pm}$ interactions using pp collisions at $\sqrt{s} = 7$ TeV," Phys. Lett. B **790** (2019), 22-34

89. S. Acharya, ..., **S. P. Rode** *et al.* [ALICE Collaboration], "Energy dependence of exclusive J/ψ photoproduction off protons in ultra-peripheral pPb collisions at $\sqrt{s_{NN}} = 5.02$ TeV," Eur. Phys. J. C **79** (2019) no.5, 402

90. S. Acharya, ..., **S. P. Rode** *et al.* [ALICE Collaboration], "Charged jet cross section and fragmentation in proton-proton collisions at $\sqrt{s}$ = 7 TeV," Phys. Rev. D **99** (2019) no.1, 012016

91. S. Acharya, ..., **S. P. Rode** *et al.* [ALICE Collaboration], "Multiplicity dependence of light-flavor hadron production in pp collisions at $\sqrt{s}$ = 7 TeV," Phys. Rev. C **99** (2019) no.2, 024906

92. S. Acharya, ..., **S. P. Rode** *et al.* [ALICE Collaboration], "Medium modification of the shape of small-radius jets in central Pb-Pb collisions at $\sqrt{s_{NN}} = 2.76$ TeV," JHEP **10** (2018), 139

93. S. Acharya, ..., **S. P. Rode** *et al.* [ALICE Collaboration], "Measurement of dielectron production in central Pb-Pb collisions at $\sqrt{s_{NN}}$ = 2.76 TeV," Phys. Rev. C **99** (2019) no.2, 024002

94. S. Acharya, ..., **S. P. Rode** *et al.* [ALICE Collaboration], "p-p, p-Λ and Λ-Λ correlations studied via femtoscopy in pp reactions at $\sqrt{s}$ = 7 TeV," Phys. Rev. C **99** (2019) no.2, 024001

95. S. Acharya, ..., **S. P. Rode** *et al.* [ALICE Collaboration], "Analysis of the apparent nuclear modification in peripheral PbPb collisions at 5.02 TeV," Phys. Lett. B **793** (2019), 420-432

96. S. Acharya, ..., **S. P. Rode** *et al.* [ALICE Collaboration], "Azimuthal Anisotropy of Heavy-Flavor Decay Electrons in p-Pb Collisions at $\sqrt{s_{NN}}$ = 5.02 TeV," Phys. Rev. Lett. **122** (2019) no.7, 072301

97. S. Acharya, ..., **S. P. Rode** *et al.* [ALICE Collaboration], "Dielectron and heavy-quark production in inelastic and high-multiplicity protonproton collisions at $\sqrt{s_{NN}} = 13$TeV," Phys. Lett. B **788** (2019), 505-518

98. S. Acharya, ..., **S. P. Rode** *et al.* [ALICE Collaboration], "Υ suppression at forward rapidity in Pb-Pb collisions at $\sqrt{s_{\rm NN}}$ = 5.02 TeV," Phys. Lett. B **790** (2019), 89-101

99. S. Acharya, ..., **S. P. Rode** *et al.* [ALICE Collaboration], "Centrality and pseudorapidity dependence of the charged-particle multiplicity density in XeXe collisions at $\sqrt{s_{\rm NN}}$ =5.44TeV," Phys. Lett. B **790** (2019), 35-48

100. S. Acharya, ..., **S. P. Rode** *et al.* [ALICE Collaboration], "Anisotropic flow of identified particles in Pb-Pb collisions at $\sqrt{s}_{\rm NN} = 5.02$ TeV," JHEP **09** (2018), 006

101. S. Acharya, ..., **S. P. Rode** *et al.* [ALICE Collaboration], "Measurement of the inclusive J/ ψ polarization at forward rapidity in pp collisions at $\sqrt{\rm s} = 8$ TeV," Eur. Phys. J. C **78** (2018) no.7, 562

102. S. Acharya, ..., **S. P. Rode** *et al.* [ALICE Collaboration], "Inclusive J/ψ production at forward and backward rapidity in p-Pb collisions at $\sqrt{s_{\rm NN}}$ = 8.16 TeV," JHEP **07** (2018), 160

103. S. Acharya, ..., **S. P. Rode** *et al.* [ALICE Collaboration], "Direct photon elliptic flow in Pb-Pb collisions at $\sqrt{s_{\rm NN}}$ = 2.76 TeV," Phys. Lett. B **789** (2019), 308-322

104. S. Acharya, ..., **S. P. Rode** *et al.* [ALICE Collaboration], "Dielectron production in proton-proton collisions at $\sqrt{s} = 7$ TeV," JHEP **09** (2018), 064

105. S. Acharya, ..., **S. P. Rode** *et al.* [ALICE Collaboration], "Production of the $\rho(770)^0$ meson in pp and Pb-Pb collisions at $\sqrt{s_{\rm NN}}$ = 2.76 TeV," Phys. Rev. C **99** (2019) no.6, 064901

106. S. Acharya, ..., **S. P. Rode** *et al.* [ALICE Collaboration], "Inclusive J/ψ production in XeXe collisions at $\sqrt{s_{\rm NN}}$ = 5.44 TeV," Phys. Lett. B **785** (2018), 419-428

107. S. Acharya, ..., **S. P. Rode** *et al.* [ALICE Collaboration], "Suppression of $\Lambda(1520)$ resonance production in central Pb-Pb collisions at $\sqrt{s_{\rm NN}}$ = 2.76 TeV," Phys. Rev. C **99** (2019), 024905

108. S. Acharya, ..., **S. P. Rode** *et al.* [ALICE Collaboration], "Two particle differential transverse momentum and number density correlations in p-Pb and Pb-Pb at the LHC," Phys. Rev. C **100** (2019) no.4, 044903

109. S. Acharya, ..., **S. P. Rode** *et al.* [ALICE Collaboration], "Transverse momentum spectra and nuclear modification factors of charged particles in Xe-Xe collisions at $\sqrt{s_{\rm NN}}$ = 5.44 TeV," Phys. Lett. B **788** (2019), 166-179

110. S. Acharya, ..., **S. P. Rode** *et al.* [ALICE Collaboration], "Measurements of low-p$_T$ electrons from semileptonic heavy-flavour hadron decays at mid-rapidity in pp and Pb-Pb collisions at $\sqrt{s_{\rm NN}} = 2.76$ TeV," JHEP **10** (2018), 061

111. S. Acharya, ..., **S. P. Rode** *et al.* [ALICE Collaboration], "Anisotropic flow in Xe-Xe collisions at $\sqrt{\mathbf{s}_{\rm NN}} = \mathbf{5.44}$ TeV," Phys. Lett. B **784** (2018), 82-95

Conference Proceedings:

1. "Production of electrons from Heavy-flavour hadron decays in different collision systems in ALICE at the LHC", DAE-BRNS Symposium on High Energy Physics (2018), **S. P. Rode** on behalf of ALICE collaboration **Under review**. **[2018]**, http://arxiv.org/abs/arXiv:1906.05570

2. "Differential elliptic flow of charged hadrons at FAIR SIS100", **S. P. Rode**, A. Roy and P. P. Bhaduri, DAE Symp. Nucl. Phys. **62**, 892 (2017), http://www.sympnp.org/proceedings/62/E45.pdf

Contents

Figures

Tables

Chapter 1

Introduction

In this chapter, a brief introduction to the high energy physics in the context of this thesis is given. This includes a short overview of the standard model, the formation of Quark-Gluon Plasma, its evolution and ways to probe it in the heavy-ion experiments.

1.1 Standard Model

Matter around us is built from elementary particles and interactions among them. As per the traditional wisdom, there are four fundamental forces that exist in nature viz. Strong, Electromagnetic, Weak and Gravitational force. The standard model is a theory which encapsulates these fundamental interactions except gravitational force. The fundamental particles can be characterized by their intrinsic properties such as, spin, baryon number, lepton number, electric and color charge etc. As shown in Figure 1.1, the particles and their anti-particles can be broadly classified into two groups, fermions and bosons according to their spin quantum number. Quarks and leptons are fermions. There are six quarks (up (u), down (d), strange (s), charm (c), bottom (b) (or beauty) and top (t)) and their anti-quarks, each with three color (*red*, *green* and *blue*) and their corresponding anti-color charges as an additional quantum number [1, 2]. There are three generations of quarks (leptons) in which up and down (electrons (e) and electron neutrino (ν_e)) being the first generation of quarks (leptons), strange and charm (muon (μ) and muon neutrino (ν_μ)) being the second, and top and bottom (tau (τ) and tau neutrino (ν_τ)) are the third generation of quarks (leptons). Another category of the particles is bosons which consist of gauge bosons and

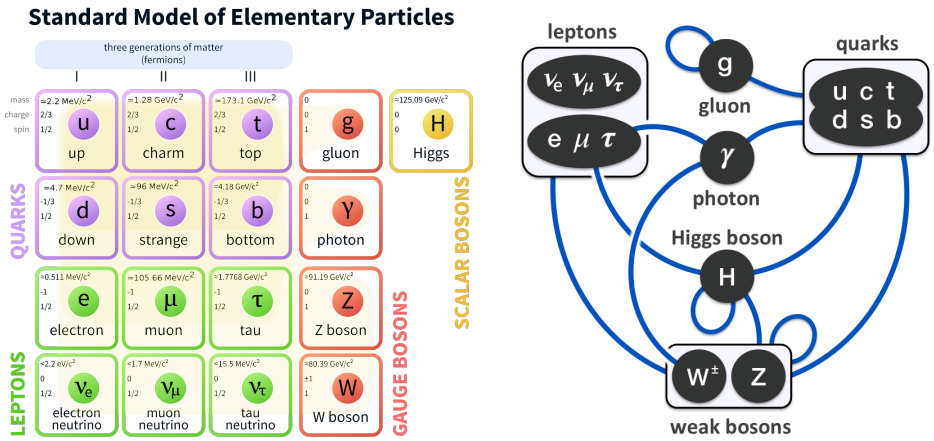

Figure 1.1. Classification of the particles and their interactions included in the standard model

scalar bosons. Gauge bosons are the force carriers of fundamental forces. $W^{\pm}$, Z bosons govern the weak interactions whereas electromagnetic interactions are governed by photons. Moreover, gluons are the force carriers of strong forces. The recently discovered Higgs boson [3, 4] is a scalar boson responsible for giving the masses to quarks and leptons by interacting with them and itself.

1.2 Quark Gluon Plasma and Relativistic Heavy-Ion Collisions

Quantum ChromoDynamics (QCD) [5] is a quantum field theory of the strong interactions. It is developed in close analogy with Quantum ElectroDynamics (QED). Quarks and gluons are point-like structures and are the basic degrees of freedom in QCD. Since gluons carry "color" charge, this gives rise to self interactions which is responsible for the running of the QCD coupling constant $\alpha_s(r, Q)$ with the separation between quarks (r) or the momentum transfer (Q) [6, 7] as shown in Figure 1.2. Under normal circumstances, quarks and gluons are confined, and therefore, their direct observation is not possible, a phenomenon known as *confinement*. However, at the higher temperature or pressure, i.e. at large momentum transfer or small distance, the strength of α_s weakens and the quarks and gluons become asymptotically free which is known as *Asymptotic*

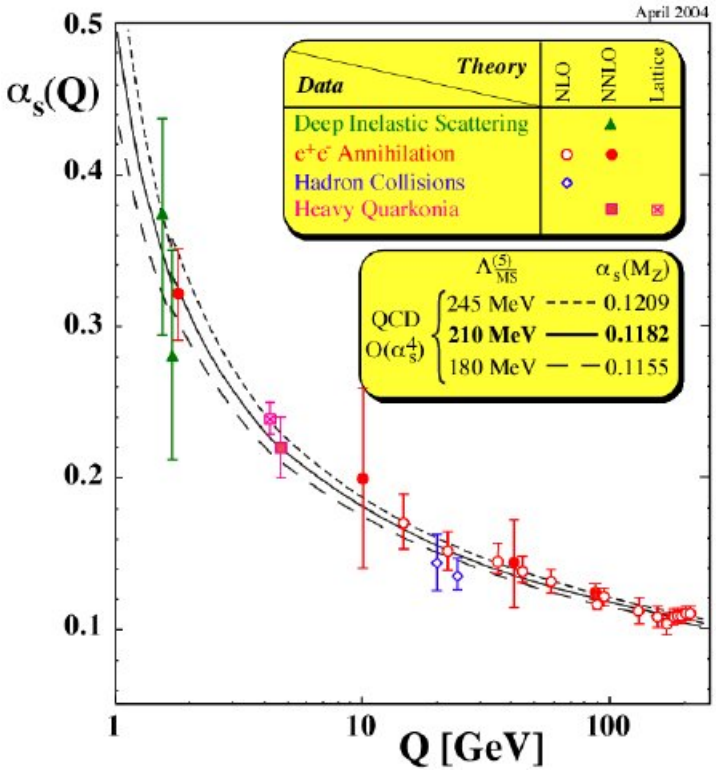

Figure 1.2. Running of QCD coupling constant as a function of momentum transfer (Q) [8].

freedom. *Confinement* and *Asymptotic freedom* are the two unique properties of the QCD.

The strongly interacting state of deconfined quarks and gluons, popularly known as Quark-Gluon Plasma (QGP), was expected to have prevailed just after the Big-Bang. Exploration of the phase structure of such a strongly interacting matter of quarks and gluons has been one of the driving forces behind the modern physics research. This novel state of strongly interacting matter is expected to be produced at very high temperature or baryon chemical potential as shown in the QCD phase diagram in Figure 1.3. At sufficiently high temperature and/or high density, the nuclear matter undergoes a phase transition from hadronic stage to a phase where the quarks and gluons are no longer confined. According to the first principle Lattice QCD [9] calculations, the transition is believed to be a smooth cross-over at high temperatures and very small baryonic densities. On the other hand, at high baryonic densities, the phase transition is predicted to be of the first order. This points towards a possible existence

of critical endpoint (CEP) on the phase diagram. The transition temperature of about 160 MeV at zero baryon chemical potential ($\mu_B = 0$) is predicted by the Lattice QCD. Another type of phase transition was predicted by Lattice QCD related to the shift in the mass of the particles, i.e. Chiral phase transition. The mass of a proton is 0.938 GeV/c^2 and therefore, mass of each constituent quark (M_q) is about 300 MeV/c^2. Since bare masses of quarks are small ($m_q \approx 0$), bare quarks dress themselves with gluons to form hadrons in a vacuum. This dressing of gluons is expected to melt ($M_q \rightarrow m_q$) in the hot and dense medium of quarks and gluons. Lagrangian of the QCD is chirally symmetric for massless quarks ($m_q \approx 0$) which implies the spontaneous breaking of chiral symmetry for constituent quark mass ($M_q \neq 0$). This means that the system undergoes a chiral phase transition from $M_q \rightarrow m_q$, which leads to restoration of the chiral symmetry.

In the laboratory, such hot and dense matter of quarks and gluons can be produced when two heavy-ions collide at relativistic speeds. A central goal of the relativistic heavy-ion collision experiments is the quantitative mapping of the QCD phase diagram from low to high temperatures and baryon densities [11, 12]. The major drive behind such investigations is to search for a first and (or) second-order phase transition together with the existence of critical endpoint (CEP) of the QCD matter at non-zero baryon chemical potentials. Exploration of the different phases of strongly interacting matter in the full range of temperatures and baryon densities necessitates the simultaneous measurements of various observables over a wide range of beam energies.

Over the past two decades, the region of high temperature and vanishing baryon densities of the QCD phase diagram has been extensively studied in experiments carried out at accelerator facilities such as Relativistic Heavy-Ion Collider (RHIC) [13, 14] in Brookhaven National Laboratory (BNL) and Large Hadron Collider (LHC) [15–17] in European Organization for Nuclear Research (CERN). Experiments such as A Large Ion Collider Experiment (ALICE) at LHC and Solenoidal Tracker at RHIC (STAR) and Pioneering High Energy Nuclear Interaction eXperiment (PHENIX) at RHIC are dedicated for the heavy-ion research. Data collected by the experiments at these two collider fa-

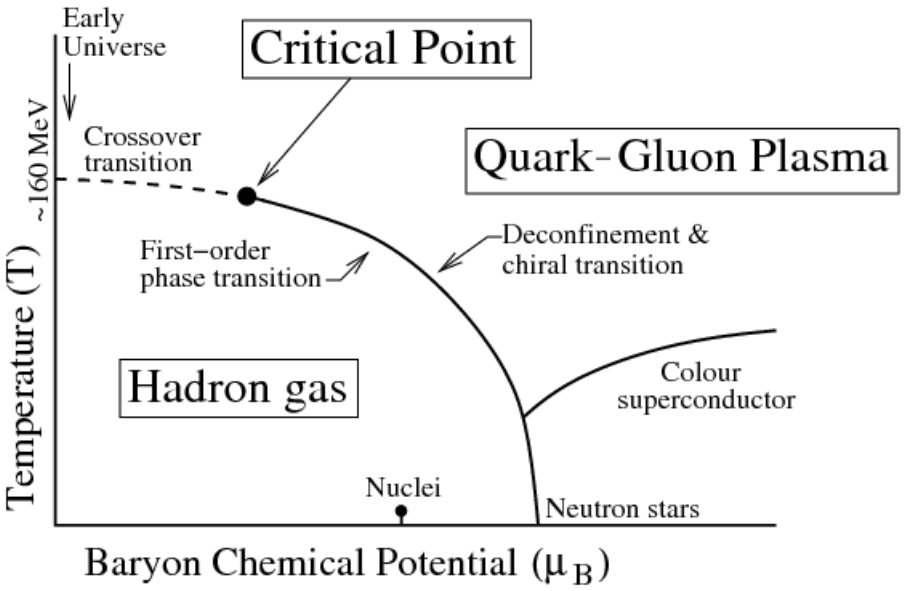

Figure 1.3. Conjectured picture of the QCD phase diagram [10].

cilities [13–17] have provided conclusive evidence for the formation of strongly coupled Quark-Gluon Plasma (QGP) [18]. Compared to that, our understanding of the QCD equation of state at non-zero baryon densities is somewhat limited. Hence, the ongoing Beam Energy Scan (BES) program at RHIC [19, 20] and the upcoming heavy-ion collision experiments at the Nuclotron-based Ion Collider fAcility (NICA) [21] at the Joint Institute for Nuclear Research (Dubna) and at the Facility for Antiproton and Ion Research (FAIR, Germany) [22, 23] aim at probing the moderate temperature and high baryonic chemical potential regime of the QCD phase diagram.

1.2.1 Evolution of the Quark-Gluon Plasma in Relativistic Heavy-Ion Collisions

Quark-Gluon Plasma is locally thermally equilibrated strongly interacting phase of quarks and gluons which can be created in the laboratory by colliding two Lorentz contracted heavy ions at relativistic energies. After the collisions, a series of events leads to the formation of QGP and eventually hadronization as depicted in Figure 1.4 and explained briefly. Here, one make use of co-ordinate transformation from (t,z) to (τ,η) where, $\tau = \sqrt{t^2 - z^2}$ and $\eta = \frac{1}{2}\, ln(\frac{t+z}{t-z})$,

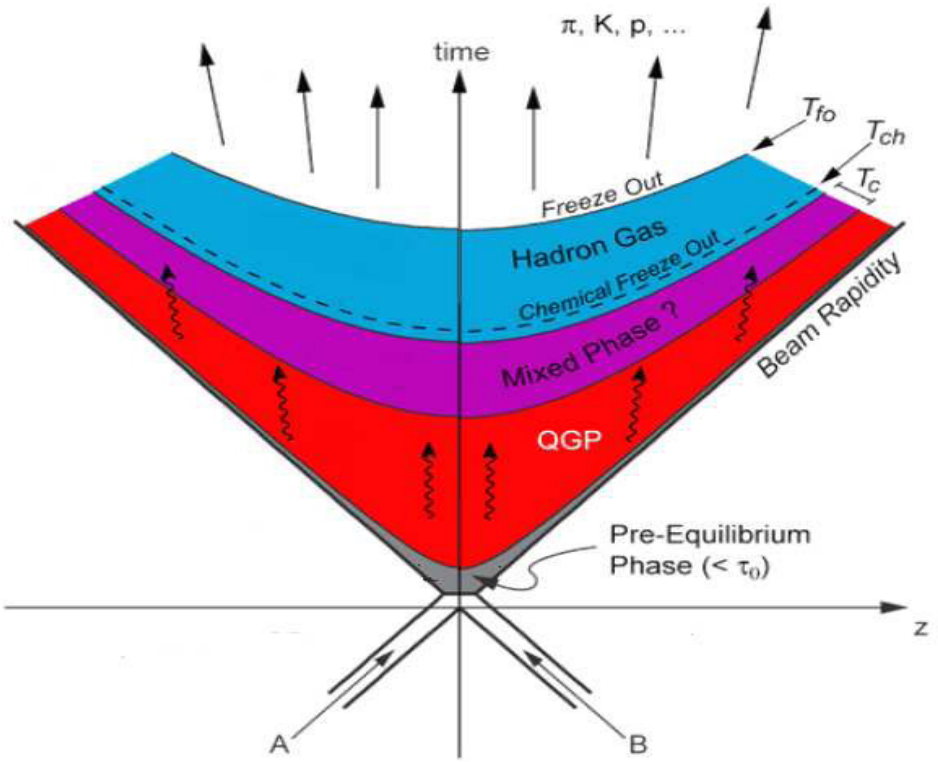

Figure 1.4. Space-time evolution picture of the relativistic heavy-ion collision [24].

where τ is the proper time and η is space-time rapidity.

Pre-equilibrium stage

The two Lorentz contracted nuclei collide with each other with certain impact parameter (b). Just after the collision, depending on b, the energy carried by the nuclei is deposited inside the small volume of the collision zone. This results in the liberation of a large fraction of partons (quarks and gluons) and leads to the inelastic interactions among them, forming the pre-equilibrium phase.

Formation of QGP and its evolution

Large energy density in the overlap region of the two nuclei allows the constituents to undergo multiple re-scatterings due to the smaller mean free path compared to the system size. This drives the system towards thermalisation. After the energy density becomes high enough and at a time, $\tau = \tau_0$, the system

comes to thermal equilibrium, and the QGP is formed. The evolution of the QGP can be explained using the laws of relativistic hydrodynamics.

Freeze-out stage

After some time (duration of QGP, $\tau_{\mathrm{QGP}} \approx 3$–$5$ fm/c), the energy density begins to drop below critical value ($\varepsilon_c \approx 1$ GeV/fm^3), required for the formation of the QGP. As the system cools down, quarks and gluons start to form hadrons. These hadrons interact inelastically and produce new particles. The stage where the inelastic collisions between the hadrons cease to exist, that stage is called as *chemical freeze-out* (CFO) and the temperature is called as *chemical freeze-out temperature* (T_{ch}). Even after this, hadrons still interact with each other elastically and can change the momentum distribution. When mean free path becomes larger than the system size, they are no longer able to interact with each other, and this stage is known as *kinetic or thermal freeze-out* (KFO) and the corresponding temperature is known as *kinetic freeze-out temperature* (T_{kin}). Following this, momentum distributions of the particles are fixed, and then they are freely streamed into the detector. These particles are then detected by the detector using different detection techniques.

1.3 What to look for in the experiments?

Since the state of Quark-Gluon Plasma is very short-lived, it is not possible to probe its existence directly in the experiments. The only way to examine is to develop some observables which can be measured in the experiment, and the information on the QGP can be extracted indirectly. Some of the signatures of the QGP such as strangeness enhancement, photons and dileptons, jet quenching, quarkonium suppression are briefly discussed in this section. Apart from these, heavy-flavours and collective flow are also considered as promising probes to study this state of matter. Since the objective of the thesis is related to study these two, they are explained in details in the later sections.

1.3.1 Strangeness enhancement

Enhancement in the production of strange particles in final yield in heavy-ion (AA) collisions in contrast to pp and pA collisions is considered as one of the important probes of the QGP [25, 26]. There are no strange quarks present in the initial colliding nuclei. Production of strange quark pairs is more favourable in parton-parton interactions in comparison to the hadronic interactions [26]. So in the QGP phase, the partonic interactions are prominent and lead not only more rapid strange production, but the abundances of the higher strange species also enhance. In hot hadronic medium, the threshold to produce the strange hadrons in the reaction like $\pi + \pi \rightarrow \mathrm{K} + \bar{\mathrm{K}}$ is about 600 to 700 MeV which is quite higher than the one required for the production of $s\bar{s}$ pairs i.e $2m_s \approx 300$ MeV. The gluon fusion ($gg \rightarrow s\bar{s}$) is one of the dominant processes for the $s\bar{s}$ pair production. So consequently, in the QGP phase, this reflects in the enhanced production of strange particles in comparison to the hadronic scenario.

Due to the initial conditions in collisions, u and d quarks are available in abundance than their corresponding anti-quarks ($\bar{u}$,$\bar{d}$). So at the time of hadronization, already produced strange pairs ($s\bar{s}$) can combine to form ϕ ($s\bar{s}$) meson or $\bar{s}$ can form K^+ ($\mathrm{u}\bar{s}$) by hadronizing with u quark. It is more preferable for s quark to hadronize with two quarks (u, d) to form a strange baryon than to combine with $\bar{u}$ or $\bar{d}$ to form meson due to the presence of more quarks than anti-quarks. So in heavy-ion collisions, large production of $s\bar{s}$ pairs leads to more strange hadrons in the final state than pp and pA systems.

To quantify this strangeness enhancement in the experiments, apart from the yield of strange and multi-strange hadrons, ratio of the strange to non-strange hadrons is also measured, and indeed strangeness enhancement is observed in heavy-ion collisions. The first observation of strangeness enhancement was seen at NA57 experiment at the SPS [27]. Recently [28], evidences of strangeness enhancement in high multiplicity pp and pA collisions were presented. These results are in agreement with those in heavy-ion collisions which is very surprising. This has opened new doors for the physics in high multiplicity collisions of small systems.

1.3.2 Photons and dileptons

Photons (real or virtual) are believed to be produced and decay into dileptons (i.e. e^+e^-, $\mu^+\mu^-$) in almost every stage of the relativistic heavy-ion collisions. In 1976, the importance of the electromagnetic probes was first pointed out by Feinberg [29]. Since these are electromagnetic radiations, their inability to interact strongly makes them a perfect probe to investigate the produced strongly interacting medium. Even at the highest of the temperatures in the heavy-ion collisions, the mean free path (typically 10^2 – 10^4 fm) [30] of these probes is way larger than the system size (about 10 fm) which means they would come out without interacting with the medium carrying the information about the medium where they are produced.

Depending on the stages where they are produced, the photons are categorized. For instance, (i) prompt photons are originated from very early stages of the collisions via initial hard scatterings in processes such as quark-gluon Compton scattering ($q + g \rightarrow g + \gamma$), quark anti-quark annihilation ($q + \bar{q} \rightarrow g + \gamma$) and so on, (ii) photons which are produced before the medium gets thermalized are called as pre-equilibrium photons, (iii) thermal photons come from the quark-gluon plasma as well as via hadronic interactions in the hadronic phase, and (iv) other photons can originate through the passage of jets through the plasma.

Dileptons are massive in size compared to photons and therefore, are sometimes considered advantageous over photons. They can be classified into three regimes depending on their pair invariant mass:

- Low mass region ($M \leqslant M_\phi$): Dilepton production from mesons ($\pi^0 \rightarrow e^+e^-\gamma$, $\eta \rightarrow e^+e^-\gamma$, $\omega \rightarrow e^+e^-\pi^0$, $\phi \rightarrow e^+e^-$) dominate this mass region.

- Intermediate mass region ($M_\phi < M < M_{J/\psi}$): This mass region is dominated by the dileptons produced from continuum radiations coming from the QGP and therefore, this region is crucial to extract the information about the QGP.

- High mass region ($M \geqslant M_{J/\psi}$): In high mass region, the dileptons orig-

inate from radiation coming from primordial stage and heavy quarkonia such as J/ψ and Υ.

At first, photons and dileptons were studied with the hope to get information about the temperature of the fireball. With time, their applications were realized in other aspects of the collisions such as (i) use of photons to study the system size evolution using intensity interferometry [31–33] (ii) investigation of the formation time of the quark-gluon plasma [34] and study of momentum anisotropy of the initial partons using elliptic flow of the thermal photons [35, 36]. (iii) Dileptons are a handy tool to study the medium modifications of the vector mesons [37], moreover, used as a tool to characterize the QGP phase using dilepton interferometry [38].

1.3.3 Jet quenching

When two partons with high transverse momentum interact, two outgoing partons with large virtuality Q are produced back-to-back. These partons subsequently lose their energy by radiating gluons and (or) splitting into $q\bar{q}$ pairs which result in a collimated spray of hadrons in the final state called as *"Jet"*. While passing through the QCD medium produced in the nuclear collisions, these jets undergo multiple rescattering with the medium and eventually lose their energy. This results in the attenuation of the jet yield coming out, which is called as *Jet quenching*. Experimentally, the jet quenching is measured via observable called as Nuclear Modification Factor, which quantifies the amount of suppression in the yield of the jets in the nucleus-nucleus collisions with respect to proton-proton collisions. Another way to observe the jet quenching in experiments is by measuring the azimuthal correlation between the particles [39].

1.3.4 Quarkonium suppression

Quarkonium are the stable bound states of heavy quarks (Q) and anti-quarks ($\bar{Q}$) where Q can either be *charm* or *bottom (or beauty)* quark. Bound state of

$c\bar{c}$ is called as *charmonium* and $b\bar{b}$ as *bottomonium*. The ground state of charmonium family is known as J/ψ, and bottomonium family is Υ. Unlike light hadrons whose masses come from the interactions between their nearly massless constituents, the masses of quarkonia come largely from the bare masses of their quark content which are determined via Higgs mechanism from the electroweak sector of the standard model. Moreover, another specific property of these quarkonia is their small size of about 0.1 to 0.3 fm in contrast to light hadrons which are of radius $\approx$ 1 fm. This suggests their large binding energy compared to those of light hadrons. Since masses of $c\bar{c}$ and $b\bar{b}$ pairs are less than two times the masses of corresponding open heavy-flavour hadrons i.e. $M_{c\bar{c}} < 2M_D$ ($D = c\bar{u}$) and $M_{b\bar{b}} < 2M_B$ ($B = b\bar{u}$), their decay into D$\bar{\text{D}}$/B$\bar{\text{B}}$ pairs are not allowed.

J/ψ suppression was first proposed by Matsui and Satz in 1986 [40]. It was argued that due to the Debye screening by the free color charges in the QGP, the suppression in the final yield of J/ψ and other quarkonia could be observed. For different quarkonium states, the amount of suppression should be decided by their binding energy. For instance, the strongly bound states like Υ show less or no suppression. This suppression suggests that produced $c\bar{c}$ pairs either unable to evolve into the bound states or those bound states are destroyed as a result of a weakening of the $c\bar{c}$ bond due to the Debye screening. J/ψ suppression was first observed experimentally at the SPS [41] and then later measured at different experiments such as PHENIX, STAR and ALICE [42–45] at the RHIC and the LHC, respectively.

1.4 Heavy-Flavour Production

The measurement of the heavy-flavours (charm (c) and beauty (b) quarks) is one of the important tools to extract the information about the produced medium. Due to the large bare masses of the heavy-flavours ($m_c \approx 1.5$ GeV/c^2 and $m_b \approx 4.5$ GeV/c^2) [46] which are quite greater than $\Lambda_{QCD} \approx 200$ MeV, they are produced at the very early stages of the collision via initial hard scattering witnessing the whole evolution of the Quark-Gluon Plasma (QGP) (see Figure 1.4).

The production of these heavy-flavours can be treated in the framework of perturbative QCD (pQCD) even at zero transverse momentum due to the hard scale introduced by their mass unlike in the case of gluons and light quarks as they can only be treated perturbatively at high transverse momentum [47]. Consequently, heavy flavours provide the essential foreground to improve our understanding of the pQCD. Moreover, their measurements in proton-proton (pp) collisions provide required baseline for the corresponding investigations in proton-nucleus (pA) collisions, where effects due to the presence of a nucleus in the collision system play a role, and in nucleus-nucleus (AA) collisions, where the heavy quarks propagate through the produced hot and dense medium and interact with its constituents.

The production process of heavy-flavour hadrons in relativistic collisions can be factorized in the following components within the pQCD approach:

- Non-perturbative nature of initial conditions: The nature of the initial conditions is crucial, and it depends on the fraction of momenta x, carried by the parton inside the hadron. It also depends on the square of momentum transfer, Q^2 between two interacting partons. The distributions of various partons as a function of x have been examined by deep inelastic scattering experiments. These distributions are parameterized and used in various calculations in the form of parton distribution functions (PDF).

- Scattering cross-section of partons (perturbative): The partonic scattering cross-section can be determined in the domain of perturbative QCD. Contribution on Leading Order (LO) level comes mainly from gluon fusion and quark anti-quark annihilation processes, whereas processes such as gluon splitting or flavour excitation are considered as well at the next-to-leading order level. Apart from this picture, the cross-section has been attempted to determine at fixed order with next-to-leading-log resummation of higher orders in α_s.

- Fragmentation of heavy flavours into hadrons (non-perturbative): This can further be distinguished in the following ways.

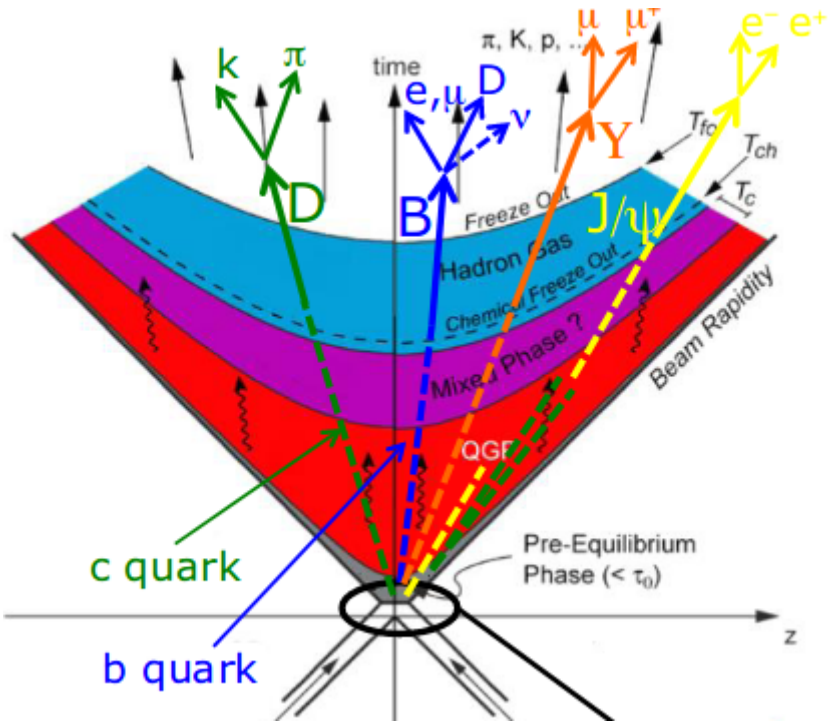

Figure 1.5. Production of heavy quarks in the relativistic heavy-ion collision

- Once the pairs of heavy-quarks are produced, only about $1-2\%$ of them can form a bound state of quarkonia.
- Otherwise, the produced heavy-quark pairs can fragment with light quark into open heavy-flavour hadrons (hadrons with a single charm or beauty quark).

Furthermore, measurement of open heavy-flavour hadrons can be performed via their hadronic and semi-leptonic decay channel due to their short lifetime (see Table 1.1 for details). In their hadronic channel, full kinematics can be accessed whereas it is not possible in case of semi-leptonic decay channel. In this thesis, the measurement of the heavy-flavours via their semi-electronic decay channel with substantial 10% branching ratio is discussed. The measurements of the electrons from heavy-flavour hadron decays can be confronted with the pQCD predictions such as Fixed Order with Next-to-Leading-Log resummation (FONLL) calculations [48–50].

Yields of heavy-flavours in nucleus-nucleus collisions scale with the number of binary collisions in the absence of nuclear effects since their thermal pro-

Particle (Quark content)	Mass (GeV/c^2)	Decay mode	B.R. (%)	$c\tau$ (μm)
D^+ ($c\bar{d}$)	1.8696 ± 0.0001	$K^- \pi^+ \pi^+$	9.38 ± 0.16	
		e^+ anything	16.07 ± 0.30	312
		μ^+ anything	17.6 ± 3.2	
D^0 ($c\bar{u}$)	1.8648 ± 0.0001	$K^- \pi^+$	3.95 ± 0.03	
		e^+ anything	6.49 ± 0.11	123
		μ^+ anything	6.8 ± 0.6	
D_s^+ ($c\bar{s}$)	1.9683 ± 0.0001	$\phi \pi^+$	4.5 ± 0.4	
		e^+ anything	6.5 ± 0.4	151
Λ_c (udc)	2.2865 ± 0.0001	$pK^- \pi^+$	6.3 ± 0.3	60
B^+ ($u\bar{b}$)	5.2793 ± 0.0001	D^0 anything	8.6 ± 0.7	
		$l^+ \nu_l$ anything	10.99 ± 0.28	491
B^0 ($d\bar{b}$)	5.2796 ± 0.0001	D^0 anything	8.1 ± 1.5	
		$l^+ \nu_l$ anything	10.33 ± 0.28	455
B_s^0 ($s\bar{b}$)	5.3669 ± 0.0001	D_s^- anything	93 ± 25	
		$l^+ \nu_l$ anything	9.6 ± 0.8	453

Table 1.1. Summary of some open heavy-flavour hadrons, their masses, decay modes, branching ratios and life time [51].

duction is not quite possible. So, violation of this binary scaling would mean the modifications of heavy-flavour observables in the nuclear medium. These modifications can be originated from two different sources such as initial and final state effects, which need to be differentiated.

The distribution functions of partons in the nucleons are different from the parton distribution functions embedded in nuclei. These initial state effects can lead to some nuclear modifications. As mentioned earlier, the parton distribution functions are different for different values of x and Q^2. At medium values of x ($x \approx 0.1$), the parton density in nucleons is smaller than in nuclei and the region is called as the anti-shadowing region. In shadowing region, parton density at low x ($x \approx 10^{-2}$) is depleted in nuclei with respect to nucleons. There are other effects such as gluon saturation, which may lead to a reduction in their densities at low x.

In final state effects, due to presence of the hot and dense matter, in-

medium modifications of the heavy-flavour observables occur in relativistic heavy-ion collisions. Understanding of such modifications enables the possibility to shed light on the properties of the hot QCD matter. Of course, this would imply to have a good understanding of the initial state effects to separate these effects from one another. Experimentally, these modifications are studied in terms of the nuclear modification factor ($R_{\rm AA}$). As mentioned earlier, the study of heavy-flavour observables in proton-proton collisions provide good cross-check with respect to heavy-ion collisions.

In the context of heavy ion experiments, open heavy-flavours are measured in hadronic and semi-leptonic channels in PHENIX [52–56] and STAR [57–61] experiments at RHIC. ALICE experiment at the LHC provides an important platform because of its excellent Particle Identification (PID) and tracking abilities due to which more precise measurements can be achieved. Recently, the nuclear modification factor ($R_{\rm AA}$) of electrons from heavy-flavour hadron decays has been studied at both available energies ($\sqrt{s_{NN}}$ = 2.76 and 5.02 TeV) at the LHC [62, 63].

1.5 Collective Flow

Collective flow has drawn some attention as a probe to study the strongly interacting matter produced in relativistic heavy-ion collisions. The shape of the interaction or overlapping region depends on the impact parameter (b) of the collision in heavy-ion collisions, as shown in Figure 1.6. As a result, in the central collisions where the impact parameter is close to zero, the collective flow has two components viz. longitudinal and transverse flow, due to the isotropic nature of the initial geometry. Different descriptions are available in the literature to explain the dynamics of the produced medium. For instance, to extract the information related to the longitudinal and transverse dynamics at the freeze-out, the rapidity and transverse momentum spectra can be explained using one such description known as the blast-wave model. This model is very successful and known to give a better understanding of the freeze-out conditions.

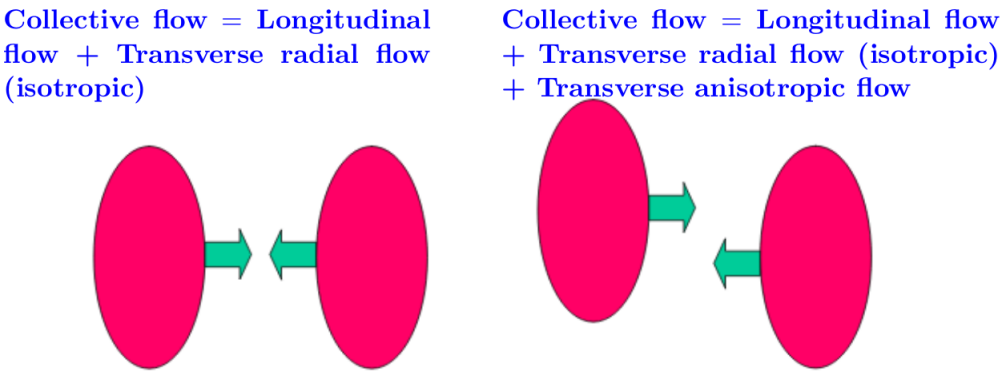

(a) Central collision (b) Non-central collision

Figure 1.6. Components of the collective flow in (a) central ($b \approx 0$) and (b) non-central ($b > 0$) collisions.

On the other hand, in non-central collisions, initial anisotropy in the spatial distribution leads to an additional component in the collective flow decomposition, i.e. transverse anisotropic flow. This can provide insights about the collectivity of the medium. Particles are produced isotropically in the transverse plane in the proton-proton collisions. On the same line, if all proton-proton collisions in the heavy-ion collisions are independent of each other, the production would be isotropic in the transverse plane too. However, due to the anisotropy of the interaction volume in non-central collisions, particles in the collision system undergo multiple scattering and the azimuthal distribution of the transverse momentum of the produced particles would be modified. In other words, the initial spatial anisotropy transforms into the momentum anisotropy due to the multiple re-scatterings occurred at the early stage as depicted in Figure 1.7. Moreover, these re-scatterings will also drive the medium into thermal equilibrium which will further expand collectively. This collectivity might reflect in the distributions of the produced particles. The Fourier expansion of the azimuthal distribution of the final state particles is given by the formula,

$$E\frac{d^3N}{d^3\mathbf{p}} = \frac{1}{2\pi}\frac{d^2N}{p_T dp_T dy}\left[1 + \sum 2v_n \cos(n(\phi - \psi_r^n))\right]$$

Where, ϕ, ψ_r^n and v_n are azimuthal angle of the particle, reaction plane

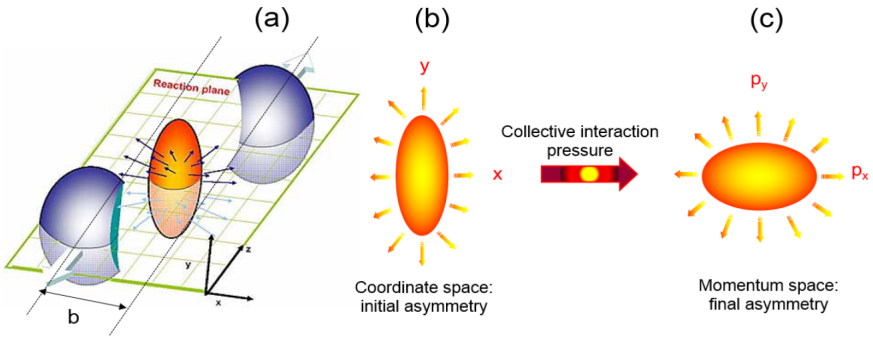

Figure 1.7. Anisotropy in non-central heavy-ion collision [64].

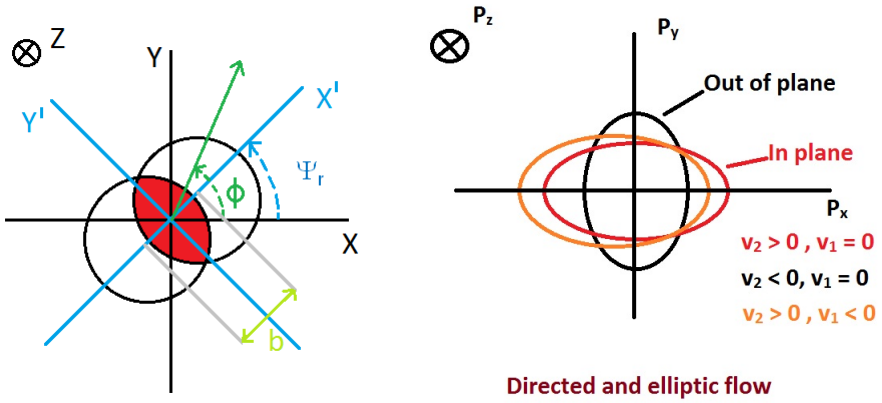

Figure 1.8. Harmonic coefficients of the azimuthal distribution of the final state particles

angle and nth Fourier coefficient of the azimuthal distribution, respectively. v_n can be further obtained as,

$$v_n = < \cos[n(\phi - \psi_r^n)] >$$

Where, v_1, v_2, v_3,..... are known as directed flow, elliptic flow, triangular flow respectively and so on. Figure 1.8 (right plot) shows the pictorial representation of directed and elliptic flow (in plane and out of plane) in the momentum space. More detailed study about these coefficients of different identified hadrons will be provided later in the thesis.

1.6 Motivation

Probing the strongly interacting matter produced in relativistic collisions is one of the primary motivations behind the modern heavy-ion program. Quark-gluon plasma is expected to form at high temperature (and low baryon density) as well as at moderate temperature (and finite baryon densities) regime of the QCD phase diagram. This is enough to motivate one to explore the nature of such matter at these conditions. The experiments which perform this study are in huge collaborations and it is not easy to get the opportunity to explore the physics at both these regimes simultaneously. However, running experiments are not the only way to examine the properties of the produced medium; one can perform the phenomenological study by confronting the measurements already performed by the experiments with theoretical models. In this thesis, the attempt has been made to explore the low as well as high energy regimes of the QCD phase diagram. As mentioned earlier, ALICE at the LHC is one of the experiments in the world which is designed to probe such matter in heavy-ion collisions at very low baryon density and high temperature whereas; in the past there are several experiments performed to probe the baryon rich matter at low energies at AGS and SPS.

In the case of exploring the high-temperature regime of the QCD phase diagram, heavy flavours are suitable choice for investigating the nature of the quark-gluon plasma. Heavy flavours can be measured via decay products of open heavy flavour hadrons in semi-electronic channels. The electrons originating from both charm and beauty quark decays are measured using different analyses techniques in proton-proton collisions, where the possibility of production of QGP is little. These measurements are very important as a baseline for the corresponding study in heavy-ion collisions, where the in-medium modifications of these heavy flavours due to the presence of medium can be observed. Mass dependent energy loss of the quarks in the medium can be performed in heavy-ion collisions, and the corresponding reference is provided by measuring electrons coming solely from beauty quarks in proton-proton collisions in this thesis. Since these measurements are performed using the detectors and differ-

ent criteria, they suffer from systematic uncertainties, and it is important to have control over them to achieve better precision. The analyses techniques used to perform these measurements have helped to reduce the systematic uncertainties with respect to the published ALICE results and other analyses techniques, which is one of the highlights of this thesis.

In the low energy regime of the QCD phase diagram, the comparative study of published measurements by experiments is performed using different phenomenological models. Moreover, apart from heavy-flavours, there are other observables which can provide some insight into the medium. Collective flow in central and non-central nuclear collisions is one of such observables which can lead to some information about the dynamics of the medium prevailed. In central collisions, transverse as well as the longitudinal flow of the bulk particles can reveal information about the collision dynamics at freeze-out surfaces whereas, in non-central collisions, the anisotropic flow of those particles provides insight about the thermalization of the hydrodynamic driven QCD medium. In the former case, the measurements of light hadrons and heavy strange hadrons from low energy experiments are confronted with a blast-wave description in a non-boost invariant scenario to study the mass-dependent hierarchy of the kinetic freeze-out parameters such as kinetic freeze-out temperature and average transverse velocities at different bombarding energies. However, in the latter case, a feasibility study of anisotropic flow coefficients using the Ultra-relativistic Quantum Molecular Dynamics (UrQMD) model [65, 66] is performed which is essential and can provide important predictions required by the upcoming experiments at different accelerator facilities such as FAIR and NICA.

1.7 Organization of the Thesis

The organization of the thesis is as follows.

Chapter 1 In this chapter, we give a brief introduction to the high energy physics in the context of this thesis.

Chapter 2 The layout of the ALICE detector and its sub-systems is described. Along

with this, the description of the framework in which data analyses are performed is given.

Chapter 3 It is dedicated to the analysis of the measurement of p_{T}-differential production cross-sections of electrons from charm and beauty quarks in proton-proton collisions at $\sqrt{s} = 7$ and 13 TeV with standard (0.5 Tesla) and low (0.2 Tesla) magnetic field up to transverse momentum 4 GeV/c. The former analysis is performed down to $p_{\mathrm{T}} = 0.5$ GeV/c whereas, the latter one is extended to 0.2 GeV/c due to available low magnetic field which can help in improving reconstruction efficiency towards low transverse momentum region. These measurements are compared with theoretical predictions.

Chapter 4 The electrons from beauty hadron decays are measured in proton-proton collisions at $\sqrt{s} = 5.02$ TeV. Due to small signal to background ratio along with low tracking and PID efficiencies at small transverse momentum, the separation of beauty electrons from the charm and other background electrons is difficult. Therefore, a different technique in contrast to heavy-flavour electron analysis is used to perform this measurement. The measured production cross-sections are compared with theoretical predictions. Also, the relative beauty contribution to the total heavy-flavour electrons is determined.

Chapter 5 In this chapter, the focus is shifted to study properties of nuclear matter produced at moderate temperature and finite baryon chemical potential. We examine the mass-dependent hierarchy of the kinetic freeze-out parameters of the different identified hadrons such as light hadrons, heavy strange hadrons at different beam energies. These parameters are obtained by fitting the transverse momentum distribution with blast-wave descriptions within the non-boost-invariant scenario.

Chapter 6 In this chapter, the study of the anisotropic flow of the charged hadrons by simulating non-central low energy nuclear collisions at various beam energies using the UrQMD model is carried out. These results would serve as predictions for the upcoming experiments in the near future.

Chapter 7 Finally, we summarize the results presented in this thesis and provide possible future plans.

Chapter 2

Experimental Setup: ALICE

To perform heavy-ion experiment, one require ingredients like accelerator to accelerate the beams, fast detectors to detect the produced particles along with good computing facility. In this chapter, brief introduction to the accelerator facility LHC, the sub-detectors of ALICE apparatus and the event and track selection criteria used for the analyses performed in this thesis are presented.

2.1 Large Hadron Collider (LHC)

The Large Hadron Collider (LHC) [67] is world's largest and most powerful accelerator with circumference of 27 km, situated near Geneva, Switzerland, built by European Organisation for Nuclear Research (CERN) during 1998 to 2008. The designed luminosity of the LHC is $10^{34} cm^{-2} s^{-1}$ and $10^{27} cm^{-2} s^{-1}$ for colliding protons and lead ions respectively and the designed centre-of-mass energies are 14 TeV and 5.5 TeV for pp and Pb-Pb collisions respectively.

As depicted in Figure 2.1, at LHC, two beams which travel with relativistic speeds through the accelerators in the opposite direction collide at four main interaction points. Four main experiments are situated at those points namely, ATLAS (A Toroidal LHC Apparatus), CMS (Compact Muon Solenoid experiment), LHCb (LHC beauty) and ALICE (A Large Ion Collider Experiment).

CMS and ATLAS are general-purpose experiments, built with the same goal and designed mainly for pp collisions to detect Higgs boson and study physics beyond the standard model. But the experimental set-ups of each of these experiments are different. LHCb experiment is a small experiment dedicated to the study of matter and anti-matter by studying the beauty quark.

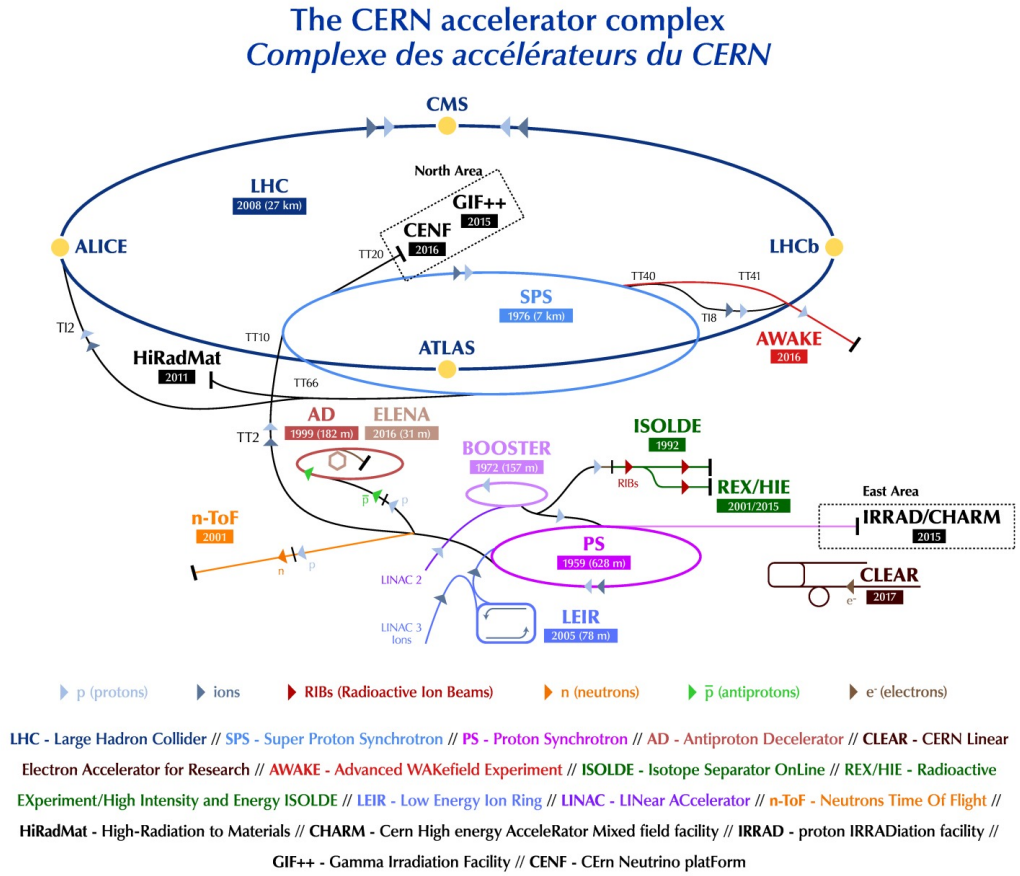

Figure 2.1. CERN's accelerator complex [68]

ALICE is a collider experiment built to study the strongly interacting matter, i.e. Quark-Gluon Plasma (QGP), formed at very high temperature/energy density by colliding two heavy-ions at relativistic energies. ALICE collects the data for different collisions systems like p + p, p + Pb and Pb + Pb (Xe + Xe) collisions at various colliding energies.

2.2 A Large Ion Collider Experiment(ALICE)

A Large Ion Collider Experiment (ALICE) is one of the four major experiments built at the LHC. It is specially designed for the heavy-ion program to focus on understanding the nature of the strongly interacting matter at high temperature and small net baryon density. It has excellent particle identification capabilities in a wide transverse momenta range i.e. 100 MeV/c to 100 GeV/c.

Detector	Acceptance (η, ϕ)	Position (m)
ITS layer 1,2 (SPD)	$\lvert\eta\rvert < \pm 2, \pm 1.4$	0.039, 0.076
ITS layer 3,4 (SDD)	$\lvert\eta\rvert < \pm 0.9, \pm 0.9$	0.150, 0.239
ITS layer 5,6 (SSD	$\lvert\eta\rvert < \pm 0.97, \pm 0.97$	0.380, 0.430
TPC	$\lvert\eta\rvert < \pm 0.9$ at r = 2.8 m $\lvert\eta\rvert < \pm 1.5$ at r = 1.4 m	0.85, 2.50
TOF	$\lvert\eta\rvert < \pm 0.9$	3.70, 3.99
TRD	$\lvert\eta\rvert < \pm 0.8$	2.90, 3.68
HMPID	$\lvert\eta\rvert < \pm 0.9$ $1.2^\circ < \phi < 58.8^\circ$	5.0
PHOS	$\lvert\eta\rvert < \pm 0.12$ $220^\circ < \phi < 320^\circ$	4.6, 4.78
EMCal	$\lvert\eta\rvert < \pm 0.7$ $80^\circ < \phi < 187^\circ$	4.30, 4.55
ACORDE	$\lvert\eta\rvert < \pm 1.3$ $-60^\circ < \phi < 60^\circ$	8.5
	Muon spectrometer	
Tracking chambers	$-4 < \eta < -2.5$	-0.142, -0.054
Trigger chambers	$-4 < \eta < -2.5$	-0.171, -0.161
ZDC	$\eta > 8.8$ $\phi < 10^\circ$, $6.5 < \eta < 7.5$ $\phi < 32^\circ$, $4.8 < \eta < 5.7$	$\pm$ 113 $\pm$ 113
PMD	$2.3 < \eta < 3.7$	3.67
FMD disc 1	$3.6 < \eta < 5.0$	3.2
FMD disc 2	$1.7 < \eta < 3.7$	0.80
FMD disc 3	$-3.4 < \eta < -1.7$	-0.70
V0A	$2.8 < \eta < 5.1$	3.4
V0C	$-3.7 < \eta < -1.7$	-0.90
T0A	$4.6 < \eta < 4.9$	3.75
T0C	$-3.3 < \eta < -3.0$	-0.70

Table 2.1. Summary of the subsystems in the ALICE detector which includes acceptance and positions from the interaction point.

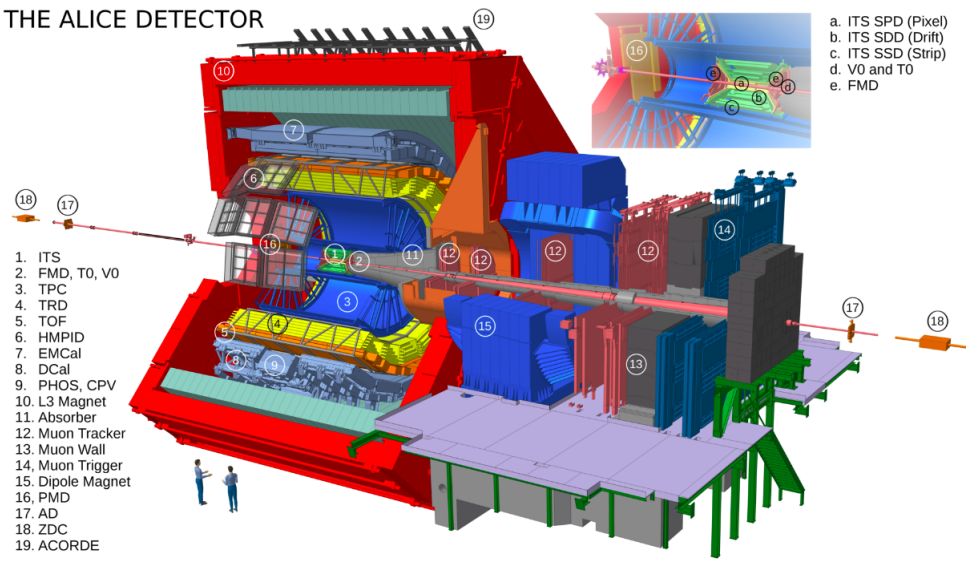

Figure 2.2. Schematic of the ALICE detector with its 19 sub-detector subsystems.

2.2.1 Detector layout

ALICE apparatus is composed of several sub-detectors built on the basis of different detection techniques required by the kinematics and nature of different particles, as shown in Figure 2.2. The sub-detectors are generally classified into two broad groups:

- **Central barrel detectors:** These detectors are placed inside the standard magnetic field strength (B) of 0.5 T (low magnetic field strength of 0.2 T for Xe–Xe at $\sqrt{s_{NN}} = 5.44$ TeV and few data samples of pp collision systems at $\sqrt{s} = 13$ TeV in 2015–2018) and are used for the tracking and particle identification (PID) purpose. It consists of sub-detectors namely Inner Tracking System (ITS) [69], Time Projection Chamber (TPC) [70], Time Of Flight (TOF) [71], Transition Radiation Detector (TRD) [72], High Momentum Particle Identification (HMPID) [73], PHOton Spectrometer (PHOS) [74], Electro Magnetic Calorimeter (EMCAL) [75] and ALICE Cosmic Ray Detector (ACORDE) [76] situated in the mid-rapidity region. All these detectors have full azimuthal coverage around the beam pipe except HMPID, PHOS, EMCAL and ACORDE.

- **Forward detectors:** The detectors in forward rapidity regions are clas-

sified under this category. It consists of the sub-detectors such as Forward Multiplicity Detector (FMD) [77], Photon Multiplicity Detector (PMD) [78], Muon Spectrometer [79], Zero Degree Calorimeter (ZDC) [80] and detectors for trigger and timing (VZERO (V0) and TZERO (T0)) [81].

Summary of these sub-detectors is shown in Table 2.1. The detectors used for the analyses (ITS, TPC, TOF, V0 and T0) in this thesis are described in brief.

Inner Tracking System (ITS):

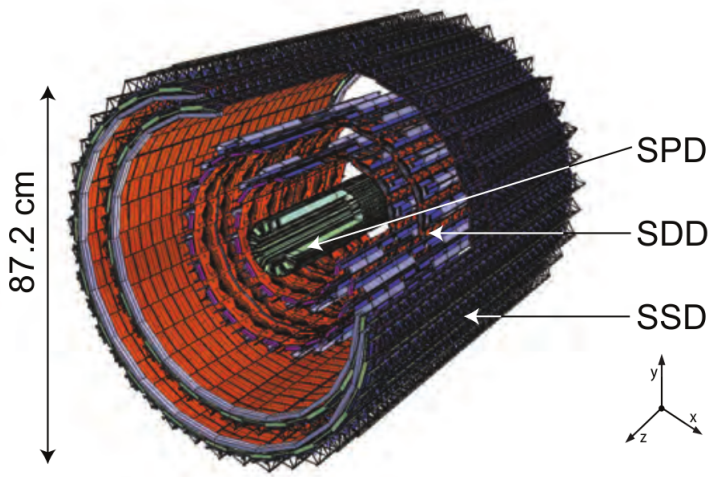

Figure 2.3. Inner tracking system [69] of the ALICE detector.

Inner Tracking System (ITS) [69] is the first sub-detector in the ALICE detector set-up just after the beam pipe (situated at 3 cm). The schematic diagram of the ITS is shown in Figure 2.3. At present, ITS consists of six layers of silicon detectors with three sub-detectors viz. Silicon Pixel Detector (SPD), Silicon Drift Detector (SDD) and Silicon Strip Detector (SSD) within the radius between 3.9 to 43 cm. Each of these sub-detectors has two layers. All of them are used for tracking purpose whereas SDD and SSD are also used for Particle Identification of the low-momentum charged particles produced in the heavy-ion collisions using their specific energy loss (dE/dx) while traversing through the detector (see Figure 2.4). High particle density requires very high precision in the tracking, which is exactly what is provided by this detector. ITS is

also used for the determination of the primary vertex of the interaction. SPD

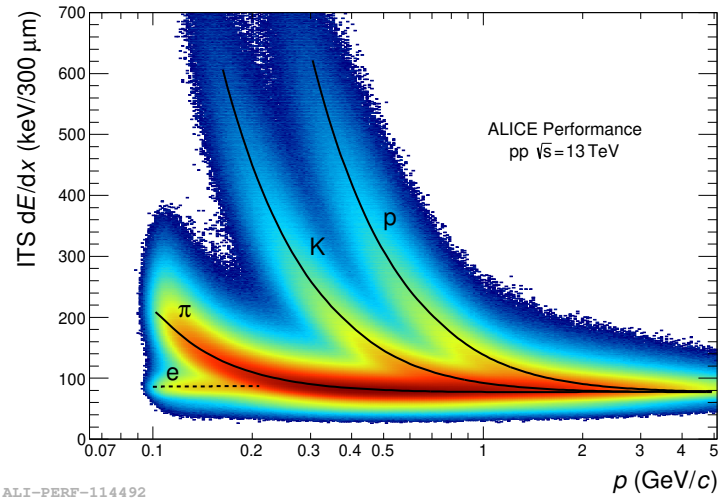

Figure 2.4. PID using Inner tracking system [69] of the ALICE detector.

is the innermost sub-detector in ITS with two layers made up of hybrid silicon pixels. It has 9.8 million pixels each with size 50 ($r\phi$) $\times$ 425 (z) μm^2 which provides the spatial resolution of 12 and 100 μm in $r\phi$ and z-direction, respectively. Next sub-detector is SDD which provides the spatial resolution of 35 and 25 μm along the $r\phi$ and z-direction, respectively. It also helps in particle identification using specific energy loss measurement. The last two layers in ITS is SSD which consists of double-sided silicon strip sensor modules. It has a precision with a spatial resolution of 20 and 830 μm along the $r\phi$ and z-direction respectively and also provides dE/dx measurement. For the precise reconstruction of the space points, the alignment of the ITS modules plays a vital role. This is required to extract the information of the low momentum and Distance of Closest Approach (DCA) to the primary vertex.

Time Projection Chamber (TPC):

In ALICE central barrel, TPC [70] is the main tracking and PID detector with full azimuthal coverage (2π) and pseudo-rapidity coverage of $|\eta| < 0.9$. TPC is cylindrical in shape with inner and outer radius are about 85 cm and 250 cm respectively and 5 m in length along the beam direction as shown in Figure 2.5. It is filled with the gas mixture of Ne–CO_2–N_2. The gas volume is divided

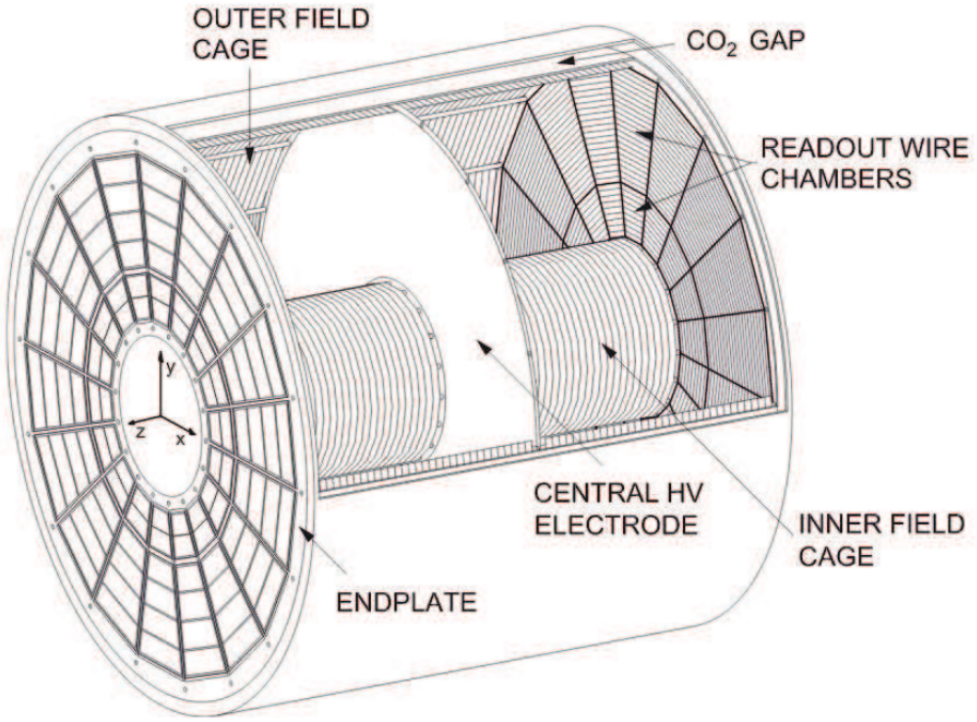

Figure 2.5. Schematic diagram of Time Projection Chamber [70].

into two drift regions of 250 cm each in length by central high voltage (HV) electrode. This creates a highly uniform electrostatic field throughout the gas volume of TPC. The readout chambers are placed at the two end plates which are based on the Multi-Wire Proportional Chamber (MWPC) technique. Every end-plate is divided into 18 trapezoid shape sectors with cathode pad. The gas inside the TPC active volume is ionised by the traversing charged particle, which in result produce the electrons. These electrons which drift parallel to the electric and magnetic field, accumulates the charge on one of the end-plates which is proportional to the energy loss of that charged particle in the gas.

Identification of these particles is done based on specific-energy loss ($\mathrm{d}E/\mathrm{d}x$) of the traversing particle in the gas volume using the Bethe-Bloch formula. Figure 2.6 depicts the particle identification in TPC using specific energy loss ($\mathrm{d}E/\mathrm{d}x$) and provides clear separation among the different species of particles. It also provides a good vertex reconstruction. These capabilities of TPC allow the measurement of the charged particles in the wide range of the momentum ($p_{\mathrm{T}} = 100$ MeV/c up to 100 GeV/c). TPC provides about 5.2% $\mathrm{d}E/\mathrm{d}x$

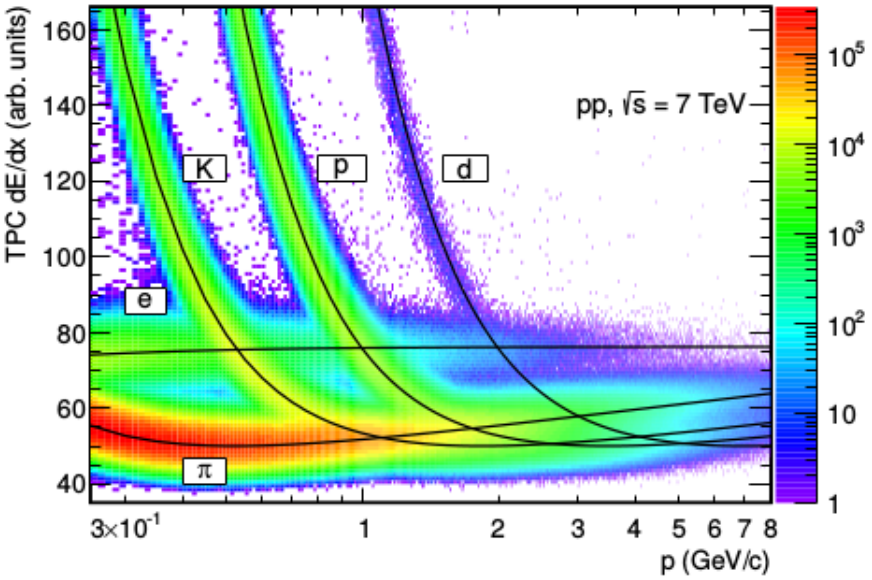

Figure 2.6. PID using Time Projection Chamber [70] of the ALICE detector.

resolution in pp collisions and 6.5% dE/dx resolution in Pb–Pb collisions.

Time Of Flight (TOF)

TOF [71] detector is situated between 370 and 399 cm with length of 745 cm with pseudo-rapidity coverage of $|\eta| < 0.9$ and full azimuthal coverage (2π). It compliments TPC by identifying the particles like kaons and pions in intermediate momentum range up to 2.5 GeV/c and protons upto 4 GeV/c. This helps to eliminate the contamination from hadrons in case of electron measurements.

Time of Flight information of the particles is used to identify the particles as demonstrated in Figure 2.7. The mass of the particle can be calculated as,

$$m^2 = \frac{p^2}{c^2}\left(\frac{c^2t^2}{L^2} - 1\right) \tag{2.1}$$

Where, t is the time of flight and L is trajectory length of the particle in TOF detector. So, by measuring the mass, particles can be separated. One can also avail alternative way by estimating its velocity β,

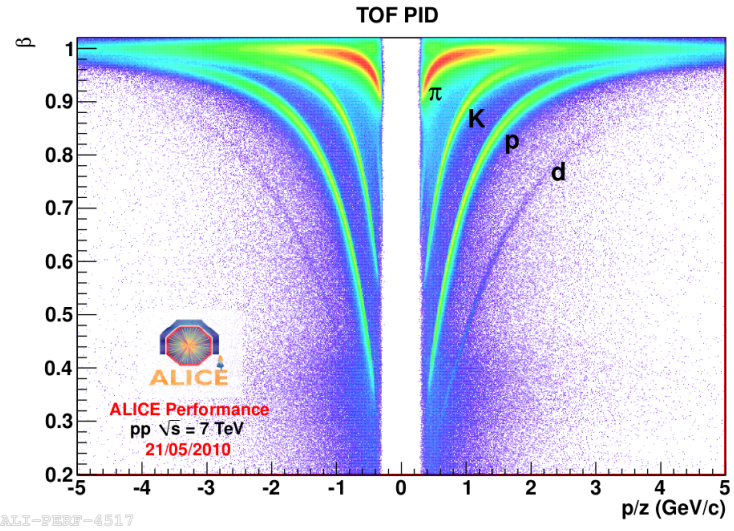

Figure 2.7. PID using Time of Flight [71] of the ALICE detector

$$\beta = \frac{p}{\sqrt{m^2c^2 + p^2}}. \tag{2.2}$$

Figure 2.7 illustrates the particle identification performed by TOF using eq. 2.2 which is plotted as a function of momentum over atomic number.

VZERO (V0) detector

V0 [81] detector consists of two scintillator arrays V0A and V0C situated at 90 cm and 340 cm on either side of the collision vertex (z = 0) with pseudo-rapidity coverage of -3.7 $< \eta <$ -1.7 and 2.8 $< \eta <$ 5.1 respectively. V0 detector is used as a minimum bias trigger and high-multiplicity triggers. It can also be used to reject the beam-gas background as well as to estimate the centrality in the heavy-ion collisions.

TZERO (T0) detector

Similar to the V0 detector, T0 [81] detector also consists of two arrays T0A and T0C located at 375 cm and 70 cm on the either side of the interaction point with pseudo-rapidity coverage of $4.6 < \eta < 4.9$ and $-3.3 < \eta < -3.0$ respectively. T0 detector can be used to provide the start signal for the estimation of the Time

of Flight for particle identification.

2.2.2 ALICE trigger and data reconstruction

ALICE Trigger

At the moment, there are two different level trigger systems in ALICE. Central Trigger Processor (CTP) is a low-level and hardware trigger which collects the information from different sub-detectors. The decision on whether to record an event or not is taken by CTP. Other trigger is a pure software trigger and known as High-Level trigger (HLT) which provides further sophisticated logic triggers.

At every machine clock cycle (25 ns), the trigger inputs are evaluated by CTP. There are three level triggers Level 0 (L0), Level (L1) and Level (L2) depending on the different readout time. The L0 trigger inputs are sent to CTP by V0, T0, SPD, EMCal, PHOS, and MTR. CTP sends a trigger signal to corresponding read-out detectors at 1.2 μs after the collision. Furthermore, L1 inputs are sent to CTP to further evaluate the events by ZDC, TRD, EMCal detectors. After making the decision, CTP sends the trigger signal to read-out. It takes around 6.5 μs due to the propagation and computation time.

The last low-level trigger is L2 which waits until the so-called *past-future protection interval* in order to reject the piled-up events (more than one collision are superimposed) and this time is equivalent to the TPC drift time (100 μs). The events which satisfy the L2 trigger are then sent to the Data AcQuisition System (DAQ) and HLT, to perform detailed analysis filtering which helps to reduce the size before storage. For different analyses, the event types can be categorised under different trigger conditions. For instance, Minimum-bias (MB) events, which are the L0 triggered events, are kept under kMB (or kINT7) trigger. They have the least requirements while avoiding the empty events. In proton-proton collisions, this can be obtained by requiring OR logic i.e. hit in either of the two arrays of V0 (V0A or V0C) or AND logic i.e. having hits in both arrays of the V0 detector [82].

Data reconstruction

During the first pass reconstruction (pass1), high precision calibration data are produced. Offine Condition Data Base (OCDB) is used to store the detector alignment and calibration data. With the help of information from data reconstruction, an Event Summary Data (ESD) is produced, which further can be used to produce the first Analysis Object Data (AOD) for specific physics analyses. Furthermore, using the inputs from analyses and the feedback from pass1 data, pass2 data is reproduced.

2.3 ALICE framework

To store, handle and analyse the huge amount of collected and reconstructed data, the special framework of computing Grid resources in ALICE environment is developed. It is also known as AliEn [83]. Since 2000, AliEn is in development and used for data production as well as for the user data analysis since 2005. AliEn is also very important in the production of the simulated data. Moreover, based on the ROOT framework [84], AliRoot offline framework is built to simulate, calibrate, reconstruct and analyse experimental and simulated data. Many of the codes inside this framework are written in C++ programming language, and the flowchart of this framework is shown in Figure 2.8. The analyses discussed in this thesis are performed using C++ classes/tasks. These tasks can be found in the AliPhysics directory of the AliRoot software.

2.4 Selection criteria for Analyses

There are three data analyses discussed in this thesis. They are performed by following a set of selection criteria, and some of the general selection criteria are described in this section.

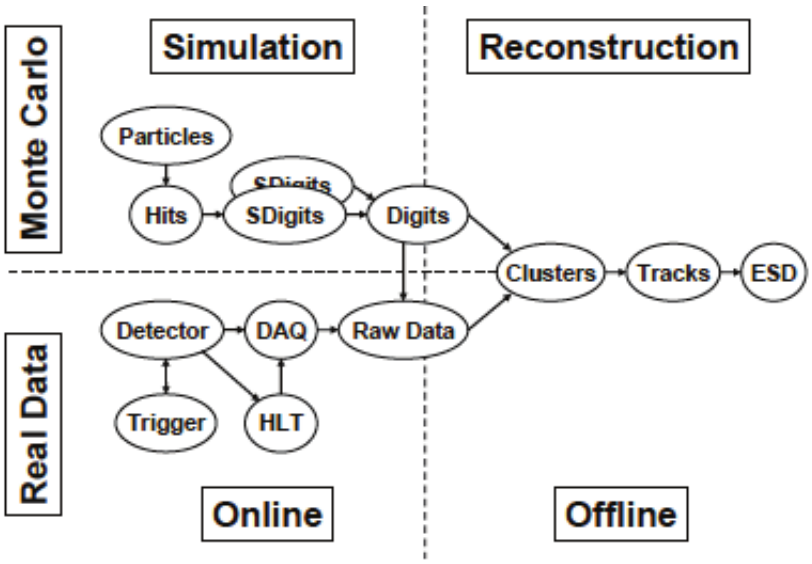

Figure 2.8. Flowchart of AliRoot framework [67]

2.4.1 Event selection

In data analysis, the selection of events is performed by applying some basic physics selection criteria. Reconstruction of the primary vertex (interaction point) is one of the important event selection criteria. The tracks reconstructed using TPC and ITS are identified as global tracks which are further used to find the primary vertex. Events with at least two tracks and a primary vertex within 10 cm ($|Vz| \leqslant 10$ cm) from the centre of the detector set-up along the beam axis are used for the analyses presented in this thesis. The pile-up events are removed using standard physics selection criteria. Moreover, the events satisfying Minimum Bias trigger (kINT7) condition are selected for the analysis.

2.4.2 Selection and Identification of electron tracks

After selecting the events to be used for further analysis which passed through the criteria such as trigger and vertex selection and removal of pile-up events, the next step is to select the reconstructed tracks therein. Tracks coming from various detectors considered for analyses which satisfy different requirements are discussed below (and mentioned in Table 3.1, 3.2 and 4.1 in the next chapters):

- Number of clusters are used to characterise the track quality in the TPC. Clusters found in TPC are used for the reconstruction and re-fit of the track. However, not all tracking clusters are used for the energy loss calculation, e.g. clusters close to the border of TPC sectors are avoided for the calculation. Only tracks which are having at least 100 or 120 (maximum clusters 159) clusters used for the tracking and at least 80 or 90 clusters used for the energy loss calculation were accepted in the analysis. The requirement on a large number of TPC clusters for track selection is used to improve the discrimination of pion and electron. This is because on average, electron tracks consist of a large number of clusters.

- In addition to the restriction on a minimum number of ITS hits (ITS hits $\geqslant$ 3), the contribution of electrons due to conversion of photons in the detector material of ITS is minimised by requiring hits in both SPD layers (kBoth) of ITS.

- Tracks having a significant number of TPC clusters resulting from more than one charged particle are considered as fake tracks and those were rejected by requiring χ^2/ndf of momentum fit less than 4.

- Figure 2.9 illustrates the pictorial representation of Distance of Closest Approach (DCA) of the tracks to the primary vertex, which is obtained by extrapolating the track at a secondary vertex to the primary vertex. Requirement on the DCA was restricted to 1 cm in the radial direction and 2 cm along the beam direction to reject background and non-primary tracks in the analysis.

For the identification of the electrons, TPC and TOF detectors are used for the analyses. TPC measures the specific energy loss (dE/dx) of the traversing particles which is expressed as the deviation from the expected dE/dx [85] of electrons in terms of dE/dx resolution (σ) i.e. nσ = TPC $\frac{dE}{dX}$ - $<$ TPC $\frac{dE}{dX}>|_{el}$. Similarly, TOF signal is expressed as deviation from expected time of flight of

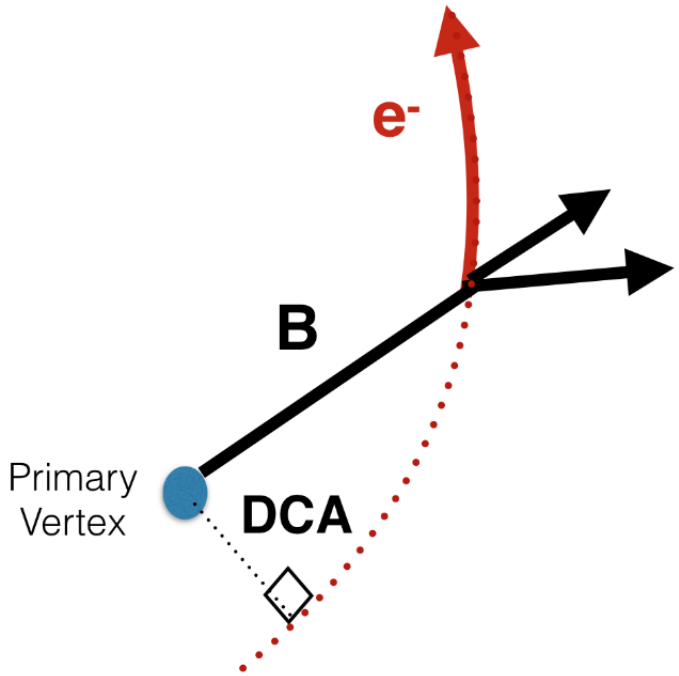

Figure 2.9. Pictorial representation of Distance of Closest Approach to the primary vertex

electrons in terms of time resolution (σ) (nσ = TOF t - $<$ TOF t $>|_{el}$). Tracks with a TPC $n\sigma$ between -1 and 3 are selected as electron candidates. TPC gives a similar response to electrons, kaons and protons at low momentum regions, therefore, the time of flight information using TOF is used further to separate kaons and protons from electrons up to 2.5 and 4 GeV/c respectively. Tracks outside the region $\pm$ 3 σ around the expected time of flight of the electrons are rejected resulting in the removal of hadrons from the electron sample. The above selection criteria can also minimise the contribution from the kaons and protons in the very low p_T region (around $p_T \approx$ 0.5 and 1.0 GeV/c) where their lines cross the electrons. TPC $n\sigma$ distribution before (upper panel) and after (lower panel) TOF is shown in Figure 2.10. From the lower panel of the Figure, it can be seen that most of the hadrons are eliminated after using TOF information.

The track reconstruction and PID efficiencies need to be estimated due to the limitations from selection and identification criteria. The reconstruction efficiency ($\varepsilon^{geo} \times \varepsilon^{reco}$) is estimated by taking the ratio of the tracks survived after the track selection criteria to the total tracks within the geometrical acceptance of the detector. The electron identification efficiency (ε^{eID}) of TPC is calculated

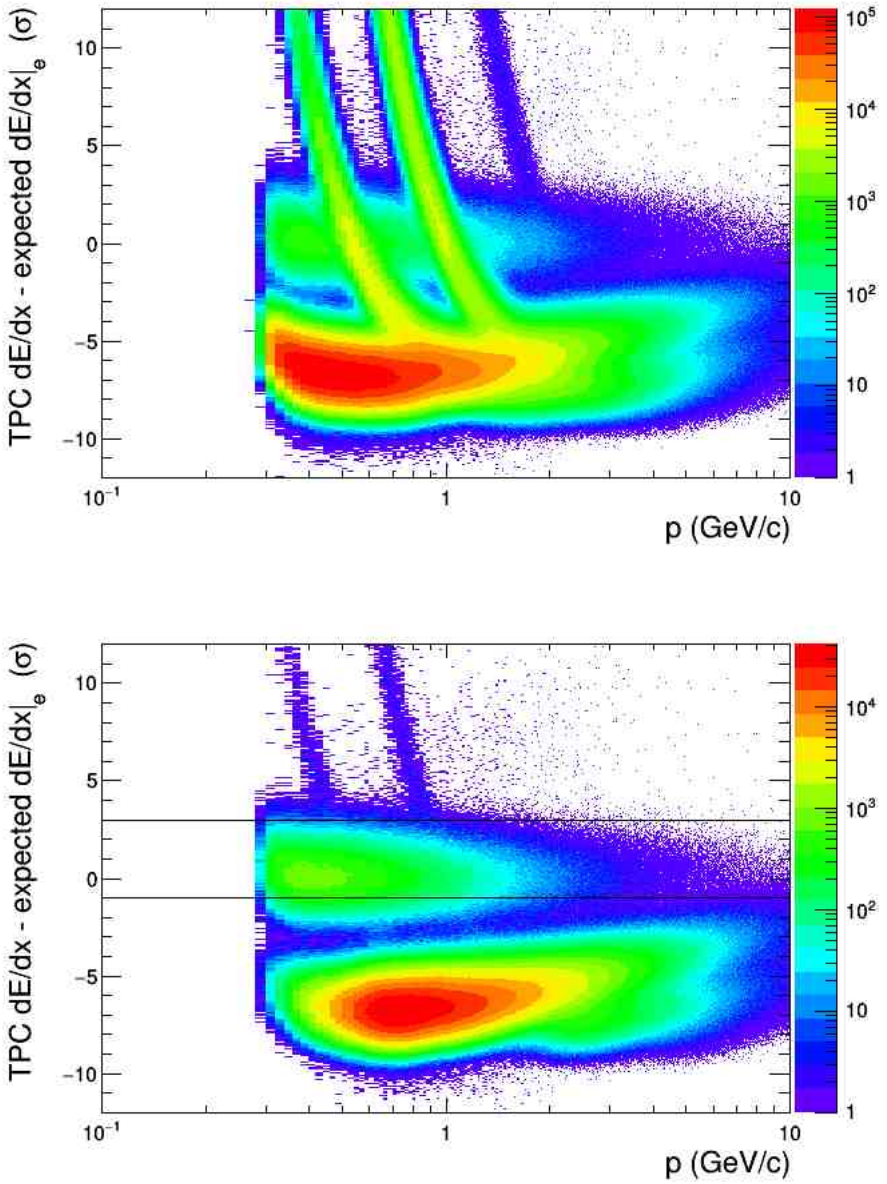

Figure 2.10. $n\sigma_{TPC}$ as a function of momentum before TOF selection [upper panel] and after TOF selection [bottom panel]. Tracks inside the black lines shown in lower panel are used for the further analysis.

by taking the ratio of the number of tracks before and after the TPC selection criteria. It is estimated using Monte Carlo (MC) simulations assuming mean and sigma of the electron TPC nσ distribution at 0 and 1 respectively. However, in data, this may not always be the case. In that scenario, the efficiency is determined using the data-driven way by integrating the electron TPC nσ distribution between -1 and 3 nσ at particular mean and sigma. This calculation

is performed in each momentum bin assuming the Gaussian shape of electron TPC nσ distribution. Similarly, TOF PID efficiency is estimated using Monte Carlo simulations.

Chapter 3

Electrons from heavy-flavour hadron decays

In this chapter, analyses of the measurement of electrons from heavy-flavour hadron decays in pp collisions at $\sqrt{s}$ = 7 and 13 TeV using the data-driven photonic electron tagging method have been discussed. The primary source of background to the signal electrons, i.e. electrons from the conversion of photons and Dalitz decays, are subtracted from inclusive electrons by building their transverse momentum distributions using the invariant mass technique.

3.1 Analysis strategy

For heavy-flavour electrons (HFE), the signal to background ratio at low transverse momentum regime is very small and therefore, it is very difficult to separate signal from background and the systematic uncertainties are dominated by the background subtraction. The main sources of background to the heavy-flavour electrons are listed as follows:

- Electrons from Dalitz decays of π^0 and η (π^0 or $\eta \rightarrow e^+e^-\gamma$) and the conversion of photons ($\gamma \rightarrow e^+e^-$) in the detector material, termed as photonic in the text.
- Electrons from J/ψ (J/$\psi \rightarrow e^+e^-$) and weak K_{e3} ($K^{0/\pm} \rightarrow e^{\pm}\ \pi^{0/\mp}\ \nu_e$) decays.
- Electrons from low mass vector mesons ($\rho \rightarrow e^+e^-$, $\omega \rightarrow e^+e^-$, $\phi \rightarrow e^+e^-$).

Previously, the so-called cocktail method [86] has been employed to measure the electrons coming from heavy-flavours. In this method, the cocktail of electrons from different background sources is calculated from the measured spectra of these sources using the Monte-Carlo simulations. However, those measurements had sizable systematic uncertainties coming from the cocktail subtraction. Therefore, recently, a data-driven method has been developed in which the distribution of electrons from Dalitz decays, and photon conversions are built by reconstructing the invariant mass distributions of unlike-like sign pairs.

In this chapter, measurements of the electrons from heavy-flavor hadron decays in proton-proton (pp) collisions at center-of-mass energy, $\sqrt{s} = 7$ TeV with standard magnetic field (0.5 Tesla) and at center-of-mass energy, $\sqrt{s} =$ 13 TeV with low magnetic field (0.2 Tesla) are discussed. As mentioned in the Section 1.7 of Chapter 1, due to low magnetic field, the reconstruction efficiency is expected to be improved at low transverse momentum regions. Therefore, the p_{T}-differential cross-section at $\sqrt{s} = 13$ TeV is measured down to $p_{\mathrm{T}} = 0.2$ GeV/c whereas cross-section at $\sqrt{s} = 7$ TeV starts from $p_{\mathrm{T}} = 0.5$ GeV/c. The analyses are performed on the data and Monte Carlo samples shown in Table 8.1 and 8.2 and corresponding run numbers are mentioned in the Appendix 8.1 and 8.2.

Tracks used for the analyses are selected by applying certain selection criteria and furthermore, these tracks are identified as electrons using TPC and TOF detector as described in the previous chapter. The track selection and identification criteria are listed in the Table 3.1 and 3.2. The analysis at $\sqrt{s} = 7$ TeV is performed with the tracks within $|\eta| < 0.8$ whereas, the analysis at $\sqrt{s} = 13$ TeV is within $|\eta| < 0.5$ due to the underestimation of photonic background in $|\eta| < 0.8$ region. This will be discussed in the systematic study of the $|\eta|$ cut variation in section 3.2.4.

Table 3.1. Summary of the track selection criteria imposed on the electron candidates and the associated tracks in pp $\sqrt{s} = 7$ TeV analysis with normal magnetic field (B = 0.5 T)

Track and PID cuts	Inclusive electron candidates	Associated electron candidates
p_T^{min}	0.5 GeV/c	0.0 GeV/c
$\|\eta\|$	< 0.8	< 0.8
Number of TPC clusters	≥ 120	≥ 60
Number of TPC $\frac{dE}{dX}$ clusters (PID)	≥ 90	≥ 60
Number of ITS hits	≥ 4	≥ 2
χ^2 /clusters of the momentum fit in the TPC	< 4	< 4
Requirement of hits in SPD layers	**kBoth**	**–**
DCA to the primary vertex in xy	< 1 cm	< 1 cm
DCA to the primary vertex in z	< 2 cm	< 2 cm
TOF t - $< \text{TOF } t >\|_{el}$ in between	-3 to 3 σ	not used
TPC $\frac{dE}{dX}$ - $< \text{TPC } \frac{dE}{dX} >\|_{el}$ in between	-1 to 3 σ	-3 to 3 σ

3.1.1 Subtraction of hadron contamination

Even though we are able to identify the electrons using TPC and TOF detectors, however, there is still some residual contamination from hadrons in the sample which needs to be removed. So, we fit the TPC nσ distribution in different momentum (p) regions, and example of such a fit in a single momentum slice is shown in Figure 3.1 (left (right) plot for $\sqrt{s} = 7$ (13) TeV) to obtain the amount of contamination. The plots for other transverse momentum bins can be found in Appendix 8.5 and 8.6. The TPC nσ distributions of electrons are fitted and well described using the Gaussian function. Whereas, at high momenta, the kaon and proton lines start to approach each other [86] and hence, they are fitted using the parameterised templates from the data. Pions give rise to dominant contribution to the contamination above $p \approx 1$ GeV/c which is coming from its tail and not well described by the Gaussian function, so it is fitted by multiplying the Landau function with an exponential function. This approach is validated by fitting the clean sample of pions coming from K^0_s decays [87]. Then the fraction of hadron contamination (f_{had}) is estimated in each momentum slice using Eq. 3.1 and plotted as a function of the momentum as shown in the left (right) plot of Figure 3.2 for $\sqrt{s} = 7$ (13) TeV.

Table 3.2. Summary of the track selection criteria imposed on the electron candidates and the associated tracks in pp $\sqrt{s}$ = 13 TeV analysis with low magnetic field (B = 0.2 T)

Track and PID cuts	Inclusive electron candidates	Associated electron candidates
p_T^{min}	0.2 GeV/c	0.0 GeV/c
$\|\eta\|$	< 0.5	< 0.8
Number of TPC clusters	≥ 100	≥ 60
Number of TPC $\frac{dE}{dX}$ clusters (PID)	≥ 80	≥ 60
Number of ITS hits	≥ 3	≥ 2
χ^2 /clusters of the momentum fit in the TPC	< 4	< 4
Requirement of hits in SPD layers	**kBoth**	–
DCA to the primary vertex in xy	< 1 cm	< 1 cm
DCA to the primary vertex in z	< 2 cm	< 2 cm
TOF t - $< \text{TOF } t >\|_{el}$ in between	-3 to 3 σ	not used
TPC $\frac{dE}{dX}$ - $< \text{TPC } \frac{dE}{dX} >\|_{el}$ in between	-1 to 3 σ	-3 to 3 σ

$$f_{had} = \frac{\int_{x_{min}}^{x_{max}} (f_\pi(x) + f_K(x))dx}{\int_{x_{min}}^{x_{max}} (f_\pi(x) + f_K(x) + f_{el}(x))dx} \tag{3.1}$$

where x_{min} = -1.0 and x_{max} = 3.0 are the TPC PID cuts and $f_i(x)$ are the fit functions for the respective particle type i.

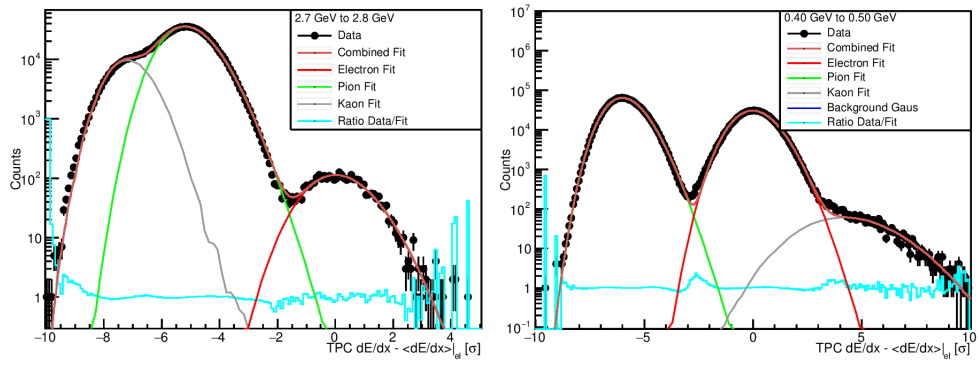

Figure 3.1. TPC nσ distribution with simultaneous fit of electrons (red), pion (green) and kaon (grey) distributions. In addition, the ratio (blue) between data and fit is shown. Left: pp at $\sqrt{s} = 7$ TeV (2.7 GeV/c $< p <$ 2.8 GeV/c) and Right: pp at $\sqrt{s} = 13$ TeV (0.4 GeV/c $< p <$ 0.5 GeV/c)

It is observed in case of $\sqrt{s} = 13$ TeV (also in $\sqrt{s} = 5.02$ TeV analysis [88]) analysis that the kaon and proton lines cross the electrons lines at low momenta and furthermore, pions at very low momenta (around 0.2 – 0.3 GeV/c). These features give rise to peaks in those momentum regions which are fairly

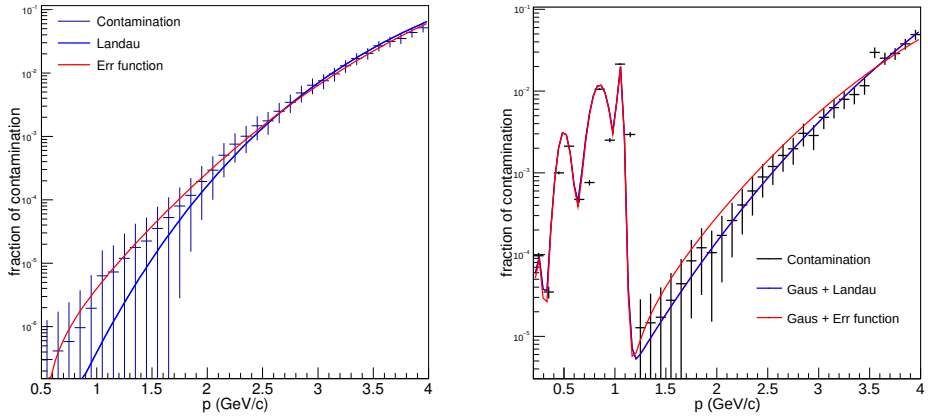

Figure 3.2. The fraction of hadrons selected with the PID requirements on the TOF signal for pp at $\sqrt{s} = 7$ TeV (left) and 13 TeV (right).

well described using the Gaussian function as shown in the right plot of the Figure 3.2. These features are not observed in $\sqrt{s} = 7$ TeV analysis discussed in this thesis, previously published 7 TeV [86] and also 2.76 TeV [62, 89] analyses which are performed on the Run 1 data from ALICE. Apart from the peaks, the rest of the fractions of the contamination shown in Figure 3.2 are fitted using the Landau and Error function (see Figure 8.1 and 8.2 in Appendix 8.4). The amount of contamination is below 5–6% at high momentum regions in both analyses and it is statistically subtracted from the inclusive electron spectrum to get the pure sample of electrons in both cases.

3.1.2 Subtraction of Photonic background

As mentioned earlier, the electrons from Dalitz decays and the conversion of photons are the main sources of the background. So, the subtraction of this background is done in a data-driven way by using so-called Photonic-electron tagging method [62, 90]. The electron-positron pairs from all the final state particles of Dalitz decays are used to estimate the contribution from the background electrons in each transverse momentum (p_{T}) bin. For this purpose, the pools of the electrons with tighter (second column of the Table 3.1) selection criteria to select the signal and looser (third column of the Table 3.1) selection criteria to allow as much photonic background as possible, are built. Then the invariant

mass distributions of like (e^+e^+ or e^-e^-) and unlike (e^+e^-) pairs are obtained by "tagging" electron (positron) from one pool (inclusive electron candidates) with the electron (positron) from other pool (associated electron candidates) and contribution below certain pair invariant mass ($m_{inv} < 0.14$ GeV/c) is selected in each transverse momentum (p_{T}) bin as shown in left plot of Figure 3.4. However, due to the acceptance and the detector limitations, we are not able to get all the photonic electrons. So, using MC sample, we estimate the conditional probability (also called as tagging efficiency) that how much of the electrons are being "tagged" within the acceptance out of total produced by using Eq. 3.3. From Eq. 3.2, the actual amount of the photonic electrons in the sample is then obtained.

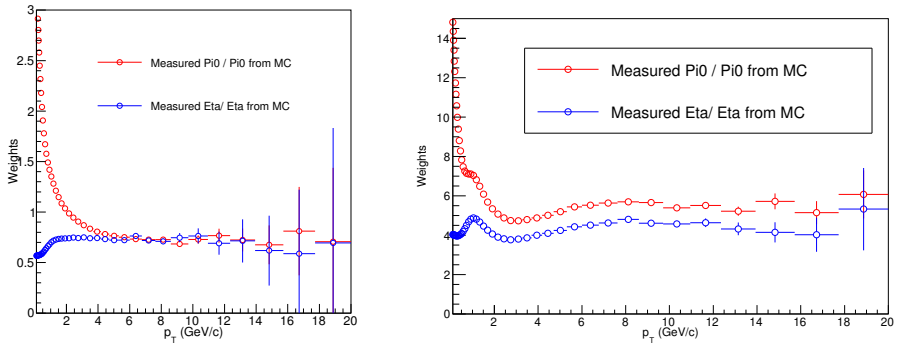

Figure 3.3. Weights calculated for π^0 ($\pi^{\pm}$) and η as the ratio of measured p_T spectra of π^0 ($\pi^{\pm}$) and η to p_T spectra of π^0 and η from the MC MB sample for pp at $\sqrt{s} = 7$ (left) and $\sqrt{s} = 13$ TeV (right).

$$N_{photonic} = \frac{N_{ULS} - N_{LS}}{\varepsilon_{tagging}} \tag{3.2}$$

where,

$$\varepsilon_{tagging} = \frac{N_{found}}{N_{photonic}} \tag{3.3}$$

The tagging efficiency as a function of transverse momentum used in $\sqrt{s}$ = 7 (13) TeV analysis is shown in the left (right) plot of Figure 3.5. The tagging efficiency depends on the shape of the p_T distributions of mothers of the

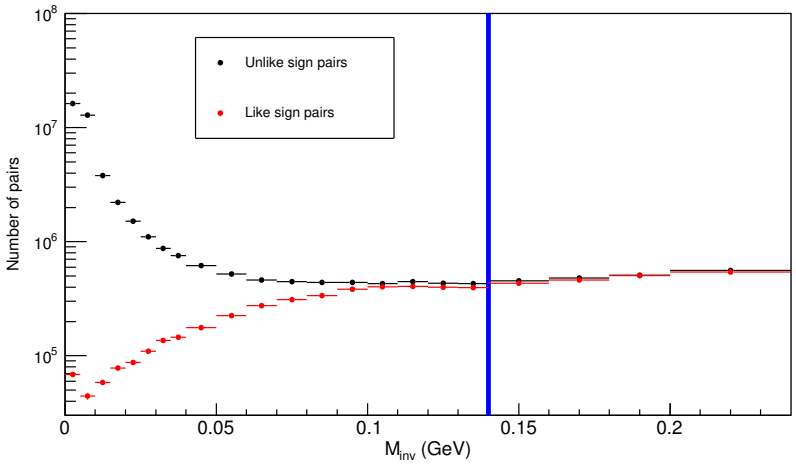

Figure 3.4. The distributions of the unlike and like sign pairs as a function of the pair invariant mass. The maximal mass of the pair used in this analysis is indicated by a blue line.

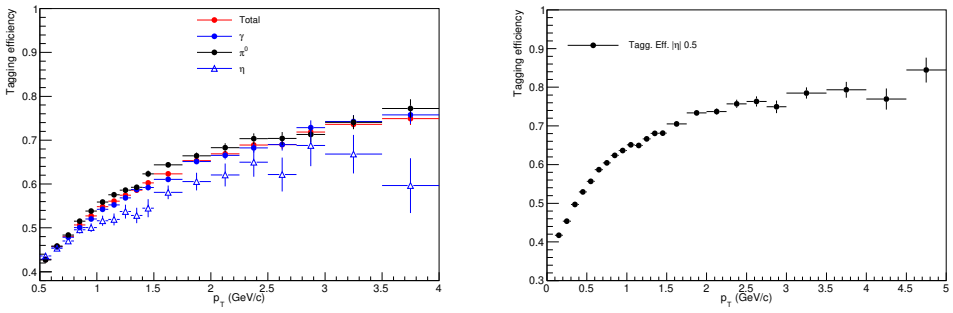

Figure 3.5. The tagging efficiency as a function of the transverse momentum of photonic electron candidate used in $\sqrt{s} = 7$ (left) and $\sqrt{s} = 13$ (right) TeV analysis.

photonic electrons, i.e. π^0 and η, since, more the p_T, smaller the opening angle between the e^+-e^- pairs and more the probability that they will get "tagged" whereas smaller the p_T, larger will be the opening angle and chances of losing one of the e^+ or e^- will be more due to the acceptance of the detector. Therefore, to make sure that the shapes of the p_T distributions of mothers of the photonic electrons are well reproduced in the MC as data, they need to be re-weighted. Those weights are obtained by taking the ratio of measured π^0 [91] ($\pi^{\pm}$) and η spectra in data to the corresponding spectra in the MC as shown in the left plot ($\sqrt{s} = 7$ TeV) and right plot ($\sqrt{s} = 13$ TeV) of Figure 3.3. In the case of $\sqrt{s} = 13$ TeV analysis, the charged pions ($\pi^{\pm}$) are used instead of π^0, as the measured

spectra of the latter is not reported. Moreover, the measured η spectra in $\sqrt{s}$ = 13 TeV analysis is calculated by applying m_{T}-scaling approach [92, 93] to measured $\pi^{\pm}$ spectra.

The obtained photonic electron background is subtracted from the inclusive electrons to get the raw yield of the heavy flavour electrons (non-photonic electrons). Figure 3.6 shows the obtained raw Heavy-Flavour electrons (HFE) spectra after subtracting the photonic spectra and contamination from raw inclusive spectra in both $\sqrt{s} = 7$ TeV (left) and $\sqrt{s} = 13$ TeV (right) analyses.

The raw yield still contains electrons from J/ψ di-electron decays and weak Kaon decays ($\mathrm{K_{e3}}$) which are very small in comparison to the photonic background. These contributions will be subtracted after correcting the heavy-flavour raw yield for acceptance and efficiency and normalisation. The cocktail components of electrons from dielectron decays and weak Kaon decays ($\mathrm{K_{e3}}$) were taken from the cocktail belonging to the published ALICE result [86]. This cocktail subtraction is done in case of $\sqrt{s} = 7$ TeV analysis; however, not in the case of $\sqrt{s} = 13$ TeV analysis. The contribution from dielectron decays of light vector mesons (ρ , ω and ϕ) are negligible compared to contributions from the photonic sources due to their small branching ratio into electronic channels [86].

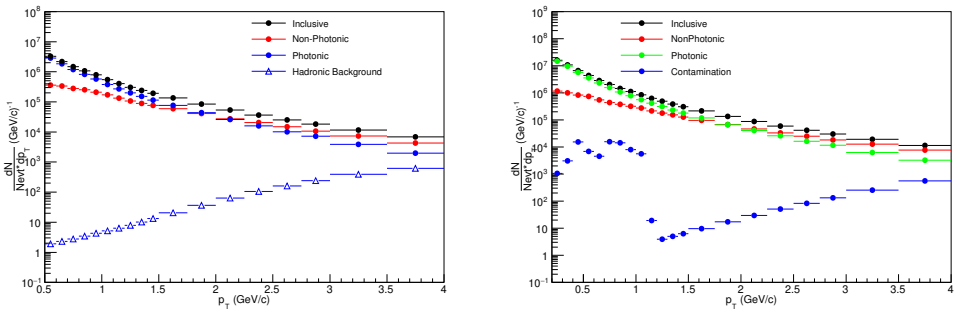

Figure 3.6. The raw inclusive, photonic and non-photonic spectrum as a function of transverse momentum as well as the hadron contamination.

3.1.3 Estimation of p_{T}-differential production cross-section

To obtain the efficiency corrected yield of electrons from heavy-flavour hadron decays, the raw yield (N^{e}_{raw}) is to be corrected for the number of events (N_{MB}),

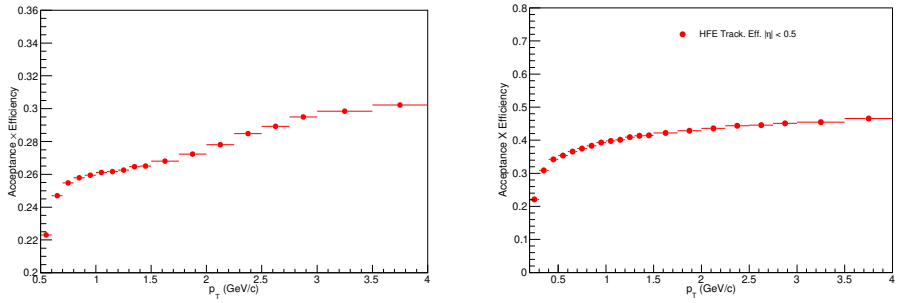

Figure 3.7. The total reconstruction efficiency ($\varepsilon^{geo} \times \varepsilon^{reco} \times \varepsilon^{eID}$) as a function of the transverse momentum calculated using the enhanced MC sample for $\sqrt{s} = 7$ (left) and $\sqrt{s} = 13$ (right) TeV.

reconstruction ($\varepsilon^{geo} \times \varepsilon^{reco}$) and PID efficiencies ($\varepsilon^{eID}$). The TPC and TOF PID efficiencies of the electrons are estimated using the Monte Carlo (MC) in case of pp at $\sqrt{s} = 7$ TeV analysis. Whereas, TPC PID efficiency of the electrons in $\sqrt{s} = 13$ TeV analysis is not estimated using Monte Carlo since due to problems associated with TPC splines, the mean and sigma of the TPC nσ of the electrons are not at 0 and 1 respectively as shown in the right plot of Figure 3.8. Therefore, it is estimated using the data-driven method as described earlier in the section 2.4 of chapter 2.

The momentum resolution and energy loss in the detector material due to bremsstrahlung distort the shape of the transverse momentum distribution and affects its precision as well. Therefore, in addition to the efficiency correction, the measured p_T spectrum has to be corrected for these effects. This correction increases with the steepness of the distribution and also with the bin widths. These modifications of the p_T spectrum can be expressed by a response matrix which acts on the natural distribution. To estimate the inverted response matrix, which is needed to restore the natural distribution, a Bayesian unfolding procedure was applied [94].

The final invariant production cross-section for electrons $\left(\frac{e^+ + e^-}{2}\right)$ from heavy-flavour hadron decays was thus calculated using the following equation:

$$\frac{1}{2\pi p_T}\frac{d\sigma^e}{dp_T d\eta} = \frac{1}{2}\frac{1}{2\pi p_T^{centre}}\frac{1}{\Delta y \Delta p_T}\frac{N^e_{raw}}{\varepsilon^{geo} \times \varepsilon^{reco} \times \varepsilon^{eID}}\frac{\sigma_{MB}}{N_{MB}} \tag{3.4}$$

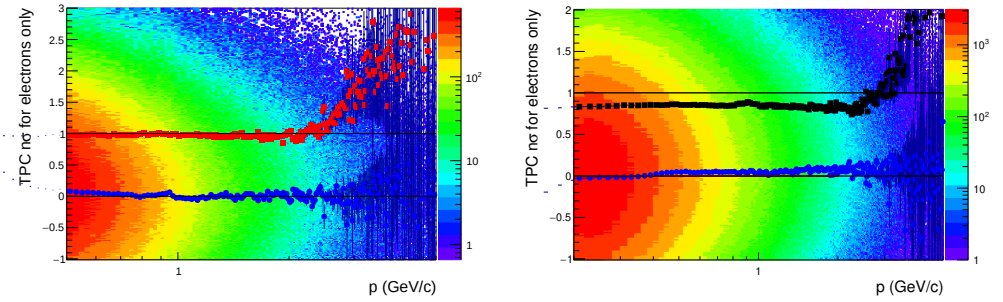

Figure 3.8. $n\sigma_{TPC}$ distributions, after the TOF cut, for data with the values of the mean (blue) and sigma (red) of the electron fit by a gaussian for $\sqrt{s} =$ 7 (left) and $\sqrt{s} = 13$ (right) TeV.

Where N_{MB}, the number of events are estimated using following formula.

$$N_{MB} = N_{vertex} + f_{vertex} \times N_{novertex} \tag{3.5}$$

Where, N_{vertex} is the number of events with a vertex from tracks which have passed the event selection, f_{vertex} is the fraction of events with a vertex from tracks which have passed the event selection criteria and $N_{novertex}$ is the number of events where no vertex from tracks could be found. The second term in the equation 3.5 denotes the estimate of a number of events with hits from tracks in V0 detector, which have passed the event selection criteria but no tracks in the central detectors.

Moreover, the measured yield of electrons (N^{e}_{raw}) from heavy-flavour decays was normalised to unit rapidity by dividing by the rapidity range Δy = 1.6 (1.0) for 7 TeV (13 TeV) analysis. For electron, which usually has negligible mass compared to their momentum, the pseudorapidity and rapidity are the same. Therefore the rapidity range was determined by the pseudorapidity range $\Delta\eta = 2 \times 0.8$ (2×0.5) for $\sqrt{s} = 7$ (13) TeV analysis.

To obtain a production cross-section, the spectra were multiplied with the minimum bias cross-section σ_{MB}, of pp collisions at $\sqrt{s}$ = 7 TeV and $\sqrt{s}$ = 13 TeV. The value for σ_{MB} is 62.2 mb [95] (57.8 mb [96]) for pp at $\sqrt{s}$ = 7 TeV ($\sqrt{s}$ = 13 TeV).

At last, in $\sqrt{s} = 7$ TeV analysis, the backgrounds from $\mathrm{K_{e3}}$ and J/ψ decays

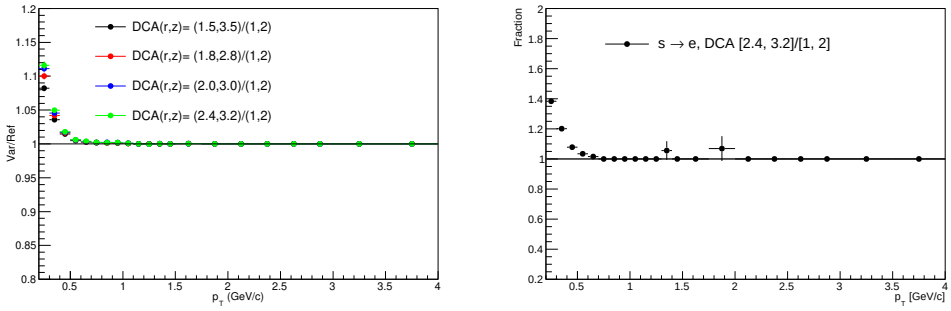

Figure 3.9. Left: Ratios of Varied/Reference cross-sections, where the variation is done in DCA selection cuts for pp at $\sqrt{s} = 13$ TeV. Right: Relative contribution of strange decay electrons in DCA [2.4,3.2] region with respect to DCA [1.0, 2.0].

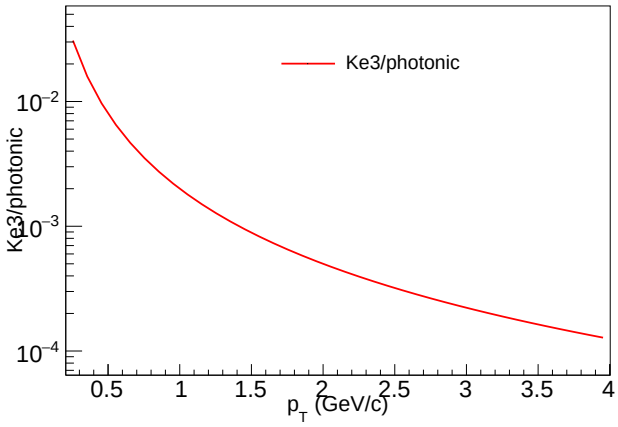

Figure 3.10. Ratio of K_{e3}/photonic electrons in published pp at $\sqrt{s} = 7$ TeV results for DCA [1.0, 2.0].

are subtracted from this fully corrected spectra using the cocktail approach [86]. The contribution of electrons from K_{e3} decays is also subtracted in 13 TeV analysis however, using cocktail parameterizations of K_{e3}/photonic electrons shown in Figure 3.10. Electrons from K_{e3} decays has wider DCA distributions compared to others which show up as a variation when cross-sections in different DCA regions are estimated and compared with default case, loosest being DCA between 2.4 and 3.2 cm in radial and z-direction, respectively and default being DCA [1 cm, 2 cm], as shown in the left plot of Figure 3.9. This suggests that their contributions are somewhat significant as very low transverse momentum region ($p_{\mathrm{T}} < 0.5$ GeV/c). The right plot of Figure 3.9 presents relative contri-

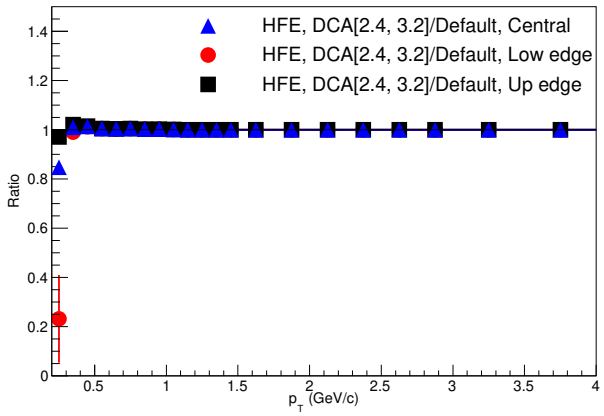

Figure 3.11. Ratios of cross-sections in DCA [2.4,3.2] region with respect to DCA [1.0, 2.0] after K_{e3} subtraction using parameterization at central (blue), lower edge (red) and upper edge (black) of p_T in for pp at $\sqrt{s} = 13$ TeV.

butions of electrons from strange decays in DCA regions [2.4 cm, 3.2 cm] to [1.0 cm, 2.0 cm]. To estimate the contribution of electrons from K_{e3} decays, the cocktail parameterisation of K_{e3}/photonic electrons is used which was previously used for published 7 TeV cross-section and believed to be suitable for other energies as well. However, in case of $\sqrt{s} = 13$ TeV, the cross-section is estimated below $p_T < 0.5$ GeV/c. This was not the case for published 7 TeV results and therefore, may not work as per expectations in that region. Consequently, it is found that the K_{e3} spectra obtained using the parameterisation at the central point of the p_T bin over-subtract in the first transverse momentum bin, i.e. 0.2–0.3 GeV/c as shown in Figure 3.11, however, rest of the bins remain unaffected. The K_{e3} spectra in DCA [2.4 cm, 3.2 cm] region is obtained by scaling the one in DCA [1 cm, 2 cm] region using the ratio shown in the right plot of Figure 3.9. From Figure 3.10, one can see that the parameterisation rises sharply below $p_T < 0.5$ GeV/c. Therefore, we subtract the K_{e3} spectra obtained using the parameterisation at the upper edge of the p_T bin to avoid the over-subtraction and assign the systematics associated with it in section 3.2.4. Note that the contributions of di-electrons from J/ψ decays are not subtracted as it is negligible at low p_T in $\sqrt{s} = 13$ TeV analysis. The statistical errors on the raw yield of heavy-flavour electrons are computed in each bin as a $\sqrt{N}$ where N is the number of entries in that bin. The measured cross-sections of electrons from

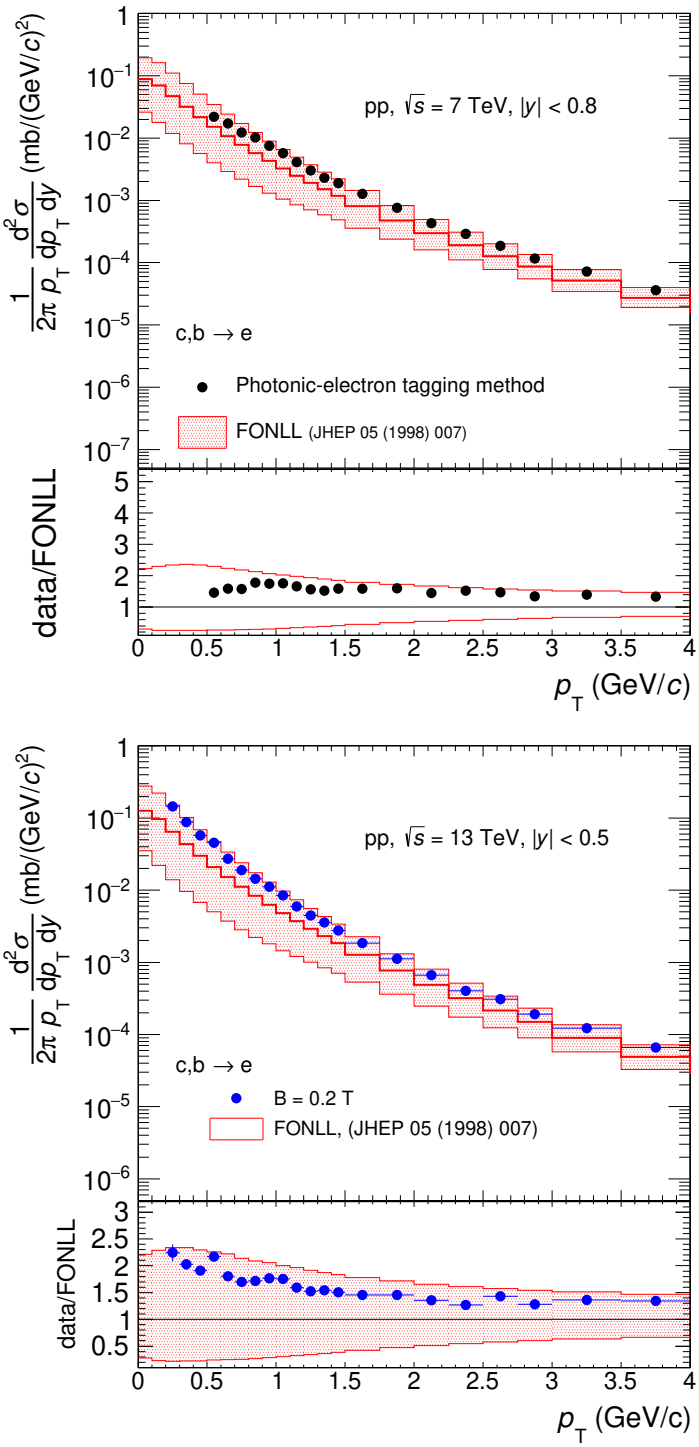

Figure 3.12. The p_T-differential invariant production cross section (black, circle symbols) of electrons from semileptonic heavy-flavour hadron decays measured at mid-rapidity in pp collisions at $\sqrt{s} = 7$ TeV (upper plot) and at $\sqrt{s} = 13$ TeV (lower plot) with the FONLL pQCD calculations [48] (upper panel), and the ratio of the data to the FONLL calculation (lower panels of the plots).

heavy-flavour hadron decays at $\sqrt{s} = 7$ and 13 TeV are shown in Figure 3.12 and compared with the FONLL predictions.

3.2 Estimation of the systematic uncertainties

The tracks are selected and identified using the set of selection criteria, which can lead to systematic uncertainties. Apart from this, the method which has been adopted to estimate the cross-section can give rise to some systematics as well. The systematic uncertainties due to the following possible sources are considered and estimated in these analyses:

- Systematic uncertainties due to inclusive track and PID selection;
- Systematic uncertainties due to the subtraction of electron from photonic sources;
- Systematic uncertainties due to π^0 and η weight;
- Systematic uncertainties due to other sources
  - Pseudo-rapidity (η) cut variations;
  - SPD requirement;
  - Hadron contamination parametrizations;
  - TPC–TOF and ITS–TPC track matching;
  - Systematic uncertainties due to J/ψ and K_{e3} cocktail subtraction;

3.2.1 Systematic uncertainties due to inclusive track and PID selection

The different variations of the selection criteria for inclusive tracks are mentioned in Table 3.3 (3.4) for pp at $\sqrt{s} = 7$ (13) TeV analyses.

pp at $\sqrt{s} = 7$ TeV: The cross-sections for each variation of applied selection criteria (Table 3.3) are estimated and the ratios of the estimated to the

Table 3.3. Summary of cut variations to estimate the systematic uncertainties linked to the track selection and particle identification for electron candidate tracks at $\sqrt{s} = 7$ TeV

Sources of Uncertainties	Reference	Variations
TPC clusters	$\geqslant 120$	$\geqslant 90$,$\geqslant 95$,$\geqslant 100$,$\geqslant 105$, $\geqslant 110$,$\geqslant 125$,$\geqslant 130$
TPC PID clusters	$\geqslant 90$	$\geqslant 80$,$\geqslant 85$,$\geqslant 95$,$\geqslant 100$
ITS hits	$\geqslant 4$	$\geqslant 3$,$\geqslant 5$
TOF PID	$\pm$ 3.0 σ	$\pm$ 2.0 σ, $\pm$ 2.5 σ, $\pm$ 3.5 σ, $\pm$ 4.0 σ
TPC PID lower boundary	-1.0 σ	0.0 σ, 0.5 σ, -1.0 σ,-1.5 σ
TPC PID upper boundary	3.0 σ	2.0 σ, 2.5 σ,3.0 σ,3.5 σ
DCA_{xy} [cm]	< 1	< 0.5, < 2.4
DCA_{z} [cm]	< 2	< 1,< 3.2

Table 3.4. Summary of cut variations to estimate the systematic uncertainties linked to the track selection and particle identification for electron candidate tracks at $\sqrt{s} = 13$ TeV

Sources of Uncertainties	Reference	Variations
TPC clusters	$\geqslant 100$	$\geqslant 90$,$\geqslant 95$, $\geqslant 105$,$\geqslant 110$
TPC PID clusters	$\geqslant 80$	$\geqslant 90$,$\geqslant 85$,$\geqslant 95$,$\geqslant 100$
TOF PID	$\pm$ 3.0 σ	$\pm$ 2.0 σ, $\pm$ 2.5 σ
TPC PID lower boundary	-1.0 σ	0.0 σ, -0.5 σ, -1.0 σ, -1.5 σ
TPC PID upper boundary	3.0 σ	2.0 σ, 2.5 σ, 3.0 σ, 3.5 σ

default cross-section were plotted as shown in Figure 3.13. The distribution of the ratio of difference between the varied and reference spectra to the reference for difference p_T bins is built and is shown in Figure 3.14 for the p_T bin $0.5 < p_T < 0.6$ GeV/c. Plots for rest of the p_T bins can be found in Appendix 8.7. Then the mean and sigma (see Figure 3.15) of these distributions are assigned as a systematic uncertainty in the different transverse momentum bins. Systematic uncertainty is 5.5 % between $0.5 < p_{\mathrm{T}} < 1.4$ GeV/c and 2.5 % $1.4 < p_{\mathrm{T}} < 4.0$ GeV/c.

pp at $\sqrt{s} = 13$ TeV: In this analysis, similar as above, we estimate the ratios of varied cross-sections (Table 3.4) with respect to the default case as shown in Figure 3.16. We do not consider DCA selection variations because

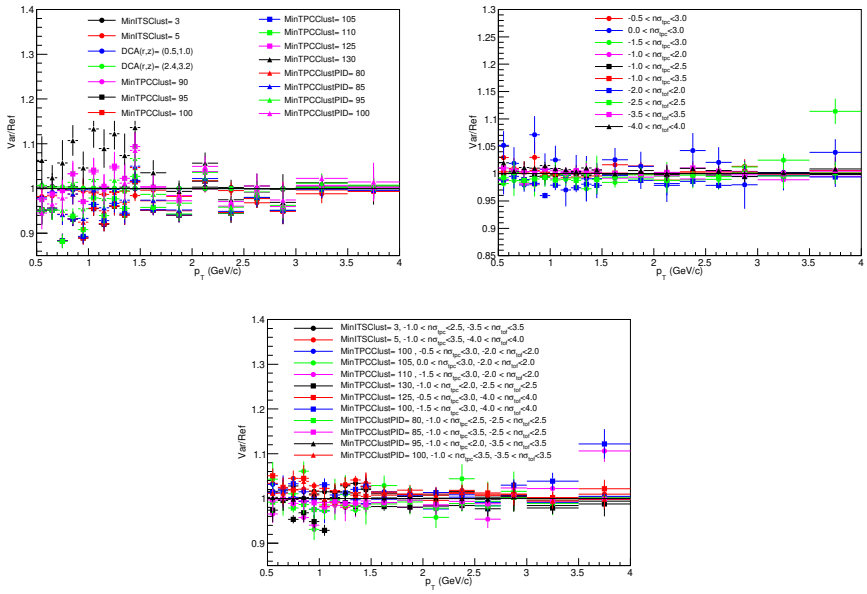

Figure 3.13. Ratios of Varied/Reference cross-sections, where the variation is done in the inclusive track selection cuts (left plot) and in the PID cuts (right plot) and varying both cuts simultaneously (bottom plot) for pp at $\sqrt{s} = 7$ TeV.

it is correlated to the contribution of electrons from K_{e3} decays as discussed in subsection 3.1.3. The top left plot of Figure 3.16 shows negligible effect of variations of TPC clusters. However, the top right plot of the Figure 3.16 shows the ratios of cross-sections with variation of PID selection criteria to the default. Hence, systematic uncertainties of 5.0 % between $0.2 < p_{\mathrm{T}} < 2.0$ GeV/c is assigned. Also, it is important note that the variations listed in Table 3.3 do not include number of ITS hits since maximum of 4 layers instead of 6 layers of ITS are available for 13 TeV data sample.

3.2.2 Systematic uncertainties due to the subtraction of electron from photonic sources

The list of different variations of the selection criteria for selecting associated tracks in both pp at $\sqrt{s} = 7$ and 13 analyses are mentioned in Table 3.5.

pp at $\sqrt{s} = 7$ TeV: Similar to the previous case, the ratios of cross-sections by varying the selection criteria to select the associated tracks with respect to the reference are estimated and shown in Figure 3.17. The distribu-

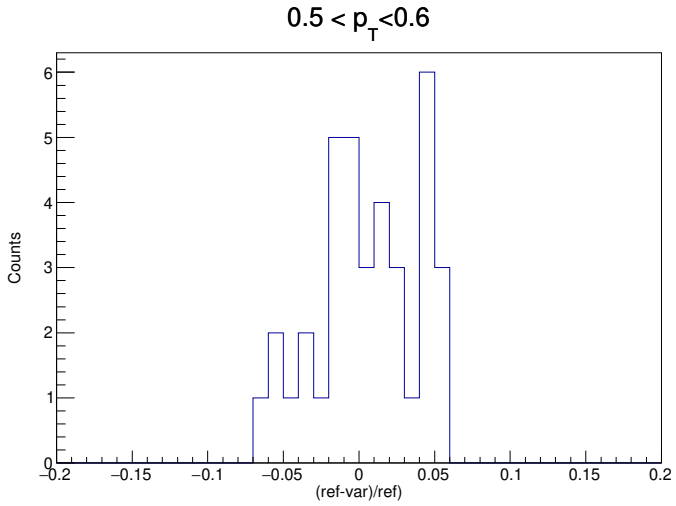

Figure 3.14. Distribution of the difference between the varied and reference spectra, divided by the reference value for inclusive track selection and PID cuts, in one bin of p_T for pp at $\sqrt{s} = 7$ TeV.

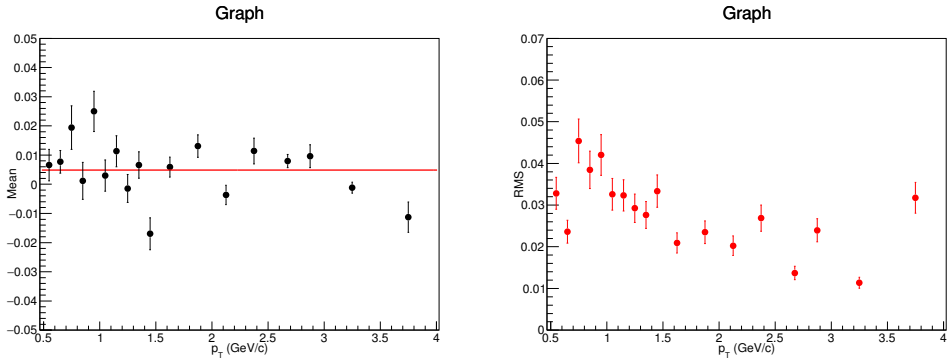

Figure 3.15. Mean and RMS of the distributions $(\frac{ref-var}{ref})$, related to the track selection and PID cuts, as function of p_T for pp at $\sqrt{s} = 7$ TeV.

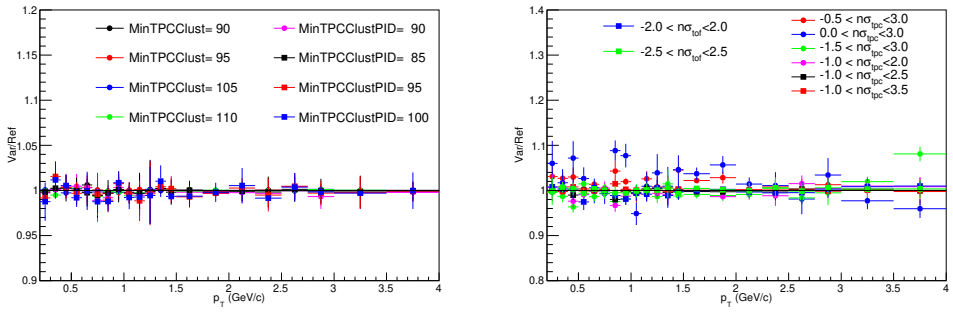

Figure 3.16. Ratios of Varied/Reference cross-sections, where the variation is done in the track selection cuts (upper left plot) and in the PID cuts (upper right plot) for pp at $\sqrt{s} = 13$ TeV.

Table 3.5. Summary of cut variations to estimate the systematic uncertainties linked to the track selection and particle identification for associated candidate tracks at $\sqrt{s} = 7\ (13)$ TeV

Sources of Uncertainties	Reference $\sqrt{s} = 7\ (13)$ TeV	Variations
p_T^{Min} (GeV/c)	> 0.0	$> 0.14\ (0.10)$, $> 0.15\ (0.12)$, $> 0.16\ (0.14)$
Mass cut (GeV/c^2)	< 0.14	$< 0.07\ (0.08)$, < 0.10, < 0.12, < 0.16
TPC clusters	$\geqslant 60$	$\geqslant 50$,$\geqslant 70$,$\geqslant 80$,$\geqslant 90$,
TPC PID clusters	$\geqslant 60$	$\geqslant 50$,$\geqslant 70$,$\geqslant 80$,$\geqslant 90$
DCA$_{xy}$ [cm]	< 1	< 0.5 ,< 2.4
DCA$_z$ [cm]	< 2	< 1 ,< 3.2

tion of the absolute deviation between the reference spectrum and all the varied spectra, divided by the reference value, for the p_T bin $0.5 < p_T < 0.6$ GeV/c is shown in Figure 3.18. Distributions like this one were made for all the p_T intervals of the spectrum and can be found in Appendix 8.8. As minimum $p_T = 0.16$ GeV/c cut acts too strongly on the spectrum, therefore variations involving minimum $p_T = 0.16$ GeV/c are not taken into account while doing RMS distribution. In Figure 3.19, the mean and RMS of the distributions for all p_T bin are shown as a function of p_T .

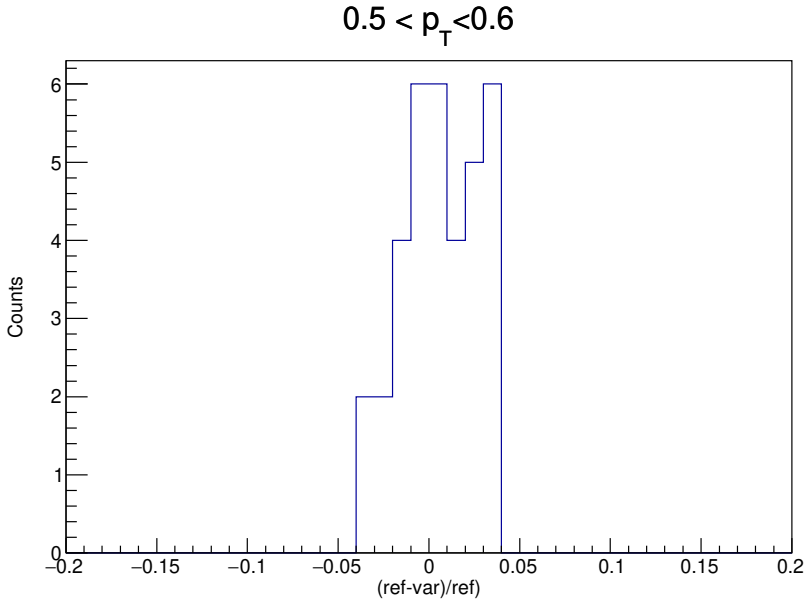

Figure 3.18. Distribution of the difference between the varied and reference spectra, divided by the reference value for associated track selection cuts, in one bin of p_T for pp at $\sqrt{s} = 7$ TeV.

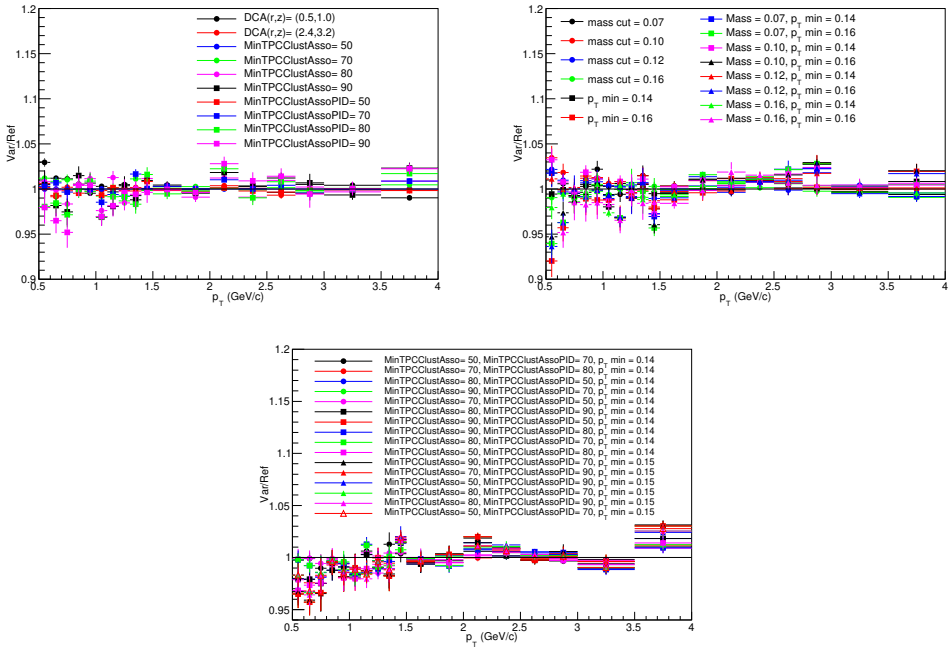

Figure 3.17. Ratios of Varied/Reference cross-sections, where the variation is done in the associated track selection cuts (left) and in the Associated minimum p_T cuts (right) and varying both cuts simultaneously (bottom plot) for pp at $\sqrt{s} = 7$ TeV.

In this case, systematic uncertainty is calculated by adding the absolute value of mean with RMS in each p_T bin. As shown in Figure 3.19, the mean and RMS show a systematic trend as a function of p_T. Therefore, total systematic value of 3 % was assigned at low p_T (0.5-1.2 GeV/c) and 1 % was assigned at high p_T (1.2–4.0 GeV/c).

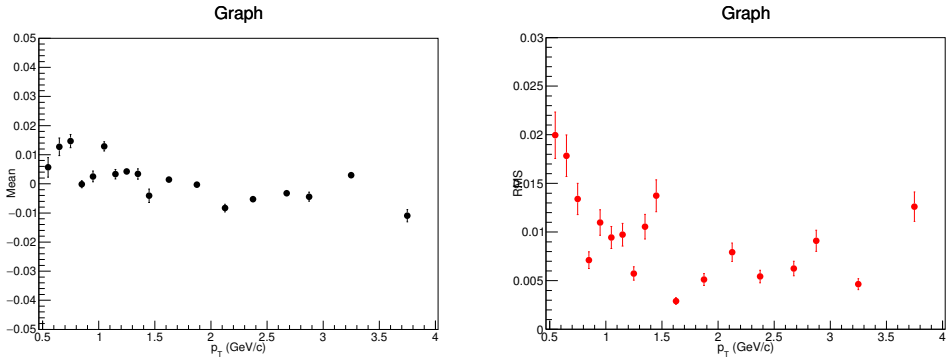

Figure 3.19. Mean and RMS of the distributions $(\frac{ref-var}{ref})$, related to the associated track selection cuts, as function of p_T for pp at $\sqrt{s} = 7$ TeV.

pp at $\sqrt{s} = 13$ TeV: Similar to systematics of the inclusive track cuts, for

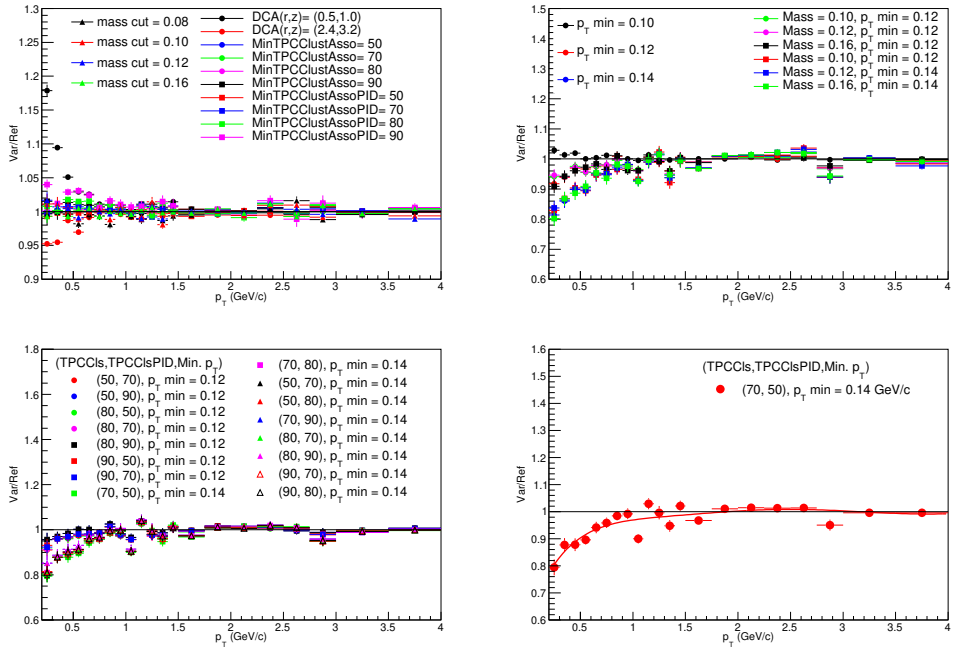

Figure 3.20. Ratios of Varied/Reference cross-sections, where the variation is done in the associated track selection cuts and in the Associated minimum p_T cuts (upper plots) and varying both cuts simultaneously (bottom left plot) for pp at $\sqrt{s} = 13$ TeV. On bottom right plot, the parameterized largest deviation used for assigning systematic uncertainties.

photonic background subtraction, the ratios between varied and default cross-sections with associated track cut variations are shown in the upper two panels of Figure 3.20 and with simulaltaneous track cut variations in lower left panel of Figure 3.20. As we can see, it shows a systematic trend for the different minimum associated p_{T} cuts. Similar to the systematic due to the inclusive track cut variations, the largest deviation is assigned as a systematic. That deviation is parameterized using 8th order polynomial to avoid the statistical fluctuations as shown in the bottom right plot of Figure 3.20 and the systematic values are 20.0 % (0.2-0.3 GeV/c), 15.0 % (0.3-0.4 GeV/c), 11.0 % (0.4-0.5 GeV/c), 8.0 % (0.5-0.6 GeV/c), 7.0 % (0.6-0.7 GeV/c), 5.0 % (0.7-0.9 GeV/c), 3.0 % (0.9-1.1 GeV/c), 2.0 % (1.1-1.3 GeV/c) and 1.0 % (1.3-1.5 GeV/c).

3.2.3 Systematic uncertainties due to π^0 and η weight

As mentioned earlier, the transverse momentum distributions of the photonic electron sources (i.e. π^0 and η) are not well reproduced in the MC simulations. Therefore, these distributions are re-weighted to match with experimentally measured distributions. The weights were calculated using the central values of the measured spectrum of π^0 and η in case of $\sqrt{s} = 7$ TeV and $\pi^{\pm}$ (instead of π^0 as the measurement of π^0 is not available) and mt-scaled η mesons in case of $\sqrt{s} = 13$ TeV. Therefore, the estimation of these weights can introduce some systematics.

To estimate the systematic uncertainty due to the weights applied on electrons that come from photonic sources, we observe how the final HFE spectrum changes by the use of different weights. The π^0 (or $\pi^{\pm}$) and eta spectrum were tilted up in such a way that the measured values at low p_{T} are shifted up by their systematic uncertainties attributed to it and the measured values at high p_{T} are shifted down.Similarly, the π^0 ($\pi^{\pm}$) and eta spectrum were tilted down, and in this way, two weights were obtained.

The HFE cross sections are computed for the three cases: using the standard weight and using the tilted weights (obtained by using the tilted π^0 ($\pi^{\pm}$) and η spectra). The systematic due to the different weights are estimated by looking at the ratio between the reference HFE cross-section and the ones obtained by using the tilted weights. The resulting systematic uncertainty is about 5% in the p_T interval 0.5–0.6 GeV/c, 3% in 0.6–0.7 GeV/c, 2% in 0.7–0.8 GeV/c, 1% in 0.8–1.5 GeV/c and negligible for higher p_T for the pp data at $\sqrt{s} = 7$ TeV as is shown in the left plot of Figure 3.21. From right plot of Figure 3.21, systematics of about 3% in 0.2–0.3 GeV/c, 1% in 0.3–0.4 GeV/c and negligible in rest of p_T range are assigned due to the weights in case of $\sqrt{s} =$ 13 TeV analysis.

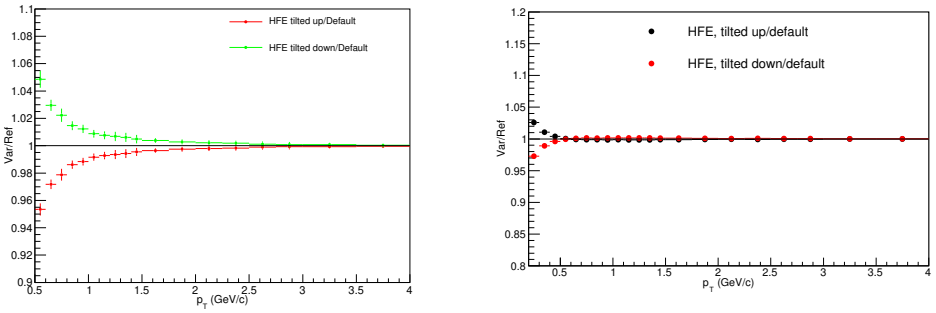

Figure 3.21. Comparison of the production cross-sections obtained using weights from tilted pion and η spectra to the reference weights for pp at $\sqrt{s}$ = 7 (13) TeV in left (right) plot.

3.2.4 Systematic uncertainties due to other sources

Table 3.6 shows the variations done to obtain the systematic uncertainties linked to neither inclusive nor associated track selection and particle identification viz. η acceptance, SPD requirement, hadron contamination parametrization, TPC–TOF and ITS–TPC track matching and subtraction of contribution from J/ψ and K_{e3} cocktail.

Table 3.6. Summary of the systematic uncertainties from other sources in pp at $\sqrt{s}$ = 7 (13) TeV.

Sources of	$\sqrt{s} = 7$ TeV		$\sqrt{s} = 13$ TeV	
Uncertainties	Reference	Variations	Reference	Variations
$\|\eta\|$	< 0.8	< 0.5 ,< 0.6, < 0.7	< 0.5	< 0.4 , < 0.6
SPD requirement	kBoth	kFirst,kAny	kBoth	kFirst,kAny
Hadron contamination	Error function	Landau function	Landau function	Error function

Eta cut variation:

- **pp at $\sqrt{s} = 7$ TeV:** The cross-section was estimated within different pseudo-rapidity regions ($|\eta| < 0.7$, $|\eta| < 0.6$ and $|\eta| < 0.5$) and compared with the reference ($|\eta| < 0.8$). No systematic uncertainty is as-

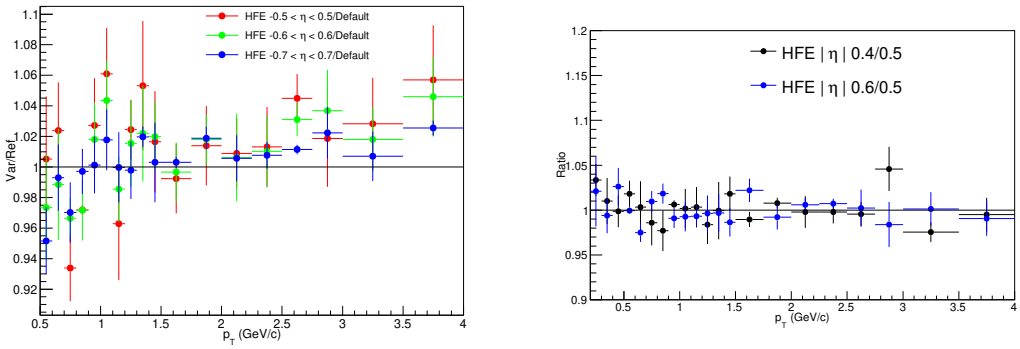

Figure 3.22. Ratio of Varied/Reference cross-sections, where the variation is done in the pseudo-rapidity interval considered left (right) plot for $\sqrt{s} = 7$ (13) TeV.

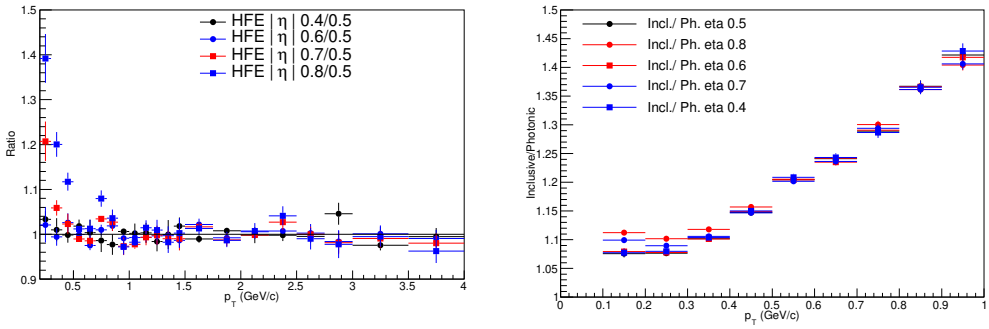

Figure 3.23. Variation of cross-section in different η regions with respect to default case (left plot) and Inclusive to photonic ratio in different η regions (right plot) for pp at $\sqrt{s} = 13$ TeV.

signed at low p_T. However, 5 % systematic value was assigned at high p_T (see Figure 3.22 (left plot)) since a trend was observed.

- **pp at $\sqrt{s} = 13$ TeV:** As discussed earlier, the analysis at 13 TeV was performed using tracks inside $|\eta| < 0.5$. In the right plot of Figure 3.23, the inclusive to photonic electrons ratio in $|\eta| < 0.7$ and 0.8 regime is shown which seem to be saturated at $p_{\mathrm{T}} < 0.4$ GeV/c which indicate that the photonic background is underestimated in $|\eta| < 0.7$ and 0.8 acceptance. Therefore, the analysis was restricted to the tracks within $|\eta| < 0.5$.

  To estimate the systematic due to the $|\eta|$ acceptance selection, the cross-sections inside $|\eta| < 0.4$ and $|\eta| < 0.6$ (see Figure 3.22 (right plot)) were determined and compared to the reference result. No systematic uncertainty associated to the η-range variation was found.

SPD requirement:

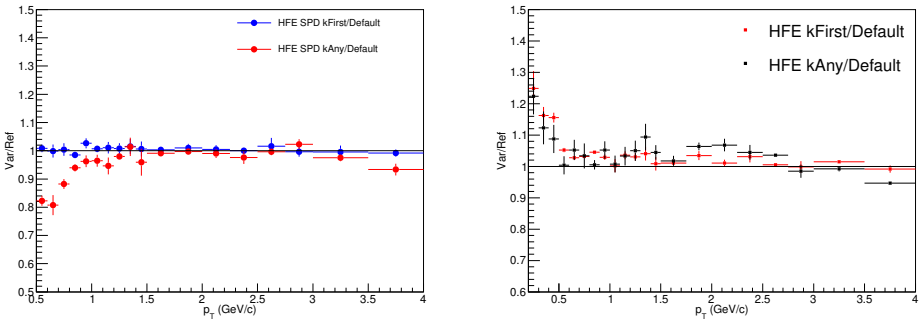

Figure 3.24. Ratio of Varied/Reference cross-sections, where the variation is done in the SPD requirement for pp at $\sqrt{s} = 7$ TeV (left) and 13 TeV (right).

- **pp at $\sqrt{s} = 7$ TeV:** The SPD default requirement, to have one hit in each layer (kBoth), was relaxed to ask for at least one hit in any of the two layers (kAny). This adds all electrons from photons converting in the first layer and in the very first part of the second layer to the electron candidate tracks. In addition to this, the cross-section was determined with the SPD selection with the requirement of at least one hit in the first layer (kFirst). As can be seen in the left plot of Figure3.24, at least one hit in any of the SPD layers (kAny) as the SPD requirement shows systematic trend at low p_T. Therefore, systematics of 20.0 % (0.5-0.6 GeV/c), 15.0 % (0.6-0.7 GeV/c), 10.0 % (0.7-0.8 GeV/c), 5.0 % (0.8-0.9 GeV/c), 2.0 % (0.9-1.0 GeV/c) and negligible (1.0-4.0 GeV/c) were assigned as shown in Table 3.7.

- **pp at $\sqrt{s} = 13$ TeV:** Similarly, systematics due to SPD requirements were estimated as shown in the right plot of Figure 3.24. Here, both cases of the SPD requirement show systematic trend at low p_T. Systematic uncertainties of 25 % for 0.2–0.3 GeV/c, 15 % for 0.3-0.5 GeV/c and 5 % for 0.5-2.5 GeV/c were assigned as shown in Table 3.8.

Hadron contamination parameterization:

- As a source of systematic uncertainty due to hadron contamination, the different parameterizations of the hadron contamination which were used to fit the fraction of hadron contamination in the inclusive sample as shown in the left plot of Figure 3.2 were considered. The ratio of the final HFE spectrum obtained by these two different hadron parameterisations are shown in the left (right) plot of Figure 3.25 for $\sqrt{s} = 7$ (13) TeV analyses. It shows no systematic trend at low p_T of final HFE spectrum, but at high p_T, a systematic trend was observed, so, 1 (2)% systematic value was assigned for hadron contamination in 3.5-4.0 GeV/c (3.0-4.0 GeV/c) for $\sqrt{s} = 7$ (13) TeV analyses.

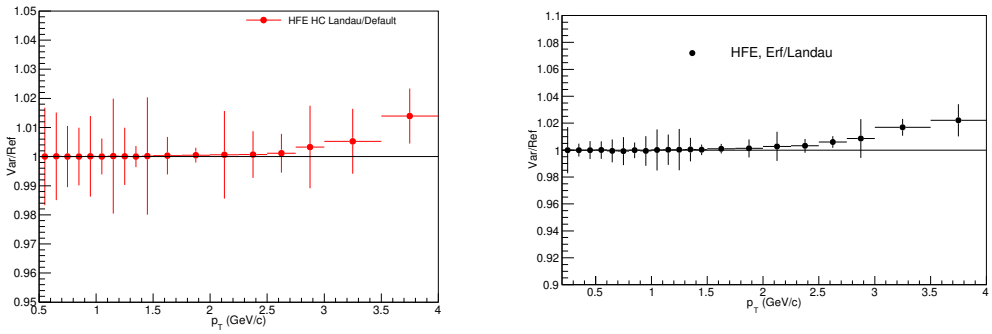

Figure 3.25. Ratio of Varied/Reference cross-sections, where the variation is done in the hadron contamination fitting function left (right) plot for $\sqrt{s} = 7$ (13) TeV.

TPC–TOF and ITS–TPC matching:

The incomplete knowledge of the efficiency in matching tracks reconstructed in the ITS and TPC as well as track matching between the TPC and TOF can introduce systematic uncertainties which should be estimated.

- **pp at $\sqrt{s} = 7$ TeV:** To estimate the effects of matching between the TPC and TOF tracks on the measurement, the systematics are calculated by taking the double ratio of the number of tracks before and after TOF in data and MC as shown in the left plot of Figure 3.26, and a systematic

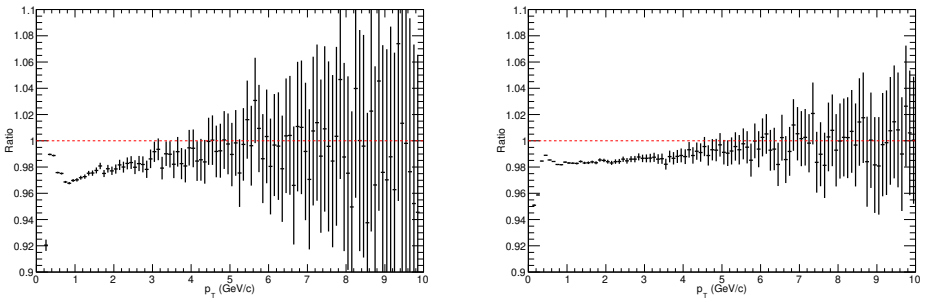

Figure 3.26. Systematics due to TPC-TOF track matching: ratio between efficiencies of tracks before and after TOF in data and MC for pp at $\sqrt{s} = 7$ TeV (left) and 13 TeV (right).

uncertainty of 2% was assigned in the whole transverse momentum range, and 2% is assigned due to ITS and TPC track matching which is taken from published analysis [86].

- **pp at $\sqrt{s} = 13$ TeV:** Similar procedure was used as shown in the right plot of Figure 3.26 and a systematic uncertainty of 2% was assigned for all bins except for first bin where it was 4% for TPC–TOF matching. p_T-dependent systematics of 2% in 0.2–1.0 GeV/c, 3% in 1.0–2.0 GeV/c and 4% in 2.0–4.0 GeV/c, due to ITS-TPC track matching is assigned which is taken from DPG.

Systematic uncertainties due to J/ψ and K_{e3} cocktail subtraction

Systematics due to cocktail subtraction of electrons from J/ψ and K_{e3} are estimated. The subtraction of the background electron contribution from the J/ψ and K_{e3} decays is affected by the uncertainties coming from the input distributions employed for the cocktail calculation.

In 7 TeV analysis, the systematic uncertainties were estimated as discussed in [86], where systematic uncertainty of 100% was assigned to the K_{e3} contribution as shown in left plot of Figure 3.27. Due to K_{e3} subtraction, contribution to the systematic uncertainties of about 6% in the p_T interval 0.5–0.6 GeV/c, 3% in the p_T interval 0.6–0.7 GeV/c, 2% in the p_T interval 0.7–0.8 GeV/c and 1% in the p_T interval 0.8–0.9 GeV/c is assigned, while for $p_T >$

0.9 GeV/c this uncertainty is estimated to be negligible. Similar strategy was adopted for the J/ψ subtraction and the systematic uncertainties of about 1% in the p_{T} interval 2.0–2.5 GeV/c, 2% in the p_{T} interval 2.5–3.5 GeV/c and 3% in the p_{T} interval 3.5–4.0 GeV/c is assigned. Whereas, at low p_{T} this uncertainty is negligible as shown in left plot of Figure 3.27.

In $\sqrt{s} = 13$ TeV analysis, the systematic uncertainties due to subtraction of Ke3 contribution are estimated by taking into account the over-subtraction of Ke3 contribution when the default parameterization is used at central p_{T} value, shown in the left plot of Figure 3.11. Moreover, as shown in the right plot of Figure 3.27, it can be seen that cross-section is reduced by 47% when parameterization at central p_{T} value is used to estimate Ke3 contribution and reduced by 33% when parameterization at the upper edge of p_{T} bin is used. So the difference between these two as a systematic, i.e. 15% in first bin (0.2–0.3 GeV/c), 4% in (0.3–0.4 GeV/c), 1% in (0.4–0.5 GeV/c) and negligible in rest of the p_{T} region are assigned. Moreover, systematics due to subtractions of electrons from J/ψ are not assigned as their contribution is not subtracted.

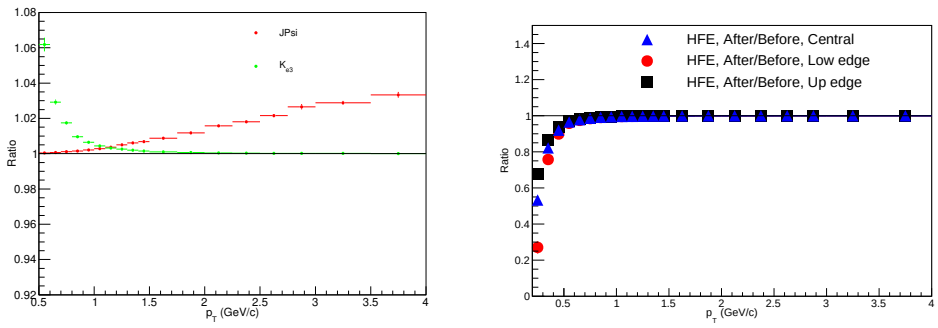

Figure 3.27. Left: Ratio between K_{e3} contribution subtracted twice and once from the reference cross section and same for J/ψ in pp at $\sqrt{s} = 7$ TeV analysis. Right: ratio of cross-section before and after K_{e3} subtraction using parameterization at central (blue), lower edge (red) and upper edge (black) of p_{T} bin in pp at $\sqrt{s} = 13$ TeV analysis

Systematics due to all contributions are listed in Table 3.7 and 3.8 for both $\sqrt{s} = 7$ TeV and 13 TeV analyses respectively. The final systematic uncertainties are estimated by adding the systematics due to all sources in quadrature and are summarized in Table 3.9 for the different transverse momentum bins. The

systematic uncertainties using this method are reduced significantly by about factor 3 compared to the cocktail method used before at low transverse momentum.

Table 3.7. Summary of values of the systematic uncertainties assigned in pp at $\sqrt{s} = 7$ TeV

Sources of Uncertainties	Value
Track and PID cuts	5.5 % (0.5-1.4 GeV/c) and 2.5 % (1.4-4.0 GeV/c)
Asso. particle cuts	3.0 % (0.5-1.2 GeV/c) and 1.0 % (1.2-4.0 GeV/c).
SPD requirement	20.0 % (0.5-0.6 GeV/c), 15.0 % (0.6-0.7 GeV/c),
	10.0 % (0.7-0.8 GeV/c), 5.0 % (0.8-0.9 GeV/c)
	2.0 % (0.9-1.0 GeV/c) and negligible (1.0-4.0 GeV/c)
$\lvert\eta\rvert$ variation	negligible at low p_T and 5 % (3.5-4.0 GeV/c)
hadron	negligible at low p_T
contamination	and 2 % (3.5-4.0 GeV/c)
Weights for π^0 and η	5% (0.5–0.6 GeV/c), 3% (0.6–0.7 GeV/c), 2% (0.7–0.8 GeV/c), 1% (0.8–1.5 GeV/c) and negligible at high p_{T}.
TPC-ITS	2 %
TPC-TOF	2 %
track matching	
Remaining	For K_{e3}, 6.0 % (0.5-0.6 GeV/c), 3.0 % (0.6-0.7 GeV/c),
cocktail components	2.0 % (0.7-0.8 GeV/c), 1.0 % (0.8-0.9 GeV/c)
(J/ψ , K_{e3})	negligible at high p_T
	For J/ψ , negligible at low p_T, 1.0 % (2.0-2.5 GeV/c), 2.0 % (2.5-3.5 GeV/c), 3.0 % (3.5-4.0 GeV/c)

3.3 Results and Conclusion

After estimating the systematic uncertainties from all the possible sources, it is time to plot the final production cross-section of the electrons from heavy-flavour hadron decays with those systematics which is shown in the upper and bottom plot of Figure 3.28 for pp at $\sqrt{s} = 7$ and 13 TeV respectively. Statistical and systematic uncertainties of the data are depicted as vertical bars and boxes, respectively.

Table 3.8. Summary of values of the systematic uncertainties assigned in pp at $\sqrt{s} = 13$ TeV

Sources	Systematics
Incl. track and PID cuts	5.0 % (0.2-2.0 GeV/c)
Asso. particle cuts	20.0 (0.2-0.3 GeV/c), 15.0 (0.3-0.4 TeV GeV/c), 11.0 (0.4-0.5 GeV/c), 8.0 (0.5-0.6 GeV/c), 7.0 (0.6-0.7 GeV/c), 5.0 (0.7-0.9 GeV/c), 3.0 (0.9-1.1 GeV/c), 2.0 (1.1-1.3 GeV/c) and 1.0 (1.3-1.5 GeV/c)
Eta variation	negligible
SPD req.	25 % (0.2-0.3), 15 % (0.3-0.5) and 5 % (0.5-2.5).
hadron cont.	2 % (3.0 - 4.0 GeV/c)
π^0, η weights	3 % (0.2-0.3) and 1 % (0.3-0.4)
Subtraction of Ke3 contribution	15% (0.2-0.3) GeV/c, 4% (0.3-0.4) GeV/c and 1% (0.4-0.5) GeV/c
ITS-TPC matching	2% (0.2-1) GeV/c, 3% (1-2) GeV/c and 4% (2-4) GeV/c
TPC-TOF matching	2% beyond 0.3 GeV/c and 4% between 0.2 to 0.3 GeV/c

Table 3.9. Summary of the total systematic uncertainties

p_T in GeV/c	Total systematic uncertainty (%)	
	$\sqrt{s} = 7$ TeV	$\sqrt{s} = 13$ TeV
0.2-0.3	-	36
0.3-0.4	-	22
0.4-0.5	-	20
0.5-0.6	22	11
0.6-0.7	17	10
0.7-0.8	13	9
0.8-0.9	9	9
0.9-1.0	7	8
1.0-1.1	7	9
1.1-1.2	7	8
1.2-1.4	6	8
1.4-2.0	4	8
2.0-2.5	4	7
2.5-3.5	4	5
3.5-4.0	7	5

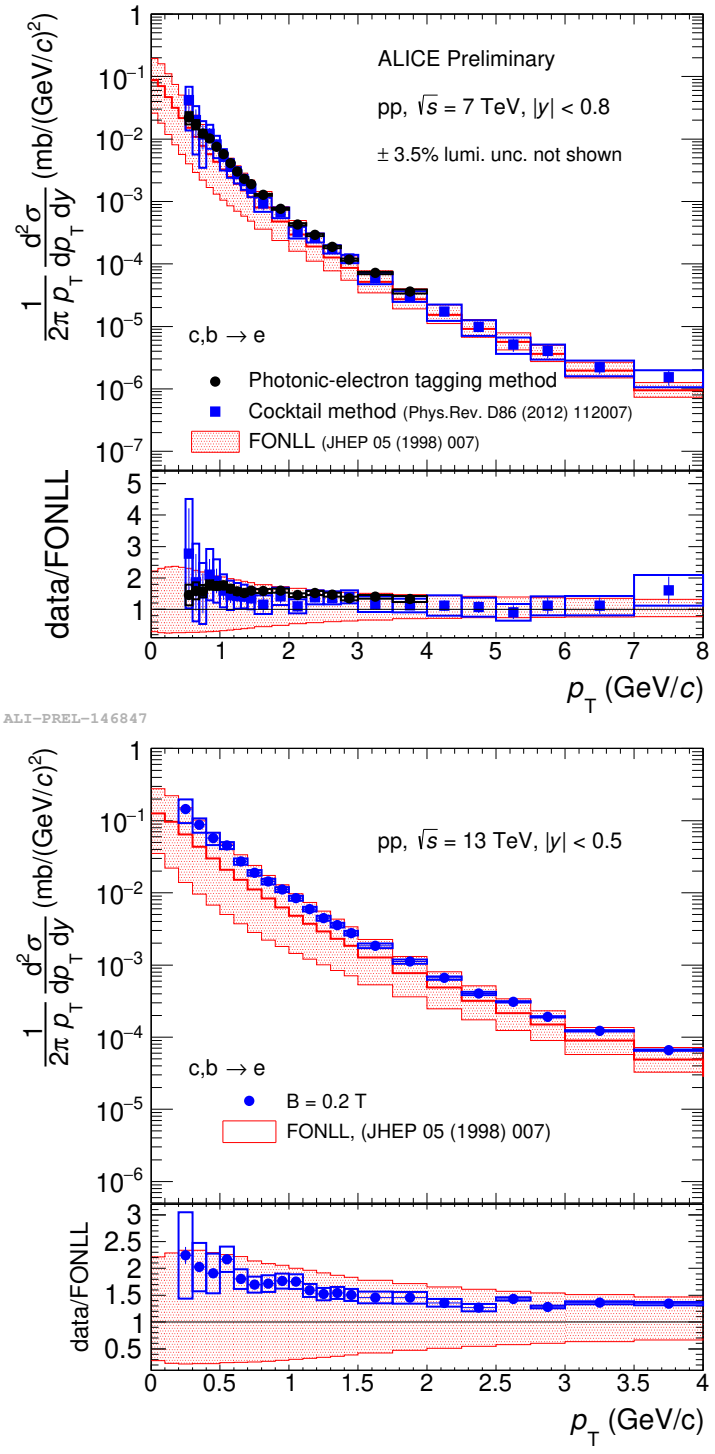

Figure 3.28. The p_{T}-differential invariant production cross-section of electrons from semileptonic heavy-flavour hadron decays measured at mid-rapidity in pp collisions at $\sqrt{s} = 7$ TeV (black circle symbol in upper plot) and at $\sqrt{s} = 13$ TeV (blue circle symbol lower plot) with the FONLL pQCD calculations [48] (upper panel), and the ratio of the data to the FONLL calculation (lower panels of the plots). The cross-section at 7 TeV is also compared with the previously published result (blue, square symbol) and shows nice agreement.

The red lines indicate the uncertainty band of Fixed-Order Next-to-Leading Logarithmic resummation (FONLL) calculations [48]. The upper and lower limit of the FONLL predictions denotes the uncertainty range of the calculations originating from the quark masses, perturbative scales and uncertainty related to the Parton distribution functions (PDFs) [50].

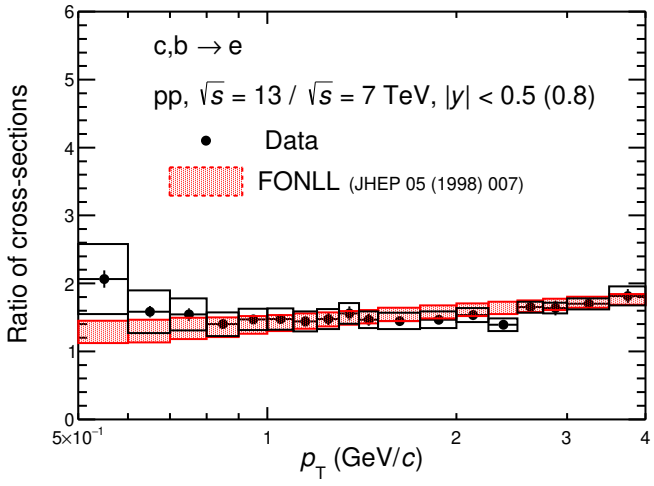

Figure 3.29. Ratio between the cross-sections at 13 TeV to 7 TeV and its comparison with the ratio of corresponding FONLL predictions.

In the upper plot of Figure 3.28, the measured production cross-section of electrons from heavy-flavour hadron decays at $\sqrt{s} = 7$ TeV is compared the published production cross-section which was measured using cocktail method [86]. The measured cross-section is consistent with the published spectra within statistical and systematic uncertainties. It also shows good agreement with the FONLL predictions and always lies on the upper edge. Whereas, as shown in the bottom plot of Figure 3.28, production cross-section measured with the low magnetic field at $\sqrt{s} = 13$ TeV is shown with the systematic uncertainties. Similar to 7 TeV cross-section, it also shows a nice agreement with FONLL pQCD predictions and lies on the upper edge. The cross-section at 13 TeV is measured down to $p_{\mathrm{T}} = 0.2$ GeV/c which gives access to large amount of electron yield in contrast to $\sqrt{s} = 7$ TeV which is measured down to $p_{\mathrm{T}} = 0.5$ GeV/c. Moreover, the ratio of these two cross-sections is obtained and then compared with the ratio of corresponding FONLL predictions as shown in Figure 3.29. The un-

certainties on FONLL are reduced after taking the ratio and precise comparison with the data can be observed.

The measurements of cross-sections of charm and beauty electrons with such good precisions help to constrain the pQCD calculation and improve our understanding.

Chapter 4

Electrons from beauty hadron decays

In this chapter, analysis of the measurement of electrons from beauty hadron decays in pp collisions at $\sqrt{s} = 5.02$ TeV is performed by using the Distance of closest approach (DCA) information of the electrons. Other than photonic electrons, the electrons from charm hadrons are also one of the sources of background to the beauty electrons. Maximum likelihood fit method is implemented for this analysis. Here, the DCA distributions of the electrons from different sources are obtained from Monte Carlo simulations and used to fit the measured inclusive electron DCA distribution.

4.1 Analysis strategy

The strategy to measure electrons from beauty hadron decays is different from the one used for electrons from heavy-flavour hadron decays in the previous chapter. Although, the electrons are identified in a similar way as discussed in chapter 2, however, DCA information is used to measure the contribution of the electrons from beauty hadron decays in pp collisions at $\sqrt{s} = 5.02$ TeV. Due to the long lifetime of the beauty hadrons, the DCA of beauty electrons is quite large in comparison to the other background electrons. This DCA information helps to separate the beauty electrons from the rest of the background. However, small signal to background ratio, tracking and PID efficiencies at low transverse momentum region make this analysis a bit challenging. Therefore, we have restricted our measurement down to $p_{\mathrm{T}} = 2$ GeV/c in the low transverse mo-

mentum region.

Principle of this analysis is such that the DCA distributions, also referred as templates, of electrons from different sources are built using Monte Carlo simulations, and those distributions are used to fit the measured inclusive electron DCA distribution using the maximum likelihood method.

Details of the data and Monte Carlo periods and corresponding run numbers used for this analysis are mentioned in Table 8.3 in the Appendix 8.3. Summary of the track selection criteria imposed on the electron candidates in pp collisions at $\sqrt{s} = 5.02$ TeV analysis is shown in the table 4.1.

Table 4.1. Summary of the track selection criteria imposed on the electron candidates in pp collisions at $\sqrt{s} = 5.02$ TeV analysis

Track and PID cuts	Electron candidates
p_T^{min}	2 GeV/c
$\|\eta\|$	< 0.8
Number of TPC clusters	≥ 100
Number of TPC $\frac{dE}{dX}$ clusters (PID)	≥ 80
Number of ITS hits	≥ 3
χ^2 /clusters of the momentum fit in the TPC	< 4
Requirement of hits in SPD layers	**kBoth**
DCA to the primary vertex in xy	< 1 cm
DCA to the primary vertex in z	< 2 cm
TOF t - $< \text{TOF } t >\|_{el}$ in between	-3 to 3σ
TPC $\frac{dE}{dX}$ - $< \text{TPC } \frac{dE}{dX} >\|_{el}$ in between	-1 to 3σ

4.1.1 Maximum likelihood method

Maximum likelihood method is useful to fit the distribution with distributions which have no analytical formula but consist of different distributions (templates) from Monte Carlo. This method is based on the Barlow and Beeston approach [97].

Let's assume that the number of entries in each DCA bin i in data is d_i and f_i is the expected number of electrons in that bin. Similarly, in MC, a_{ji} is the number of electrons in DCA bin i from each source j and A_{ji} is corresponding expected number of electrons. The expectation value of number of electrons in

each DCA bin f_i, consists of the sum of the expectation value of each source, A_{ij}, scaled by the amplitude p_j:

$$f_i = \sum_{j=1}^{m} p_j \times A_{ji} \tag{4.1}$$

p_j is associated amplitude of template for each source j. Like this, one can determine the amount of electrons from beauty hadron decays in every p_{T} bin. The Poisson statistics gives the likelihood of having d_i counts in a bin where the expected number of counts is f_i:

$$p(d_i|f_i) = e^{-f_i}\frac{f_i^{d_i}}{d_i!} \tag{4.2}$$

Similarly, the likelihood of having the amount a_{ij} in the template j and bin i when the expected value A_{ji} is given by:

$$p(a_{ji}|A_{ji}) = e^{-A_{ji}}\frac{A_{ji}^{a_{ji}}}{a_{ji}!} \tag{4.3}$$

The total likelihood is given by the product between the likelihood of the observed d_i (p($d_i|f_i$)) and the likelihood of the a_{ij} taken from MC (p($a_{ji}|A_{ji}$)), for all the DCA bins i and template source j:

$$L = \prod_{i=1}^{n} e^{-f_i}\frac{f_i^{d_i}}{d_i!} \times \prod_{i=1}^{n}\prod_{j=1}^{m} e^{-A_{ji}}\frac{A_{ji}^{a_{ji}}}{a_{ji}!} \tag{4.4}$$

For maximum likelihood, the logarithm of the total likelihood is obtained:

$$lnL = \sum_{i=1}^{n} d_i ln f_i - f_i + \sum_{i=1}^{n}\sum_{j=1}^{m} a_{ji} ln A_{ji} - A_{ji} \tag{4.5}$$

There are total of $m \times (n+1)$ free parameters, $m \times n$ being the expected number of entries and m being the number of amplitudes of the distribution. In this analysis, there are 200 bins and 4 templates which makes 804 free parameters. It is possible to look at the maximum by implementing the Minuit package [98], however, iterative approach is suggested in [97]. Therefore, differentiate eq. 4.5 w.r.t. A_{ji}, to get, $dlnL/dA_{ji} = 0$;

$$\frac{dlnL}{dA_{ji}} = \frac{d_i p_j}{fi} - p_j + \frac{a_{ji}}{A_{ji}} - 1 = 0; \forall i, j \tag{4.6}$$

For fixed value of p_j above are separate sets of equations for each DCA bin, this leads to,

$$A_{ji} = \frac{a_{ji}}{1 + p_j(1 - \frac{d_i}{f_i})} \tag{4.7}$$

It is observed in [99] that above equation does not provide stable result. Therefore, there is another possibility which is to solve eq. 4.6 for A_{ji} using the following definition,

$$f_{i\setminus j} = \sum_{k=1;k\neq j}^{m} p_k \times A_{ki} \tag{4.8}$$

this yields,

$$A_{ji} = -\frac{1}{2}\frac{d_i p_j - f_{i\setminus j}(p_j+1) + a_{ji}p_j}{p_j(p_j+1)} + \sqrt{\frac{1}{4}\left(\frac{d_i p_j - f_{i\setminus j}(p_j+1) + a_{ji}p_j}{p_j(p_j+1)}\right)^2 + \frac{a_{ji}f_{i\setminus j}}{p_j(p_j+1)}} \tag{4.9}$$

The iteration is started from a previously obtained value of A_{ji} for each new step in the maximisation w.r.t. p_j. In general, with five iterations, the stable results can be observed, but to be on the safe side, ten iterations are performed. Figure 4.1 depicts the example of the fit performed using this method. After performing the fit, the raw beauty electron yield is obtained by integrating the fitted beauty electron template in each p_T bin independently. A more detailed explanation of this method is given here [99].

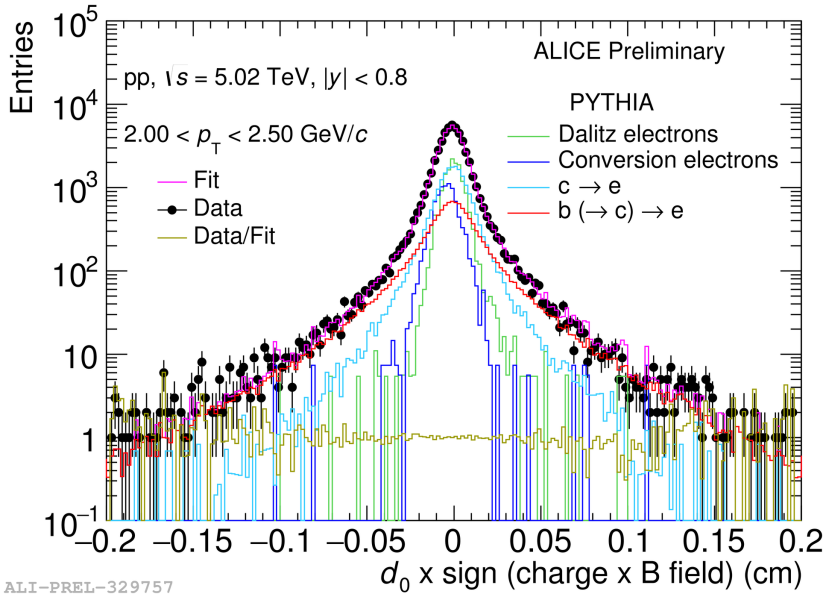

Figure 4.1. Distribution of DCA of electron candidates in one bin of p_{T} together with the templates scaled by the normalisation factors estimated by the fit method.

4.1.2 Selection of electron sources

Followings are the sources of electrons considered in the fit method:

- **Electrons from beauty hadron decays:**

  Due to larger decay length of the beauty hadrons (ranges from $c\tau \approx 400$ to 500 μm), electrons from beauty hadron decays (signal) have wider DCA distribution in comparison to the other background electrons. The distributions become more wider since beauty hadrons can also decay into charmed hadrons which further decay into the electrons.

- **Electrons from charm hadron decays:**

  One of the background sources is the electrons coming from charm hadron decays (excluding from beauty hadrons). The decay lengths of Λ_c^+ baryon, D^0, D^+ and $\mathrm{D_s}$ are $c\tau \approx 60$ μm, 100 μm, 300 μm and 100 μm respectively.

- **Electrons from Dalitz decays:**

  Another source of background is electrons coming from Dalitz decays of π^0 and η. These electrons have very narrow DCA distribution because

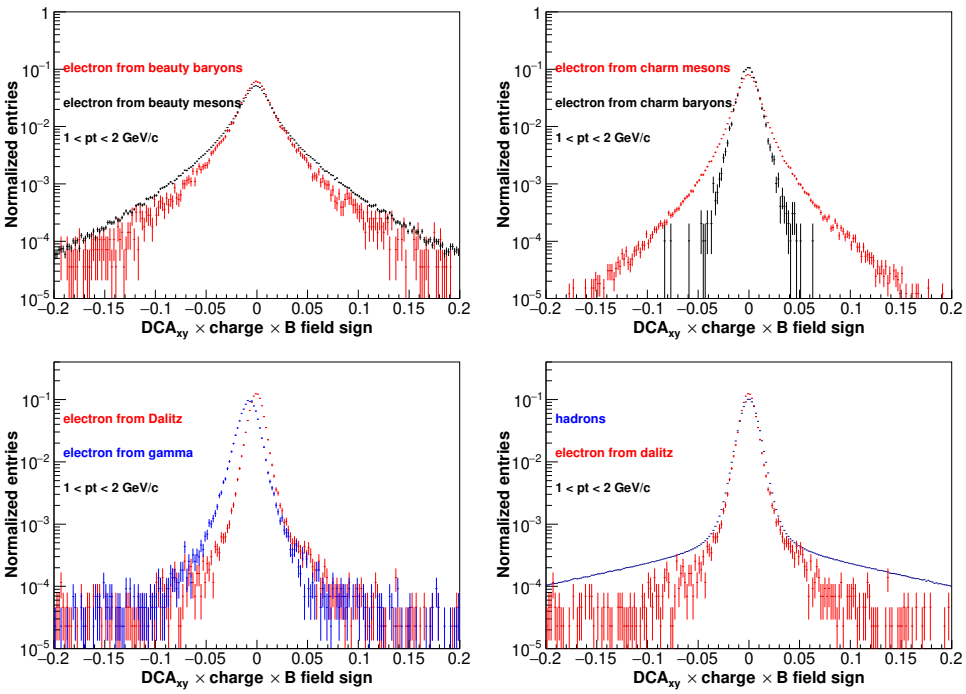

Figure 4.2. DCA templates of electrons coming from beauty mesons and baryons (top left), charm mesons and baryons (top right), Dalitz decays and gamma conversions (bottom left) and Dalitz decays and charged hadrons (bottom right).

effectively they are coming from the primary vertex with a decay length of 20 nm of their mother (π^0 and η). The width of these distributions reflects the DCA resolution of the detectors.

- **Electrons from photon conversions:**

  The last source of electrons is from photon conversions in the detector material. Electrons from this source are produced far away at the beam pipe which is situated at 3 cm from the primary vertex. It is well known that the electrons from these conversions have a very small opening angle and so, the DCA (impact parameter) of these electrons appear mainly due to the magnetic field. Due to this, the DCA distributions of the electrons and positrons from this source have mirror images of each other. It is better to build the templates with the quantity $\mathrm{DCA_{xy}} \times \mathit{charge} \times \mathit{B\ field\ sign}$ instead of just $\mathrm{DCA_{xy}}$ as it will make the conversion electron templates asymmetric which will be helpful to differentiate among the other templates as those remain unaffected by the use of this quantity.

Figure 4.2 shows the templates of electrons from different sources. The shape of the charged hadrons and Dalitz electrons (in the bottom right plot of Figure 4.2) templates at small DCA values are similar. Therefore, in this analysis, Dalitz electron template is used to take care of the contribution from hadron contamination in the sample.

4.1.3 Corrections to the templates

Monte Carlo simulations are not always able to reproduce the data. In such cases, one needs to correct it in order to match with the data using experimental measurements itself. So, in this section, the corrections which are implemented in the simulations to reproduce the data are discussed.

Fraction of shared clusters in ITS

As already mentioned, one of the reasons behind the requirement of hits in both layers of SPD is to suppress the background from conversion electrons. If electrons from late gamma conversions have two hits on SPD, at least one hit is not really originated by them. So, the probability of having shared these hits with other track is expected to be high. Figure 4.3 shows the signal to background ratio for various fractions of shared clusters (f). By looking at the signal to background ratio, the tracks having fraction of shared clusters below 0.5 are selected for this analysis.

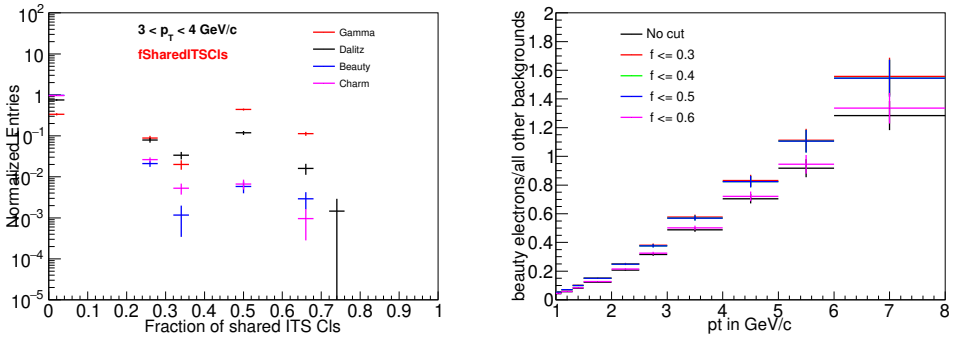

Figure 4.3. Distribution of fraction f of shared clusters on the ITS of electrons from all sources.

Impact parameter (DCA) mean and resolution correction

As a consequence of the misalignment of some SPD modules during data taking of the data used in this analysis, DCA mean in data is shifted towards the negative value. This shift has a dependence on transverse momentum, azimuthal angle and polarity of the magnetic field. However, this is not incorporated in the corresponding MC samples. Therefore, a separate task named "Improver task" is created to mimic that mean shift in MC. The Improver task, AliAnalysisTaskSEImproveITS, is implemented in the PWGHF directory of the AliPhysics in the AliRoot software [83]. The effect of this Improver task can be checked

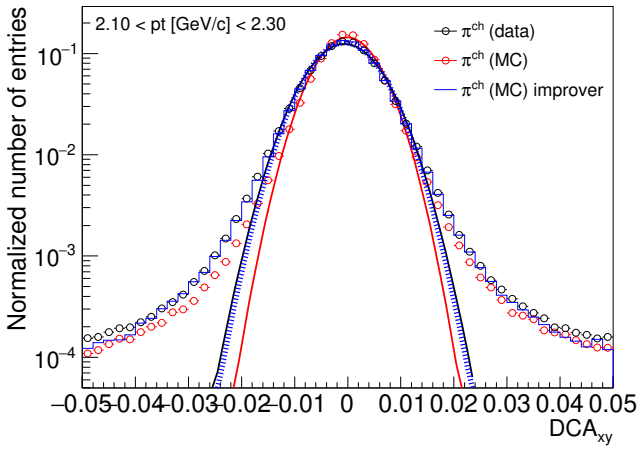

Figure 4.4. DCA distribution of charged hadrons in data (black) and MC before (red) and after (blue) the improver, and the Gaussian fits performed for the extraction of the mean and sigma.

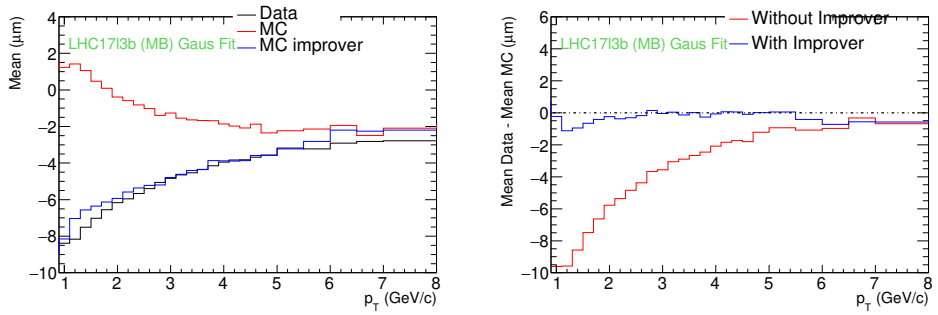

Figure 4.5. Mean of DCA in data (black) compared to the mean of DCA in MC before (red) and after (blue) the correction performed by the improver task.

by looking at the DCA distribution of the charged hadrons in Figure 4.4 (see Appendix 8.10 for all bins) which are selected using TPC (-3 $<$ nσTPC $<$ -5), both in data and MC. This distribution is fitted by Gaussian function within the RMS range (-RMS $<$ DCA_{xy} $<$ RMS) in each p_T bin, in both data and MC. Then the check is made as shown in Figure 4.5 where the differences between the mean in data and MC with and without Improver are plotted. One can see that the shift in data is now successfully restored in the MC.

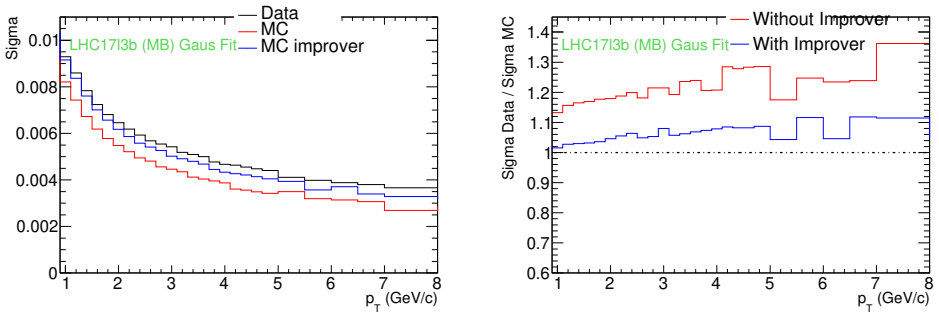

Figure 4.6. Resolution of DCA in data (black) compared to the resolution of DCA in MC before (red) and after (blue) the correction performed by the improver task.

There is also some difference found in the resolution of the DCA distributions in data and MC, as shown in Figure 4.6 (left plot). The task also helps to improve the resolution, and it can be seen in Figure 4.6 (right plot) where the ratios of the resolution in data to the MC are shown with and without Improver. Finally, the mean and resolution of the DCA distributions in MC are made similar to the data with the help of Improver task.

Charm meson p_T shape correction

The shape of the DCA distribution of the electrons depends on the shape of the p_T distribution of their mother. Since the MC does not reproduce the data correctly, the shape of the mother p_T distribution has to be restored and made similar as in data.

For this, the p_T spectra of D^0 meson in both data [100] and MC are fitted using Hagedorn function (left plot in Figure 4.7) and then weight is obtained by

taking the ratio of data and MC as shown in the Figure 4.7 (right plot). This weight is then applied to the electrons in the MC according to the p_T of their mother. The effect of this correction the shape of the DCA distribution of the electrons from the charm mesons can be seen in the Figure 4.10 (left plot) as template (distribution) has become narrower.

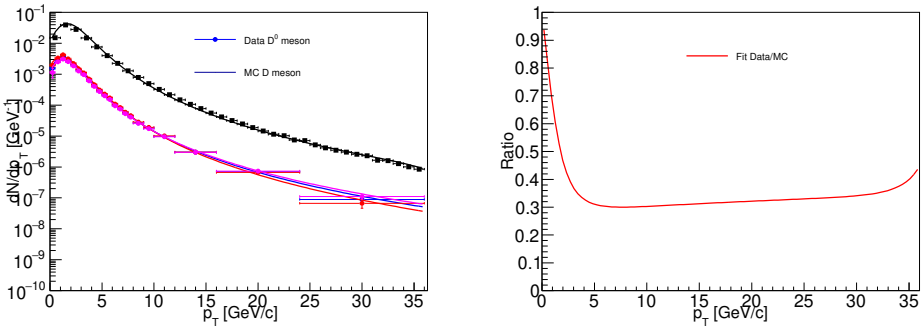

Figure 4.7. Left: p_{T} spectrum of the D meson used in this analysis and p_{T} spectrum of D^0 mesons measured in data. Right: Ratio of D^0 measurement by the spectrum of D mesons from MCs.

Beauty meson p_{T} shape correction

Similar correction is required to be implemented for the mother of the beauty electrons as their shape is also not well reproduced in the data. However, the measured spectra of B meson is not available from ALICE as well as from other experiments in similar kinematic ranges of the spectra. In the absence of the experimental measurement, theoretical predictions from FONLL are used as a reference for the B meson instead of data. Therefore, the weight is obtained by taking the ratio of the B meson FONLL central values to B meson in MC, as shown in Figure 4.8 (right plot). The weight is applied to the electrons from beauty decays according to their mother p_T and shape of the beauty electron template does not change much after this correction as shown in the right plot of Figure 4.10.

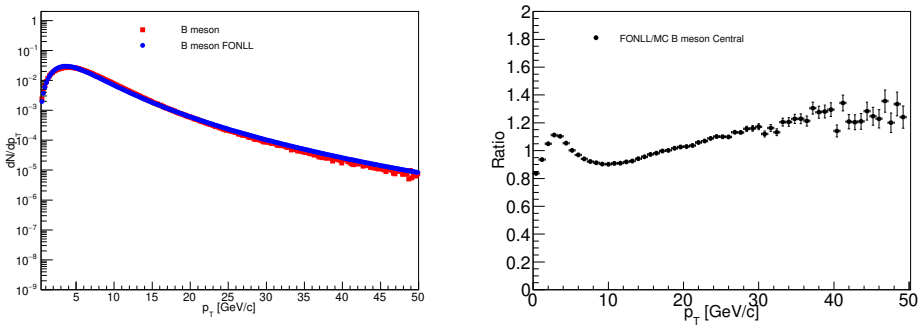

Figure 4.8. Left: p_{T} spectrum of the B meson used in this analysis and p_{T} spectrum of B mesons from FONLL. Right: Ratio of B meson from FONLL by the spectrum of B mesons from MC.

Charm hadrons to D^0 fraction correction

Similar to the shape of the mother spectra, the fractions of the charmed hadrons with respect to the D^0 meson are also not well reproduced in the MC. The wrong fraction can certainly affect the shape of the template since the lifetimes of the different species of the charmed hadrons are different, as discussed in section 4.1.2.

For this correction, the ALICE measurements of these ratios ($\Lambda_{\mathrm{c}}^{+}/D^0$, $\frac{D^{\pm}}{D^0}_{data}$, $\frac{D^{*\pm}}{D^0}_{data}$, $\frac{D_s^{\pm}}{D^0}_{data}$) were used to get the weight (w). The measured $\Lambda_{\mathrm{c}}^{+}/D^0$ ratio [101] has a p_{T} dependence whereas, others are independent of p_{T}, i.e. $\frac{D^{\pm}}{D^0}_{data} \approx 0.5$, $\frac{D^{*\pm}}{D^0}_{data} \approx 0.5$, $\frac{D_s^{\pm}}{D^0}_{data} \approx 0.25$ [100] (see Appendix 8.9 for the plots). The correction to the electrons in the MC is performed track by track according to the estimated weight so that the fractions in MC matches with the experimental measurements. The weight (w) for $\Lambda_{\mathrm{c}}^{+}/D^0$ fraction correction in MC is given by:

$$w = \left(\frac{\Lambda_{\mathrm{c}}^{+}}{D^0}\right)_{data} \times \left(\frac{D^0_{data}}{\Lambda_{\mathrm{c}}^{+}{}_{MC}}\right)$$

– $\frac{\Lambda_{\mathrm{c}}^{+}}{D^0}_{data}$ is the correct fraction in measured in data and $\Lambda_{\mathrm{c}}^{+}{}_{MC}$ is Λ_{c}^{+} contribution in MC;

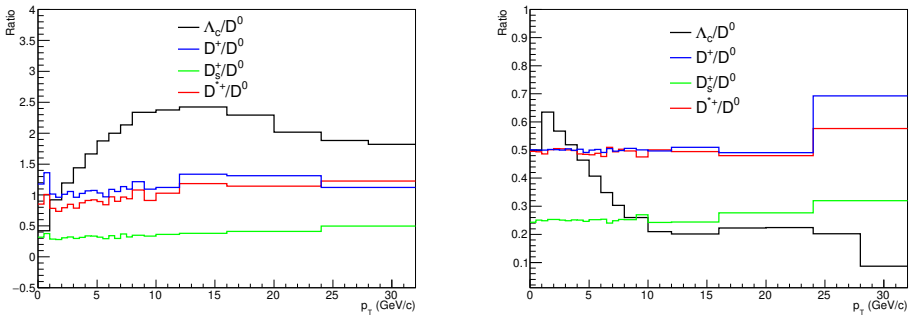

Figure 4.9. Ratios of charmed hadrons to D^0 before (left) and after (right) the correction in the MC.

Similarly, the fraction correction of other ratios in the MC is performed using weight:

$$w = \left(\frac{D}{D^0}\right)_{data} \times \left(\frac{D^0_{data}}{D_{MC}}\right)$$

where, D can be $D^{\pm}$, $D^{*\pm}$ and $D_s^{\pm}$ mesons.

– $\frac{D}{D^0}_{data}$ is the correct fraction in measured in data and D_{MC} is D contribution in MC;

After correcting the fraction of charmed hadrons to D^0 by applying weights to the MC templates, the effect on the shape of the charm electron template is shown in the left plot of Figure 4.10.

4.2 Estimation of p_T-differential production cross-section

The raw spectrum of electrons from beauty hadron decays obtained from the template fits is normalised by the factors discussed below in order to become an invariant yield.

The final invariant production cross-section for electrons from beauty

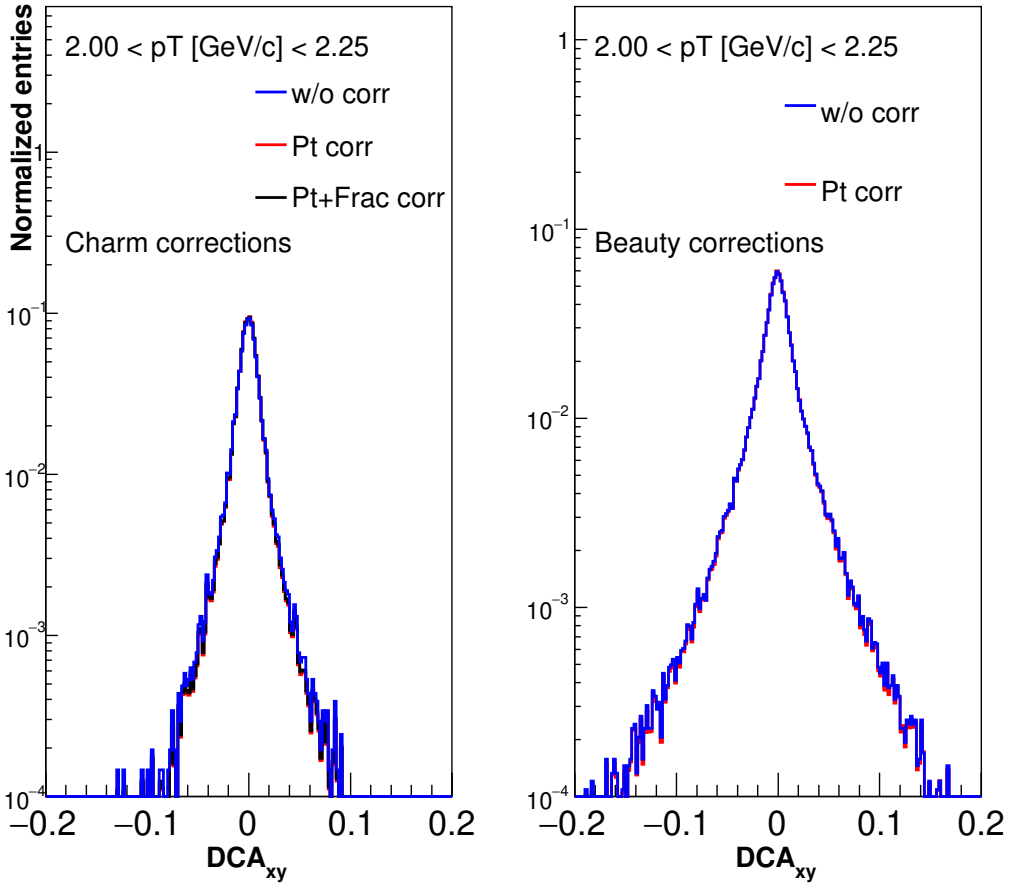

Figure 4.10. Templates of electrons from charm and beauty decays before and after the corrections.

hadron decays was calculated using the following equation:

$$\frac{1}{2\pi p_T}\frac{d\sigma^e}{dp_T dy} = \frac{1}{2}\frac{1}{2\pi p_T^{\text{centre}}}\frac{1}{\Delta y \Delta p_T}\frac{N^e_{raw}}{\varepsilon^{\text{geo}} \times \varepsilon^{\text{reco}} \times \varepsilon^{\text{eID}}}\frac{\sigma_{\text{MB}}}{N_{\text{MB}}}$$

The raw yield (N^e_{raw}) is corrected by reconstruction efficiency ($\varepsilon^{geo} \times \varepsilon^{reco}$) and electron identification efficiency, ε^{eID} of TPC and TOF. The TPC PID efficiency is estimated using data driven method since the mean and sigma of electrons in TPC are not at 0 and 1 respectively as shown in Figure 4.11. Estimated TPC PID efficiency is about 88%. Figure 4.12 shows the track reconstruction, eID and total efficiencies as function of p_{T}.

In addition, the measured yield of beauty electrons is normalised to unit

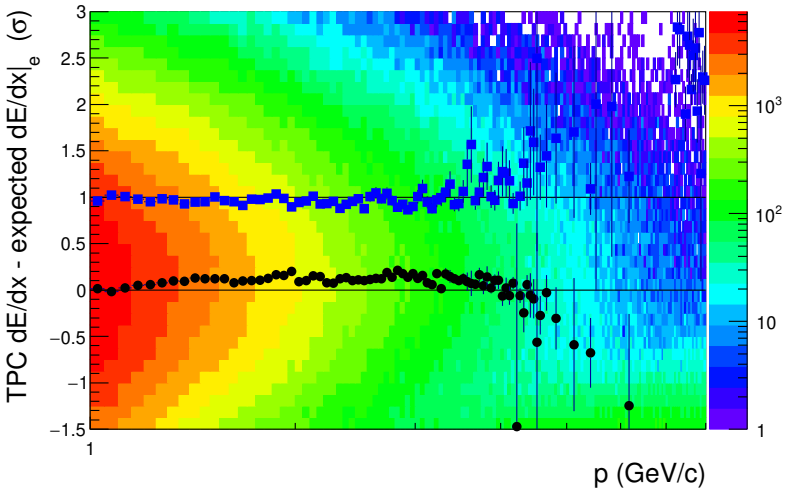

Figure 4.11. TPC nσ distribution of electrons after TOF selection in data.

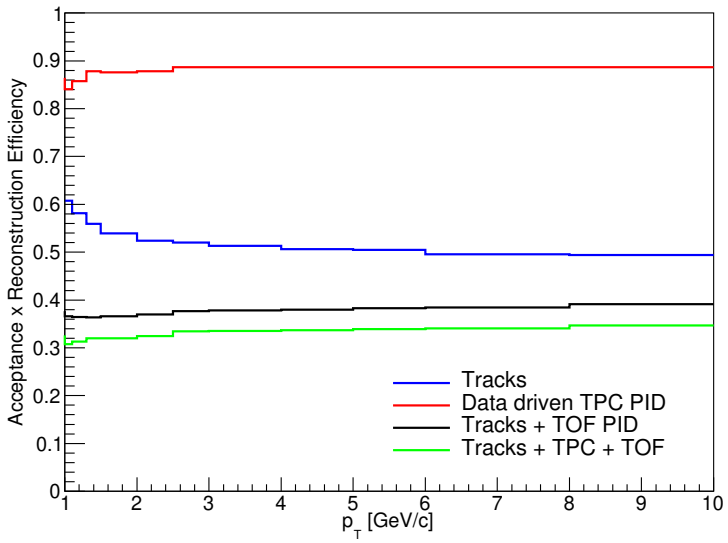

Figure 4.12. Tracking and PID efficienies of beauty electrons at $\sqrt{s} = 5.02$ TeV.

rapidity by dividing by the rapidity range Δy (or $\Delta\eta$) = 1.6. The yield is also normalised to the unity of the azimuthal angle ϕ ($\Delta\phi = 2\pi$). Each p_{T} bin is normalized by its width (Δp_{T}) and by its central value (p_{T}^{centre}). The yield is also normalised by the number of analysed events N_{MB}. Finally, the fully corrected yield is multiplied by the minimum-bias cross-section of pp collisions at $\sqrt{s} =$ 5.02 TeV ($\sigma_{MB} = 50.77\ mb$ [102]) to get invariant production cross-section of

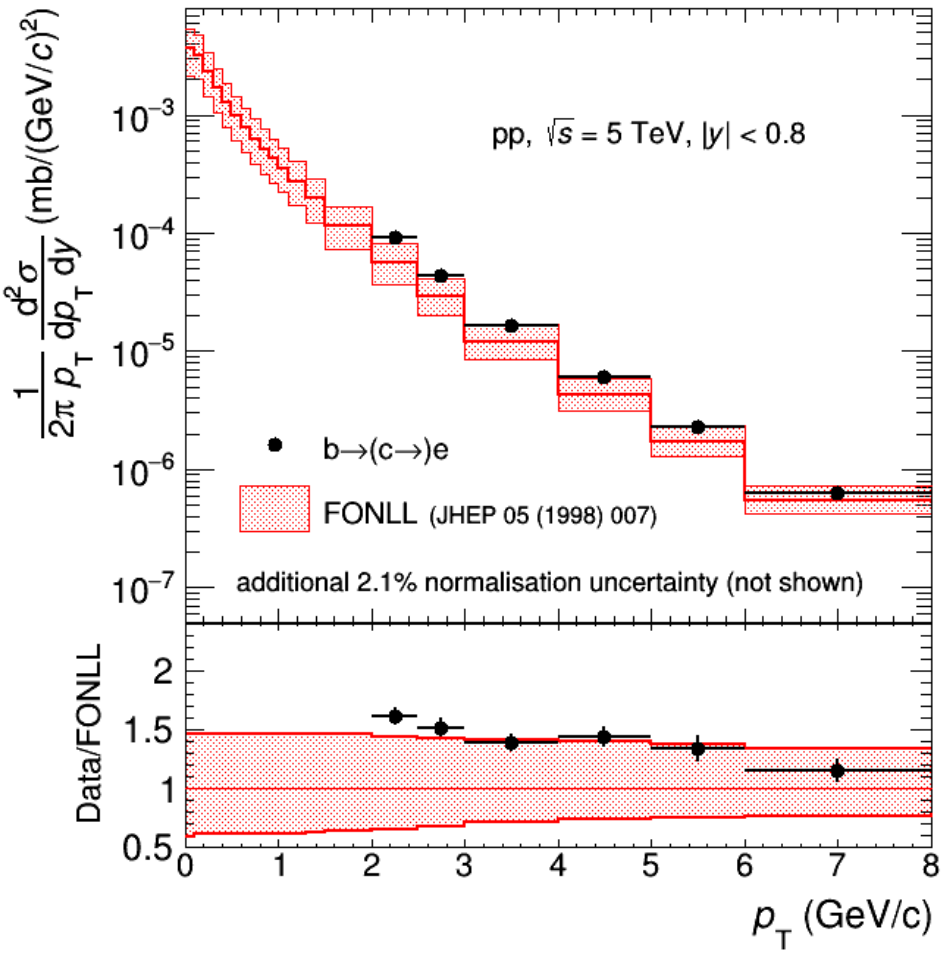

Figure 4.13. Invariant cross-section of electrons from beauty hadron decays and its comparison with the FONLL prediction [48]. Vertical bars denote the statistical errors.

electrons originating from beauty hadron decays which is shown in Figure 4.13.

4.3 Estimation of statistical uncertainties

Statistical uncertainties on the measured raw yield of beauty electrons were estimated using so-called toy model approach. These are extracted from the template fits and estimated by taking into account the statistical uncertainties of the data as well as the templates. For each fit, MC templates are rebuilt by sampling from the original one according to its statistics. An analogous sampling is also done for the data DCA distribution in that p_T bin. The procedure is repeated many times, and the distribution of the measured quantity is obtained and the

width of this distribution is assigned as the statistical uncertainty of the original measurement. This procedure of repeating the fit many times using data and templates sampled from the original ones is named a toy model approach.

4.4 Estimation of Systematic uncertainties

After estimating the cross-section, the next step is to estimate the systematic uncertainties due to different selection criteria and the corrections. Followings are the different sources of systematic uncertainties considered:

- D meson p_{T} shape correction.
- B meson p_{T} shape correction.
- Charmed hadrons yield fraction correction.
- Hadron contamination.
- Fit stability.
- TPC PID.
- TOF PID.

4.4.1 D meson p_{T} shape correction

Systematic uncertainty which may arise due to the D meson p_{T} shape correction is estimated by calculating two more D meson weights by tilting the D meson spectra up and down within its uncertainties as shown in the left plot of Figure 4.14.

Then the ratios of cross-sections obtained using these two variations to the default measurement are taken as shown in the right plot of Figure 4.14. The systematic uncertainty of 2 % in p_{T} range 1.0 to 6.0 GeV/c is assigned.

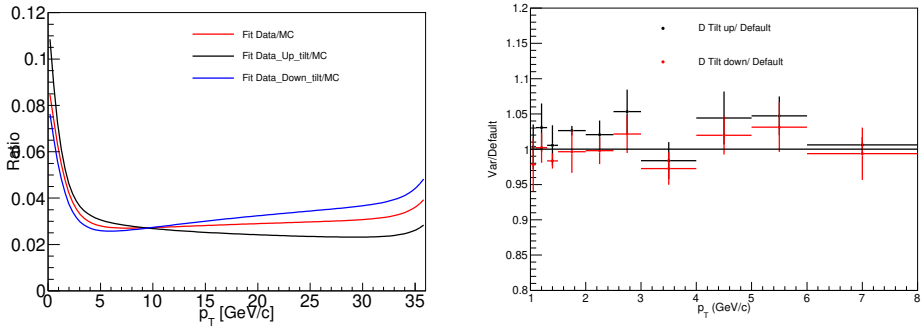

Figure 4.14. Left: D meson weights obtained by tilting D^0 spectra up and down, Right: ratios of the beauty yield with these weights to the default.

4.4.2 B meson p_T shape correction

As discussed earlier, FONLL spectra was used to correct the B meson p_{rmT} shape in the MC. Similar to above case, two variations of B meson weights are obtained by using the FONLL lower and upper edge to estimate the systematic uncertainty due to the B meson p_T shape correction as shown in the left plot of Figure 4.15. From the ratios shown in the right plot of Figure 4.15, the

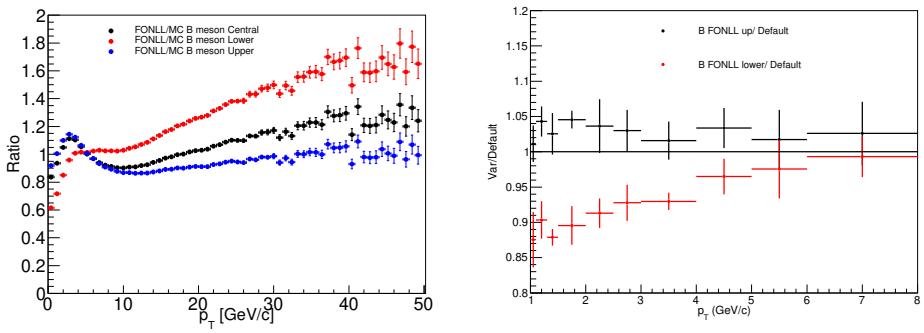

Figure 4.15. Left: B meson weights with FONLL central, lower and upper edge, Right: ratios of the beauty yield with these weights to the default.

systematic uncertainty of 10% ($1.0 \leqslant p_T < 2.5$ GeV/c), 7% ($2.5 \leqslant p_T < 4.0$ GeV/c) and 5% ($4.0 \leqslant p_T < 6.0$ GeV/c) are assigned.

4.4.3 Charmed hadrons yield fraction correction

The fractions of charmed hadrons to D^0 in MC are corrected by using experimental measurements which are affected by systematic uncertainties. This can

introduce the systematics into the final measurement. So in this case, using two variations of each ratios (Λ_c/D0 (as shown in left plot of Figure 4.16), D^+/D0, D^{*+}/D0 and D_s/D0 (see Figure 8.18)) i.e upper egde and lower edge of the systematic uncertainties, cross-sections are obtained. For instance, for $\frac{D^{\pm}}{D^0}_{data} \approx$ 0.5 being the central value, the upper edge 0.6 and lower edge 0.4 and so on for other ratios. Then the ratios with respect to the default measurement are taken.

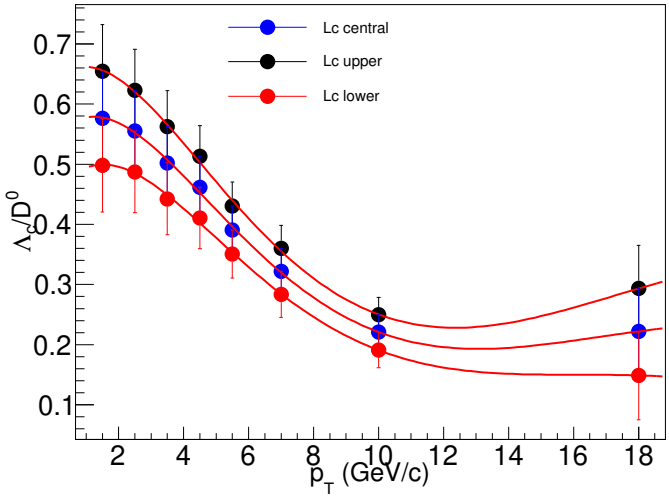

Figure 4.16. Λ_c/D^0 ratio: central (blue), lower (red) and upper (black).

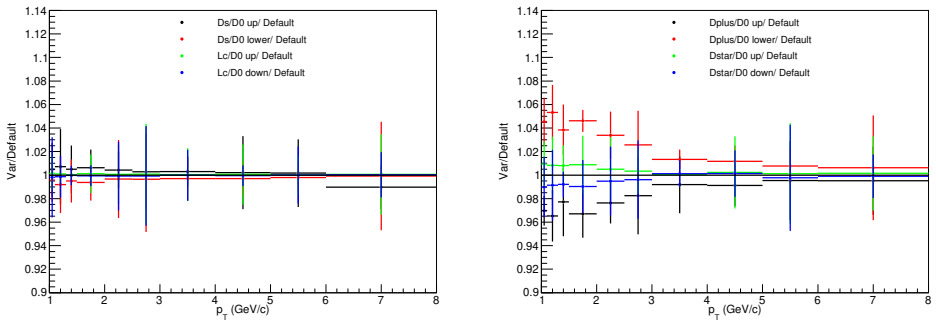

Figure 4.17. Ratios of the beauty yield obtained by varying the charged hadron to D^0 ratios to the default.

From Figure 4.17, the systematics of 4 % ($1.0 \leqslant p_T \leqslant 2.5$ GeV/c) and 2 % ($2.5 \leqslant p_T \leqslant 5.0$ GeV/c) are assigned.

4.4.4 Hadron contamination

As the Dalitz electron templates are used to take care of the contribution from hadron contamination, this can lead to some systematic uncertainties. For this, the beauty yield is obtained by subtracting the charged hadrons template from the inclusive sample (obtained by -5 to -3 TPC nσ and -3 to 3 TOF σ) which was scaled to the amount of contamination in the inclusive sample. The ratio of these two yields is taken to assign the systematics as shown Figure 4.18. The systematics at low p_{T} is negligible, and 5% between 4 to 5 GeV/c and 10% between 5 to 8 GeV/c is assigned.

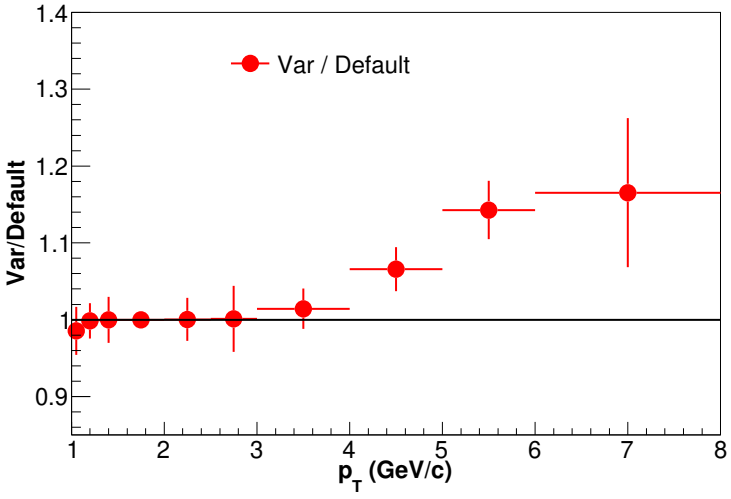

Figure 4.18. Ratio of beauty yield by subtracting the charged hadrons template from the inclusive sample, by scaling it to the amount of contamination in the inclusive sample to the default.

4.4.5 Fit stability

Fit variants such as bin width and fit range can have a systematic effect on the final result. Systematics due to these fit variants are obtained by varying the fit range and bin width of the templates. The beauty yield is sensitive to the fit range rather than bin width. Ratios of beauty electron yield varying the binwidth and fit range to the default (bin width = 20 μm and fit range [-0.2 cm, 0.2 cm]) are obtained as shown in Figure 4.19. Systematics of 20% is assigned below 2.0

GeV/c, 10% is assigned between 2.0 to 2.5 GeV/c and 5% between 2.5 $\leqslant p_{\mathrm{T}} \leqslant$ 5.0 GeV/c.

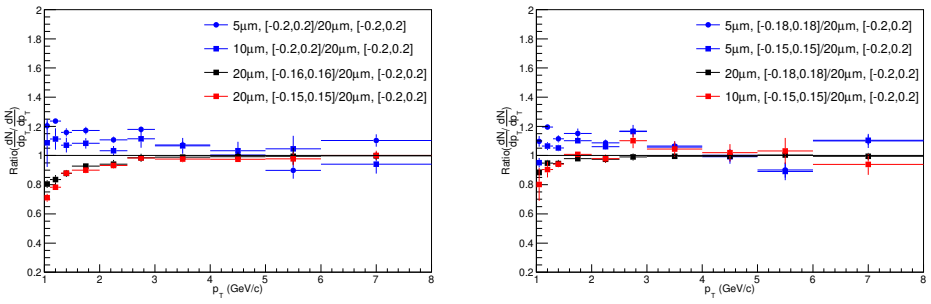

Figure 4.19. Ratios of beauty yield obtained by varying the binwidth and fit range to the default (bin width = 20 μm and fit range [-0.2 cm, 0.2 cm]).

4.4.6 TPC PID

TPC nσ distribution of electrons is fitted with Gaussian function to estimate the identification efficiency. To estimate the systematic uncertainties due to this source, the TPC nσ distributions of electrons are fitted with Gaussian (default), and Landau multiplied by exponential function to get the systematics as depicted in Figure 4.20. The ratios of the integrals of these two functions within nσ region (-1 to 3) are taken and 1% systematic is assigned in whole transverse momentum range as shown in Figure 4.21.

4.4.7 TOF PID

For TOF PID systematic uncertainty, the V0 electrons are used. V0 particles are produced in the decay of neutral mother particles and which can be selected using their decay topology. Their detailed selection process can be found in [103]. TOF PID efficiency of these electrons is estimated in both data and MC as shown a left plot of Figure 4.22. The ratio of these two efficiencies is used to assign the systematics, which is 4% below $p_{\mathrm{T}} = 6$ GeV/c and negligible above.

The systematics due to TPC-TOF matching is taken from heavy-flavour electron analysis in pp collision at $\sqrt{s} = 5.02$ TeV analysis [63] which is about

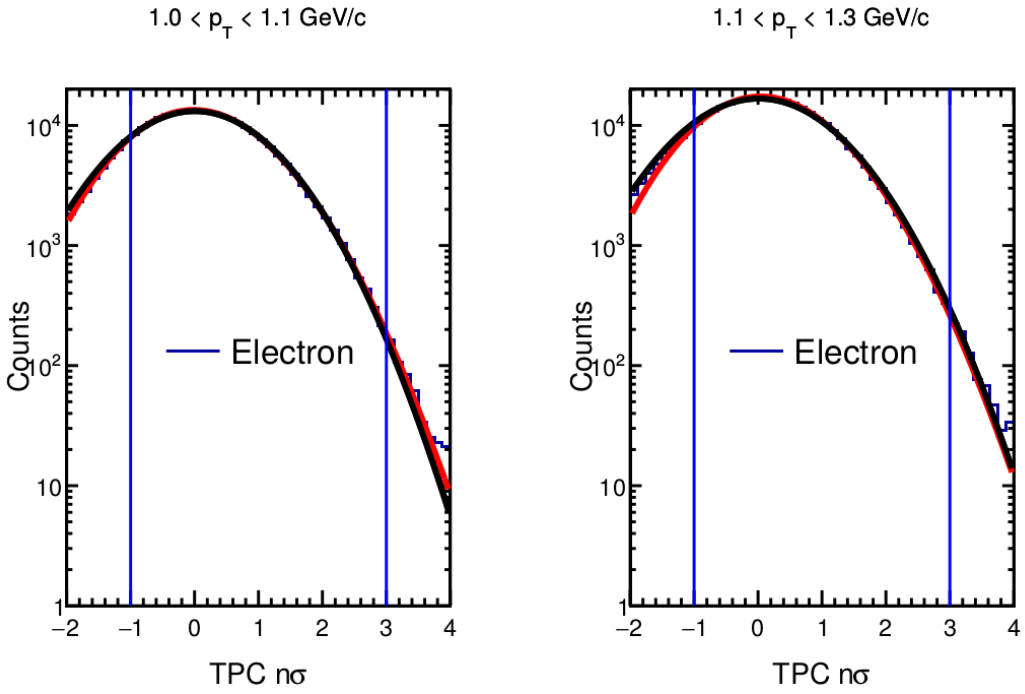

Figure 4.20. Fits to the electron nσ distributions using Landau multiplied by Exponential (red) and Gaussian functions (black).

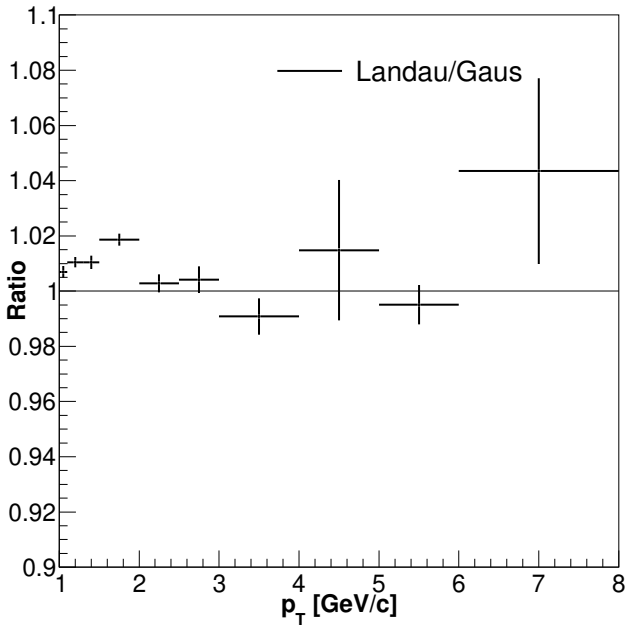

Figure 4.21. TPC PID systematics: Ratio of integral of Landau $\times$ Exp to Gaussian function in -1 to 3 nσ region of TPC nσ distribution.

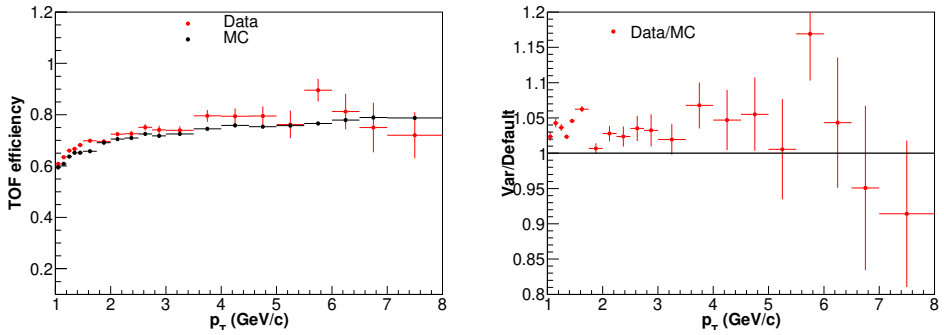

Figure 4.22. TOF efficiency of V0 electrons in data and MC (left) and their ratios (right).

2% in whole transverse momentum regime.

The systematic uncertainties due to various sources are mentioned in Table 4.2 and total uncertainties are estimated by adding them in the quadrature as mentioned in the Table 4.3.

Table 4.2. Total systematic uncertainties

Sources	Systematics in %
D meson p_{T} shape correction	2 % ($1.0 \leqslant p_{\mathrm{T}} < 6.0$ GeV/c)
B meson p_{T} shape correction	10 % ($1.0 \leqslant p_{\mathrm{T}} < 2.5$ GeV/c) 7 % ($2.5 \leqslant p_{\mathrm{T}} < 4.0$ GeV/c) 5 % ($4.0 \leqslant p_{\mathrm{T}} < 6.0$ GeV/c)
Charmed hadrons yield fraction correction	4 % ($1.0 \leqslant p_{\mathrm{T}} < 2.5$ GeV/c) 2 % ($2.5 \leqslant p_{\mathrm{T}} < 5.0$ GeV/c)
Hadron contamination	5% ($4.0 \leqslant p_{\mathrm{T}} < 5.0$ GeV/c) 10 % ($5.0 \leqslant p_{\mathrm{T}} < 8.0$ GeV/c)
Fit stability	20 % ($p_{\mathrm{T}} < 2.0$ GeV/c) 10 % ($2.0 \leqslant p_{\mathrm{T}} < 2.5$ GeV/c) 5 % ($2.5 \leqslant p_{\mathrm{T}} < 5.0$ GeV/c)
TPC PID	1 % ($1.0 \leqslant p_{\mathrm{T}} < 8.0$ GeV/c)
TOF PID	4 % ($1.0 \leqslant p_{\mathrm{T}} < 6.0$ GeV/c)
TPC–TOF matching	2% (from HFE 5.02 TeV analysis)

Table 4.3. Summary of the total systematic uncertainties for the cross-section

Transverse momentum (p_T) in GeV/c	Total systematic uncertainty (%)
2.0 - 2.5	15
2.5 - 4.0	10
4.0 - 5.0	10
5.0 - 6.0	12
6.0 - 8.0	10

4.5 Results and Conclusion

Finally, the estimated systematic uncertainties are propagated on to the measured invariant production cross-section, as shown in Figure 4.23. The measured cross-section is in agreement with the FONLL [48] predictions and lies on the upper edge within the systematic uncertainties.

It also agrees with the scaled cross-section in pp collisions at $\sqrt{s} = 5.02$ TeV within systematic uncertainties which is obtained by scaling the cross-section at $\sqrt{s} = 7$ TeV [104] to 5.02 TeV using FONLL predictions. From Figure 4.23, one can appreciate the improvement in the systematic uncertainties in the measured cross-section in comparison to the scaled one.

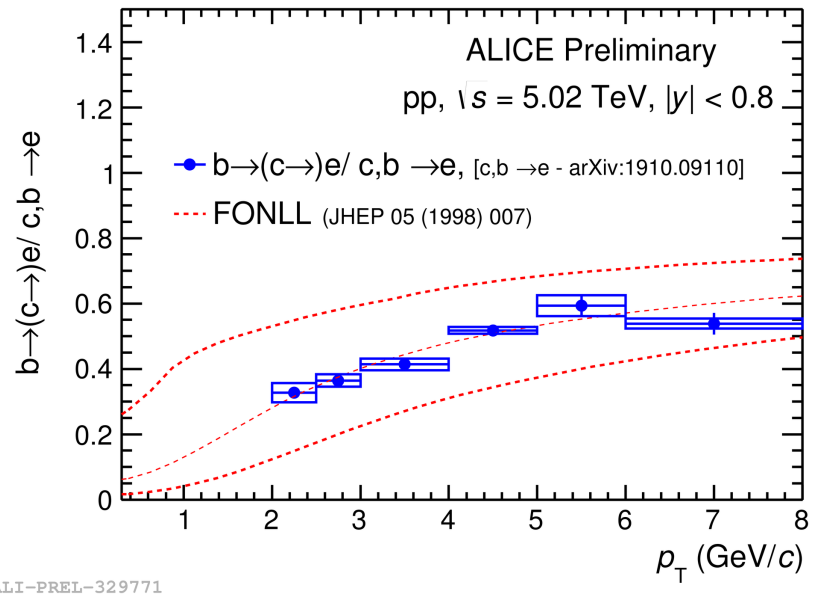

Figure 4.24. Fraction of electrons of beauty hadron decays to electron from heavy-flavour hadron decays

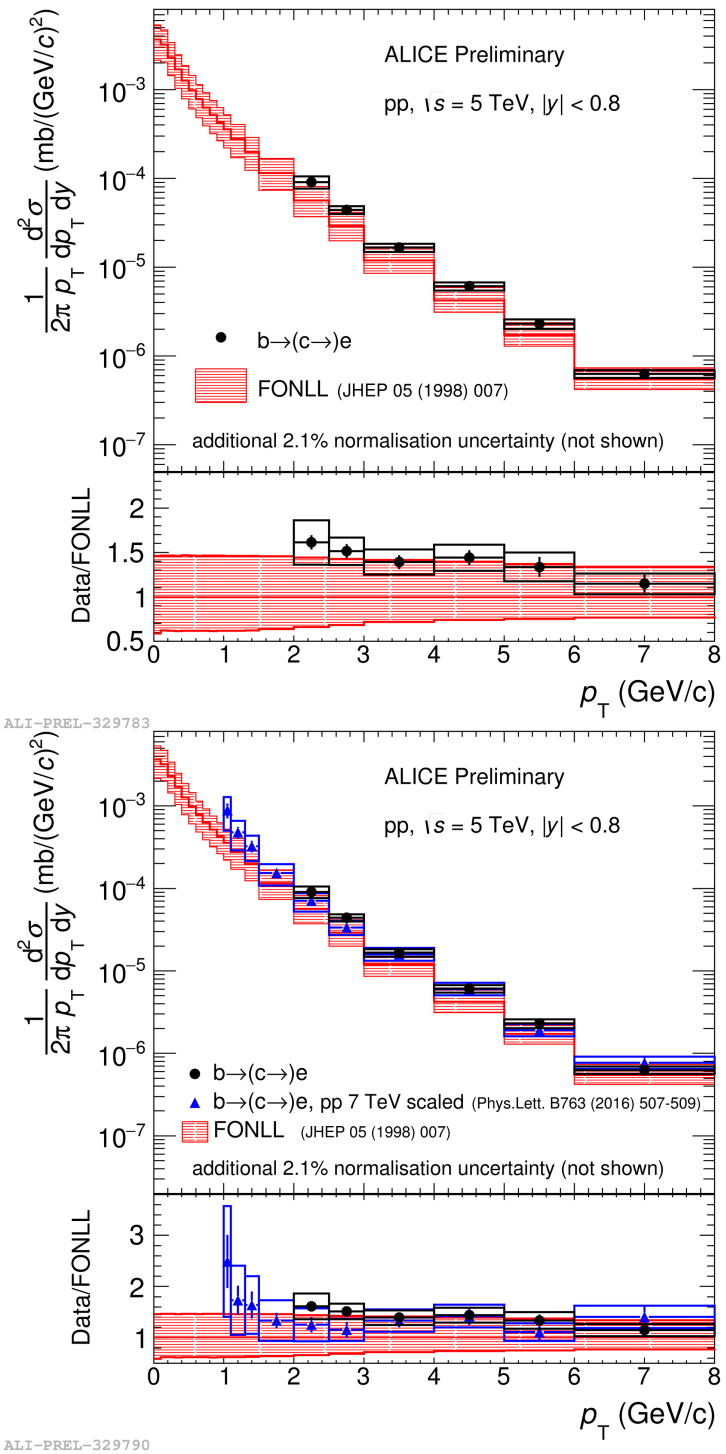

Figure 4.23. Top: p_{T}-differential cross-section of electrons from beauty hadron decays and its comparison with the FONLL prediction [48]. Bottom: Its comparison with the cross-section obtained from scaling 7 TeV cross-section using FONLL.

Along with this, the relative contribution of electrons from beauty hadron decays to the electrons from heavy-flavour hadron decays is measured. The

production cross-section of electrons from heavy-flavour hadron decays in pp collisions at $\sqrt{s} = 5.02$ TeV measured by ALICE with good precision [63] is used for the estimation of the fraction. This ratio is compared with the central, upper and lower limit of FONLL predictions as shown in Figure 4.24. One can see that the beauty contribution starts to dominate beyond $p_T > 4$ GeV/c.

The measured cross-section is then further used as a crucial reference in the measurement of the nuclear modification factor (R_{AA}) of the electrons from the beauty hadron decays in central and semi-central Pb–Pb collisions at $\sqrt{s_{NN}}$ = 5.02 TeV [105, 106]. The improvement in the uncertainties of the R_{AA} is also observed.

With this chapter, we conclude our study to explore the high-temperature regime of QCD phase diagram. From the next chapter, we set our sight on the other side of the spectrum of QCD phase diagram.

Chapter 5

Mass-dependent hierarchy of kinetic freeze-out parameters

From hereon, we shift our focus from analysis of heavy-flavour production data at the LHC energies to the phenomenological investigation of particle production in low energy collisions. In this chapter, we study the mass-dependent hierarchy of kinetic freeze-out parameters of hadrons in low energy heavy-ion collisions. For this purpose, the transverse momentum and rapidity spectra of the different identified hadrons are analysed within a generalised non-boost-invariant blast wave model. We find a clear mass-dependent hierarchy in the fitted kinetic freeze-out parameters. Further, we study the rapidity spectra using analytical Landau flow solution for non-conformal systems. It is found that the resultant value of the speed of sound in the medium also shows a similar hierarchy.

5.1 Introduction

The hot dense matter of quarks and gluons is expected to form in the wide range of the temperatures and baryonic density. At the RHIC and LHC, the matter with high temperature and nearly zero baryon densities is produced whereas, relativistic nuclear collisions at moderate energies such as those available at RHIC Beam Energy Scan (BES) program, at the upcoming FAIR accelerator facility at GSI Germany [107] and NICA facility at JINR Dubna [108], are anticipated to create hot and dense nuclear matter in the regime of moderate temperatures and large net baryon densities. So, it will be fascinating to explore the properties

Facility/ Experiment	E_{Lab} (A GeV)	y_b	Phase space hadron Species
AGS /E895	2 [109] [110]	1.39	$-0.05 < y_{c.m.} < 0.05$ (π^+, π^-, p)
AGS /E895	4	2.13	$-0.05 < y_{c.m.} < 0.05$ (π^+, π^-, p)
AGS /E895	6	2.54	$-0.05 < y_{c.m.} < 0.05$ (π^+, π^-, p)
AGS /E895	8	2.83	$-0.05 < y_{c.m.} < 0.05$ (π^+, π^-, p)
SPS /NA49	20 [112]	3.75	$0.0 < y_{c.m.} < 0.2$ (π^-) $-0.1 < y_{c.m.} < 0.1$ ($K^{\pm}$) $-0.38 < y_{c.m.} < 0.32$ (p)
RHIC BES /STAR	30.67 [111]	4.18	$-0.1 < y_{c.m.} < 0.1$ ($\pi^{\pm}$, $K^{\pm}$,p, $\bar{p}$)
SPS /NA49	30	4.16	$0.0 < y_{c.m.} < 0.2$ (π^-) $-0.1 < y_{c.m.} < 0.1$ ($K^{\pm}$) $-0.48 < y_{c.m.} < 0.22$ (p)
SPS /NA49	40 [113]	4.45	$0.0 < y_{c.m.} < 0.2$ (π^-) $-0.1 < y_{c.m.} < 0.1$ ($K^{\pm}$) $-0.32 < y_{c.m.} < 0.08$ (p)
RHIC BES /STAR	69.56	5.00	$-0.1 < y_{c.m.} < 0.1$ ($\pi^{\pm}$, $K^{\pm}$,p, $\bar{p}$)
SPS /NA49	80	5.12	$0.0 < y_{c.m.} < 0.2$ (π^-) $-0.1 < y_{c.m.} < 0.1$ ($K^{\pm}$) $-0.36 < y_{c.m.} < 0.04$ (p)
SPS /NA49 [114]	160	5.82	$0.0 < y_{c.m.} < 0.2$ (π^-) $-0.1 < y_{c.m.} < 0.1$ ($K^{\pm}$) $-0.51 < y_{c.m.} < -0.11$ (p)

Table 5.1. Details of the data sets from different experiments at different accelerator facilities along with energy (E_{Lab}), beam rapidity (y_b), Phase space and Hadron species, used for this blast wave analysis. Au + Au $(0-5\%)$ at AGS and RHIC BES and Pb + Pb $(0-7\%)$ at SPS.

of matter at these conditions. However, for optimum utilisation of these facilities to decode the QCD phase structure, it is imperative to analyse the existing data sets in the similar energy range collected by the first generation fixed-target experiments at AGS and SPS accelerator facilities.

Facility/ Experiment	E_{Lab} (A GeV)	y_{beam}	Centrality	Phase space
SPS/NA49	20	3.75	$0-7.2\%$	$0.0 < y_{c.m.} < 1.8$ (ϕ)
			$0-7\%$	$-0.4 < y_{c.m.} < 0.4$ (Λ, $\bar{\Lambda}$)
			$0-7\%$	$-0.5 < y_{c.m.} < 0.5$ ($\Xi^{\pm}$)
SPS/NA49	30	4.16	$0-7.2\%$	$0.0 < y_{c.m.} < 1.8$ (ϕ)
			$0-7\%$	$-0.4 < y_{c.m.} < 0.4$ (Λ, $\bar{\Lambda}$)
			$0-7\%$	$-0.5 < y_{c.m.} < 0.5$ ($\Xi^{\pm}$)
SPS/NA49	40	4.45	$0-7\%$	$-0.4 < y_{c.m.} < 0.4$ (Λ, $\bar{\Lambda}$)
			$0-7\%$	$-0.5 < y_{c.m.} < 0.5$ ($\Xi^{\pm}$)
			$0-7.2\%$	$0.0 < y_{c.m.} < 1.5$ (ϕ)
			$0-7.2\%$	$-0.5 < y_{c.m.} < 0.5$ ($\Omega^{\pm}$)
SPS/NA49	80	5.12	$0-7\%$	$-0.4 < y_{c.m.} < 0.4$ (Λ, $\bar{\Lambda}$)
			$0-7.2\%$	$0.0 < y_{c.m.} < 1.7$ (ϕ)
			$0-7\%$	$-0.5 < y_{c.m.} < 0.5$ ($\Xi^{\pm}$)
SPS/NA49	158	5.82	$0-10\%$	$-0.4 < y_{c.m.} < 0.4$ (Λ, $\bar{\Lambda}$) [115]
			$0-5\%$	$0.0 < y_{c.m.} < 1.0$ (ϕ) [117]
			$0-23.5\%$	$-0.5 < y_{c.m.} < 0.5$ ($\Omega^{\pm}$) [116]
			$0-10\%$	$-0.5 < y_{c.m.} < 0.5$ ($\Xi^{\pm}$) [115]

Table 5.2. Details of the data sets from different experiments at different accelerator facilities along with energy (E_{Lab}), beam rapidity (y_{beam}) in lab frame, System, Centrality, Phase space and Hadron species, used for this blast wave analysis.

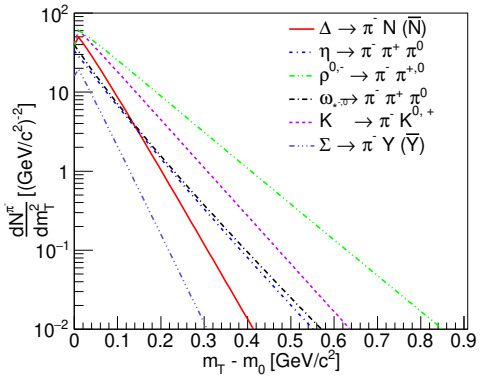

Figure 5.1. An illustration of the resonance decay contributions to the transverse mass spectra of pions. Both two and three-body decays are incorporated in the calculation. Higher mass resonances beyond $\Delta(1232)$ are neglected.

The determination of freeze-out conditions of the fireball at various collision energies is of the particular interest. During chemical freeze-out the in-

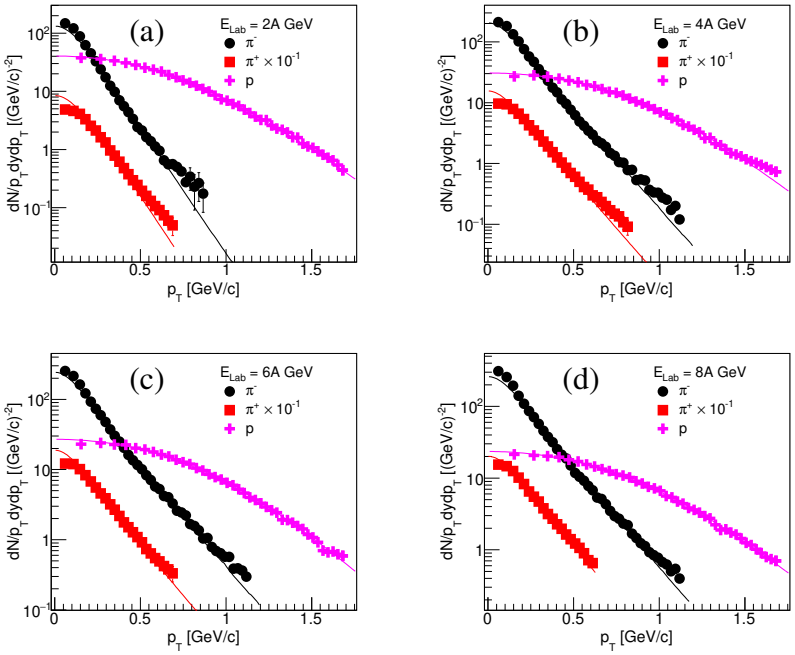

Figure 5.2. Fitted p_T spectra for Pions ($\pi^{\pm}$) (-0.05 $< y_{c.m.} <$ 0.05) and Proton (p) (-0.05 $< y_{c.m.} <$ 0.05) at (a) 2A GeV, (b) 4A GeV, (c) 6A GeV and (d) 8A GeV beam energies.

elastic scatterings cease, leading to the stabilisation of the particle chemistry in the fireball. On the other hand, at kinetic or thermal freeze-out hadrons stop to interact with each other, and their momentum distribution does not undergo further change. In the so-called "standard model" of heavy-ion collisions, chemical freeze-out occurs earlier than kinetic freeze-out due to larger mean free path of inelastic collisions. Usually, the yields and transverse momentum (p_T) spectra of the produced hadrons are analysed to extract the parameters of chemical and kinetic freeze-out. In Ref. [118] the authors advocated for a multiple chemical freeze-out scenario, with strange hadrons fixing their chemical composition earlier than the non-strange light hadrons, due to smaller inelastic cross-sections. An interesting question to ask is whether a similar hierarchical structure is also present in the case of kinetic decoupling. One may expect a mass-dependent hierarchy of kinetic freeze-out as the medium induced momentum change of heavy hadrons would be smaller compared to lighter hadrons. Therefore, as the temperature of the fireball decreases, one would expect an earlier kinetic decoupling of heavy hadrons. In the chapter, we have attempted to look for the possible hierarchy in thermal freeze-out, in low energy nuclear collisions.

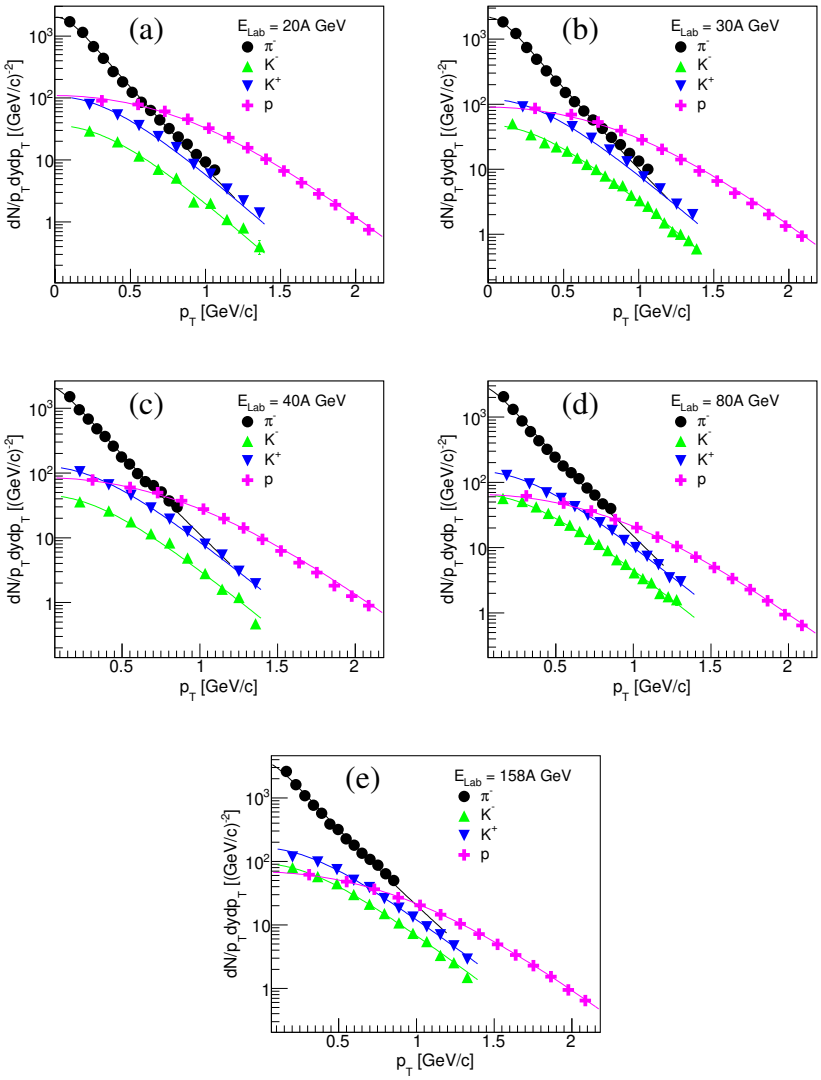

Figure 5.3. Fitted p_T spectra for Proton (p) (-0.38 $< y_{c.m.} <$ 0.32 for 20A GeV, -0.48 $< y_{c.m.} <$ 0.32 for 30A GeV, -0.32 $< y_{c.m.} <$ 0.08 for 40A GeV, -0.36 $< y_{c.m.} <$ 0.04 for 80A GeV and -0.51 $< y_{c.m.} <$ -0.11 for 158A GeV),π^- (0.0 $< y_{c.m.} <$ 0.2) and $K^{\pm}$ (-0.1 $< y_{c.m.} <$ 0.1) at (a) 20A GeV, (b) 30A GeV, (c) 40A GeV, (d) 80A GeV and (e) 158A GeV beam energies.

In literature, kinetic freeze-out conditions are commonly studied in hydrodynamics inspired blast-wave model framework [119]. Due to its simplicity, blast wave models have been used for a long time to analyse momentum distribution of the produced hadrons and provide information about the properties of the matter at kinetic freeze-out. The main underlying assumption is that the particles in the system produced in the collisions are locally thermalised (till they are emitted from the medium), and the system expands collectively with a com-

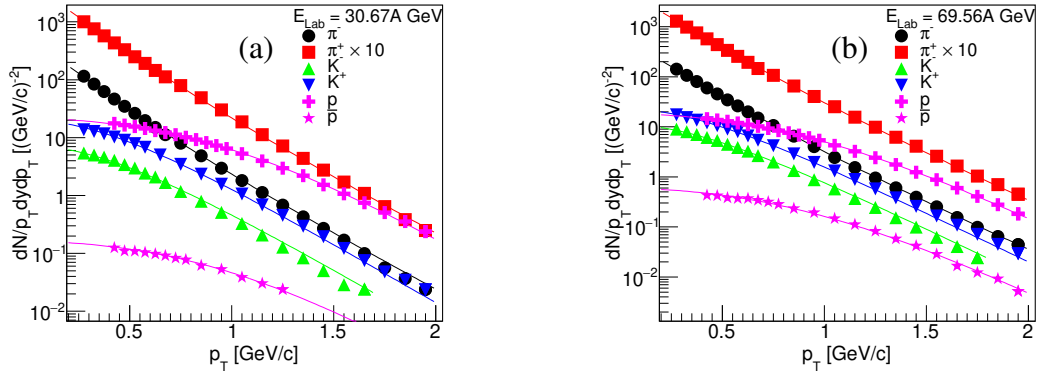

Figure 5.4. Fitted p_T spectra for Proton (p) (-0.1 $< y_{c.m.} <$ 0.1), Anti-proton ($\bar{\text{p}}$) (-0.1 $< y_{c.m.} <$ 0.1), $\pi^{\pm}$ (-0.1 $< y_{c.m.} <$ 0.1) and $\text{K}^{\pm}$ (-0.1 $< y_{c.m.} <$ 0.1) from RHIC beam energy scan (BES) program, at (a) 30.67A GeV and (b) 69.56A GeV beam energies. Since the data have a lower p_T cut off around 0.2 GeV/c, the resonance decay contribution is not included in the calculations.

mon radial velocity field undergoing an instantaneous common freeze-out. Such phenomenological models are particularly useful in nuclear collisions where a fireball is created at finite net baryon density because the detailed hydrodynamic calculations in the corresponding regime suffer from the unavailability of the realistic equation of states from the lattice QCD.

The first version of the blast-wave model was formulated about four decades ago [120], to describe the hadron production in Ne+NaF reactions at a beam energy of 800A MeV. The model assumes the radial expansion of the fireball, with constant velocity. Collective isentropic expansion of the nuclear fireball with a scaling form for the radial velocity profile was also used to analyse the then available data on transverse momentum (p_T) spectra of hadrons from 14.5A GeV Si+Au collisions at BNL AGS and 200A GeV O+Au collisions at CERN SPS [121, 122].

While the spherically expanding source may be expected to mimic the fireball created at low energies, at higher energies, a stronger longitudinal flow might lead to cylindrical geometry. For the latter case, an appropriate formalism was first developed in Ref. [123]. Using a simple functional form for the phase space density at kinetic freeze-out, the authors approximated the hydro-

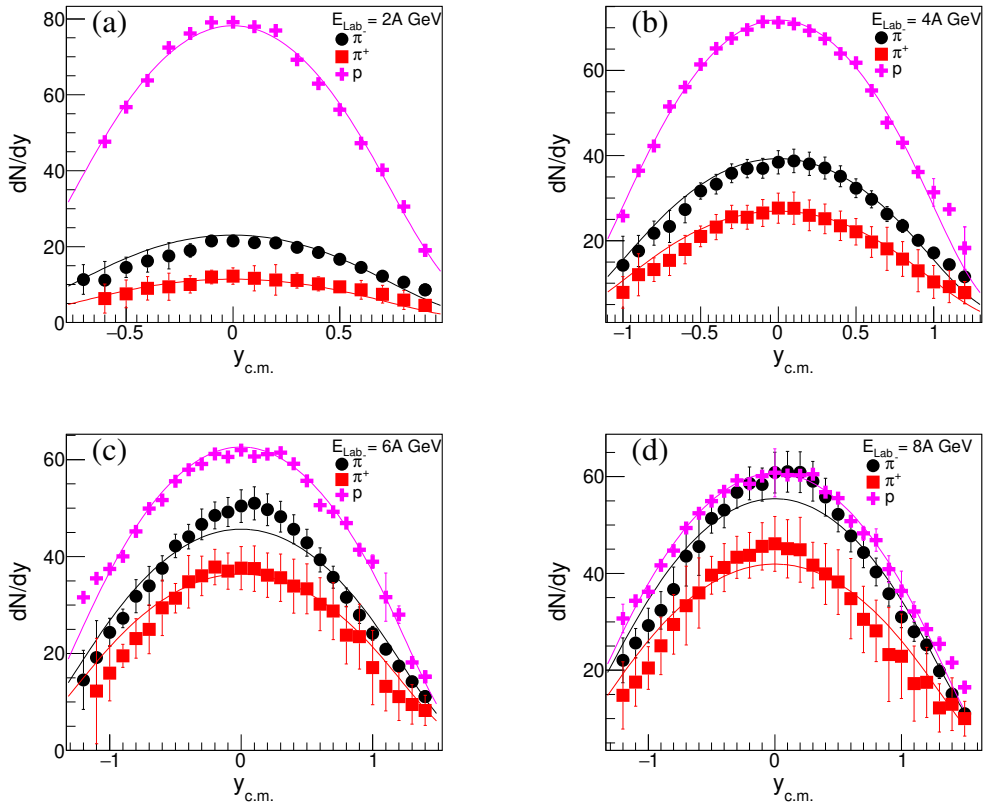

Figure 5.5. Fitted rapidity distribution of $\pi^{\pm}$ and Proton (p) in central Au+Au collisions from AGS, at (a) 2A GeV, (b) 4A GeV, (c) 6A GeV and (d) 8A GeV beam energies. For each particle species, the normalisation constant has been adjusted separately for best-fit results.

dynamical results with the boost-invariant longitudinal flow. The model was successfully used to fit the p_T spectra with only two parameters, namely a kinetic freeze-out temperature T_{kin} and a radial flow strength β_T. Though initially developed for central collisions, the model was later extended to non-central collisions with the introduction of additional parameters to account for anisotropies in the transverse flow profile [124] and in the shape of the source in the coordinate space [125]. The model has also been applied to search for collectivity in small systems [126]. Attempts have also been made to incorporate the viscous effects in the blast wave model [127, 128]. One common assumption for all these variants of the blast wave model is the underlying boost-invariant longitudinal dynamics. Although it is a reasonable assumption at RHIC and LHC energies, longitudinal boost-invariance does not hold well at AGS and SPS energies. Therefore in order to describe particle production at these energy domains,

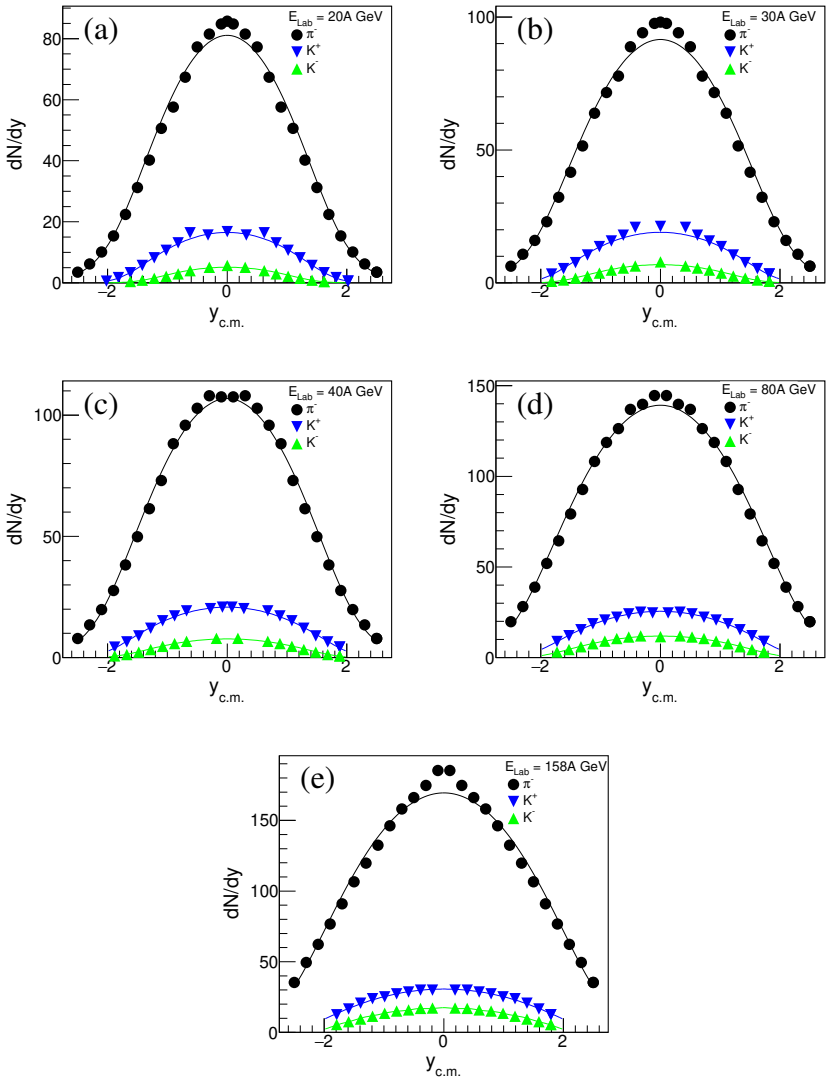

Figure 5.6. Fitted rapidity distribution of π^-, K^+ and K^- in central Pb+Pb collisions from SPS, at (a) 20A GeV, (b) 30A GeV, (c) 40A GeV, (d) 80A GeV and (e) 158A GeV beam energies.

the assumption of boost-invariance must be relaxed.

In Ref. [129], the authors proposed a non-boost-invariant extension of the blast wave model of Ref. [123]. The cylindrical symmetry is broken via the modification of the system boundaries which is suitable for low energy collisions. For a realistic parametrisation of the freeze-out surface of the expanding fireball, the model has been found to provide a very good fit to the p_T and rapidity spectra for a variety of hadrons produced in 11.6A GeV Au+Au collisions measured by E802, E877 and E891 Collaborations at AGS. The results indicated

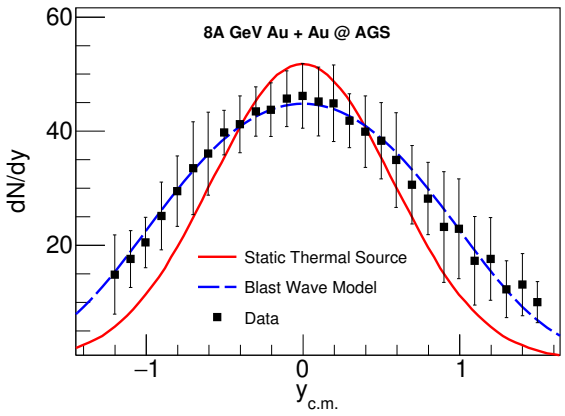

Figure 5.7. Rapidity density distributions of pions in 8A GeV central Au+Au collisions at AGS. Data are compared with predictions from a static thermal model and non boost-invariant blast wave model.

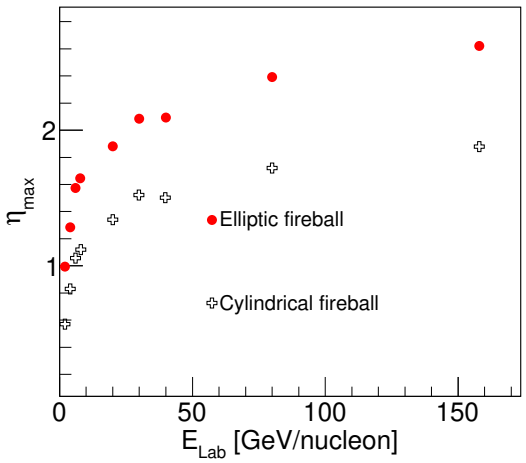

Figure 5.8. Comparison of the η_{max} values for different beam energies at AGS and SPS for an elliptic fireball and a cylindrical fireball. The value η_{max} is consistently larger for former case compared to the latter one.

a relatively low kinetic freeze-out temperature of about 90 MeV with an average transverse expansion velocity at mid-rapidity of about $0.5c$.

In this chapter, we employ the non-boost-invariant blast-wave model to analyse the transverse and longitudinal spectra of the light hadrons (p, π^-, $K^{\pm}$) from Au+Au and Pb+Pb collisions in the energy range $\mathrm{E_{Lab}} = 2 - 158$A GeV [130], as measured by different experimental Collaborations at AGS, SPS and RHIC facilities. We use these results to study the mass-dependent hierarchy

in kinetic freeze-out parameters of identified hadrons produced in central Pb+Pb collisions at SPS energies. Here, besides light hadrons, we analyse the p_T-spectra and rapidity spectra of the heavy strange hadrons, at collision energies ranging from $E_{Lab} = 20A - 158A$ GeV [131]. For the study of mass-dependent hierarchy, we consider separate simultaneous fits for light hadrons (π^-, $K^{\pm}$) and heavy strange hadrons (Λ, $\bar{\Lambda}$, ϕ, $\Xi^{\pm}$, $\Omega^{\pm}$), for which the transverse momentum spectra, as well as rapidity spectra, are available. We do not consider protons in the fits of light hadrons, because all observed protons may not be thermally produced due to stopping at low energies. However, we have checked that the main message of the present work remains unaltered irrespective of whether we include proton in light hadron or heavy hadron set. Moreover, we also perform a separate fit to transverse momentum spectra of charmed hadrons (J/ψ, ψ') at 158A GeV collisions. We find a clear mass-dependent hierarchy in the fitted kinetic freeze-out parameters. Further, we study the rapidity spectra using analytical Landau flow solution for non-conformal systems. We find that the extracted value of sound velocity in the medium also shows a similar hierarchy.

We would like to mention that we perform for the first time, a systematic analysis of the heavy strange hadrons produced in the low energy nuclear collisions using a non-boost-invariant blast-wave model. Note that the application of blast-wave dynamics to study the transverse spectra of heavy hadrons have been attempted earlier. In Ref. [132], the authors have analysed the p_T spectra of J/ψ, ψ' mesons and Ω baryon within the longitudinal boost-invariant blast-wave model, with the hypothesis that for these heavy hadrons, the rescattering effects in the hadronic phase is negligible and they leave the fireball at hadronisation. However, to the best of our knowledge, a thorough analysis of p_T and y distributions of all varieties of multi-strange hadrons produced in the low energy domain has never been attempted before using a non-boost-invariant blast wave model.

In the following section, the essential features of the non-boost-invariant model are described.

5.2 A brief description of the model

E_{Lab} (A GeV)	η_{max}	$\langle\beta_T\rangle$	T_{kin} (MeV)	χ^2/NDF
2	0.995 ± 0.001	0.4838 ± 0.0034	61.72 ± 1.36	7.2
4	1.285 ± 0.002	0.5400 ± 0.0025	55.86 ± 1.38	7.8
6	1.573 ± 0.002	0.5584 ± 0.0062	58.14 ± 3.17	9.4
8	1.645 ± 0.003	0.5655 ± 0.0031	60.63 ± 1.75	8.7
20	1.882 ± 0.005	0.5177 ± 0.0011	79.77 ± 0.05	6.5
30.67	2.078 ± 0.004	0.5448 ± 0.0002	71.25 ± 0.02	8.5
30	2.084 ± 0.004	0.5368 ± 0.0011	80.28 ± 0.05	6.7
40	2.094 ± 0.004	0.5356 ± 0.0009	81.92 ± 0.04	5.5
69.56	2.306 ± 0.005	0.5330 ± 0.0001	78.97 ± 0.01	6.7
80	2.391 ± 0.005	0.5347 ± 0.0012	82.68 ± 0.05	3.8
158	2.621 ± 0.006	0.538 ± 0.0013	84.11 ± 0.06	4.4

Table 5.3. Summary of the fit results at different energies from AGS, SPS and RHIC beam energy scan (BES). For uniformity, at RHIC the relevant centre of mass (CMS) energies are converted to the corresponding beam energies in the laboratory frame.

E_{Lab} (A GeV)	η_{max}	$\langle\beta_T\rangle$	T_{kin} (MeV)	χ^2/N_{dof}
20	1.288 ± 0.021	0.4418 ± 0.0032	93.09 ± 0.19	1.90
30	1.728 ± 0.026	0.4501 ± 0.0029	95.84 ± 0.17	2.23
40	1.752 ± 0.018	0.4536 ± 0.0026	98.82 ± 0.14	3.70
80	1.989 ± 0.021	0.4489 ± 0.0022	106.46 ± 0.12	3.59
158	2.031 ± 0.029	0.4688 ± 0.0016	109.24 ± 0.11	3.40

Table 5.4. Summary of the fit results of p_T spectra of heavy strange hadrons at different energies ranging from 20A to 158A GeV at SPS.

Details of the non-boost-invariant blast wave model that we have employed in our calculations can be found in [129]. Here we briefly outline the main features for completeness. In the blast-wave model, the single-particle momentum spectrum of the hadrons emitted from the fireball at freeze-out is usually described by the Cooper-Frye [133] prescription of particle production. Within this formalism, the single-particle spectrum is defined as the integral of the phase-space distribution function $f(x,p)$ over the freeze-out hypersurface

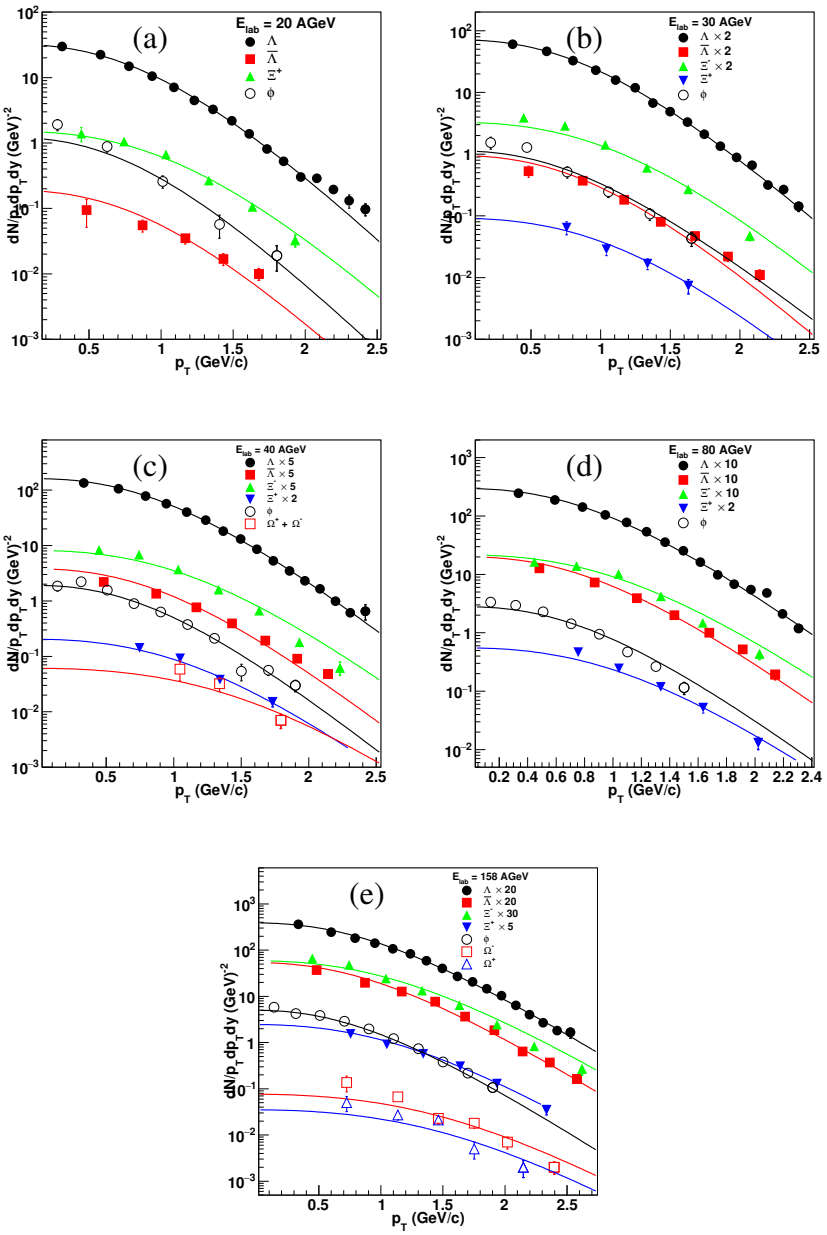

Figure 5.9. Simultaneously fitted p_T spectra of Λ, $\bar{\Lambda}$, ϕ, $\Xi^{\pm}$ and $\Omega^{\pm}$ at (a) 20A GeV, (b) 30A GeV, (c) 40A GeV, (d) 80A GeV and (e) 158A GeV beam energies. Error bars indicate available statistical error.

$\Sigma^f_\mu(x)$. The triple differential invariant spectra can be written as:

$$E\frac{d^3N}{d^3p} = \frac{g}{2\pi^3}\int d^3\Sigma^f_\mu(x)p^\mu f(x,p) \tag{5.1}$$

where g denotes the degeneracy factor. In thermal models, $f(x,p)$ is considered to be the equilibrium distribution function. In the temperature range of the heavy-ion collisions, the quantum statistics can be ignored and one usually

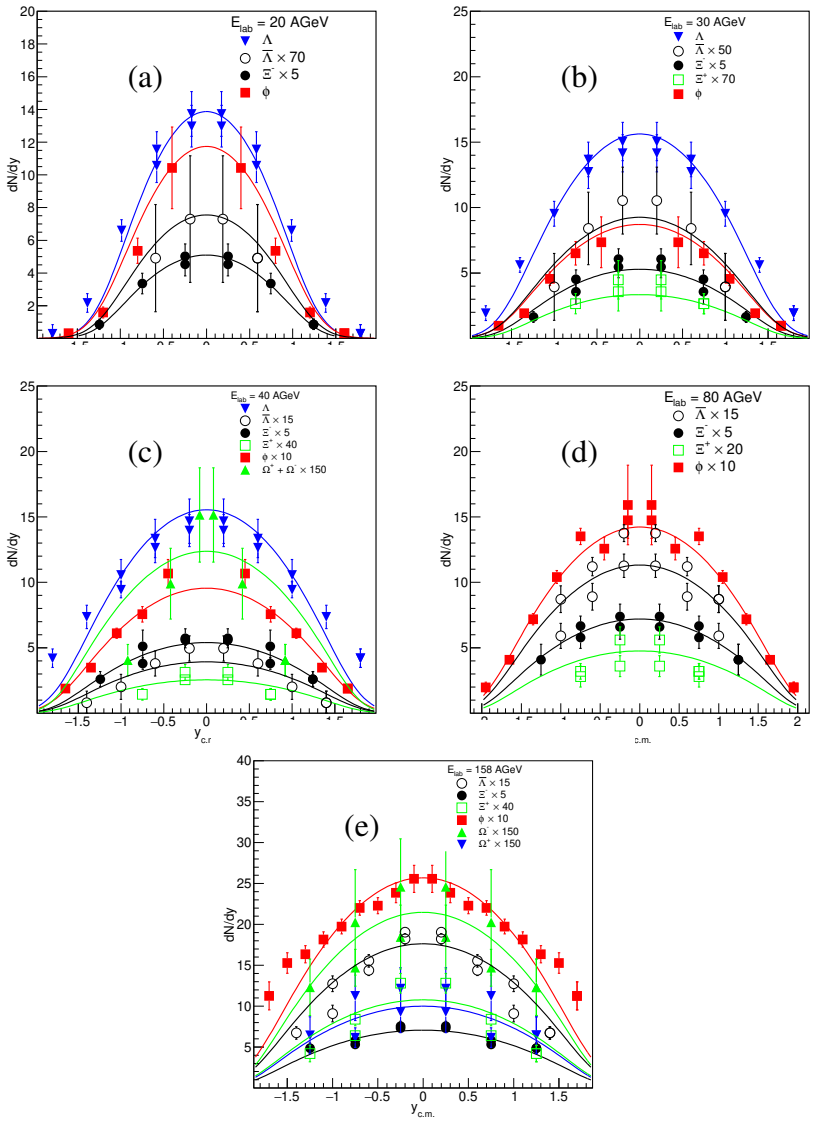

Figure 5.10. Fitted rapidity distribution of Λ, $\bar{\Lambda}$, ϕ, $\Xi^{\pm}$ and $\Omega^{\pm}$ in central Pb+Pb collisions from SPS, at (a) 20A GeV, (b) 30A GeV, (c) 40A GeV, (d) 80A GeV and (e) 158A GeV beam energies. Error bars indicate available statistical error.

works with the Boltzmann approximation. The freeze-out hypersurface $\Sigma^f_\mu(x)$ is determined from freeze-out criteria for thermal decoupling.

For an expanding fireball in local thermal equilibrium, the boosted thermal distribution is given by:

$$f(x,p) = \exp\left(-\frac{p.u(x) - \mu(x)}{T(x)}\right) \tag{5.2}$$

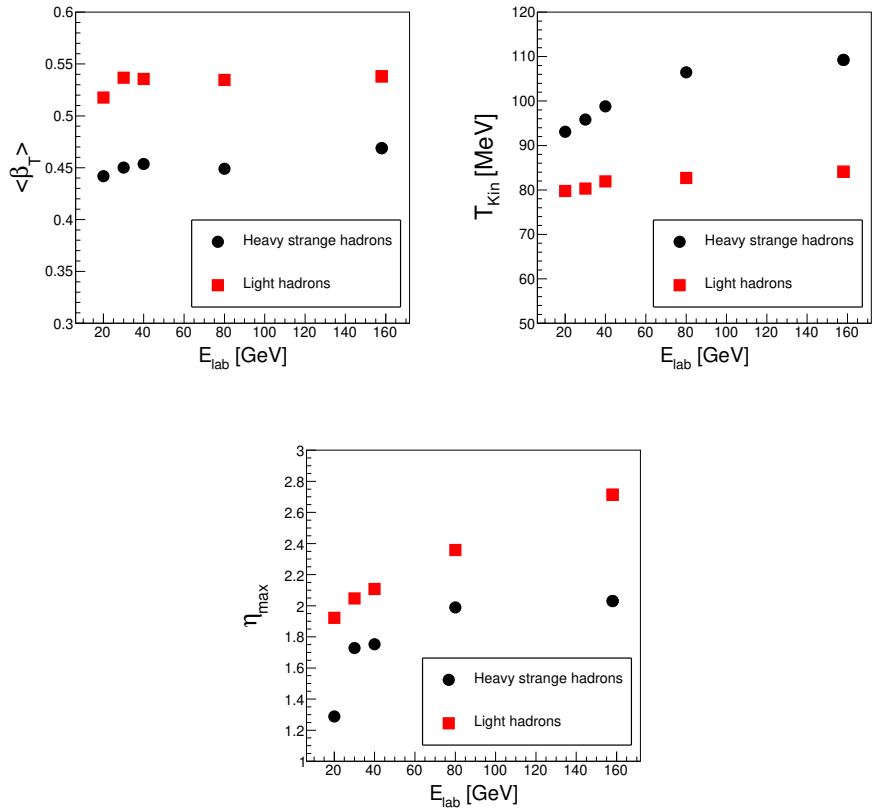

Figure 5.11. Variation of the $\langle\beta_T\rangle$ (top left), T_{kin} (top right) and η_{max} (bottom) for heavy strange and light hadrons with incident beam energy (E_{lab}). Errors are within the marker size.

where $T(x)$ and $\mu(x)$ are space-time dependent local temperature and chemical potential at kinetic freeze-out and $u^\mu(x) = \gamma(1, \beta_T(x)e_r, \beta_L(x))$ is the local fluid velocity. Focusing on central collisions, with a realistic parametrisation of the freeze-out hyper-surface and local fluid velocity, the thermal single particle spectrum in terms of transverse mass $m_T(\equiv \sqrt{p_T^2 + m^2})$ and rapidity y are given by

$$\begin{aligned} \frac{dN}{m_T dm_T dy} &= \frac{g}{2\pi} m_T \tau_F \int_{-\eta_{\max}}^{+\eta_{\max}} d\eta \, \cosh(y-\eta) \\ &\times \int_0^{R(\eta)} r_\perp \, dr_\perp \, \mathrm{I}_0\left(\frac{p_\mathrm{T} \sinh\rho(r_\perp)}{T}\right) \\ &\times \exp\left(\frac{\mu - m_\mathrm{T}\cosh(y-\eta)\cosh\rho(r_\perp)}{T}\right). \end{aligned} \tag{5.3}$$

where the system is assumed to undergo an instantaneous common freeze-out

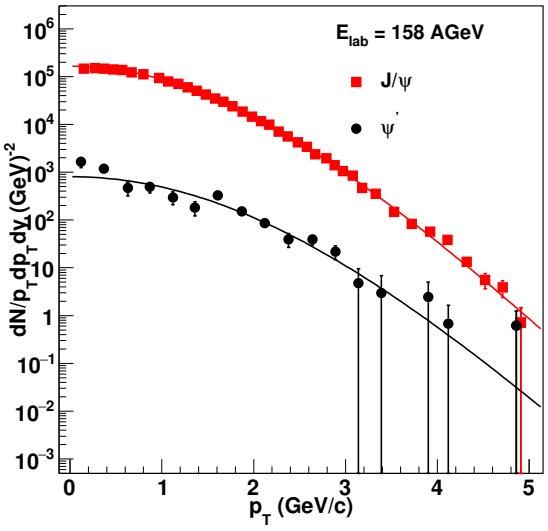

Figure 5.12. Simultaneously fitted p_T spectra of J/Ψ and $\Psi^{'}$ at 158A GeV. Uncorrelated statistical and systematic errors are added in quadrature.

at a proper time $\tau \equiv \sqrt{t^2 - z^2} = \tau_F$. In the above equation, $\eta \equiv \tanh^{-1}(z/t)$ denotes the space-time rapidity and is related to the longitudinal fluid velocity via $\beta_L = \tanh(\eta)$. In the transverse plane the flow rapidity (or transverse rapidity) ρ is related to the collective transverse fluid velocity, β_T, via the relation $\beta_T = \tanh(\rho)$.

The radial dependence of the transverse fluid velocity has been assumed to be of the form

$$\beta_T(r_\perp) = \beta_T^0 \left(\frac{r_\perp}{R}\right)^n. \tag{5.4}$$

where β_T^0 is the transverse fluid velocity at the surface of the fireball. The average transverse flow velocity can be easily obtained and is given by $\langle\beta_T\rangle = \frac{2}{2+n}\beta_T^0$. The transverse flow vanishes at the center and assumes maximum value at the edges, with the flow profile decided by the value of n. Most hydrodynamic calculations suggest $n = 1$ leading to a Hubble-like transverse rapidity flow profile which is linear in the radial coordinate [123]. Such linear parametrisation essentially leads to an exponential expansion of the fireball in the transverse direction, hence the name blast wave.

To account for the limited available beam energy, the longitudinal boost-invariant scenario is modified by restricting the boost angle η to the interval

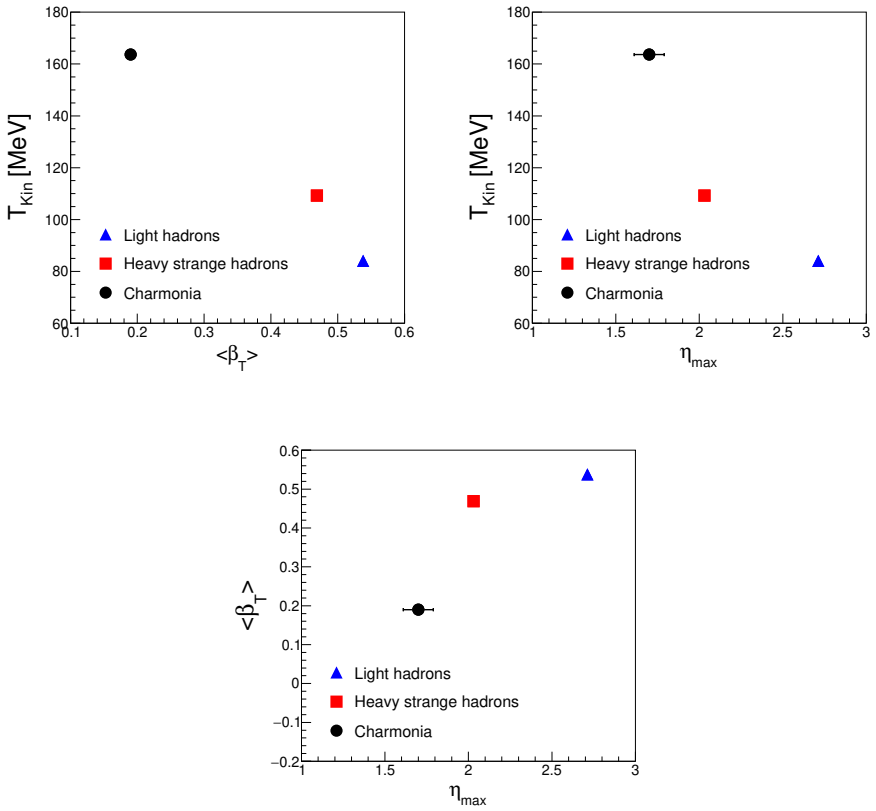

Figure 5.13. The (partial) expansion history of the fireball created in central Pb+Pb collisions at $158A$ GeV. The points indicate the temperature (T_{kin}) and mean transverse collective flow velocity ($\langle\beta_T\rangle$) of the system at the time of charm kinetic freeze-out (filled circle), heavy strange kinetic freeze-out (filled square) and light hadron kinetic freeze-out (filled triangle). The error on η_{max} for charmonia is assigned by varying it in such a way that the corresonding $\chi^2/N_{\rm dof}$ increases in magnitude by unity compared to it's minimum value. Errors on rest of the parameters are within the marker size.

$\eta_{min} \leq \eta \leq \eta_{max}$. Reflection symmetry about the center of mass ensures $\eta_{min} = -\eta_{max}$ and thus constrains the freeze out volume up to a maximum space-time rapidity η_{max}. In the transverse plane, the boundary of the fireball is given by $R(\eta)$. Two different choices of $R(\eta)$ are prescribed in Ref. [129], corresponding to different shapes of the fireball:

$$R(\eta) = R_0 \cdot \Theta\left(\eta_{\rm max}^2 - \eta^2\right), \tag{5.5}$$

$$R(\eta) = R_0 \cdot \sqrt{1 - \frac{\eta^2}{\eta_{\rm max}^2}}. \tag{5.6}$$

where R_0 is the transverse size of the fireball at $\eta = 0$. Note that changing the integral variable $r_\perp \to r_\perp/R$ in Eq. (5.3), the dependence on R_0 factors out leading to an overall volume factor $\tau_F R_0^2$. The first choice, Eq. (5.5), describes a cylindrical fireball in the $\eta - r_\perp$-space and corresponds to the usual formalism [123] which was found to work well at top SPS energies and above. However at lower AGS beam energy, the cylindrical symmetry is not fully realized and the fireball is expected to have an elliptic shape [134], as given by Eq. (5.6). Dependence of transverse size on the longitudinal coordinate explicitly breaks the assumption of boost-invariance. One can also note from Eq. (5.3) that the integral variable $r_\perp$ varies between $0 \leq r_\perp \leq R(\eta)$. Therefore, even though $R(\eta) \to 0$ as $\eta \to \pm\eta_{max}$, the transverse velocity $\beta_T(r_\perp)$ given in Eq. (5.4) is always finite and lies in the physical range (preserves causality) provided $\beta_T^0 < 1$. From our analysis of the experimental results, we find that the extracted value of β_T^0 indeed never leads to causality violation.

While analysing the AGS data, the authors of Ref. [129] had investigated a wide range of possibilities for the different freeze-out parameters. Comparison between fit quality and the number of model parameters (and the related expense in computing time) showed that an optimum description of both longitudinal and transverse spectra can be obtained by reducing the transverse size of the fireball in backward and forward rapidity regions, following Eq. (5.6), along with a constant temperature and transverse flow gradient over the freeze-out surface. In our present analysis, we would, therefore, consider the same parametrisation for describing the longitudinal and transverse spectra.

For comparison to experimental data, one needs to account for hadronic resonance decays particularly for light hadrons. In our present calculations, we follow the formalism given in Ref. [135] using thermal distributions Eq. (5.3) for the resonances. Both two and three-body decay of the sources are numerically simulated. The procedure implies the assumption of full chemical equilibrium which is sufficient for estimating the resonance feed down contributions. The resonance decay contributions to the pion spectra are illustrated in Figure 5.1. We only include hadrons with masses up to $\Delta(1232)$ resonance. As our analysis is restricted up to SPS energies, exclusion of higher resonances would have a

negligible effect.

The analysis results are presented in the following section.

5.3 Results and discussions

In the following two subsections, the blast wave prescription in the non-boost-invariant scenario is employed to examine the experimentally measured transverse momentum and rapidity distributions of the light hadrons at AGS and SPS energies, heavy strange hadrons at SPS energies and transverse momentum spectra of the charmonia at 158A GeV.

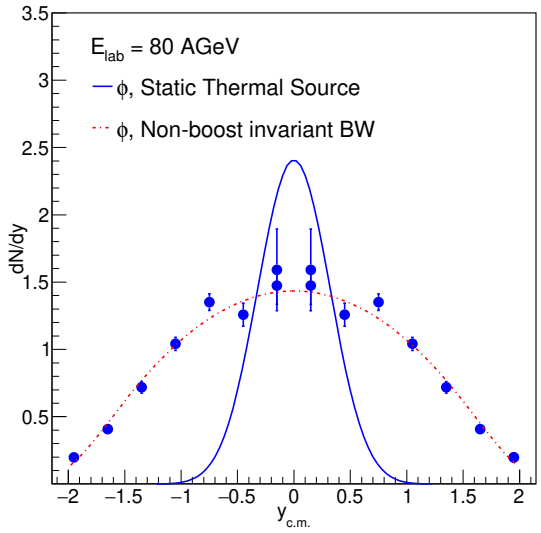

Figure 5.14. Rapidity density distributions of ϕ meson in 80A GeV central Pb+Pb collisions at SPS. Data are compared with predictions from a static thermal model (simple continuous line) and non boost-invariant blast-wave model (dot dashed line). Vertical bars indicate the statistical errors.

5.3.1 Light hadrons

In this sub-section, we present the results of our analysis of light hadrons. For this purpose we consider the measured spectra of the available bulk hadrons in central Au+Au collisions from E895 Collaboration [109, 110] at AGS in the beam energy range $E_{Lab} = 2 - 8$A GeV and from STAR Collaboration at RHIC

E_{Lab} (A GeV)	Hadrons	squared sound velocity (c_s^2)	χ^2/N_{dof}
20	Heavy strange	0.1602 ± 0.0006	2.4
	Light	0.0755 ± 0.0000	331.7
30	Heavy strange	0.2156 ± 0.0009	2.2
	Light	0.121 ± 0.0000	238.7
40	Heavy strange	0.2215 ± 0.0007	2.1
	Light	0.1682 ± 0.0001	38.4
80	Heavy strange	0.2234 ± 0.0005	2.9
	Light	0.2136 ± 0.0000	22.2
158	Heavy strange	0.2511 ± 0.0003	3.1
	Light	0.2276 ± 0.0001	26.5

Table 5.5. Summary of the fit results (squared speed of sound (c_s^2) and χ^2/N_{dof} values) of Rapidity spectra of heavy strange and light hadrons at different energies from SPS using Non-conformal Landau model.

BES program [111] for two centre of mass energies $\sqrt{s_{NN}} = 7.7$ and 11.5 GeV ($E_{Lab} = 30.67$A and 69.56A GeV). In addition data for central Pb+Pb collisions from NA49 Collaboration [112–114] at SPS, in the beam energy range $E_{Lab} = 20 - 158$A GeV are also analysed. We do not go beyond top SPS energy. Note that at AGS the distribution of secondary hadrons was measured by a series of experiments at varying energies and for various collision systems. For the present analysis, we only opt for the latest available data corpus for central Au+Au collisions, from E895 Collaboration. The data were published as acceptance corrected, invariant yield per event as a function of $m_T - m_0$ (m_0 is the particle mass), in small bins of rapidity ($\Delta y = 0.1$). For uniformity, in our analysis, we consider only the mid-rapidity bin, where the yield is maximum. For most forward/backward rapidity bins, data points are mostly not available at higher p_T. The details of the data sets under investigation, including their beam energy, beam rapidity, collision centrality, phase space coverage and analysed hadronic species are summarised in Table 5.1. As we are interested in the global properties of the fireball, we consider only bulk hadronic species, i.e., $\pi^{\pm}$ and p at AGS energies, $\pi^{\pm}$, $K^{\pm}$, p and $\bar{p}$ at energies available at RHIC beam energy scan (BES) program and π^-, $K^{\pm}$ and p at SPS energies. Due to a lower p_T cut off ($p_T^{min} \simeq 0.2$ GeV/c), the resonance decay contribution is excluded

while fitting the spectra from RHIC BES program. The MINUIT [136] package, as available in ROOT framework [137], is employed for the minimisation procedure in our analysis.

The p_T distribution of identified hadrons is fitted using Eq. (5.3) at different energies. To keep the number of fitting parameters minimal, we couple the freeze-out time τ_F, degeneracy factor g and the fugacity (chemical potential) together into a single normalisation constant $Z \equiv \frac{g}{2\pi}\tau_F \exp(\mu/T)$, which is adjusted separately for different particle species. Note that the value of chemical potential is fixed at chemical freeze-out and hence its absorption inside the normalisation would not affect the thermodynamic conditions at kinetic freeze-out. As mentioned earlier, the dependence on R_0 factors out leading to a volume factor $\tau_F R_0^2$ which can also be absorbed inside the overall normalisation. For a given transverse flow profile ($n = 1$), we are thus essentially left with three parameters namely T, η_{max} and β_T^0 which are common for all hadrons at a given energy.

It is important to note that, out of the three parameters, T_{kin}, η_{max} and β_T^0, the rapidity spectra is more sensitive to the width in space-time rapidity η_{max} and is not affected significantly by small changes in the other two parameters. On the other hand, the p_T spectra is more sensitive to T_{kin} and β_T^0 and small changes in η_{max} does not affect the slope of the p_T spectra. Here we adopt an iterative procedure to obtain the best fit values of the parameters. At a given collision energy, the value η_{max} is first fixed from the simultaneous fits of the rapidity distributions of the available heavy strange hadrons with some initial guess values of T_{kin} and β_T^0. Subsequently, we use this η_{max} to then fit the corresponding p_T distributions and extract the values of T_{kin} and β_T^0. These extracted values of T_{kin} and β_T^0 is now used to fit rapidity spectra again to obtain a refined value of η_{max}. This iterative procedure converges quickly and we obtain the fitted values to the desired accuracy. However, for light hadrons at RHIC BES, all three parameters are extracted from their p_T spectra as corresponding rapidity spectra are not reported. The best fit results for the p_T and rapidity spectra are shown in Figure 5.2, 5.3, 5.4, 5.5 and 5.6. The fit to the data is well described by the single η_{max}, $\langle\beta_T\rangle$ and T_{kin} values as can be observed from the

$\chi^2/N_{\rm dof}$ values given in Table 5.3.

As evident, the model gives a reasonable description of the p_T spectra of the bulk hadrons at all investigated energies. The freeze-out temperature is found to be relatively low which gradually increases with beam energy. Rather a strong transverse collective motion is observed even at lowest AGS energy. Hadronic p_T spectra, in this investigated energy domain, has also been analysed within the boost-invariant blast wave model. Relatively higher freeze-out temperatures ($T_{kin} > 100$ MeV) has been observed even at AGS energies with a slightly weaker transverse flow [138]. However one should take note of the fact, that in the corresponding analysis particles are chosen above a non zero p_T value (eg: 0.5 GeV/c for pions) to exclude the effect of resonance decay. Also, the transverse flow parameter n is kept free (which is about 0.5) and fixed from the data whereas we set it to $n = 1$.

In this context, we would also like to mention that at AGS, previous attempts have also been made to fit the transverse distribution of the hadrons with a static rapidity dependent two slopes empirical model in absence of any collective flow [109]. The two inverse slope parameters T_1 and T_2 respectively dominate the low and high end of the $m_T - m_0$ spectra. Both T_1 and T_2 assume maximum values at midrapidity, with T_1 around 50 MeV and T_2 around 130 MeV.

The rapidity distribution of a particle of mass m, emitted from a static thermal source at temperature T has the form

$$\frac{dn_{\rm th}}{dy} = \frac{V}{(2\pi)^2} T^3 \left(\frac{m^2}{T^2} + \frac{m}{T} \frac{2}{\cosh y} + \frac{2}{\cosh^2 y} \right) \times \exp\left(-\frac{m}{T} \cosh y \right) \tag{5.7}$$

where V denotes the source volume. It is well known that the measured particle rapidity distributions from experiments at all beam energies cannot be described by isotropic emission from static thermal models; observed distributions being much wider compared to model predictions. Thermal models incorporating collective expansion in the longitudinal direction, have been much more successful

in reproducing the observed rapidity distributions.

An illustrative comparison is presented in Figure 5.7, where rapidity distribution of the pions in 8A GeV central Au+Au collisions is contrasted with that from a static thermal model as well as from the present blast wave model calculations. As evident rapidity distribution from a static isotropic thermal source falls much faster than the data. A similar feature is observed for all other particles and at all the investigated energies. The additional collective motion is attributed to the large pressure gradients developed inside the hot and dense nuclear matter fireballs created in the early stage of the collisions. Note that the inclusion of longitudinal expansion is generally carried out with a longitudinally boost-invariant superposition of multiple boosted individual sources, locally thermalised and isotropic, in a given rapidity interval [139]. Each locally thermalised source is modelled by the m_T-integrated Maxwell-Boltzmann distribution, with the rapidity dependence of the energy, $E = m_T \cosh y$ explicitly included. Thus within a boost-invariant scenario, the rapidity distribution from a boosted thermal source can be written as

$$\frac{dn}{dy}(y) = \int_{-\eta_{\max}}^{\eta_{\max}} d\eta \, \frac{dn_{\rm th}}{dy}(y-\eta) \tag{5.8}$$

Note that Eq. (5.8) is equivalent to what we obtain by integrating Eq. (5.3) over p_T, for a cylindrical fireball as given by Eq. (5.5). For comparison, we independently fit the rapidity distribution of pions for both η dependent and η independent transverse radius of the fireball. A comparison of the extracted values of η_{max} at different energies, for elliptic fireball and cylindrical fireball, is displayed in Figure 5.8. For the non-boost-invariant model η_{max} (and hence the maximum longitudinal fluid velocity) is consistently higher than a boost-invariant case.

5.3.2 Heavy strange hadrons and charmonia

Moving on, the results of the measured p_T and y spectra of all the available heavy strange hadrons produced in central Pb+Pb collisions from NA49 Collab-

oration [115–117] at SPS, in the beam energy range $E_{Lab} = 20A - 158A$ GeV, have been presented in this sub-section. Not much data on strange hadrons are available in Au+Au collisions at AGS energies, except the measurements of Λ [140] and ϕ [141] at 11.5 and 11.7 AGeV and with different kinematic coverage, from E877 and E917 experiments respectively. Nonetheless, we confine ourselves only to the SPS energy domain. Data on p_T distribution of a variety of strange hadron species from STAR Collaboration [142] at RHIC beam energy scan (BES) program are preliminary at the moment [143]. Therefore, we have not considered it for the analysis. Moreover, the corresponding y distributions have also not been reported yet. The analysis of the data above SPS energies is beyond the scope of this work.

Details of the data sets of heavy strange hadrons under investigation are summarised in Table 5.2. The lightest hadron in our chosen set is thus ϕ meson, having a mass of 1.02 GeV. Therefore contributions from hadronic resonance decays are expected to be small and hence ignored. The model fits are done by minimising the value χ^2/N_{dof}, where N_{dof} denotes the number of degrees of freedom that is the number of data points minus the number of fitting parameters. For the mass-dependent hierarchy study, we consider results from the previous subsection for simultaneous fits to only π^- and $K^{\pm}$ at SPS energies for the case of light hadrons. As mentioned earlier, the protons are not considered in the fits and it has been checked that this does not alter the main message of this work. At 158A GeV, data are also available for p_T-spectra of J/Ψ and Ψ' for which we perform a simultaneous fit as a separate set.

Similar to light hadrons study, the p_T and rapidity distributions of all the available heavy strange hadrons are fitted simultaneously by an iterative procedure using Eq. (5.3) at 20A, 30A, 40A, 80A and 158A GeV. The best fit results are shown in Fig. 5.9 and 5.10. Note that we refrain from fitting the Λ rapidity distributions at 80A and 158A GeV because of incomplete stopping at these energies and the fact that Λ carry a significant fraction of total net baryon number, its rapidity distributions are flat [115, 144]. The fit to the data is well described by the single η_{max}, $\langle\beta_T\rangle$ and T_{kin} values as can be observed from the $\chi^2/N_{\rm dof}$ values given in Table 5.4.

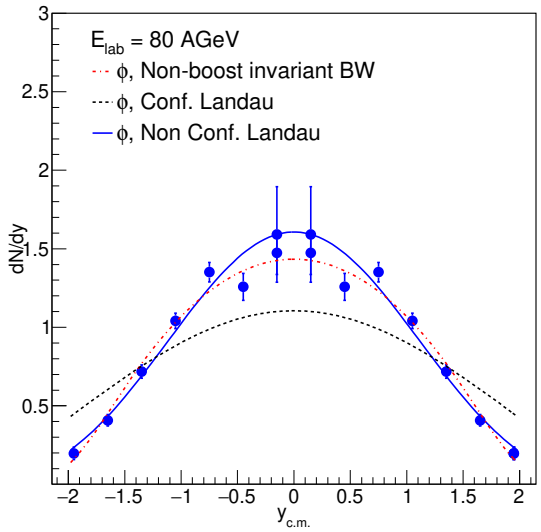

Figure 5.15. Rapidity density distributions of ϕ meson in 80A GeV central Pb+Pb collisions at SPS. Data are compared with predictions from different dynamical models namely, non boost-invariant blast-wave model (dot dashed line), conformal Landau (dotted line) and non-conformal (simple continuous line) Landau model. Statistical errors are shown as vertical bars.

In Fig. 5.11, we plot the extracted best fit parameters namely, average transverse velocity ($\langle\beta_T\rangle$) and kinetic freeze-out temperature (T_{kin}) and η_{max} as a function of the beam energy (E_{Lab}). All three quantities show an increasing trend as a function of beam energy (E_{Lab}). Moreover, at all collision energies, the extracted temperatures are larger than those for light hadrons. Also, the corresponding smaller $\langle\beta_T\rangle$ and η_{max} values indicate the heavy strange particles decouple from the fireball earlier in time compared to the light hadrons. Thus the kinetic freeze-out also seem to exhibit a hierarchical structure, with more massive particles leaving the medium earlier in time.

As mentioned earlier, in Ref. [132], the m_T spectra of J/ψ, ψ' and Ω produced in 158A GeV central Pb+Pb collisions were analyzed within boost-invariant blast-wave dynamics. Based on the hypothesis that these heavy hadrons are produced via statistical coalescence and undergo freeze-out during hadronisation, due to their small rescattering cross-sections in hadronic phase, an average transverse collective flow velocity of $\langle\beta_T\rangle \simeq 0.2$ was extracted from a simultaneous fit to the spectra, restricting $T_{kin} = 170$ MeV, from analysis of

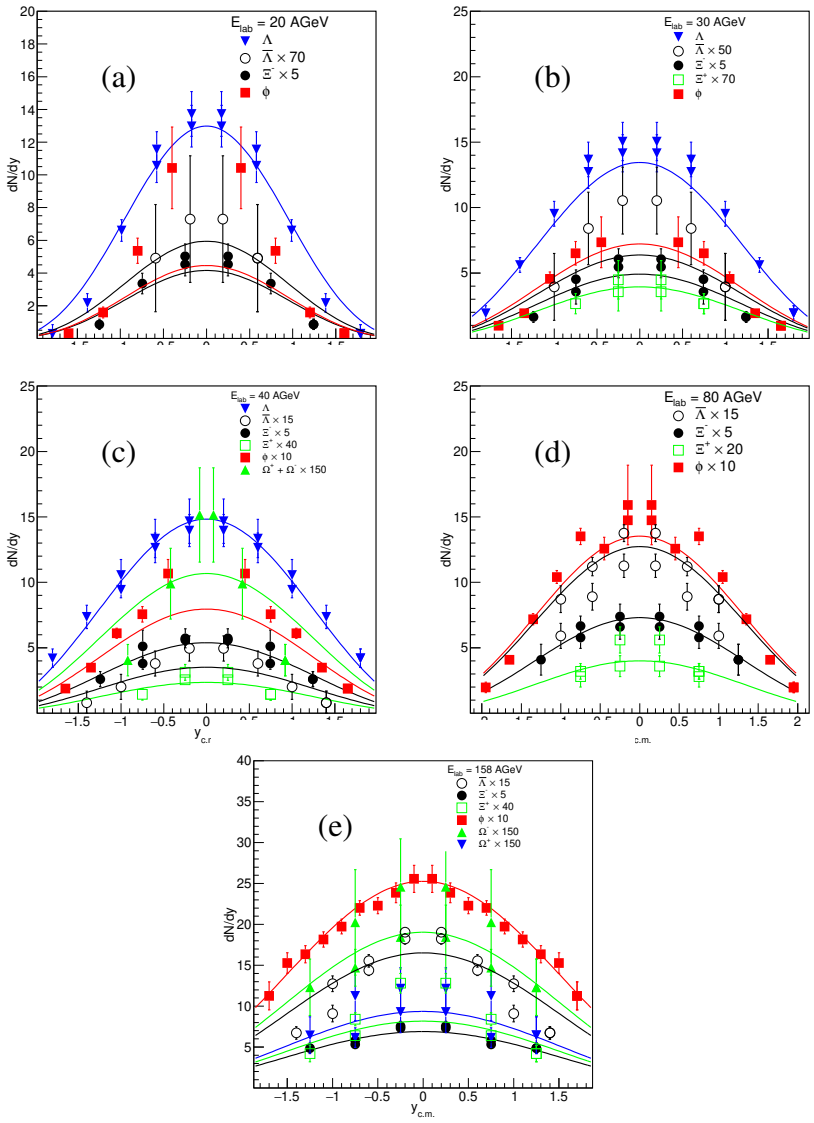

Figure 5.16. Fitted rapidity distribution of Λ, $\bar{\Lambda}$, ϕ, $\Xi^{\pm}$ and $\Omega^{\pm}$ using non-conformal Landau distribution in central Pb+Pb collisions from SPS at (a) 20A GeV, (b) 30A GeV, (c) 40A GeV, (d) 80A GeV and (e) 158A GeV beam energies. Error bars indicate available statistical error.

hadron multiplicities.

For us it would be worth analysing the available transverse distribution of charmonia in 158*A* GeV Pb+Pb collisions, measured by NA50 Collaboration [145], within the present model framework. Instead of fixing T_{kin}, we keep it free with other two parameters. Simultaneous fitting of J/ψ and ψ' [146] p_T distributions in rapidity range ($0 \leqslant y_{c.m.} \leqslant 1$) shown in Fig. 5.12, gives the following values of the parameters: $T_{kin} = 164$ MeV, $\eta_{max} = 1.70$ and $\langle \beta_T \rangle \approx 0.2$,

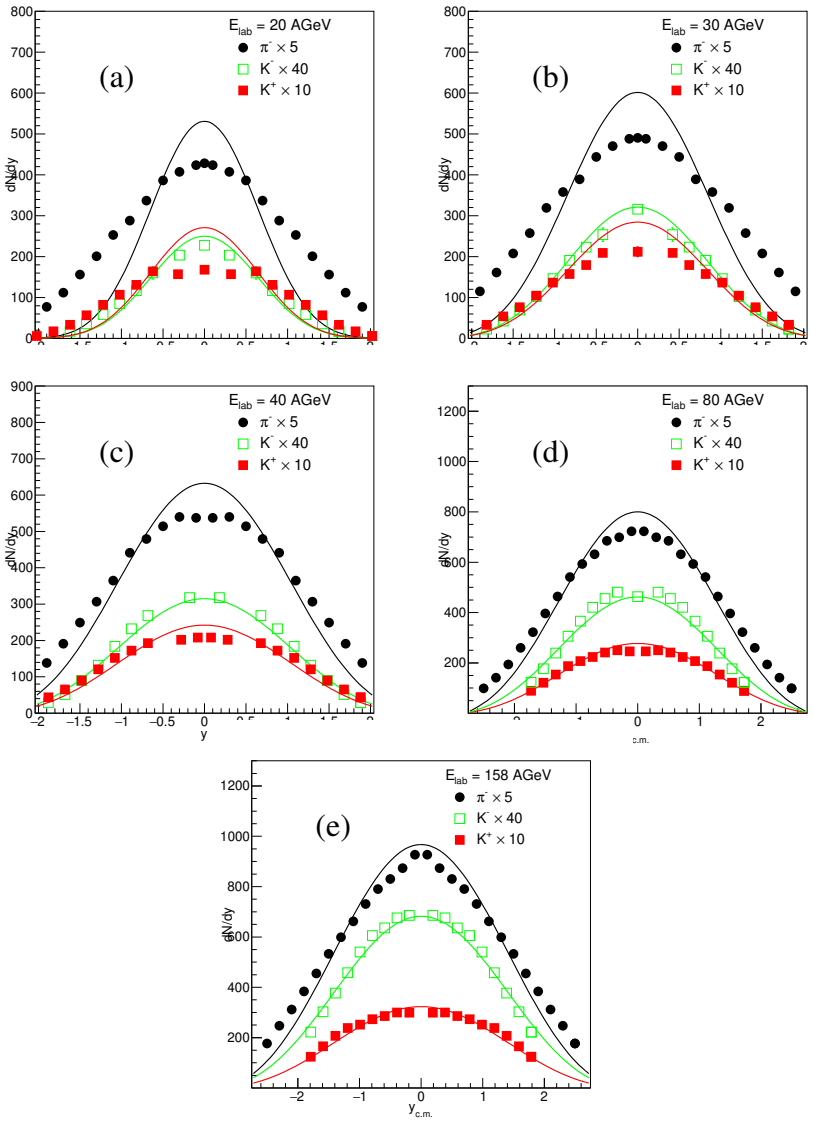

Figure 5.17. Fitted rapidity distribution of π^- and $K^{\pm}$ using non-conformal Landau distribution in central Pb+Pb collisions from SPS at (a) 20A GeV, (b) 30A GeV, (c) 40A GeV, (d) 80A GeV and (e) 158A GeV beam energies. Error bars indicate available statistical error.

indicating the emission of these heavy resonances from the fireball much earlier in time. In absence of the rapidity spectra, the precision of the η_{max} value for charmonia, extracted from p_T spectra might be questionable. To decide the associated uncertainty in η_{max}, we adopt the following strategy. The value of η_{max} is varied around the obtained value while keeping the other two parameters fixed to their respective best fit values, in such a way that the resulting $\chi^2/N_{\rm dof}$ increases in magnitude by unity from it's minimum value. The cor-

responding variation in η_{max} is assigned as the error on the parameter. The NA60 Collaboration [147] has measured J/ψ production in 158A GeV In+In collisions. However, the corresponding transverse distributions have not been published yet. Note that we exclude Ω baryon, as it is a member of our heavy strange set at 80A and 158A GeV and much lighter than the charmonium family.

In Fig. 5.13, we show the freeze-out points extracted from the measured transverse spectra of hidden charm, heavy strange and light hadrons at 158A GeV, defining the path of the expanding system in the T_{kin}-$\langle\beta_T\rangle$ plane (left panel), T_{kin}-η_{max} plane (center panel) and $\langle\beta_T\rangle$-η_{max} plane (right panel). Results show a monotonous behaviour which supports a clear existence of a mass-dependent hierarchy in thermal freeze-out of hadrons. This hierarchy of kinetic freeze-out is expected as the medium induced momentum change of heavy hadrons would be smaller compared to lighter hadrons. Hence, as the temperature of the fireball decreases, one would expect an earlier kinetic decoupling of heavy hadrons. Therefore, with a systematic investigation of the freeze-out parameters of different hadron species, one can in principle trace (partially) the expansion history of the fireball produced in nuclear collisions. Till date, no charm data are available in heavy-ion collisions below top SPS energy. The upcoming NA60+ experiment at SPS [148], aims at the measurement of charmonia in $20A - 158A$ GeV Pb+Pb collisions. Data once available at lower energies will enable to concretely establish this mass-dependent hierarchy in thermal freeze-out.

Before we move forward, it might be interesting to note that the possible existence of hierarchy in the kinetic freeze-out parameters of the produced particles has been studied earlier at RHIC and LHC energies. In Ref. [149], the authors have analysed the p_T spectra of the identified hadrons in $\sqrt{s_{NN}} = 2.76$ TeV Pb+Pb collisions, using a so-called longitudinal boost-invariant single freeze-out model, which describe both the particle spectra and particle ratios with a single value of the temperature. Their results indicated a flavour dependent kinetic freeze-out scenario, with strange hadrons leaving the fireball earlier in time than the non-strange hadrons. In Refs. [150–152], the authors have also analysed the p_T spectra of different particle species measured at mid-rapidity in p+p and

A+A collisions at various collision energies at RHIC and LHC, using different variants of Tsallis distribution. The freeze-out temperature is found to increase with the increase in particle mass, exhibiting an evidence of mass-dependent multiple kinetic freeze-out scenario. In fact, the dependence of the inverse slope parameter of the p_T spectra (effective temperature) of the identified hadrons emitted in central heavy-ion collisions at 158 A GeV Pb+Pb collisions at SPS and $\sqrt{s_{NN}} = 200$ GeV Au+Au collisions at RHIC were first reported in so the so-called "Nu-Xu" [153] plot, representing the freeze-out systematics for a set of hadronic species.

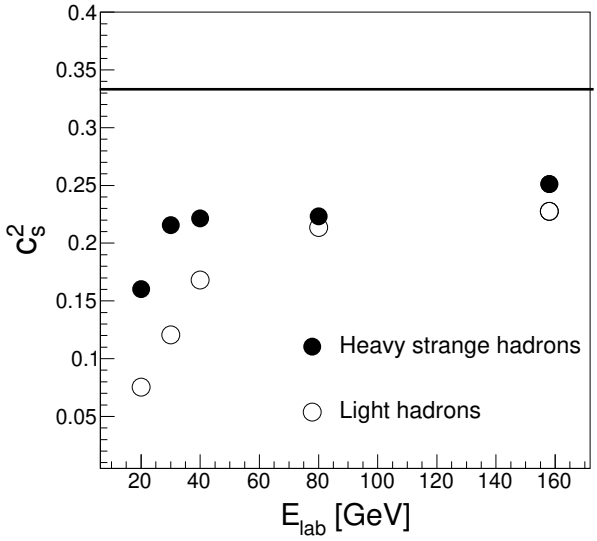

Figure 5.18. Variation of the speed of sound for heavy strange and light hadrons using non-conformal landau distribution with beam energy. Horizontal line at $c_s^2 = 1/3$ indicates the ideal gas limit. Errors are within the marker size.

We also investigate the effect of longitudinal flow on the observed rapidity distribution of the light hadrons and heavy strange hadrons. In the case of light hadrons, we have seen that isotropic emission from the static thermal model cannot describe the measured rapidity distribution of light hadrons at all beam energies. Collective expansion in the longitudinal direction is essential to reproduce the data. Similarly, an illustrative comparison to understand how the longitudinal motion influences the rapidity distribution of the heavy strange hadrons is presented in Fig. 5.14. The rapidity distribution of ϕ mesons mea-

sured in 80A GeV central Pb+Pb collisions is contrasted with that from a static thermal model as well as from the present blast-wave model calculations. The rapidity distribution as obtained from a static isotropic thermal source falls much faster than the data, a feature that is common for all heavy strange hadrons and at all investigated energies.

Furthermore, it might be useful to take a deeper look at the longitudinal dynamics particularly so due to the absence of boost-invariance at low energy collisions. Hence moving forward, the longitudinal properties of the medium are further explored by fitting rapidity spectra of light hadrons and heavy strange hadrons at beam energies 20A, 30A, 40A, 80A and 158A GeV using a different prescription, available in the literature.

The rapidity distribution as predicted by the recently developed non-conformal solution of the Landau hydrodynamics is given by [154],

$$\frac{dN}{dy} \sim \exp\left[\frac{1-c_s^2}{2c_s^2}\sqrt{{y'_b}^2 - y^2}\right], \tag{5.9}$$

where, c_s^2 is the squared sound velocity in the medium, $y'_b \equiv \frac{1}{2}\ln[(1+c_s^2)/(4c_s^2)] + y_b$, with $y_b = \ln[\sqrt{s_{NN}}/m_p]$ being the beam rapidity and m_p the proton mass. The conformal solution of Landau hydrodynamics can be restored by putting $c_s^2 = 1/3$ [155]. In Fig. 5.15, we compare the available data with predictions from different dynamical models. We find that the rapidity spectra from conformal solution falls off too slowly and does not give good agreement with the data. On the other hand, both blast-wave as well as the non-conformal solution of Landau hydrodynamics explains the data really well.

This motivates us to perform simultaneous fits to the available rapidity spectra using the non-conformal Landau distribution given in Eq. (5.9). We obtain reasonably good fits, as shown in Fig. 5.16, with good $\chi^2/N_{\rm dof}$ and the extracted values of c_s^2 are shown in Table 5.5. Here, c_s^2 is a common parameter for all species and only the overall normalisation constant is allowed to be different. In practice, the sound velocity, c_s, depends on temperature and thus varies during the evolution of the expanding medium formed in heavy-ion collisions. However the analytical expression obtained in Ref. [154] assumes

constant value of c_s^2 and therefore our extracted c_s^2 correspond to an effective mean value. Eq. (5.9) is also used to fit the rapidity spectra of light hadrons at SPS energies as shown in Fig. 5.17. However, the model does not seem to work well for light hadrons as evident from the rather poor fit quality and associated huge values of $\chi^2/N_{\rm dof}$. Resultant values of the c_s^2 are illustrated in Table 5.5 and plotted in Fig. 5.18 as a function of beam energy. We observe that c_s^2 increases monotonically as a function of beam energy for both cases implying that c_s^2 increases with temperature as the average temperature of the fireball increases with an increase in beam energy.

In Fig. 5.18, we observe that c_s^2 increases monotonically as a function of beam energy for both light and heavy strange hadrons. This may be attributed to the fact that the average temperature of the fireball increases with beam energy which is reflected as the effective temperature dependence of extracted c_s^2 [156]. This effect can also be observed in the relative hierarchy in the values of c_s^2 for light and heavy strange hadrons. Since heavy strange hadrons freeze-out at higher temperature, the average temperature experienced by them is larger compared to the light hadrons for same beam energy. This is in accordance with the fitted value of c_s^2 which is consistently larger for heavy strange hadrons as shown in Fig. 5.18. Moreover, this result is also in line with the expectation from Fig. 5.13 which support a clear existence of a mass dependent hierarchy in thermal freeze-out of hadrons. This is the reason we compare the c_s^2 values for light and heavy hadrons in Fig. 5.18, even though the quality of simultaneous fit for light hadrons is not very good.

One may note that within the blast-wave framework, the macroscopic thermodynamic parameters are directly extracted by fitting the certain phase-space density distribution of experimentally measured hadrons. Recently the kinetic freeze-out stage has been explored in central Au+Au collisions at energies ranging from $\sqrt{s_{NN}} = 2.4$ GeV to $\sqrt{s_{NN}} = 200$ GeV, using the microscopic UrQMD model and the corresponding macroscopic parameters are calculated via coarse-graining approach [157]. Results indicate the kinetic freeze-out as a continuous process, leading to a distribution of the freeze-out parameters at different collision energies. The corresponding average kinetic freeze-out tem-

peratures at different beam energies are higher than those obtained by us for light/bulk hadrons.

Chapter 6

Anisotropic flow of the charged hadrons

In this chapter, the equation of state (EoS) dependence of the anisotropic flow parameters (v_1, v_2 and v_4) of charged and identified hadrons, as a function of transverse momentum (p_T), rapidity ($y_{c.m.}$) and the incident beam energy (E_{Lab}) in mid-central Au + Au collisions in the energy range $E_{Lab} = 6 - 25$ A GeV is examined. Simulations are carried out by employing different variants of the Ultra-relativistic Quantum Molecular Dynamics (UrQMD) model, namely the pure transport (cascade) mode and the hybrid mode. The results would be useful as predictions for the upcoming low energy experiments at Facility for Antiproton and Ion Research (FAIR) and Nuclotron-based Ion Collider fAcility (NICA).

6.1 Introduction

The azimuthal anisotropy of the final-state hadrons produced in the heavy-ion collisions has long been considered as a deterministic probe to investigate collective effects in multi-particle production [158–160]. As per traditional wisdom, at relatively higher energies, the collective transverse flow in nuclear collisions is driven by the pressure gradients in the early thermalized stages of the reaction and hence encodes the information about the underlying QCD equation of state (EoS). For non-central nucleus-nucleus collisions, the asymmetry of the momentum distributions of hadrons are quantified in terms of coefficients

of Fourier expansion of the azimuthal distribution of the emitted particles as

$$v_n = < \cos[n(\phi - \psi_r^n)] >$$

where ϕ and ψ_r^n denote the azimuthal angle of the particle and reaction plane angle respectively. The first Fourier coefficient of the above azimuthal distribution is called directed flow v_1, whereas the second Fourier coefficient v_2 is known as elliptic flow and is dominant among all the coefficients at midrapidity. Similarly, the v_4 is the fourth Fourier coefficient of the azimuthal anisotropy.

Directed flow (v_1) is sensitive to the longitudinal dynamics of the produced medium. v_1 can be very useful to probe the early stages of the collision because it is expected to be built even earlier than elliptic flow [161–163]. In the vicinity of a first-order phase transition directed flow of hadrons is believed to drop and even vanish due to softening of the underlying EoS, making v_1 an interesting observable to be studied at RHIC-BES, NICA and FAIR. The directed flow which is observed at AGS energies [164–166] and below show linearity as a function of the rapidity with the slope quantifying the strength of the signal. Above SPS energies [167–169], the slope of directed flow in the mid-rapidity region is different compared to the slope in the beam rapidity region which makes the structure of $v_1(y)$ more complex.

On the other hand, the elliptic flow (v_2) of identified hadrons directly reflects the rescattering among the produced particles and hence has been studied intensively to look for thermalization of the produced medium in different experiments [158, 170] at various energies. For non-central collisions, the azimuthal anisotropy of the transverse momentum (p_T) distribution is believed to be sensitive to the early evolution of the fireball. A bulk of previous studies have been devoted to investigate the elliptic flow in low energy collisions relevant for FAIR [171, 172] and RHIC BES [173] program using transport models like UrQMD [65, 66] and AMPT [175, 176].

Apart from v_1 and v_2, there is another harmonic of the azimuthal distribution which needs due attention is v_4. The energy dependence of v_4 is sensitive to the nuclear equations of state (EoS). Calculations based on [177–179] indi-

cates that, the v_2 has influence on the generation of v_4. According to recent hydrodynamical predictions [177], v_4 encodes an important information on the underlying collision dynamics. Recently [180], the beam energy dependence of v_4 was studied using microscopic transport model JAM [162].

In this chapter, we have studied directed flow (v_1) as a function of rapidity, beam energy (E_{Lab}), elliptic flow (v_2) with respect to transverse momentum, rapidity and incident beam energy (E_{Lab}) and also, 4^{th} order Fourier coefficient (v_4) as a function of beam energy (E_{Lab}) for charged and identified hadrons, in the range $E_{Lab} = 6 - 25$ A GeV, relevant for FAIR [181]. However, we refrain from the investigation of triangular flow (v_3) that originates from initial state fluctuations and is not believed to bear any sensitivity to the underlying EoS. The publicly available version 3.4 of the UrQMD model is employed for this purpose. Within UrQMD model, the impact parameter vector is aligned along the X-axis, and the reaction plane angle (ψ_r^n) is zero. Our calculations are performed with different variants of the code, namely the pure transport (cascade) mode and hybrid mode. In the hybrid mode, two different nuclear equation of states (EoS) viz. Hadron Gas (HG) and Chiral EoS are used separately, in the intermediate hydrodynamic stage, to replicate the effects of hadronic and partonic scenarios, respectively. It is important to note that the UrQMD model has been widely used earlier to the flow coefficients in low energy nuclear collisions. The rapidity and transverse momentum dependence of v_1 and v_2 in Pb+Pb reactions at 40A and 160A GeV beam energies were calculated in [182] using UrQMD model in cascade mode (v2.2) and contrasted with the data available from NA49 experiment, for three different centrality bins. In addition the energy excitation functions of v_1 and v_2 are estimated in the energy range of $E_{Lab} = 90$A MeV to $E_{cm} = 200$A GeV and contrasted with the available data. The hybrid UrQMD approach with HG EoS has also been employed earlier [183] to calculate the beam energy dependence of v_2 for heavy-ion reactions from GSI-SIS to the highest CERN-SPS energies. With Chiral EoS, the hybrid UrQMD model has been used to study the collision energy dependence of elliptic flow v_2 and triangular flow v_3 parameters in Au+Au collisions in the energy range $\sqrt{s_{NN}} = 5 - 200$ GeV [173]. The hybrid model has also been applied examine

the collision energy dependence of v_1 for heavy-ion collisions over the range $\sqrt{s_{NN}} = 3 - 20$ GeV [184]. In this chapter, we have performed a systematic study of the different flow parameters v_1, v_2 and v_4, with the hope to access the impact of the EoS of the strongly-interacting matter on these observables.

The basic features of the different variants of the UrQMD model are briefly discussed are below.

6.2 UrQMD Model

The Ultra-relativistic Quantum Molecular Dynamics (UrQMD) model is an event generator designed to simulate high energy nucleus-nucleus collisions. The target and projectile nuclei are initialized according to the Woods-Saxon profile in the coordinate space, and the Fermi gas model in the momentum space. The initial momentum for each nucleon in the rest frame of the corresponding nucleus is thus assigned randomly between zero and local Thomas-Fermi momentum. The interaction is described via multiple interactions of the incident and newly produced hadrons, the formation and decay of hadronic resonances and the excitation and formation of color strings [66]. UrQMD employs longitudinal excitation of the strings stretched uniformly between quark, diquark and their anti states, which subsequently break into hadrons following Lund string fragmentation models [174]. The model incorporates available experimental information like hadronic cross-sections, resonance decay widths and decay modes. Propagation of particles between subsequent collisions occurs in straight-line trajectories with their velocities (p/E, with p is the momentum and E is the energy).

Pure hadronic transport models have been found to underestimate the large v_2 values measured above 40 AGeV beam energy up to RHIC energy $\sqrt{s_{NN}}$ = 200 GeV [182, 185]. The failure is attributed to the too low-pressure gradients in the early phase of the collisions to generate enough collectivity. With an aim to capture the entire evolution dynamics of the fireball, the so-called hybrid UrQMD model has been developed where the pure transport approach is

embedded with a 3−D ideal relativistic one fluid evolution for the intermediate hot and dense stage of the reaction. Within this integrated approach, the initial conditions and the final hadronic freeze-out are calculated from UrQMD on an event-by-event basis, for proper incorporation of the non-equilibrium dynamics. The hydrodynamical evolution is switched on when the two Lorentz-contracted nuclei have crossed each other [186]. Here the participants are mapped to the hydrodynamic grid, and spectators continue to propagate in the cascade. The primary collisions and fragmentations of strings in the microscopic UrQMD model generate the event wise initial conditions and thus incorporate the event-by-event fluctuations.

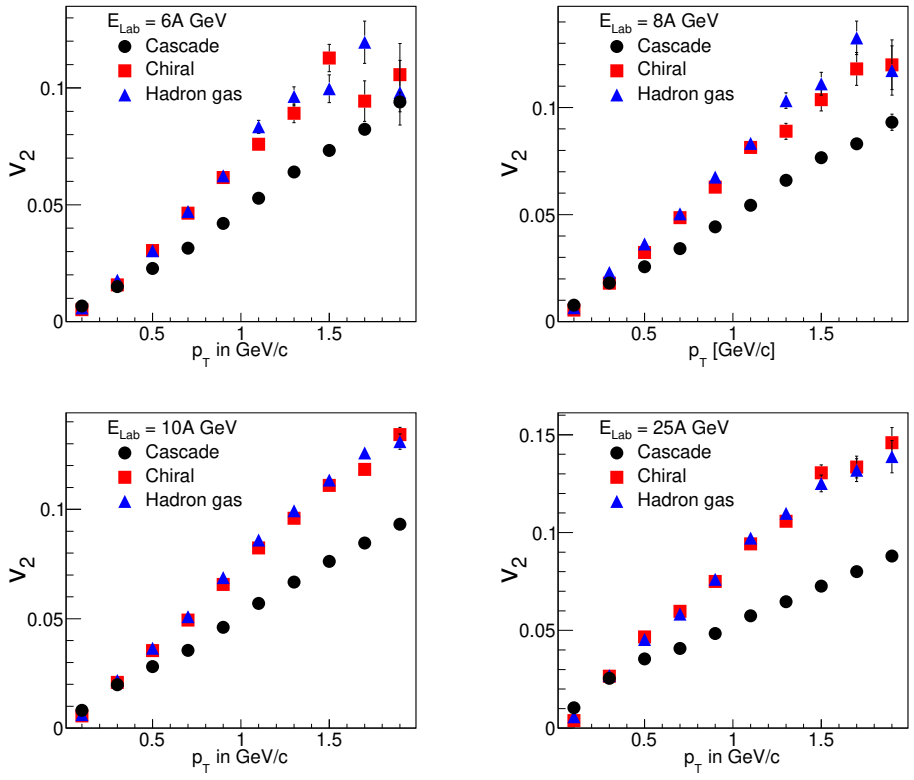

Figure 6.1. v_2 vs p_T for charged hadrons using UrQMD for different EoS for 6A, 8A, 10A [190] and 25A GeV

Even though hydrodynamics was found very successful to describe the high v_2 values measured at RHIC at $\sqrt{s_{NN}} = 130$ and 200 GeV [187, 188], it's application in low energy nuclear collisions below 25A GeV might demand some justification. Pure transport models aim at the description of heavy-ion reactions on the basis of an effective solution of the relativistic Boltzmann equa-

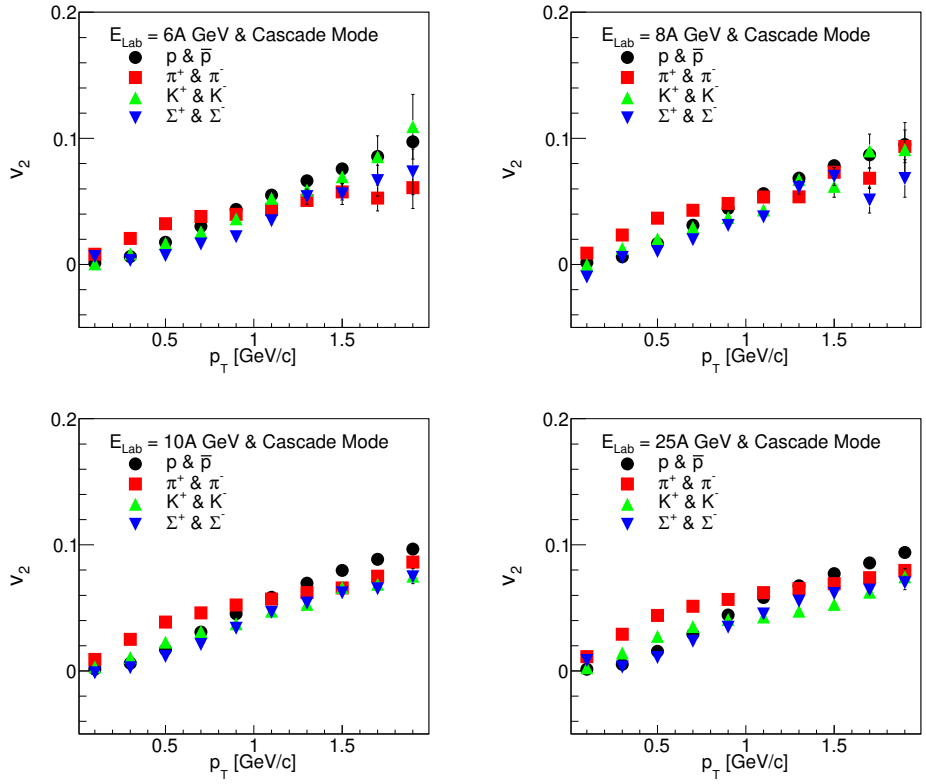

Figure 6.2. v_2 vs p_{T} of identified hadrons (p, $\bar{\mathrm{p}}$, $\pi^{\pm}$, $\mathrm{K}^{\pm}$ and $\Sigma^{\pm}$) using UrQMD in cascade mode for 6A, 8A, 10A and 25A GeV

tion. In most transport approaches, the collision kernel is usually restricted to the level of binary collisions and $2 \rightarrow n$ scattering processes to keep the calculation numerically tractable. In the restriction to binary collisions, mean free paths of the particles are assumed to be large, which becomes questionable in the hot and very dense stage of heavy-ion collisions. At FAIR energies, a dense baryonic medium is anticipated, where many-body collisions might not be negligible. At finite baryon chemical potential, the heated and compressed nuclear matter might also undergo a phase transition, signatures of which might be imprinted in the flow observables. Within a purely microscopic approach, it is difficult to account for the hadronization and the phase transition between the hadronic and the partonic phase. Within the hydrodynamical approach, in contrast, one can explicitly incorporate phase transitions by changing the EoS. Hydrodynamics is thus accepted as an effective tool to describe the collective expansion of the intermediate hot and dense stage of the heavy-ion collisions. However, application of hydrodynamics demands local thermalization and the results depend

strongly on the initial and final boundary conditions. Hence a more realistic picture of the whole dynamics of heavy-ion reactions can be achieved by so-called microscopic plus macroscopic (micro+macro) hybrid models. Such an approach allows to reduce the parameters for the initial conditions and provides a consistent freeze-out description and allows a direct comparison of the different collision dynamics - ideal fluid dynamics vs. non-equilibrium transport scenario.

In the hybrid model, the hydrodynamic evolution is stopped if the energy density ε drops below the five times the ground state energy density ε_0 in all cells [186]. After the hydrodynamical evolution, the Cooper-Frye prescription [133] is employed to map the hydrodynamical fields to the hadrons, which evolve further via hadronic cascade through rescatterings and final state decays until all interactions cease and the system decouples. Within hybrid mode of UrQMD, different choices of the underlying EoS are available for the intermediate hydrodynamic phase. In the present work, we opt for two different EoS, namely the hadron gas (HG) EoS and the Chiral EoS to mimic the hadronic and partonic scenarios, respectively.

The Hadron gas EoS [189] consists of a grand canonical description of a free and non-interacting gas of hadrons. The underlying hadronic degrees of freedom involved in this EoS are all the reliably known baryons and mesons with masses up to 2 GeV and thus in line with the degrees of freedom included in the pure UrQMD model. Note that this EoS does not include any type of phase transition. It gives us the privilege of a direct comparison of the hydrodynamic scenario with the transport simulation.

Another EoS used in this work for the dynamical evolution of the produced medium is Chiral + deconfinement EoS which is taken from the hadronic SU(3) parity doublet model in which quark degrees of freedom are included [191]. It incorporates chiral as well as deconfinement phase transition. At vanishing baryon chemical potential, this EoS agrees with the lattice QCD results qualitatively. Particularly for this investigation, it is important to note that this EoS is conjectured to be applicable at non-zero baryon chemical potentials. For

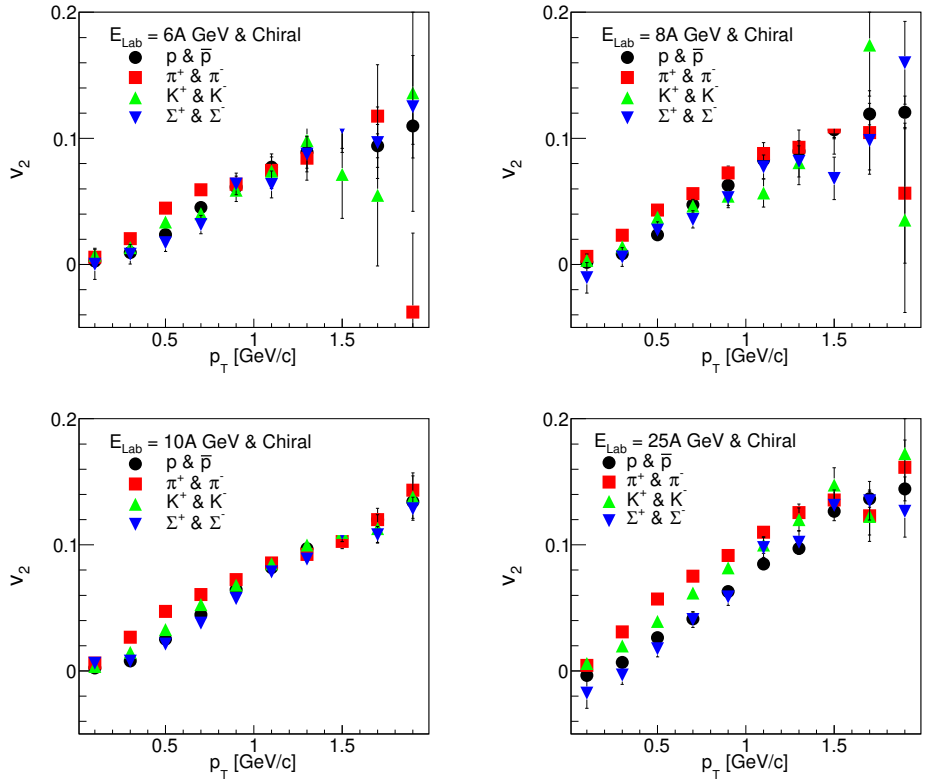

Figure 6.3. v_2 vs p_T of identified hadrons (p, $\bar{p}$, $\pi^{\pm}$, $K^{\pm}$ and $\Sigma^{\pm}$) using UrQMD in hydro mode using Chiral EoS for 6A, 8A, 10A and 25A GeV

all values of μ_B, this EoS describes the deconfinement transition as a continuous crossover. In this EoS, the deconfinement transition mainly governed by quarks and Polyakov potential and the chiral phase transition by hadronic interactions. Hadrons disappear only at higher temperatures, and quark degrees of freedom becomes dominant. For a more detailed explanation, the reader is referred to Ref [191].

The following section presents the results of our studies on the dependence of anisotropic flow parameters (v_1, v_2, v_4) on different kinematic variables over a range of bombarding energies.

6.3 Results and Discussion

In this section, we discuss the transverse momentum dependence of the elliptic flow, the rapidity dependence of directed flow and the elliptic flow of both the

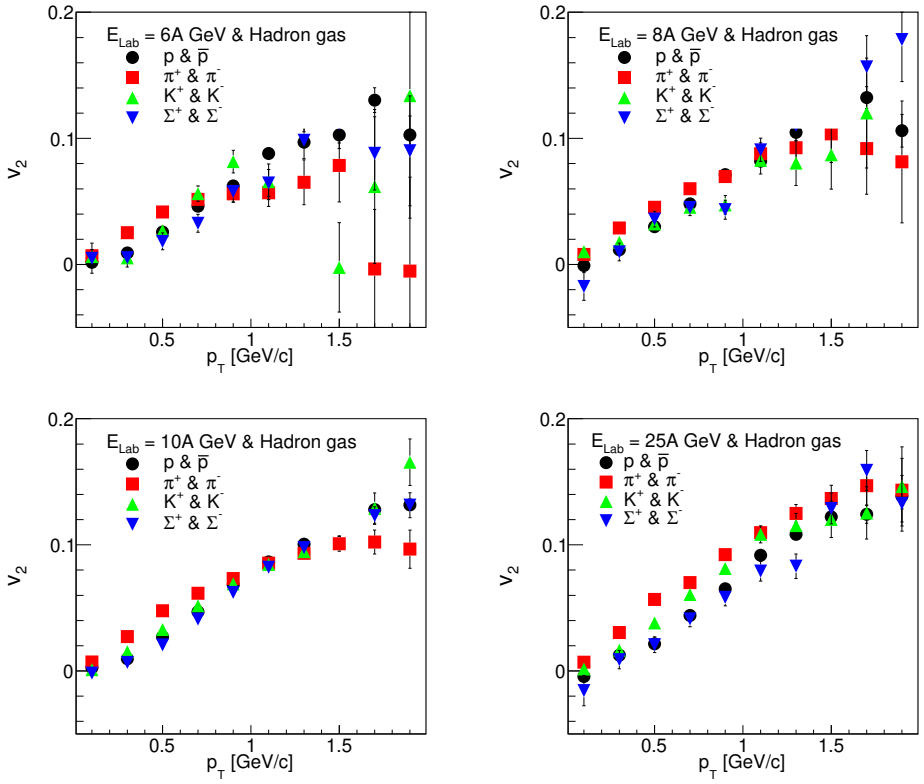

Figure 6.4. v_2 vs p_{T} of identified hadrons (p, $\bar{\mathrm{p}}$, $\pi^{\pm}$, $\mathrm{K}^{\pm}$ and $\Sigma^{\pm}$) using UrQMD in hydro mode using Hadron gas EoS for 6A, 8A, 10A and 25A GeV

identified and charged hadrons for mid-central ($b = 5-9$ fm) Au-Au collisions at bombarding energies 6A, 8A, 10A and 25A GeV. In the hybrid mode, calculations are performed for two different nuclear EoS, as mentioned before. We also compare proton v_1 with the measured data from the E895 Collaboration at the AGS [164], at 6A and 8A GeV beam energies. In addition the constituent quark number scaling of $v_2(p_T)$ is also studied. Finally, we look at the beam energy ($\mathrm{E_{Lab}}$) dependence of the slope of the directed flow ($\frac{dv_1}{dy}$), elliptic flow, v_4 and ratio $v_4/(v_2)^2$ in the midrapidity region (-0.75 $\leqslant y_{c.m.} \leqslant$ 0.75).

6.3.1 p_{T} dependence

Figure 6.1 shows the differential elliptic flow $v_2(p_T)$ of charged hadrons, at all four investigated energies. An approximate linear rise of elliptic flow v_2 with respect to p_{T} is observed for all the three cases under consideration. The magnitude of the v_2 depends on evolution dynamics of the produced medium, which

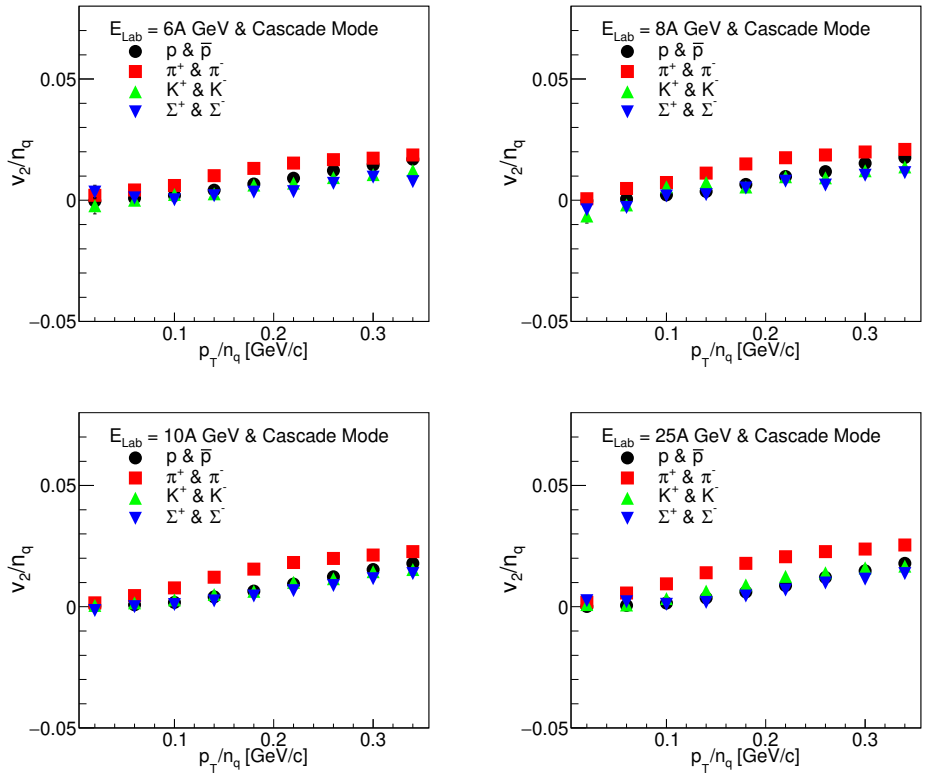

Figure 6.5. v_2/n_q vs p_T/n_q of identified hadrons (p, $\bar{p}$, $\pi^{\pm}$, $K^{\pm}$ and $\Sigma^{\pm}$) using UrQMD in cascade mode for 6A, 8A, 10A and 25A GeV

resulted in an enhancement of v_2 in case of hydrodynamic scenario compared to the pure transport scenario. From the obtained results we find that at very low p_T ($p_T < 0.5$ GeV/c), v_2 is indistinguishable in all the three different cases of evolution. This behaviour might indicate that most of the elliptic flow at such low transverse momentum is already built up during the initial scatterings in UrQMD, but by looking at the higher transverse momentum region, it can be seen that most of the elliptic flow is built up during the hydrodynamical evolution. However, the estimated v_2 does not seem to differentiate between the two EoS employed in the hydro mode over the whole p_T range under investigation. The enhancement in v_2 in hybrid mode compared to cascade mode can be attributed to the smaller mean free path in the previous case, generating larger pressure gradients due to the assumption of mean-field approximation in the former case. Similar v_2 values for two different EoS with and without explicit phase transition is due to the short duration of the hydrodynamic evolution at these low collision energies.

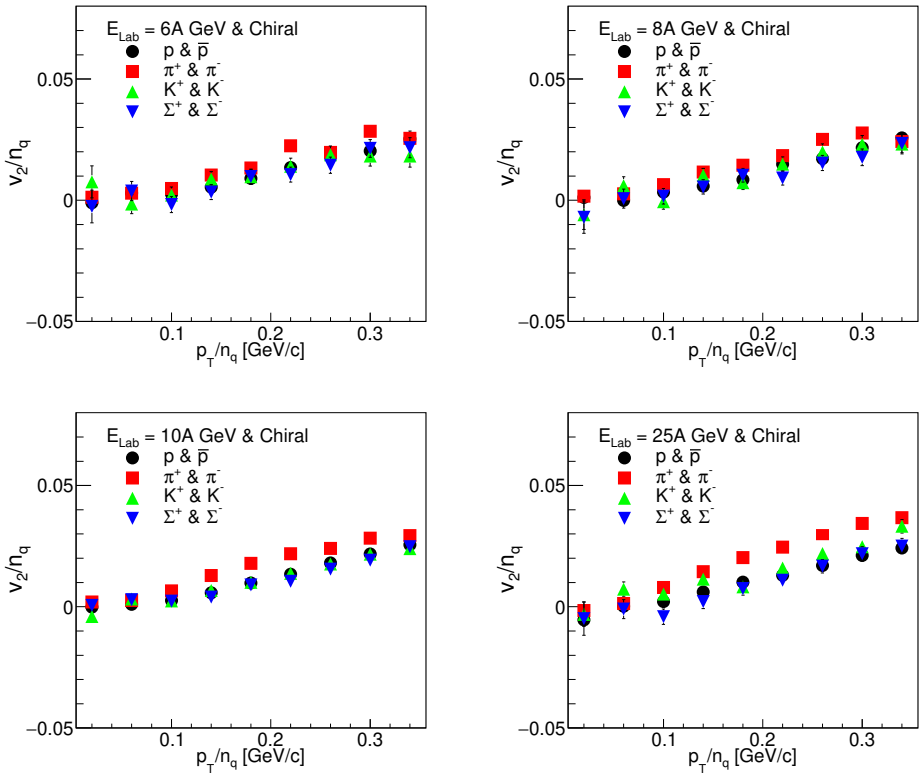

Figure 6.6. v_2/n_q vs p_T/n_q of identified hadrons (p, $\bar{p}$, $\pi^{\pm}$, $K^{\pm}$ and $\Sigma^{\pm}$) using UrQMD in hydro mode using Chiral EoS for 6A, 8A, 10A and 25A GeV

When we look at the v_2 of identified hadrons, in Figs. 6.2, 6.3 and 6.4, at low p_T ($p_T < 1$ GeV/c), mass ordering is observed in all the three cases and all the four energies, as expected from hydrodynamical calculations [192]. In the cascade mode, for all the energies under considerations, protons and pions show mass ordering up to $p_T < 1$ GeV/c and an inverse mass ordering for $p_T > 1$ GeV/c. Also in the hybrid mode with Hadron gas equation of state, mass ordering is visible up to $p_T < 1$ GeV/c and inverse mass ordering for $p_T > 1$ GeV/c is shown by mesons (pions and kaons). It should be noted that this mass ordering at low p_T and its violation at higher p_T is in agreement with the measurements at RHIC [193]. But in contrast, for the Chiral EoS which mimics a locally equilibrated partonic medium, no reverse ordering is not observed at $p_T > 1$ GeV/c.

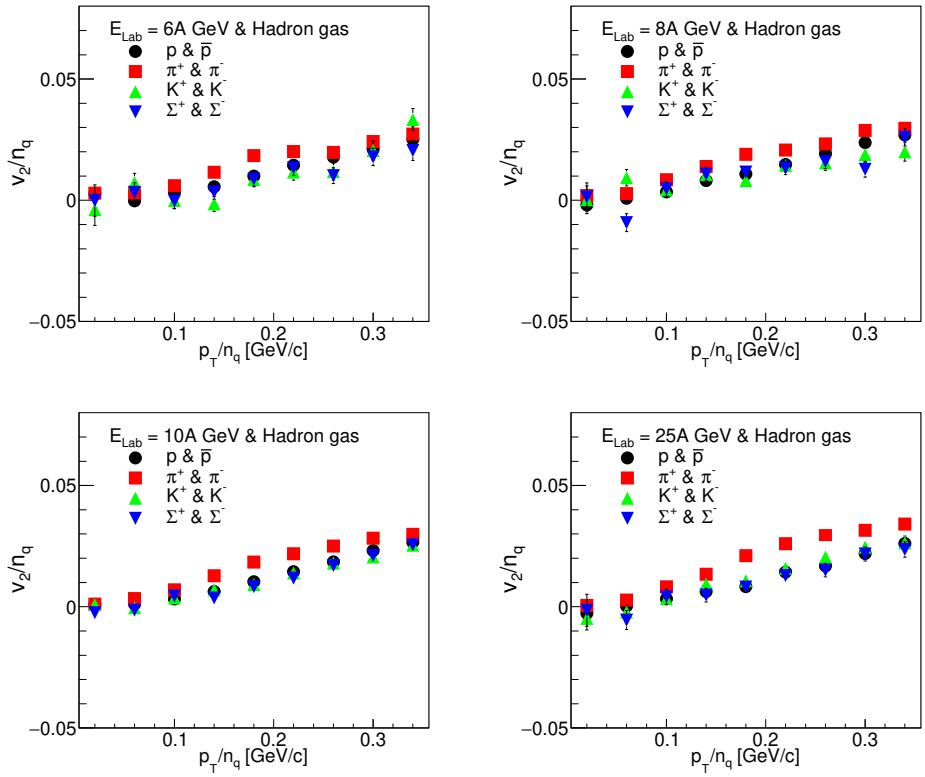

Figure 6.7. v_2/n_q vs p_{T}/n_q of identified hadrons (p, $\bar{\mathrm{p}}$, $\pi^{\pm}$, $\mathrm{K}^{\pm}$ and $\Sigma^{\pm}$) using UrQMD in hydro mode using Hadron gas EoS for 6A, 8A, 10A and 25A GeV

6.3.2 Constituent quark number scaling

The observation and mass ordering and its violation for $v_2(p_T)$ of identified hadrons naturally motivates one to investigate the effect of constituent quark number scaling (NCQ) of elliptic flow (v_2/n_q) as a function of the scaled transverse momentum (p_{T}/n_q) [194–196]. NCQ scaling is a natural outcome of the hadronization models based on coalescence and recombination of partons [197, 198] and indicates that the collectivity developed in the early stage of the collisions is of partonic origin.

Figs. 6.5, 6.6 and 6.7 show the variation of v_2/n_q with p_{T}/n_q for the three adopted versions of UrQMD model. From the figures, it is evident that v_2 shows reasonably good scaling with p_{T}/n_q at low p_{T} and the degree of scaling seems to be same for all three scenarios and all energies under consideration. The scaling becomes more prominent when observed in terms of transverse kinetic energy $KE_T(=m_T-m_0)$, a variable that takes care of relativistic effects. This indicates

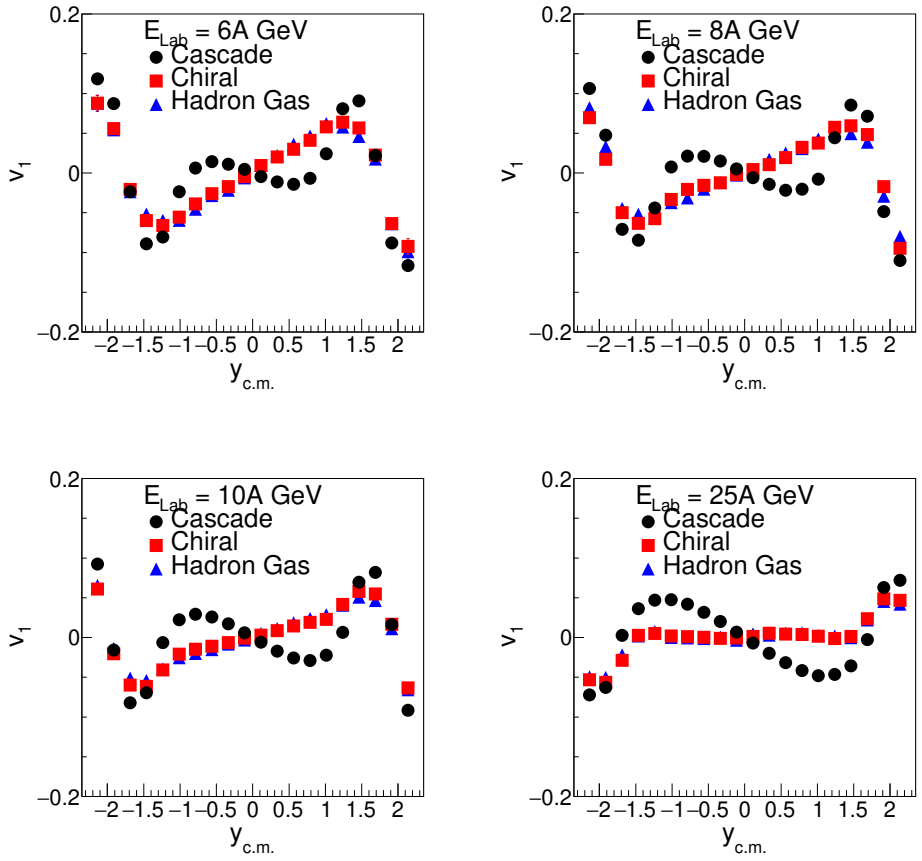

Figure 6.8. v_1 vs $y_{c.m.}$ for charged hadrons using UrQMD for different EoS for 6A, 8A, 10A and 25A GeV

that such scaling behaviour observed in terms of p_{T} (or KE_T) is insensitive to the onset of partonic collectivity, rather this is a natural outcome of the mass ordering in a boosted thermal model. This observation in line with previous calculations performed at FAIR SIS-300 energies [171].

6.3.3 Rapidity dependence

We now move on, to study the behaviour of v_1 and v_2 as a function of rapidity for different nuclear EoS. Because of its sensitivity to the longitudinal dynamics of the medium, v_1 is an interesting parameter to study as a function of the rapidity. The directed flow of charged hadrons as a function of the rapidity for different EoS and at different energies is shown in Figure 6.8. The slope of v_1 at mid-rapidity ($y_{c.m} \approx 0$) shows an interesting behaviour at different energies, which

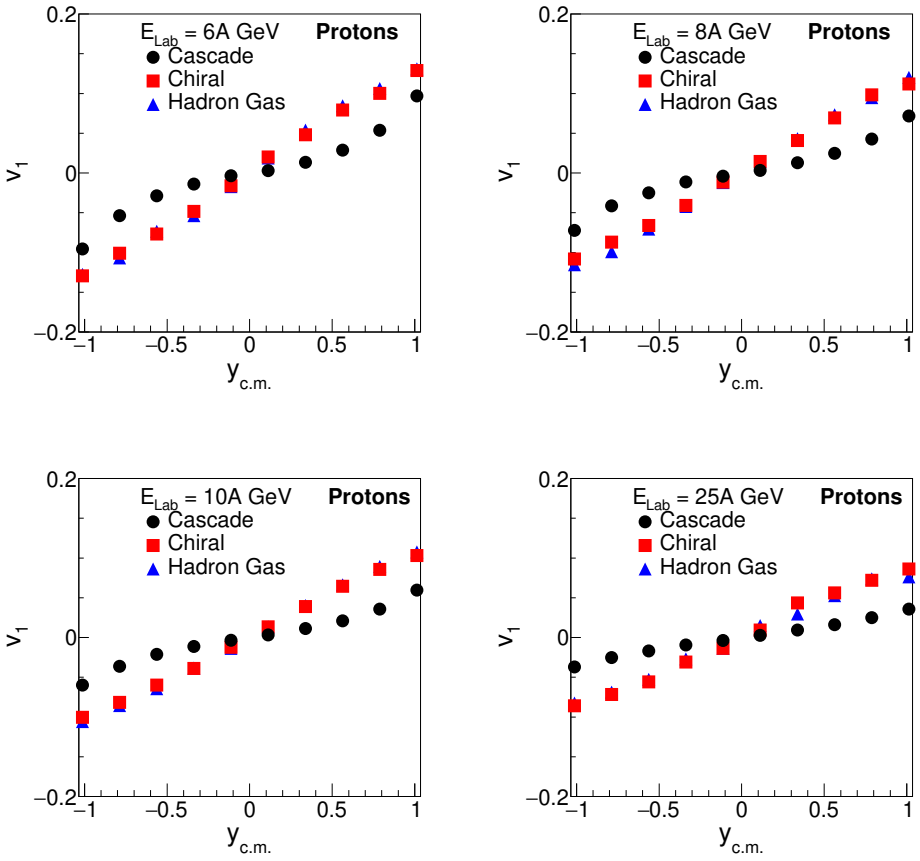

Figure 6.9. v_1 vs $y_{c.m.}$ for protons using UrQMD for different EoS for 6A, 8A, 10A and 25A GeV

is sensitive to the onset of the hydrodynamical expansion in comparison to the pure transport approach.

In the hybrid mode, the slope is positive (normal flow), and it decreases as energy goes up and almost flattens out at 25 AGeV. However, for pure transport mode, the slope is negative (anti-flow) around $y_{c.m} \approx 0$, and it is showing a decreasing trend as energy goes up. Since the directed flow is expected to develop at the early stages of the collision, Figure 6.8 suggests otherwise that early stage does not solely responsible for the determination of final directed flow of the charged hadrons and can have the contribution from the intermediate stages of evolution. In [199], the authors have claimed that the shape of $v_1(y_{c.m.})$ around mid-rapidity shows sensitivity to the space-momentum correlation along with the correlation between position of the nucleons and amount of stopping which further depends on the underlying equation of state and, in turn, affects the slope

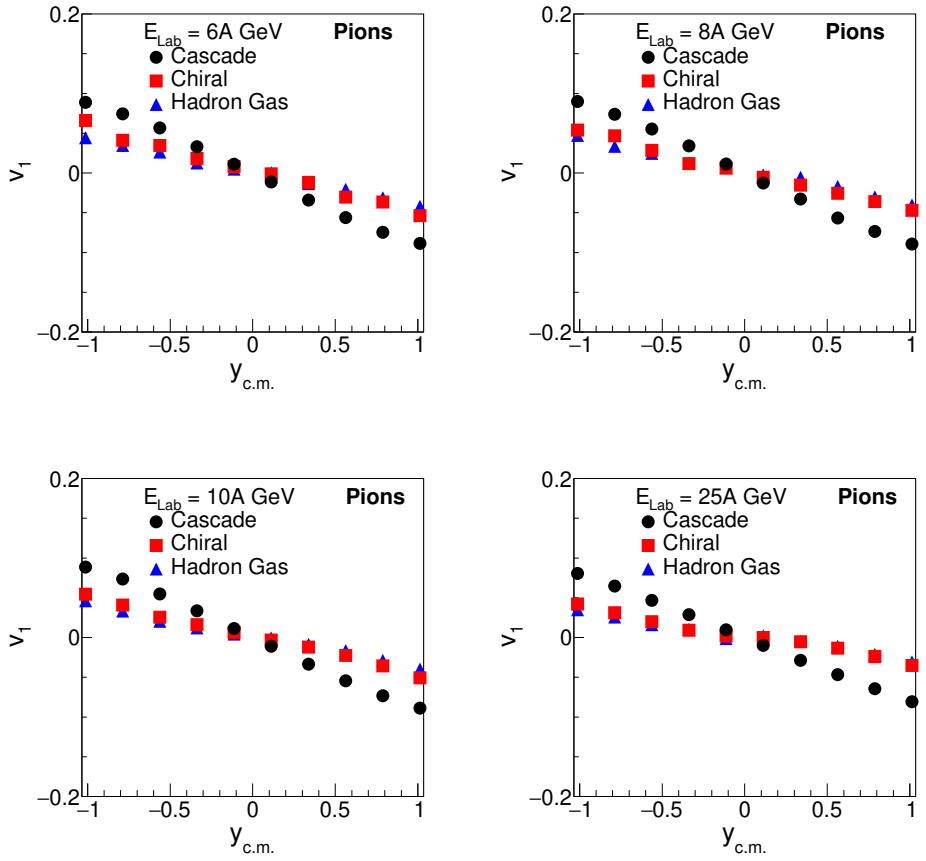

Figure 6.10. v_1 vs $y_{c.m.}$ for pions using UrQMD for different EoS for 6A, 8A, 10A and 25A GeV

around mid-rapidity.

Furthermore, to understand the species-dependent effect of directed flow for different EoS, we studied the directed flow of the protons (and anti-protons), pions ($\pi^{\pm}$) and kaons ($K^{\pm}$) as shown in Figs. 6.9, 6.10 and 6.11 respectively. The slope of the directed flow in case of protons is always positive, whereas the slope of the directed flow of pions is always negative for three cases of the EoS around mid-rapidity. It is higher in case of hybrid mode and smaller in case of the pure transport mode. For kaons, normal flow is observed in the case of hydro mode and anti-flow in case of pure transport mode. We have also studied the effect of the nuclear EoS on the directed flow of the individual charged hadrons, namely π^+, π^-, K^+, K^- as shown in Figs 6.13, 6.13, 6.14 and 6.15. In Figs. 6.14 and 6.15, it seems that K^+ and K^- are treated differently in the presence of hydrodynamic expansion which is visible by looking at the slope of $v_1(y)$ for K^+

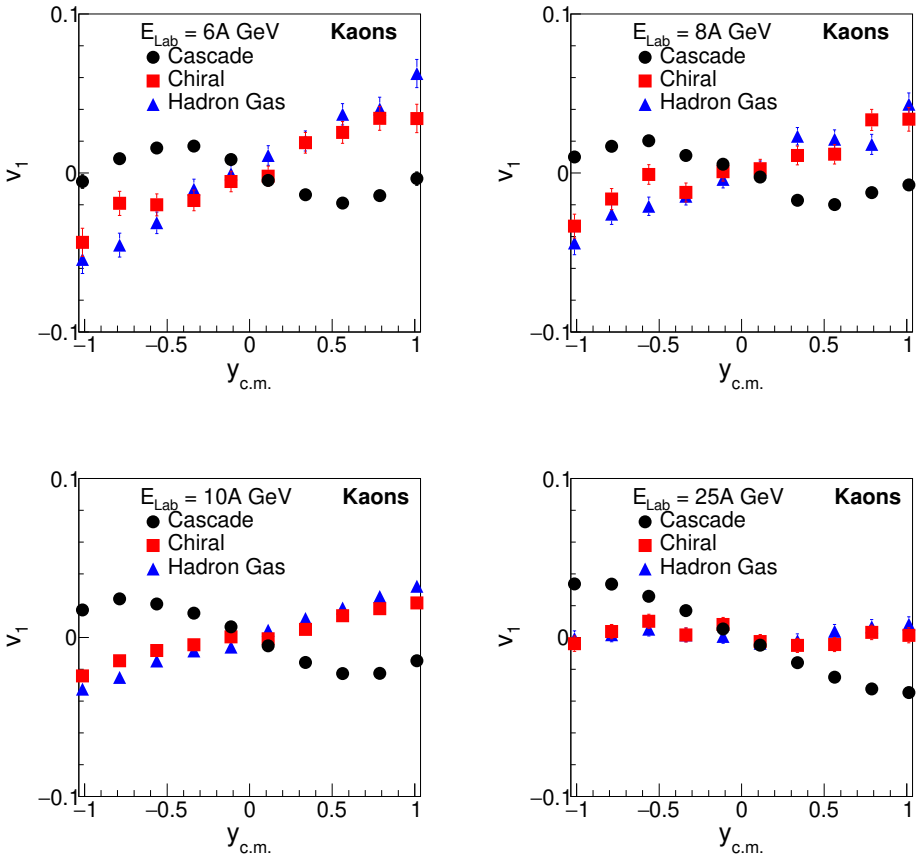

Figure 6.11. v_1 vs $y_{c.m.}$ for kaons using UrQMD for different EoS for 6A, 8A, 10A and 25A GeV

and K^- at mid-rapidity ($y_{c.m.} \approx 0$). v_1 for K^+ is similar to proton flow (normal flow) and K^- flow is anti-correlated (anti-flow) in hybrid mode. Our results are in disagreement with observations reported in [200, 201]. Experimentally, it is found that K^+ shows anti-flow and K^- shows normal flow as nucleons due to different potentials they experience while propagating through medium derived from the effective chiral models [202]. But on the other hand, such behaviour is in agreement with the UrQMD results published recently [203]. The authors have studied the influence of the inclusion of mean-field potentials on the directed flow of hadrons. This interesting feature of kaon flow in UrQMD definitely needs further investigation.

In Figure 6.16, we have compared the sideward flow ($\langle p_x \rangle$) of protons as a function of normalized rapidity (y') from E895 [164] at 6A and 8A GeV in mid-central ($b = 5 - 7$ fm) Au+Au collisions with the model results, in both cascade

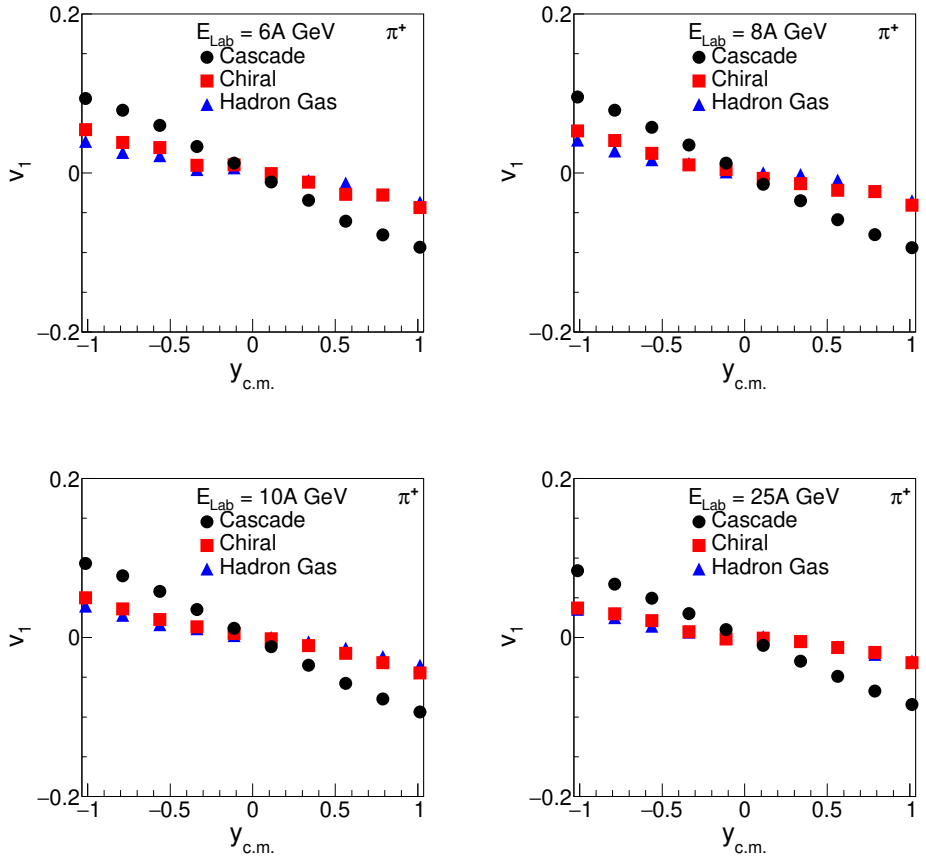

Figure 6.12. Rapidity dependence of directed flow $(v_1(y_{c.m.}))$ of positive pions (π^+) in mid-central Au+Au collisions at bombarding energies $E_b = 6A, 8A, 10A and 25A$ GeV

and hybrid mode. $y^{'}$ is normalized in a such a way that the rapidity of target and projectile become -1 and +1 respectively and is defined as, $y^{'} = y^{lab}/y^{mid}$ - 1. y^{lab} is the rapidity in laboratory frame and y^{mid} is mid-rapidity between target and projectile. From the figure, it is evident that both the EoS used in the hydrodynamic scenario, which are governed by mean-field approximation, reproduce the data quite well. The slopes of v_1 using both EoS are similar to the data. As shown in Figure 1 of [164], mean-field approximation came close to explain the data well compared to the cascade scenario with the former case allows generating additional pressure in the medium.

Elliptic flow is also studied as a function of rapidity, as shown in Fig 6.17. v_2 is highest at mid-rapidity and decreases for forward rapidities. Like mentioned above, here also elliptic flow is higher for the hydrodynamic scenario

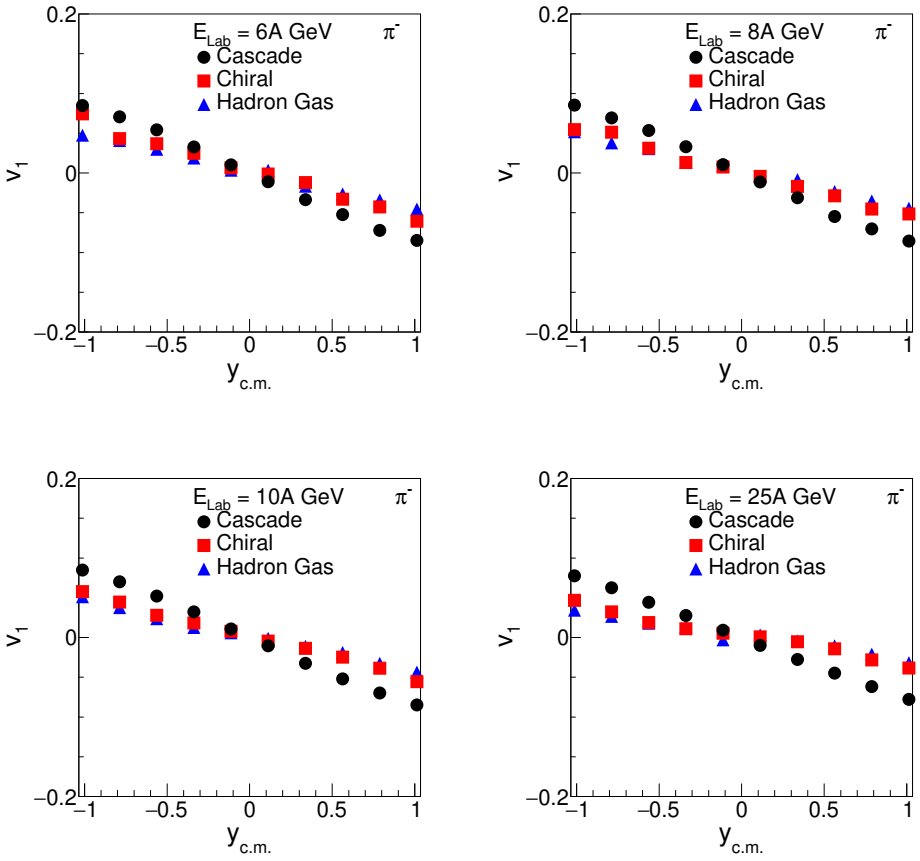

Figure 6.13. Rapidity dependence of directed flow $(v_1(y_{c.m.}))$ of negative pions (π^-) in mid-central Au+Au collisions at bombarding energies $E_b = 6A, 8A, 10A and 25A$ GeV

suggesting the generation of magnified pressure gradients in the medium.

Before we move forward, it should be noted that flow of protons at energies as low as 6 and 8 A GeV may be sensitive to the light nuclei production. However, this feature is not included in either (cascade or hybrid) public versions of the UrQMD model, which we use for simulations.

6.3.4 Energy dependence

Finally, we investigate the beam energy (E_{Lab}) dependence of the anisotropic flow parameters v_1, v_2, v_4 and $v_4/(v_2)^2$. In Figure 6.18, beam energy (E_{Lab}) dependence of integrated v_2 is shown at mid-rapidity for all three versions of the model. As expected, v_2 increases with increase in energy. In the hybrid

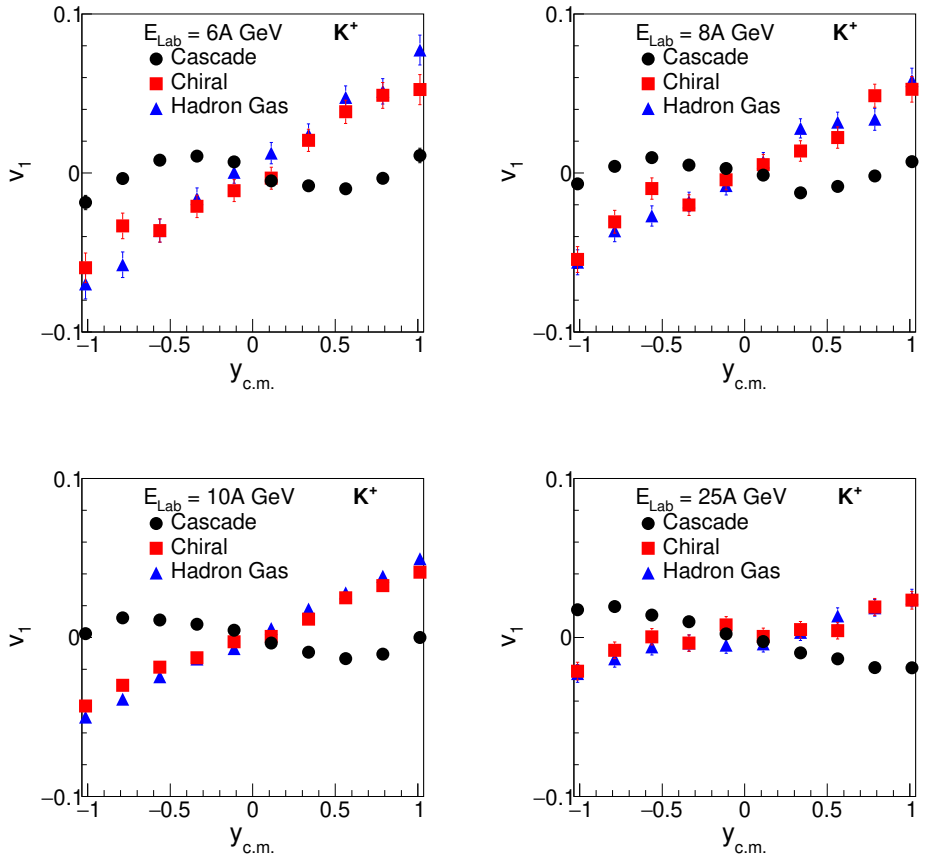

Figure 6.14. Rapidity dependence of directed flow $(v_1(y_{c.m.}))$ of positive kaons (K^+) in mid-central Au+Au collisions at bombarding energies $E_b = 6A, 8A, 10A and 25A$ GeV

mode, the integrated v_2 for both the EoS is about 30% larger compared to pure transport mode. Our calculated results are also compared with the data available from E877 and E895 experiments [182, 204]. Our results for all three configurations of UrQMD model, clearly overestimate the data, in the investigated energy range. This observation in line with the previous calculations [182], where the energy excitation function of the charged particle v_2 has been compared to data over a wide energy range, from (E_{Lab} = 90A MeV to $\sqrt{s_{NN}}$ = 200 GeV, using pure UrQMD (v2.2) model.

The slope of the directed flow as a function of beam energy is sensitive to the underlying EoS and can provide insights about the dynamics of the QCD medium. The slope $(\frac{dv_1}{dy})$ is estimated for charged hadrons, at mid-rapidity within the interval $|y_{c.m.}| \leq 0.75$, as displayed in Figure 6.19. The slope demon-

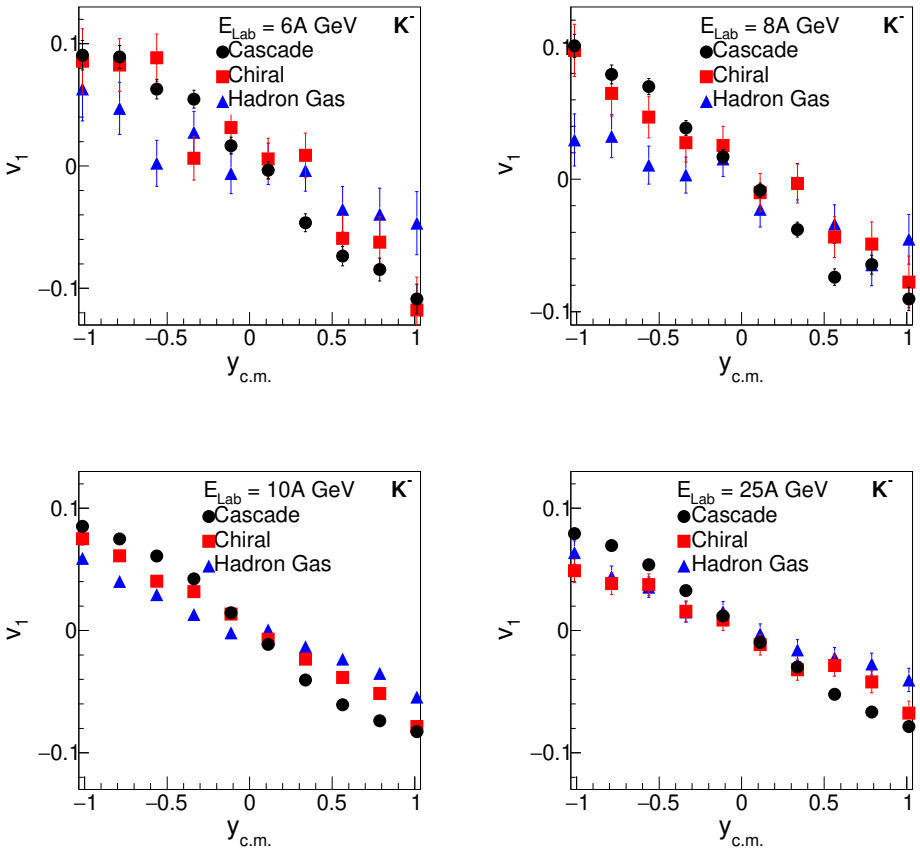

Figure 6.15. Rapidity dependence of directed flow $(v_1(y_{c.m.}))$ of negative kaons (K^-) in mid-central Au+Au collisions at bombarding energies $E_b = 6A, 8A, 10A and 25A$ GeV

strates opposite trends in the cascade and hydrodynamic mode of evolution. Note that the slope is negative in case of pure transport and positive in case of Hadron gas and Chiral EoS. The slope also shows some sensitivity to the underlying EoS. It starts to saturate at higher energies in case of hybrid mode and decreases in the absence of hydrodynamic expansion.

The variation of v_4 as a function of beam energy (E_{Lab}) is also a very important observable to study due to its sensitivity to the nuclear EoS. In Figure 6.20, we show the beam energy (E_{Lab}) dependence of the v_4 of charged hadrons in the mid-rapidity region (-0.75 $\leqslant y_{c.m.} \leqslant$ 0.75) for the three variants of the UrQMD model. Among the different evolution scenarios under study, v_4 seems to increase as energy goes up for Chiral EoS, and v_4 starts to increase for cascade case up to 8A GeV and then drops a bit down. In contrast, v_4 appears

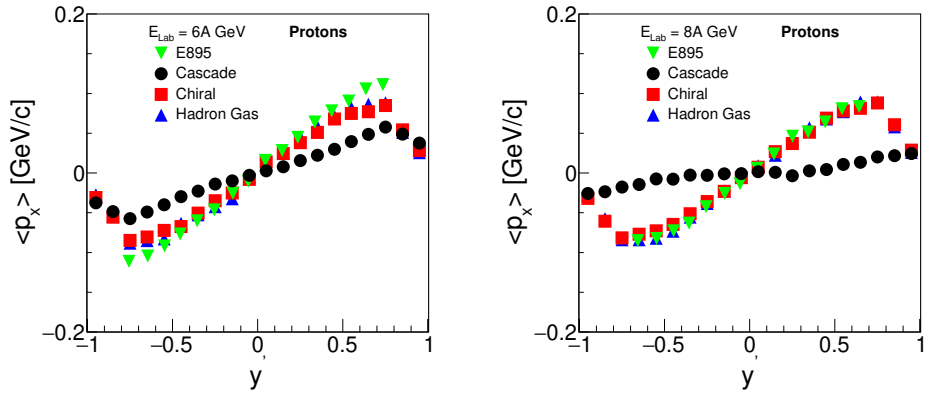

Figure 6.16. Comparison of $\langle p_x \rangle$ vs normalized rapidity (y') for protons from E895 experiment [164] at AGS energies with UrQMD for different EoS for 6A and 8A GeV

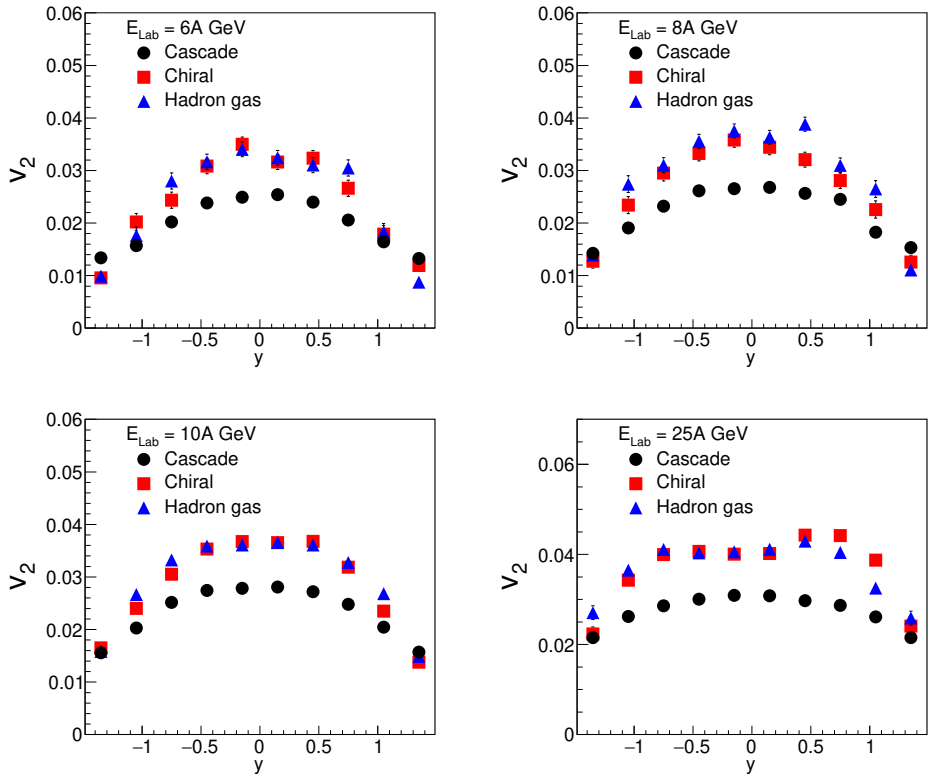

Figure 6.17. v_2 vs $y_{c.m.}$ for charged hadrons using UrQMD for different EoS for 6A, 8A, 10A and 25A GeV

to have a monotonic decreasing trend as a function of beam energy in case of Hadron gas EoS. By taking into account the large statistical fluctuations, one could make a statement that the v_4 at high baryon densities bears an effect of

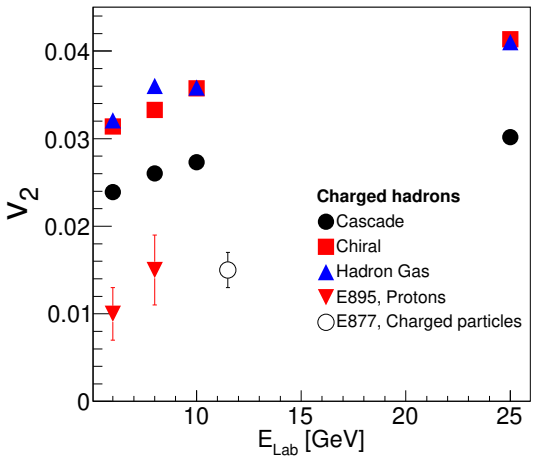

Figure 6.18. v_2 as a function of beam energy (E_{Lab}) for different EoS at midrapidity. It is compared with the v_2 of the protons and the charged particles at E895 and E877 [182, 204] respectively.

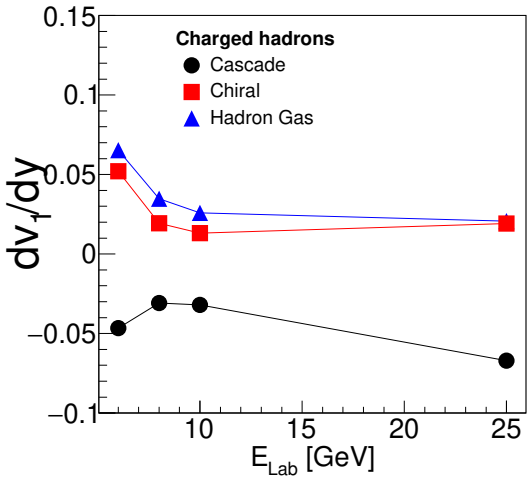

Figure 6.19. Slope ($\frac{dv_1}{dy}$) at $y_{c.m.} \approx 0$ by fitting with polynomials as a function of beam energy (E_{Lab}) for different EoS at midrapidity.

different EoS. But any concrete comment can only be made upon reduction of these uncertainties.

According to [177–179], the generation of v_4 is governed by both the intrinsic v_2 and the 4^{th} order moment of collective flow. The contribution of v_2 to v_4 is simply estimated as $v_4 = 0.5(v_2)^2$, within ideal fluid dynamics and in the absence of any fluctuations. Hence, with the ratio $v_4/(v_2)^2$, one can gain some

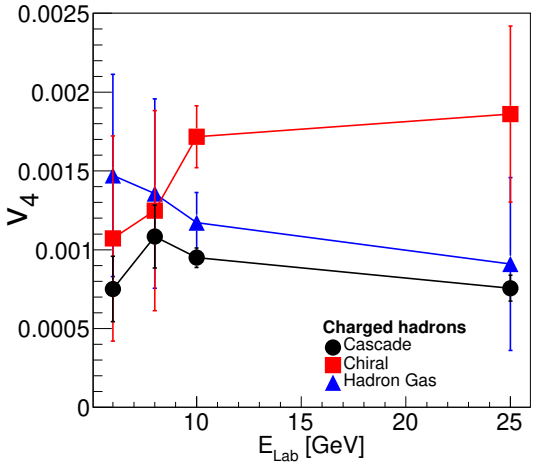

Figure 6.20. v_4 as a function of beam energy (E_{Lab}) for different EoS at midrapidity.

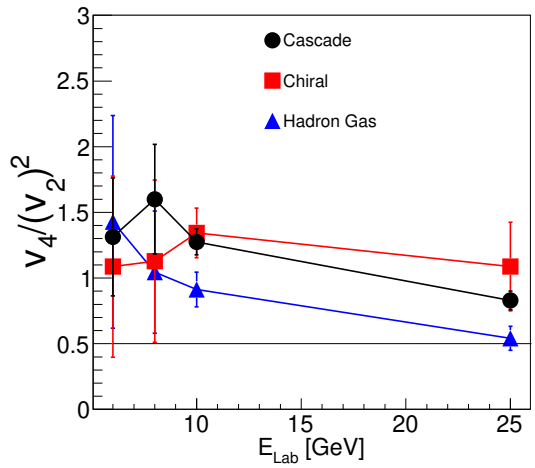

Figure 6.21. $v_4/(v_2)^2$ as a function of beam energy (E_{Lab}) for different EoS at midrapidity.

insights about the dynamics of the collision. Results available at RHIC [205–208] show double the value of v_4, $v_4/(v_2)^2 \approx 1$. Also, note that the results from Parton-Hadron-String Dynamics (PHSD) show four times higher value, $v_4/(v_2)^2 \approx 2$ [209], over a range of beam energies studied in min-bias Au + Au collisions. In [180], an attempt has been made to study this ratio using JAM model. In Fig 6.21, we show this ratio as function of beam energy (E_{Lab}). It is higher than 0.5 and goes maximum up to about 2, within the predictions from PHSD results. Here also, the results suffer from statistical fluctuations for

hybrid mode, making it difficult to make any strong conclusions, and the results can be more reliable upon reduction of these uncertainties. From Figs. 6.20 and 6.21, one can note that the descending trend in both v_4 and $v_4/(v_2)^2$ prevails for Hadron gas EoS and pure transport case.

In [210], the authors argued about the incomplete equilibration in the medium in the context of $v_4/(v_2)^2$. They explained the behaviour of $v_4/(v_2)^2$ as a function K^{-1} which is the typical number of collisions per particle, where K is the Knudsen number, a dimensionless parameter to characterize the degree of thermalization, and is related to the beam energy and system size. For $K^{-1} \gg 1$, local equilibrium is expected to be achieved. Incomplete thermalization leads to specific deviations from the ideal hydrodynamic behaviour. If the ratio $v_4/(v_2)^2 > 0.5$, the medium is not expected to be fully equilibrated which also can be seen in Fig 6.21. However, this would prevent the use of the ideal hydrodynamic model to describe the medium evolution in such low energy collisions. A viscous hydrodynamic expansion might be a more reliable tool, but this is beyond the scope of the present work. A conclusive picture can only be drawn once data on flow measurements will be available from the future experiments at FAIR and NICA.

Chapter 7

Conclusion and Outlook

In this chapter, the results from this thesis are summarised with possible future outlooks.

The aim of this thesis is to perform a comprehensive study of the collision dynamics of particles produced in proton-proton and nucleus-nucleus collisions over low as well as high-temperature regimes of the QCD phase diagram. It consists of results on data analysis of measurements of charm and beauty quark decay electrons in proton-proton collisions with ALICE at the different center-of-mass energies at the LHC and study of the collective flow of charged hadrons produced in low energy heavy-ion collisions.

At first, the p_{T}-differential cross-sections of the electrons from charm and beauty quark decays have been measured using different analysis techniques. To begin with, electrons from heavy-flavours are analysed in proton-proton collisions at $\sqrt{s} = 7$ and 13 TeV using data-driven photonic-electron tagging method. Earlier, the measurements were performed using the cocktail method which introduced large systematic uncertainties on the final measurement due to the input distributions used to make the cocktail. The production cross-sections of electrons from charm and beauty quarks are measured at $\sqrt{s} = 7$ and 13 TeV. The latter analysis is the first measurement in pp collisions with ALICE from very low transverse momentum i.e. 0.2 GeV/c. The former analysis is performed on the data obtained with the normal magnetic field (0.5 T) in the central barrel whereas, the latter one is with a low or reduced magnetic field (0.2 T). The distribution of electrons from Dalitz decays and photon conversions, being the major source of background, are built by using the invariant mass technique and then subtracted from inclusive electrons to get heavy-flavour electrons. This raw

yield of heavy flavour electrons is then corrected for the tracking and particle identification (PID) efficiencies, obtained using Monte Carlo (MC) simulations, to get the invariant yield. The data-driven method has helped to gain a very good precision on the obtained cross-section in contrast to the published measurement using the cocktail method at $\sqrt{s} = 7$ TeV. The measured cross-sections show a good agreement with the pQCD calculations in whole transverse momentum regime under investigation. A similar analysis was performed at $\sqrt{s} = 13$ TeV and cross-section at this energy also agrees with the theoretical predictions.

Moreover, the electrons from beauty hadron decays are measured using DCA template fit method using Monte Carlo information in proton-proton collisions at $\sqrt{s} = 5.02$ TeV. This measurement is important for understanding the mass-dependent energy loss of the quarks inside the QCD medium. Due to low reconstruction efficiency and small signal to background ratio at low transverse momentum region, the measurement of beauty electrons is difficult with the current ALICE set-up. Therefore, unlike heavy flavour electron analysis, the measurement is started from 2 GeV/c in p_{T}. Firstly, the DCA distributions (or templates) of the electrons from different sources are built from MC simulations. The obtained distributions are corrected using the experimental measurements since the shapes of these distributions are not well reproduced in MC compared to data. These corrected distributions are then fitted to the inclusive electron DCA distribution using the Maximum Likelihood Fit approach which determines the amplitude of the distribution for each source. From that, the raw yield of the electrons from the beauty hadron decays is estimated and then corrected for the acceptance and efficiencies to get the invariant spectrum. The cross-section is well described by the theoretical predictions. This measurement is an important reference for measuring the energy loss of the beauty quarks in the medium in Pb–Pb collision at $\sqrt{s_{NN}} = 5.02$ TeV. Furthermore, the relative contribution of beauty quark electrons to heavy-flavour electrons are measured and confronted with the theoretical predictions. It is observed that the beauty contribution hints towards dominating the total heavy-flavour electron contribution beyond certain transverse momentum region.

In future, the ongoing upgrade of ALICE detector for Run 3 and later

for Run 4 will open-up lots of exciting opportunities in nucleon-nucleon and nucleus-nucleus collisions. The improved primary vertex and impact-parameter resolution, together with the improved luminosity of the LHC accelerator complex, will provide a chance to perform the precision measurements. It will also enable the possible new measurements of the species such as Λ_b baryon and B meson, which were not achieved during Run 1 and 2 data taking periods.

In the later part of the thesis, the focus was shifted to study the properties of the QGP and freeze-out conditions of the produced particles in the low energy heavy-ion collisions which can turn out as predictions for the upcoming experiments in different accelerator facilities around the globe. Study of the collective flow, both isotropic and anisotropic, have been one of the interesting domain of the relativistic heavy-ion collisions since the start of the heavy-ion program.

We begin with the investigation of the kinetic freeze-out conditions of light/bulk hadrons in central Au + Au and Pb + Pb collisions, at AGS, SPS and partially at RHIC BES energies, using a non-boost-invariant version of the blast-wave model. The assumption of boost-invariance is explicitly broken by introducing a dependence of the transverse size of the fireball on the space-time rapidity. The transverse momentum and rapidity spectra for a variety of particle species are simultaneously analysed to obtain the best-fitted values of η_{max}, average transverse velocity ($\langle\beta_T\rangle$) and kinetic freeze-out temperature (T_{kin}). The overall fit to the data is reasonably good over a wide range of beam energy (E_{Lab}). The results indicate a relatively low T_{kin} in the range $55-90$ MeV with a substantial $\langle\beta_T\rangle$ of about $0.55c-0.6c$. We also found that T_{kin} increases gradually with the incident beam energy. Higher values of η_{max} were observed in case of the elliptic fireball than the cylindrical one. This may be attributed to the fact that one needs a larger value of η_{max} for ellipsoidal cross-section compared to the cylindrical one, in order to have an identical volume of the fireball needed to reproduce the measured rapidity spectra. For the upcoming experiments at FAIR and NICA accelerator facilities, these measurements would be useful to better understand the freeze-out conditions. Moreover, the transverse momentum and rapidity spectra of heavy strange hadrons are fitted simultaneously in the beam energy range from 20A – 158A GeV at SPS. The fit results of heavy

strange hadrons indicate that T_{kin} values are in the range $90-110$ MeV with $\langle\beta_T\rangle$ of about $0.4c-0.5c$. The temperature values are rather higher than the light particles which indicate early kinetic (thermal) freeze-out of heavy strange hadrons. The results of light hadrons along with heavy strange hadrons are used to study the mass-dependent hierarchy in the kinetic freeze-out conditions of different hadrons in central Pb+Pb collisions at different SPS energies using the same model. We found a clear mass-dependent hierarchy in the fitted kinetic freeze-out parameters. This hierarchy of kinetic freeze-out parameters is expected as the medium induced momentum change of heavy hadrons would be smaller compared to lighter hadrons. Therefore, as the temperature of the fireball decreases, one would expect an earlier kinetic decoupling of heavy hadrons. We found that the extracted freeze-out parameters for charmed hadrons at 158A GeV also corroborates this mass-dependent hierarchy.

Furthermore, the rapidity spectra of light hadrons, as well as heavy strange hadrons, are tested with a different model prescription than blast-wave to explore the longitudinal properties of the medium. For this, a non-conformal solution of the Landau hydrodynamical model as obtained in a recent work [154], is employed to describe the rapidity distributions. This prediction explains the heavy strange hadrons spectra nicely, however, not so satisfactorily for light hadrons. We found that the extracted value of sound velocity in the medium also exhibits a mass-dependent hierarchy implying an early emission of heavy strange from the fireball compared to the light hadrons. Similar feature has been obtained earlier from fits to p_T-spectra using the blast-wave model. We advocate that our findings are essential to provide predictions for upcoming experiments at FAIR and NICA accelerator facilities.

Looking forward, it will be interesting to repeat this exercise with charmed hadrons for lower energy collisions, when the data become available. This would be possible with the future measurements at SPS. The NA60+ experiment [148] at SPS aims at the measurement of charmonia in Pb+Pb collisions in the beam energy range $E_{lab} = 20A-158A$ GeV. In addition, the upgraded version of NA61/SHINE experiment at SPS plans to measure the open charm mesons (D meson) via their hadronic decay channel, in Pb+Pb collisions at beam

energies 40A and 150A GeV [211]. A large statistics data set at 150A GeV has already been collected which is presently being analysed. The existence of mass hierarchy in kinetic decoupling at low energy collisions can be tested more robustly if, in addition to charmonia, transverse spectra of D mesons are also made available, since their rest mass is closer to that of multi-strange hadrons. It will be interesting to perform this analysis in the future.

Moreover, the study of the anisotropic flow coefficients of the charged and identified hadrons in the non-central heavy-ion collisions was performed. We made an attempt to address a long-standing issue of probing the equation-of-state of the strongly-interacting matter, from the measurement of collective flow observables in heavy-ion collisions. We focus on the flow parameters v_1, v_2 and v_4 at mid-rapidity in semi-central Au+Au collisions, in the beam energy range $6-25A$ GeV, where the future FAIR and NICA accelerators would be operated. The UrQMD transport approach coupled with the ideal hydrodynamic expansion for different nuclear equations of state is employed for this purpose. We start with the examination of the elliptic flow parameter, v_2 of charged and identified hadrons as a function of transverse momentum and rapidity. We have noticed that v_2 is always higher in the hydrodynamic scenario when compared with the transport mode of the UrQMD model but fails to differentiate between the partonic and hadronic equations of state. The observed insensitivity can be attributed to the small lifetime of the hydrodynamic phase in such low energy collisions. We have also studied the constituent quark number scaling of elliptic flow for all the energies and nuclear EoS. From the results in hand, v_2 shows reasonably good scaling. Furthermore, an attempt has been made to study the directed flow of charged and identified hadrons as a function of rapidity. For the case of charged hadrons, the slope of v_1 is sensitive to the hydrodynamical scenario and able to differentiate the pure transport mode from the hydro mode. On the other hand, similar to the observation in the case of v_2, it fails to distinguish between the two EoS and is rather insensitive to the underlying degrees of freedom in the investigated energy regime. Along with this, efforts have been made to study the effect of different EoS on the slope of the directed flow ($\mathrm{d}v_1/\mathrm{dy}$), elliptic flow ($v_2$) and v_4 of charged hadrons as a function of the

beam energy (E_{Lab}). Also, the ratio $v_4/(v_2)^2$ is studied as a function of beam energy. The ratio lies within the values 0.5 and 2 which is consistent with the results obtained previously [205–209], given the statistical fluctuations. Upon the reduction in statistical errors, more conclusive remarks can be made. These predictions will be useful once data from the experiments at NICA [21], and FAIR [22, 23] become available.

In future, it will be interesting to study these observables over a wide range of beam energies to understand the insensitivity of flow coefficients to the underlying degrees of freedom in detail. It is also possible to perform the study using another available equation of state, i.e. Bag model in which the first-order phase transition is incorporated and expected to be more suitable at low beam energies.

Chapter 8

Appendix

8.1 Data sets and run numbers: pp 7 TeV

- LHC10b -

  117222, 117220, 117116, 117112, 117109, 117099, 117092, 117063, 117060, 117059, 117053, 117052, 117050, 117048, 116645, 116643, 116574, 116571, 116562, 116403, 116288, 116102, 115401, 115393, 115193, 115186, 114931

- LHC10c -

  120829, 120825, 120824, 120823, 120822, 120821, 120820, 120758, 120750, 120741, 120671,120617, 120616, 120505, 120503, 120244, 120079, 120076, 120073, 120072, 120069, 120067,119862, 119859, 119856, 119853, 119849, 119846, 119845, 119844, 119842, 119841, 119163, 119161,119159

- LHC10d -

  126158, 126097,126090, 126088, 126082, 126081, 126078, 126073, 126008, 126007, 126004, 125855, 125851, 125850,125849, 125848, 125847, 125844, 125843, 125842, 125633, 125632, 125630, 125296, 125134, 125101,125100, 125097, 125085, 125023, 122375, 122374, 126437, 126432, 126425, 126424, 126422, 126409, 126408, 126407, 126406, 126405,126404, 126403, 126359, 126352, 126351, 126285, 126284, 126283, 126168, 126160

- LHC10e -

  130840, 130834, 130848, 130847, 130844, 130842, 130799, 130798,

130795, 130793, 130704, 130696, 130608, 130601, 130520, 130519, 130517, 130480, 130375, 130356, 130354, 130343, 130342, 130179, 130178, 130172, 130158, 130157, 130149, 129983, 129961, 129960, 129959, 129744, 129742, 129738, 129736, 129735, 129729, 129726, 129725, 129723, 129667, 129666, 129659, 129654, 129653, 129652, 129650, 129647, 129641, 129639, 129599, 129587, 129586, 129540, 129528, 129527, 129523, 129520, 129514, 129513, 129512, 128913, 128855, 128853, 128850, 128843, 128836, 128835, 128833, 128824, 128823, 128820, 128778, 128777, 128678, 128677, 128621, 128615, 128611, 128609, 128605, 128582, 128507, 128505, 128504, 128503, 128498, 128495, 128494, 128486, 128483, 128452, 128263, 128260, 127942, 127941, 127940, 127937, 127936, 127935, 127933, 127931, 127822, 127719, 127718, 127714, 127712

The same numbers were used for the corresponding Monte Carlo samples.

Table 8.1. Summary of the data sample and Monte Carlo simulations used in pp 7 TeV analysis

Period/Sample	Number of events	Additional information
Data		
LHC10b, c, d & e	361.3 M	pp, $\sqrt{s}$ = 7 TeV, minimum bias, 223 runs, reconstruction pass 4
Monte Carlo simulations		
LHC15a2b	158 M	pp, 7 TeV, PYTHIA HF enriched production anchored to pass 4 reconstruction of pp 2010
LHC14j4b, c, d & e	314.8 M	PYTHIA, minimum bias, reconstruction pass 4

8.2 Data sets and run numbers: pp 13 TeV with low B

- LHC18c (FAST and CENT WoSDD sample) -

  285958, 285957, 285946, 285917, 285893, 285892, 285869, 285851,

285830, 285812, 285811, 285810, 285806, 285805, 285804, 285781, 285778, 285777, 285756, 285755, 285753, 285722, 285698, 285666, 285664, 285663, 285662, 285643, 285642, 285641, 285640, 285639, 285603, 285602, 285601, 285599, 285578, 285577, 285576, 285575, 285557, 285550, 285545, 285516, 285515, 285497, 285496, 285481, 285471

The same numbers were used for the corresponding Monte Carlo samples.

Table 8.2. Summary of the data sample and Monte Carlo simulations used in pp low B 13 TeV analysis

Period/Sample	Number of events	Additional information
Data		
LHC18c FAST and Cent WoSDD	442 M	pp, $\sqrt{s}$ = 13 TeV low B, minimum bias, 49 runs, reconstruction pass 1
Monte Carlo simulations		
LHC18l5b FAST	23M	pp, 13 TeV, PYTHIA HF enriched production anchored to pass 1 reconstruction of pp 2018
LHC18h1 FAST and Cent WoSDD	117M	PYTHIA, minimum bias, reconstruction pass 1

8.3 Data sets and run numbers: pp 5.02 TeV

The selected runlist used for the analysis is based on the good runs marked by DPG group.

`LHC17p_fast`:

TPC+TOF: 282343, 282342, 282341, 282340, 282314, 282313, 282312, 282309, 282307, 282306, 282305, 282304, 282303, 282302, 282247, 282230, 282229, 282227, 282224, 282206, 282189, 282147, 282146, 282127, 282126, 282125, 282123, 282122, 282120, 282119, 282118, 282099, 282098, 282078, 282051, 282050, 282031, 282025, 282021, 282016, 282008

`LHC17p_CENT_WoSDD`:

TPC+TOF: 282343, 282342, 282341, 282340, 282314, 282313, 282312, 282309, 282307, 282306, 282305, 282304, 282303, 282302, 282247, 282230, 282229, 282227, 282224, 282206, 282189, 282147, 282146, 282127, 282126, 282125, 282123, 282122, 282120, 282119, 282118, 282099, 282098, 282078, 282051, 282050, 282031, 282030, 282025, 282021, 282016, 282008

`LHC17q`: 282367, 282366, 282365

The Monte-Carlo sample used for the analysis include a General Purpose samples `LHC17l3b_fast` and `LHC17l3b_centWoSDD`, and a heavy-flavour and Dalitz particle enhanced sample `LHC18a4b2_Geant3_fast_HFE`.

Table 8.3. Summary of the data sample and Monte Carlo simulations used in this analysis

Period/Sample	Number of events	Additional information
Data		
LHC17p and q	930 M	pp, $\sqrt{s}$ = 5.02 TeV, minimum bias,
FAST and Cent WoSDD		41 runs, reconstruction pass 1
Monte Carlo simulations		
LHC18a4b2 FAST	26M	pp, 5.02 TeV, PYTHIA HF enriched production anchored to pass 1 reconstruction of pp 2017
LHC17l3b FAST and Cent WoSDD	190M	PYTHIA, minimum bias, reconstruction pass 1

8.4 Mathematical distributions

8.4.1 Landau probability distribution

- In principle, mean and sigma are undefined. μ and c are the location and scale parameter.
- for $\mu = 0$ and c = 1 (default values), the exact location of the maximum of the distribution (most probable value) is at x = -0.22278

$$\frac{1}{\pi c}\int_0^\infty e^{-t}\cos\left(t\left(\frac{x-\mu}{c}\right)+\frac{2t}{\pi}\log\left(\frac{t}{c}\right)\right)dt$$

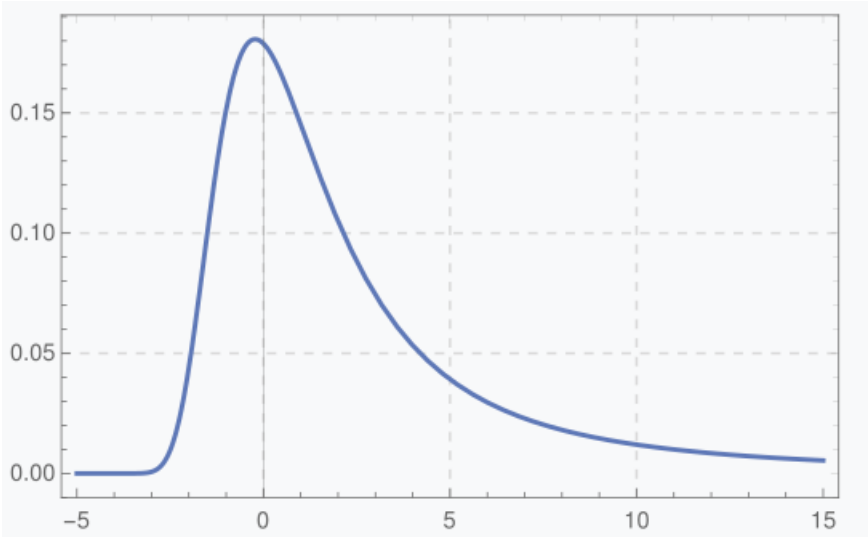

Figure 8.1. Landau Distribution [214]

8.4.2 Error function

$$\operatorname{erf} x = \frac{1}{\sqrt{\pi}} \int_{-x}^{x} e^{-t^2}\, dt$$

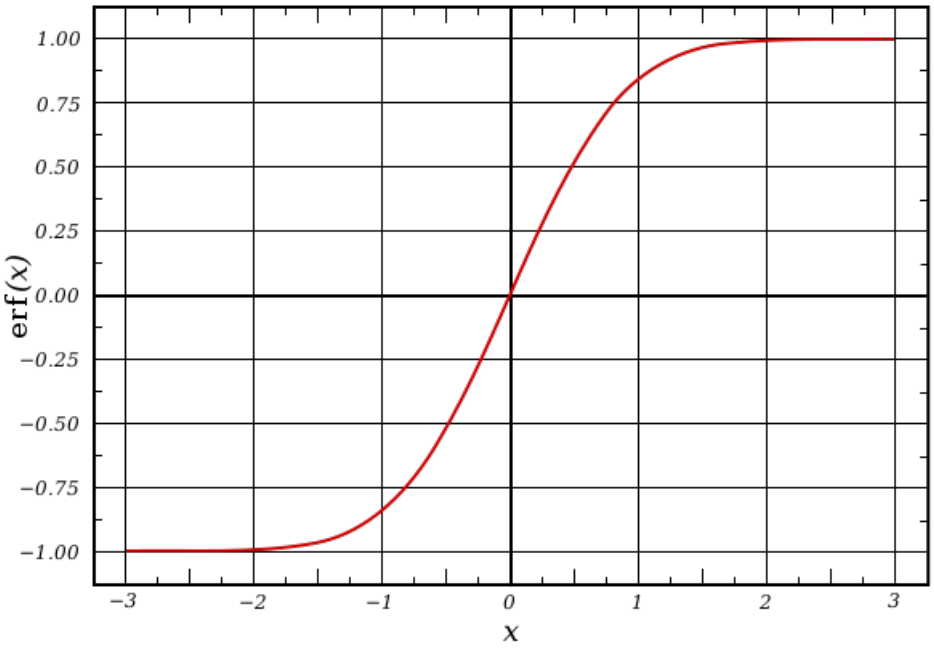

Figure 8.2. Error Function [215]

8.5 Fits of TPC nσ distributions of electrons at 7 TeV

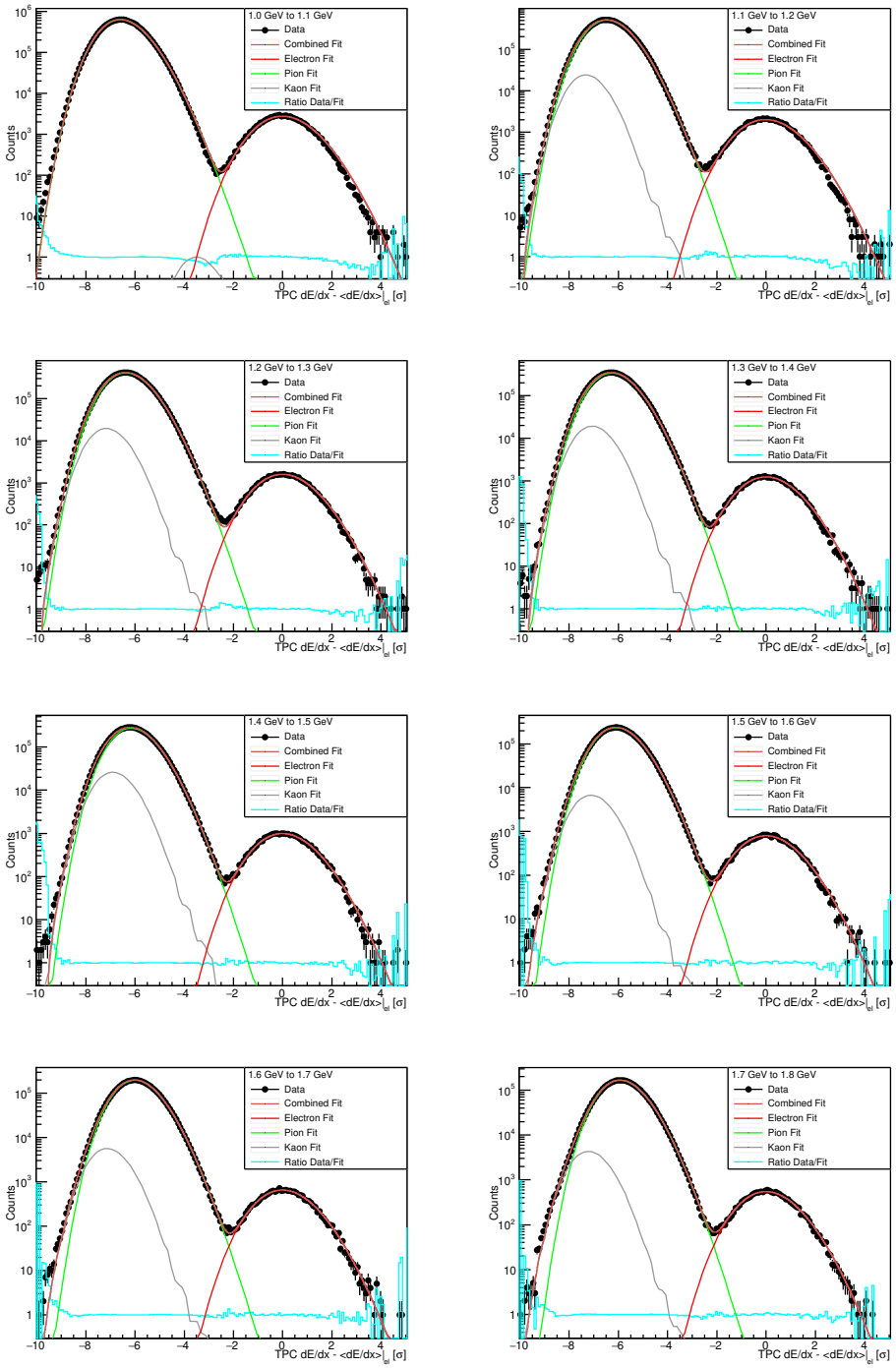

Figure 8.3. TPC nσ distribution of electrons with simultaneous fit of electrons (red), pion (green) and kaon (grey) distributions in different p_{T} bins. In addition, ratio (blue) between data and fit is shown for 7 TeV.

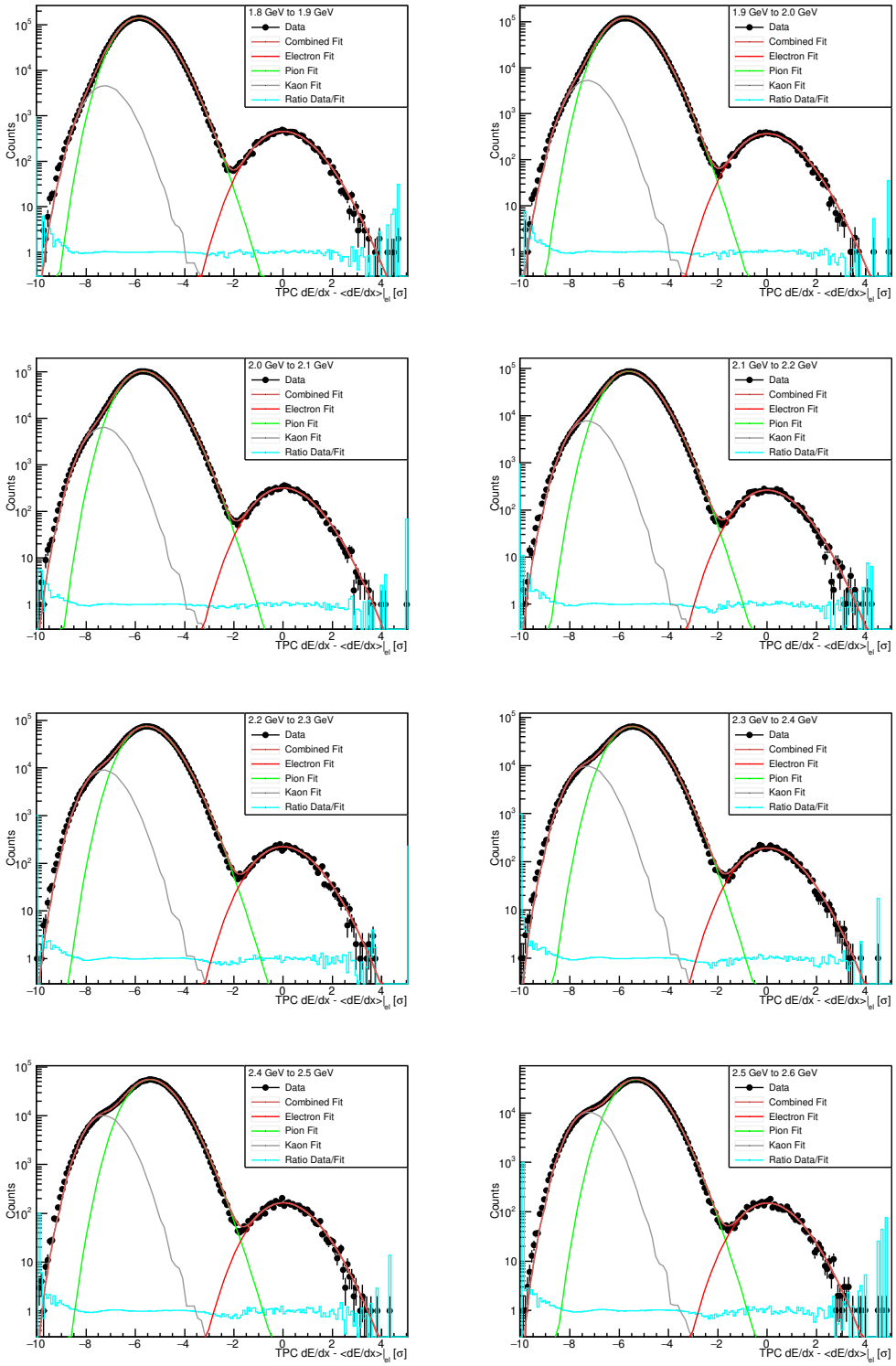

Figure 8.4. TPC nσ distribution of electrons with simultaneous fit of electrons (red), pion (green) and kaon (grey) distributions in different p_{T} bins. In addition, ratio (blue) between data and fit is shown for 7 TeV.

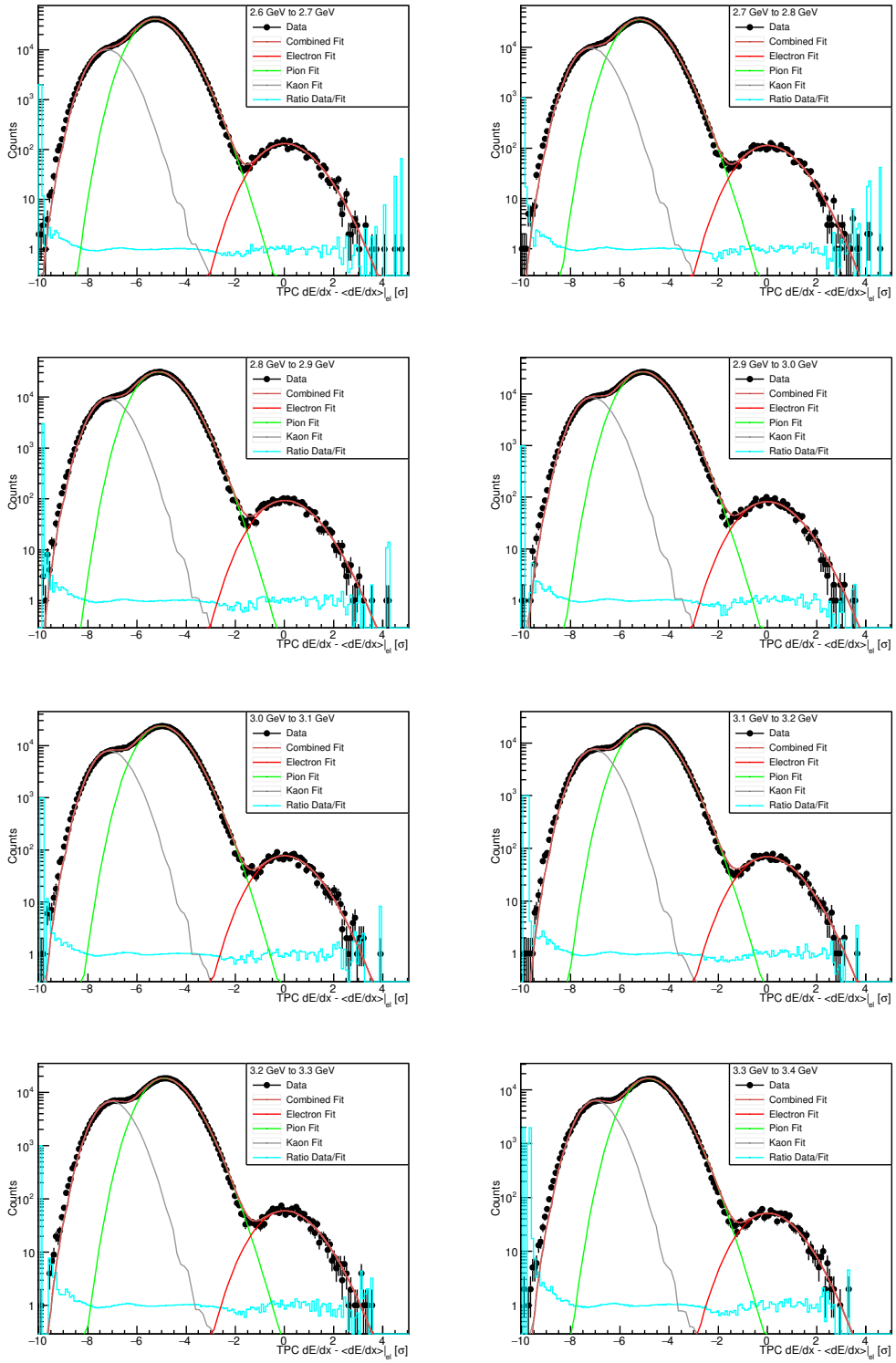

Figure 8.5. TPC nσ distribution of electrons with simultaneous fit of electrons (red), pion (green) and kaon (grey) distributions in different p_{T} bins. In addition, ratio (blue) between data and fit is shown for 7 TeV.

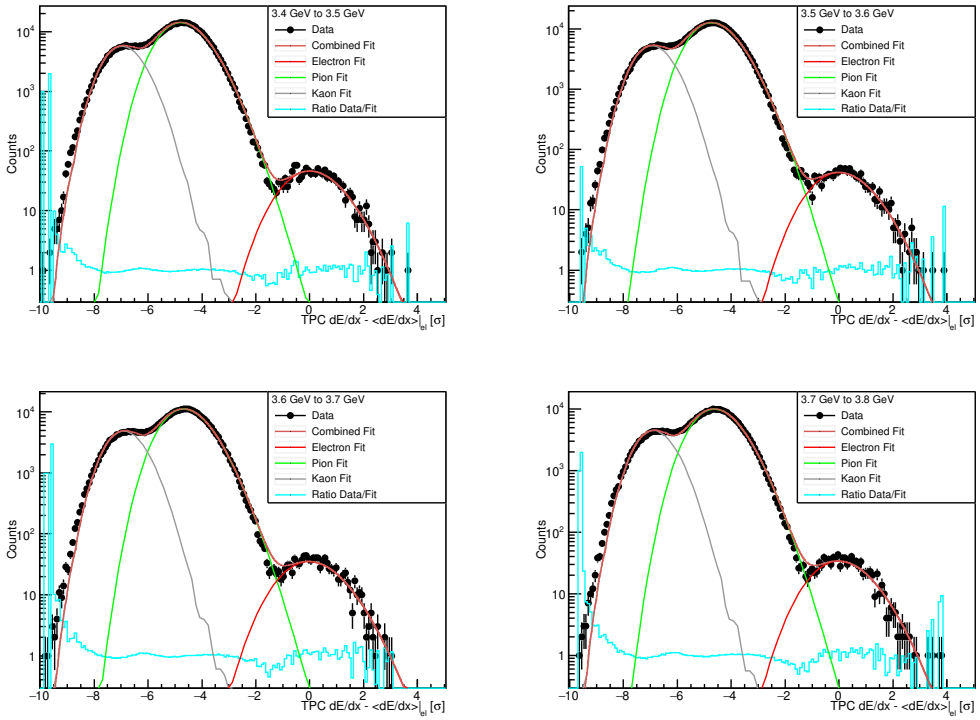

Figure 8.6. TPC nσ distribution of electrons with simultaneous fit of electrons (red), pion (green) and kaon (grey) distributions in different p_{T} bins. In addition, ratio (blue) between data and fit is shown for 7 TeV.

8.6 Fits of TPC nσ distributions of electrons at 13 TeV

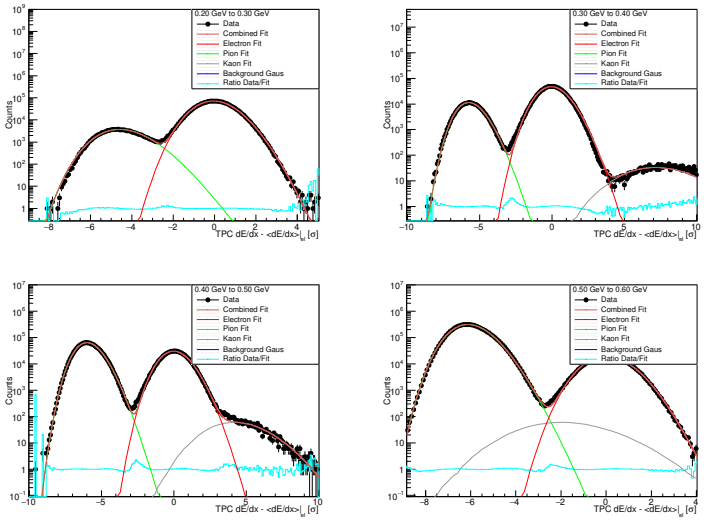

Figure 8.7. TPC nσ distribution of electrons with simultaneous fit of electrons (red), pion (green) and kaon (grey) distributions in different p_{T} bins. In addition, ratio (blue) of data and fit is shown for 13 TeV.

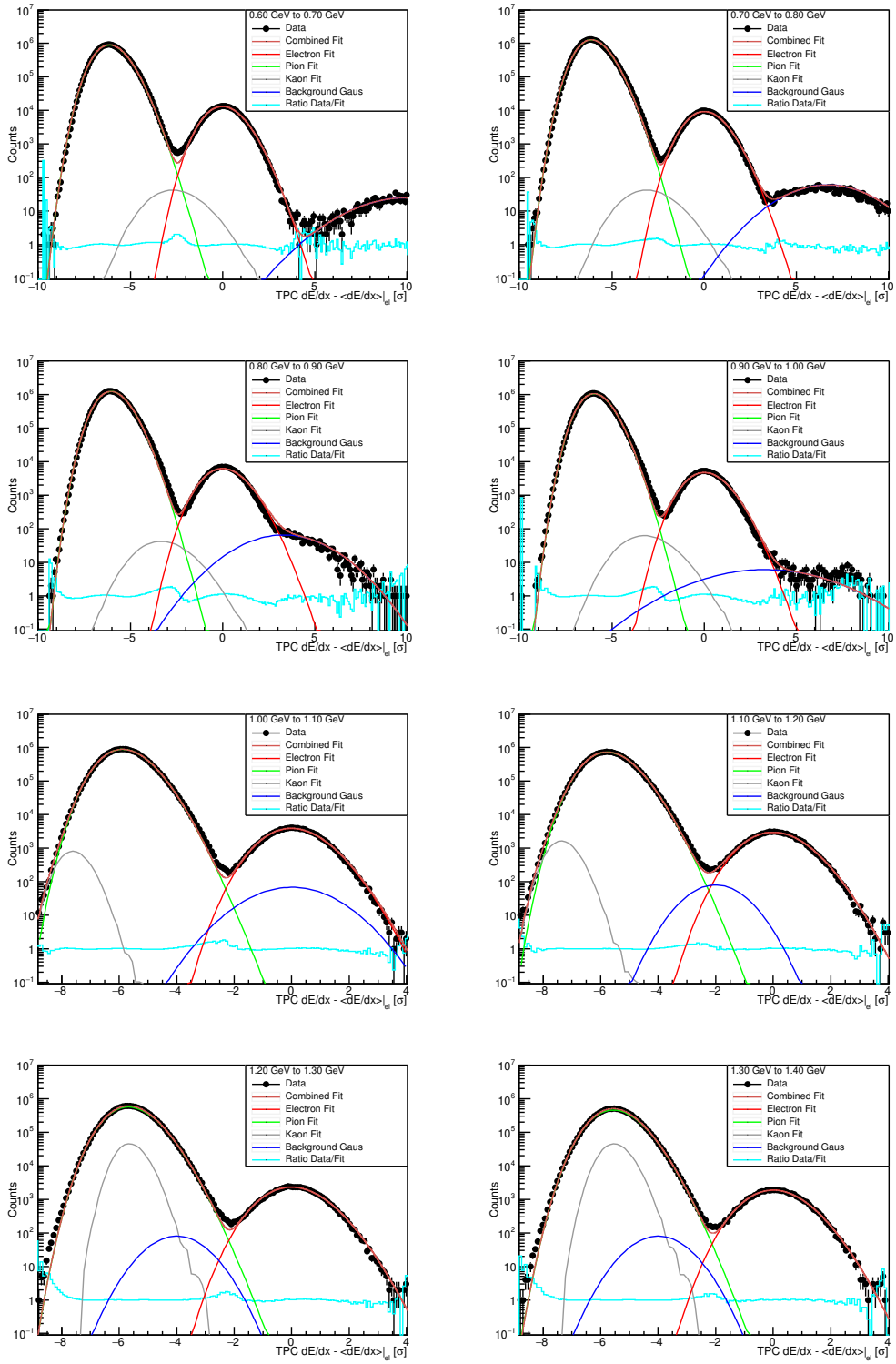

Figure 8.8. TPC nσ distribution of electrons with simultaneous fit of electrons (red), pion (green) and kaon (grey) distributions in different p_{T} bins. In addition, ratio (blue) of data and fit is shown for 13 TeV.

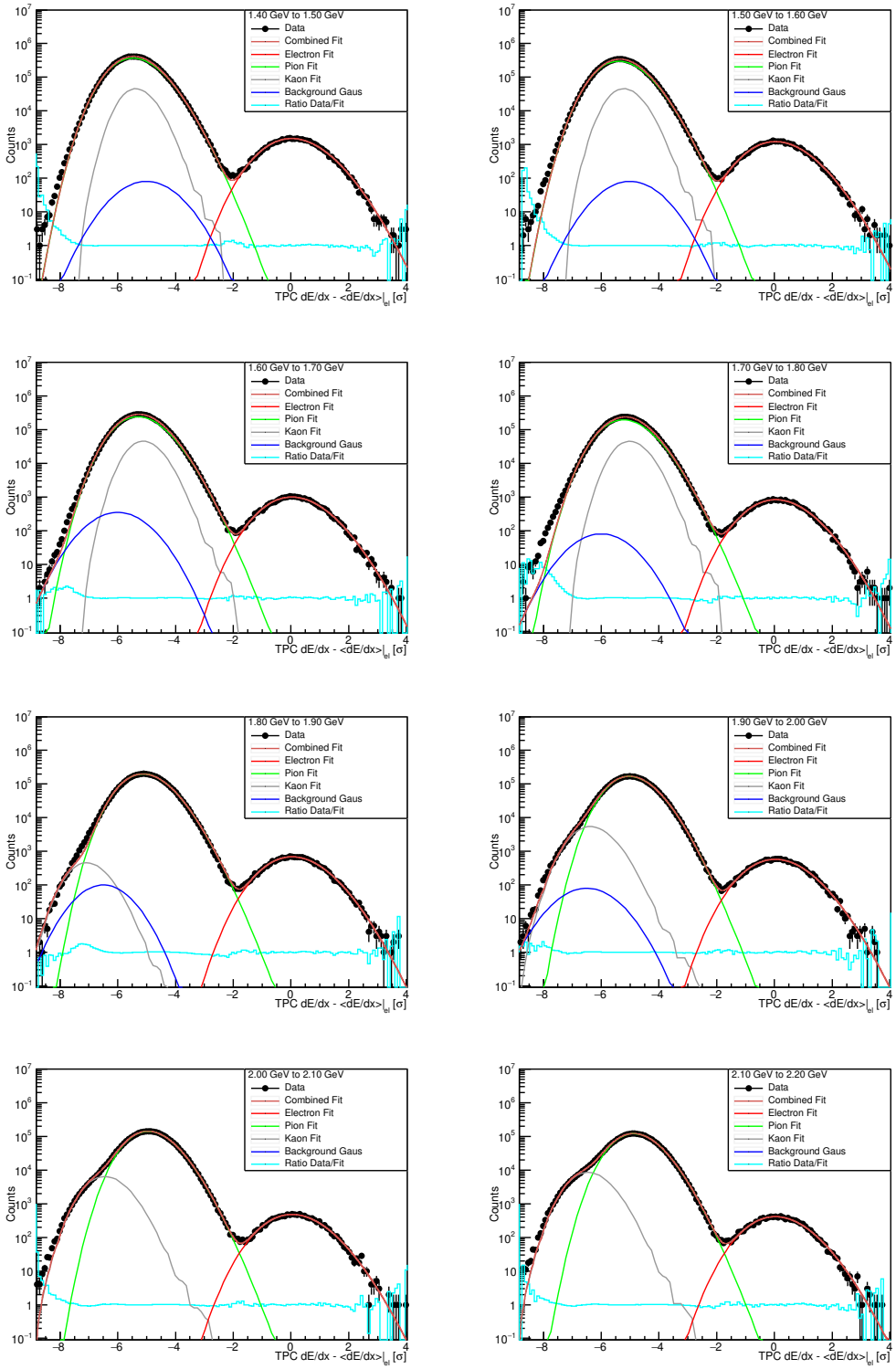

Figure 8.9. TPC nσ distribution of electrons with simultaneous fit of electrons (red), pion (green) and kaon (grey) distributions in different p_{T} bins. In addition, ratio (blue) of data and fit is shown for 13 TeV.

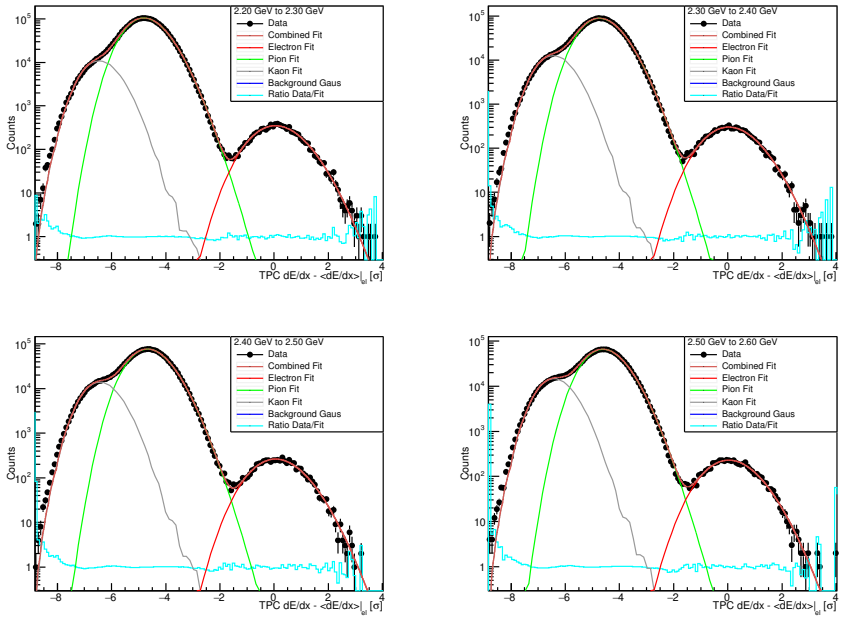

Figure 8.10. TPC nσ distribution of electrons with simultaneous fit of electrons (red), pion (green) and kaon (grey) distributions in different p_{T} bins. In addition, ratio (blue) between data and fit is shown for 13 TeV.

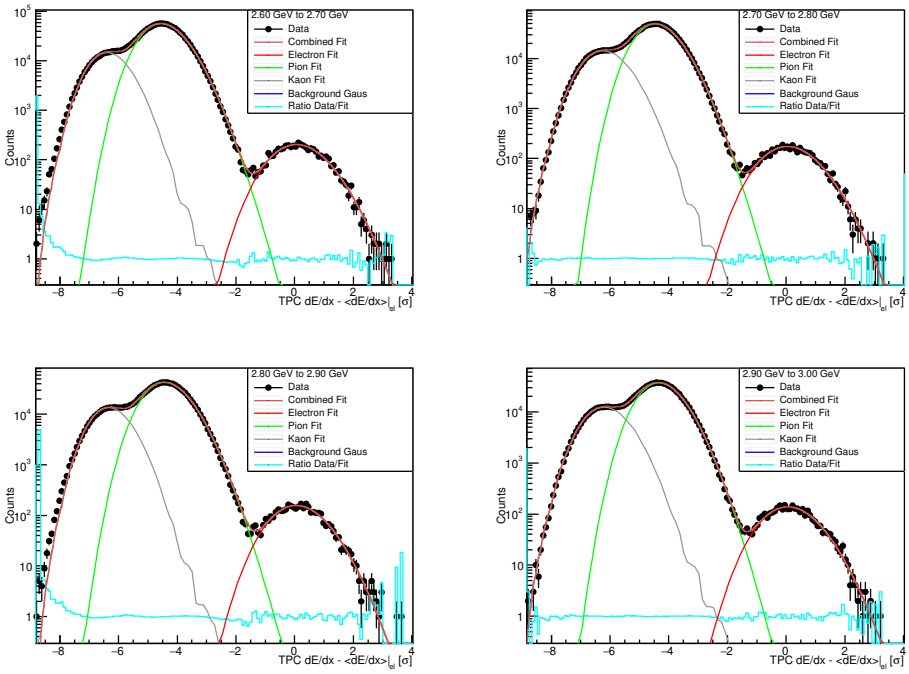

Figure 8.11. TPC nσ distribution of electrons with simultaneous fit of electrons (red), pion (green) and kaon (grey) distributions in different p_{T} bins. In addition, ratio (blue) of data and fit is shown for 13 TeV.

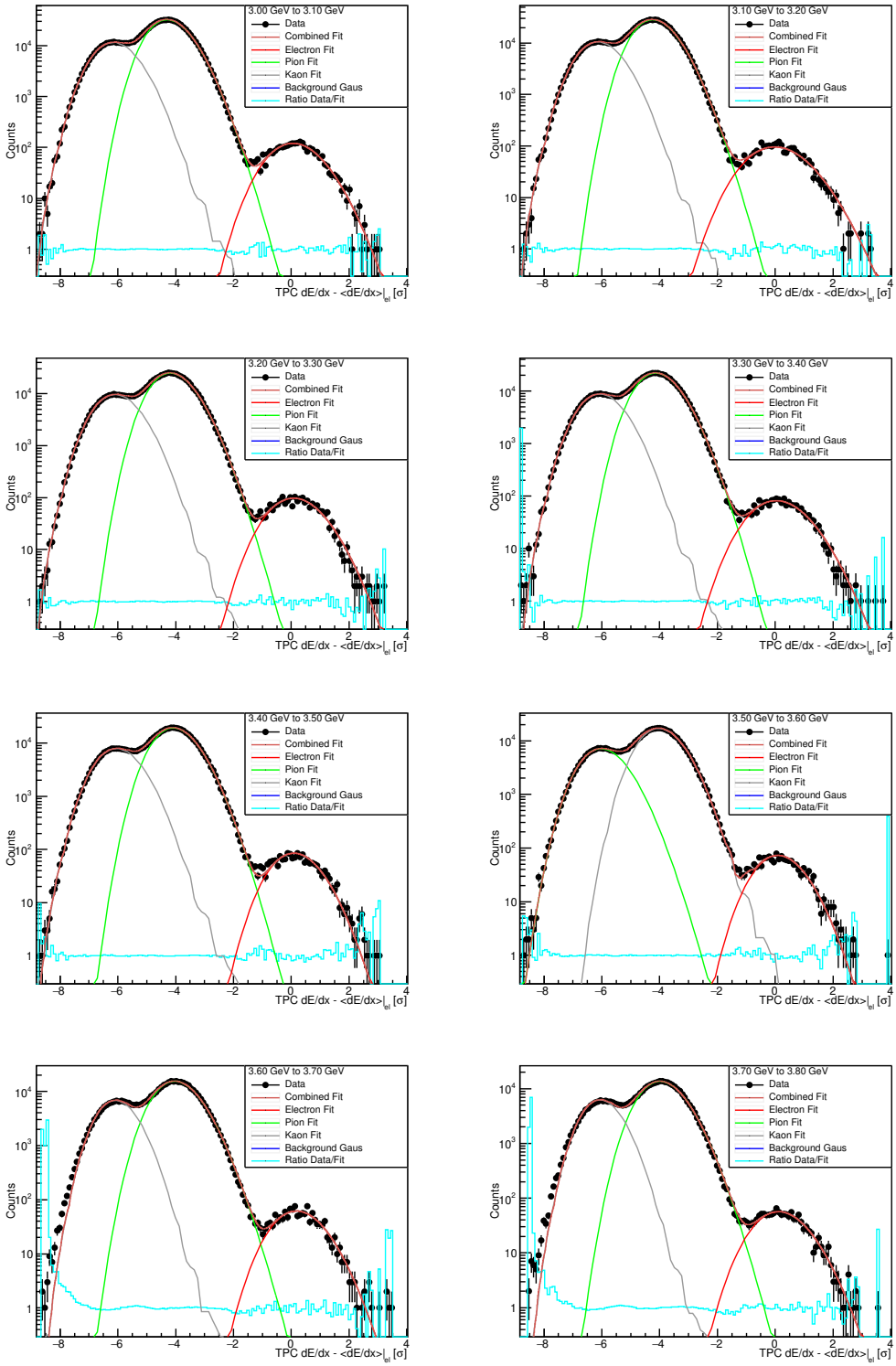

Figure 8.12. TPC nσ distribution of electrons with simultaneous fit of electrons (red), pion (green) and kaon (grey) distributions in different p_{T} bins. In addition, ratio (blue) of data and fit is shown for 13 TeV.

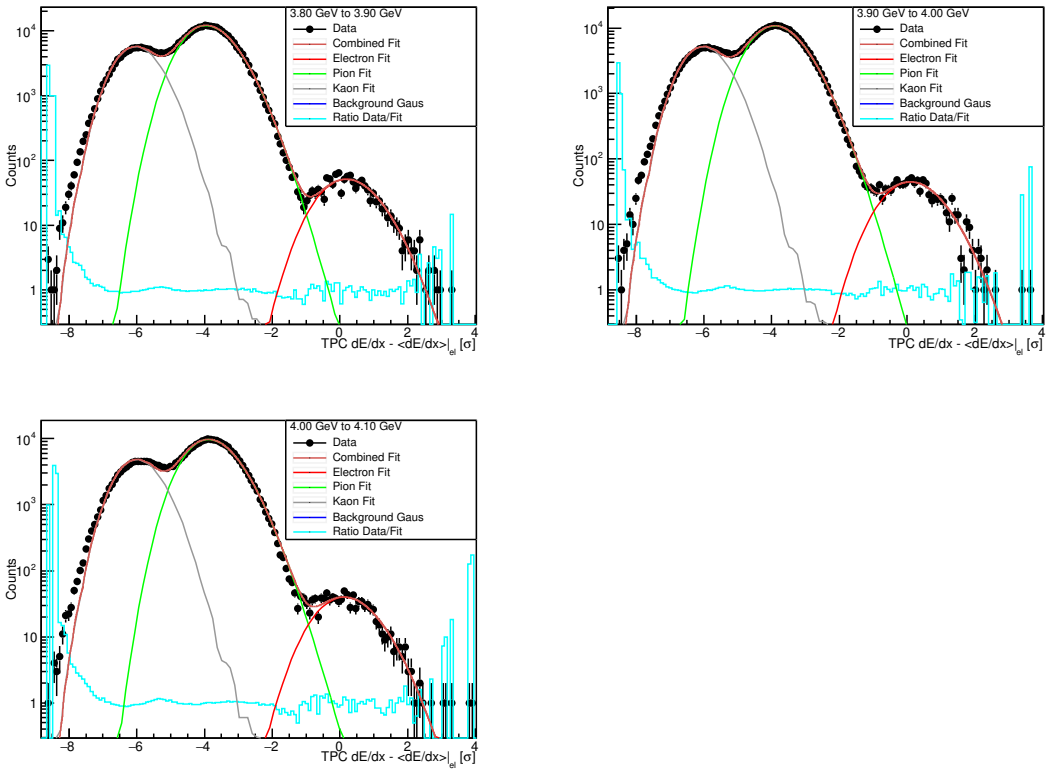

Figure 8.13. TPC nσ distribution of electrons with simultaneous fit of electrons (red), pion (green) and kaon (grey) distributions in different p_{T} bins. In addition, ratio (blue) of data and fit is shown for 13 TeV.

8.7 RMS distributions: Inclusive track selection at 7 TeV

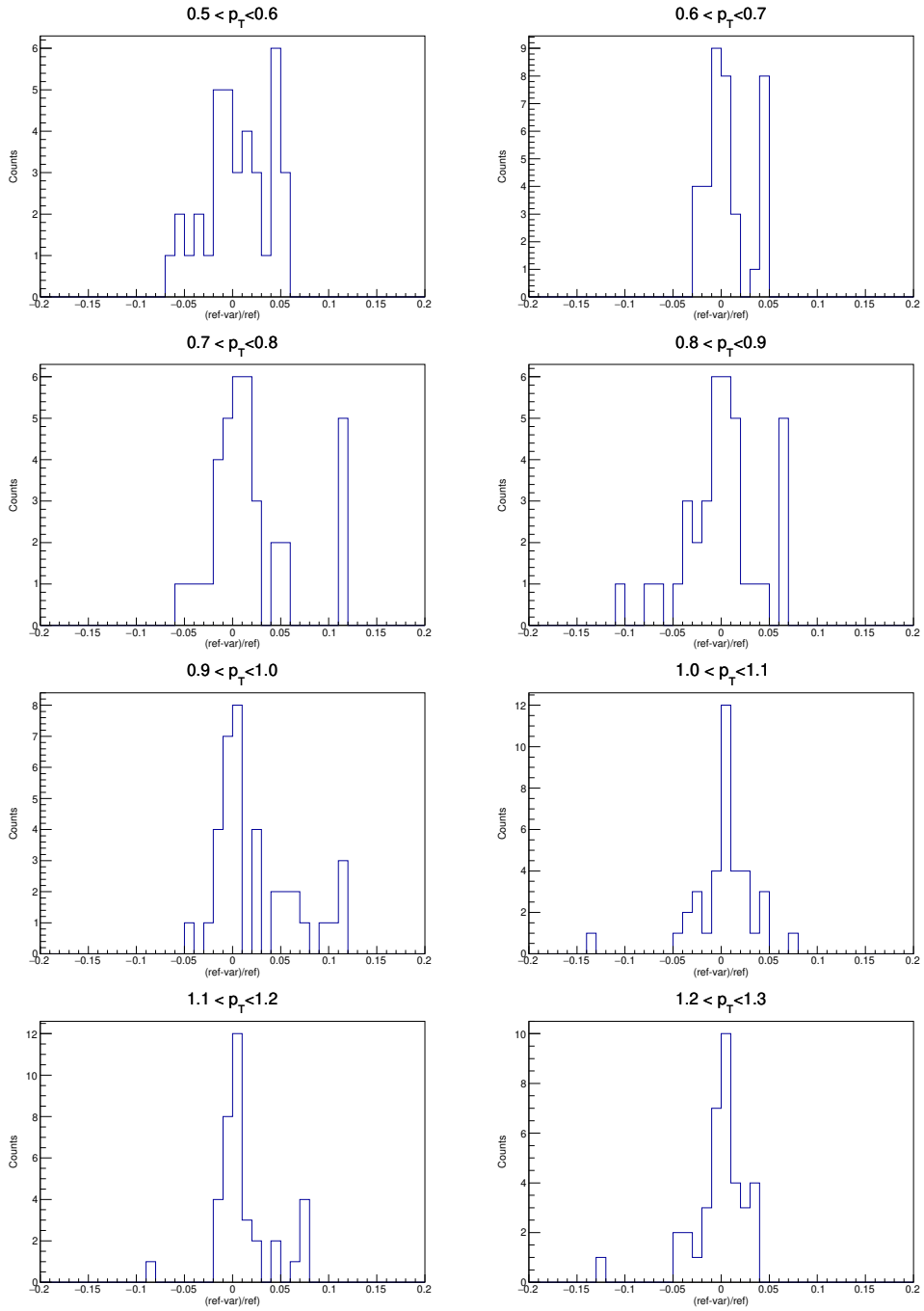

Figure 8.14. Distribution of the difference between the varied and reference spectra, divided by the reference value for inclusive track selection and PID cuts, in different bins of p_T for pp at $\sqrt{s} = 7$ TeV.

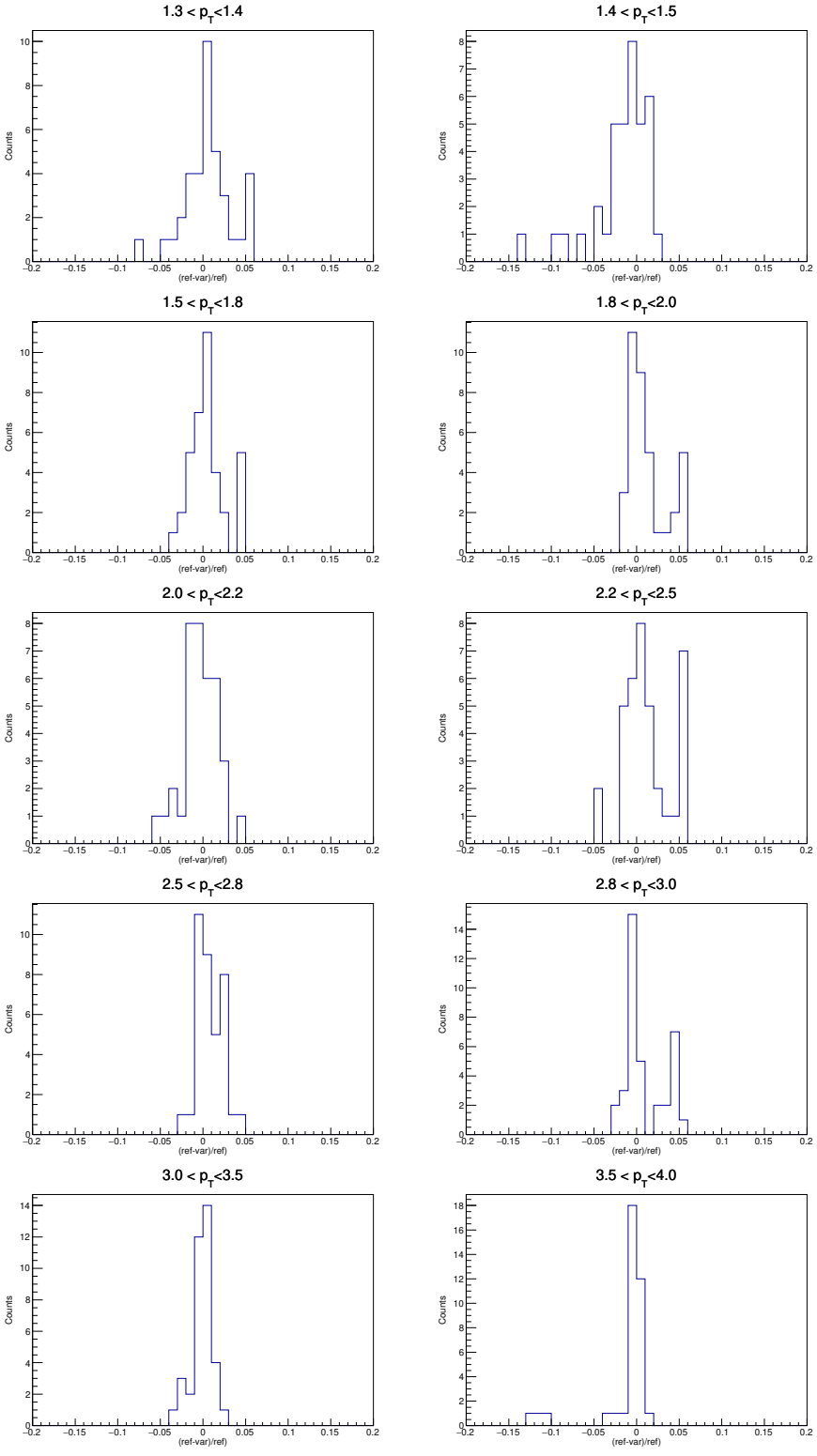

Figure 8.15. Distribution of the difference between the varied and reference spectra, divided by the reference value for inclusive track selection and PID cuts, in different bins of p_T for pp at $\sqrt{s} = 7$ TeV.

8.8 RMS distributions: Associated track selection at 7 TeV

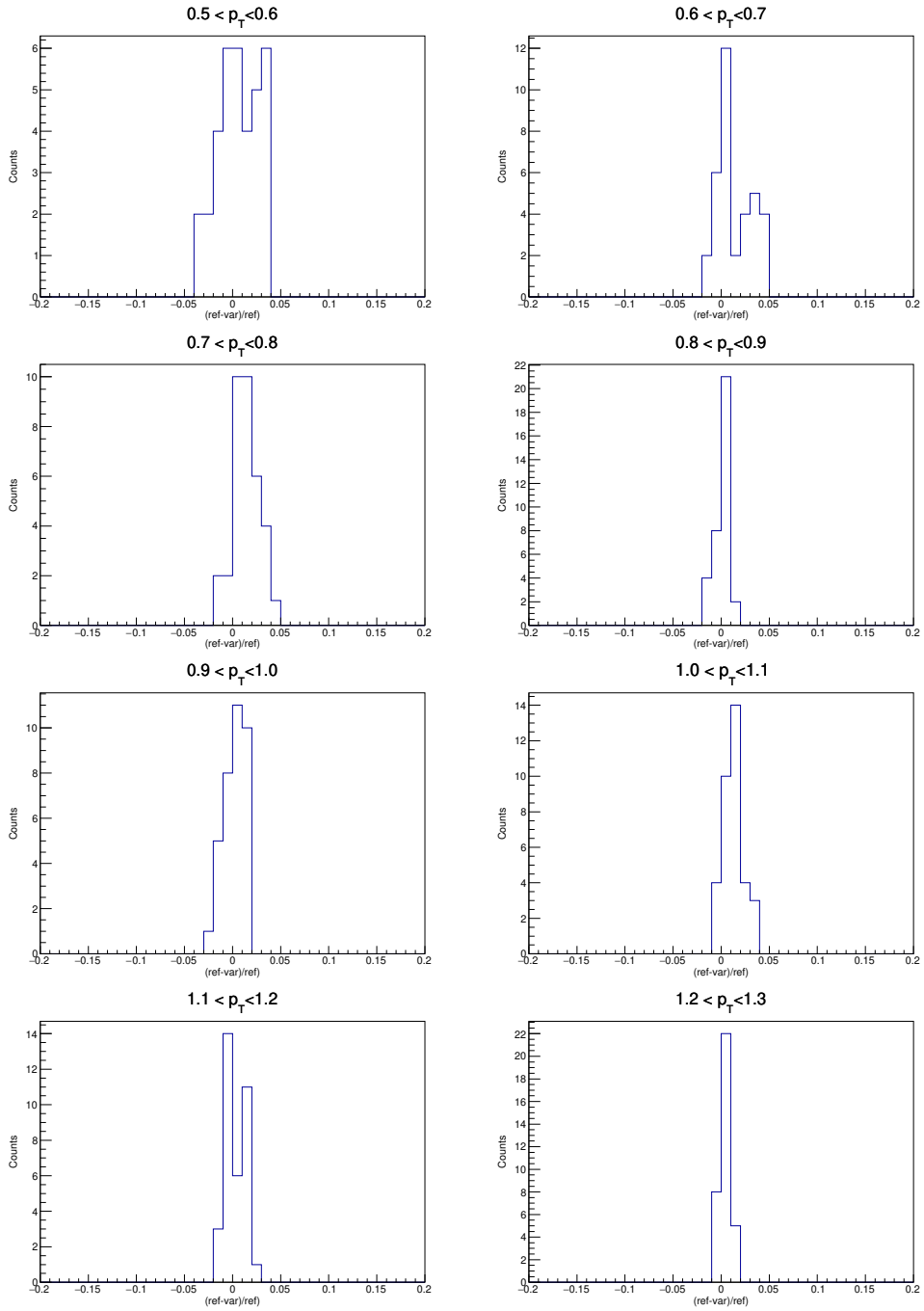

Figure 8.16. Distribution of the difference between the varied and reference spectra, divided by the reference value for associated track selection cuts, in different bins of p_T for pp at $\sqrt{s} = 7$ TeV.

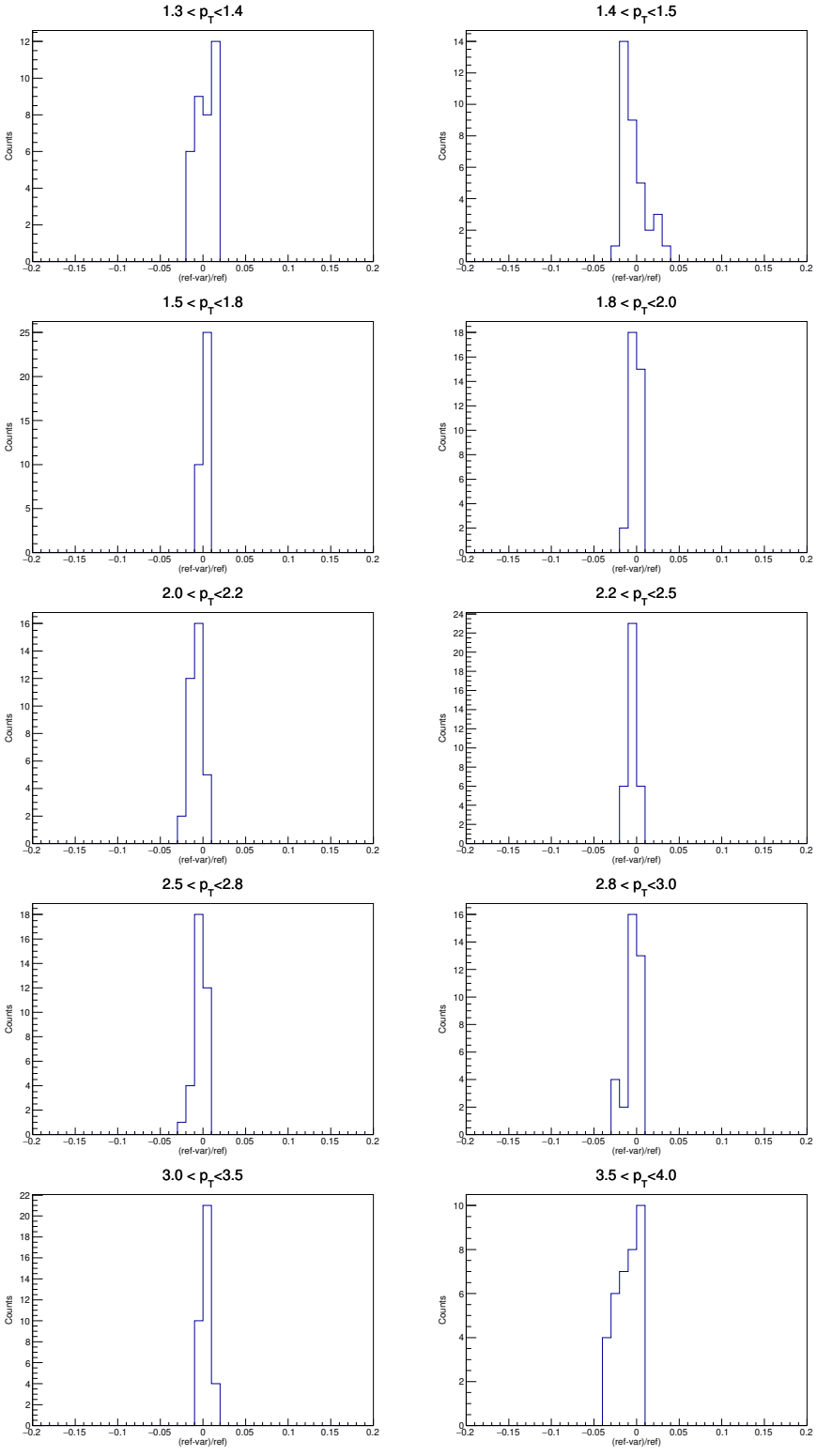

Figure 8.17. Distribution of the difference between the varied and reference spectra, divided by the reference value for associated track selection cuts, in different bins of p_T for pp at $\sqrt{s} = 7$ TeV.

8.9 Fraction of charmed hadrons to D meson in pp collisions at $\sqrt{s} = 5.02$ TeV

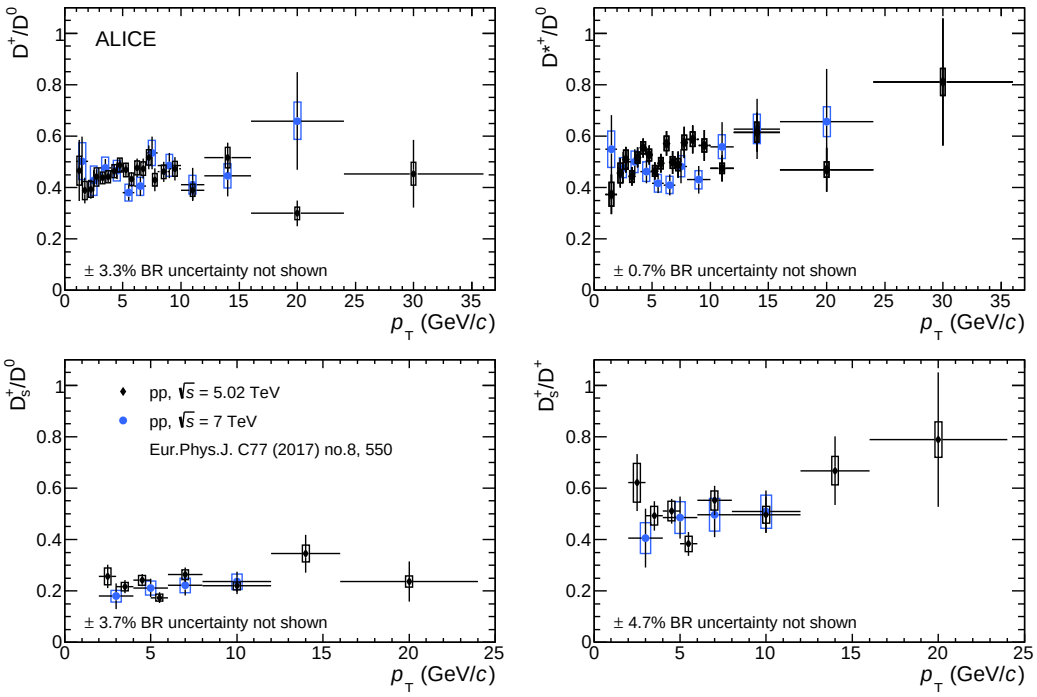

Figure 8.18. Measured $D^{\pm}/D^{0}$, $D^{*\pm}/D^{0}$, $D_s^{\pm}/D^{0}$ and $D_s^{\pm}/D^{\pm}$ ratio in pp at 5.02 TeV

8.10 DCA distributions of charged hadrons in data, MC before and after the improver

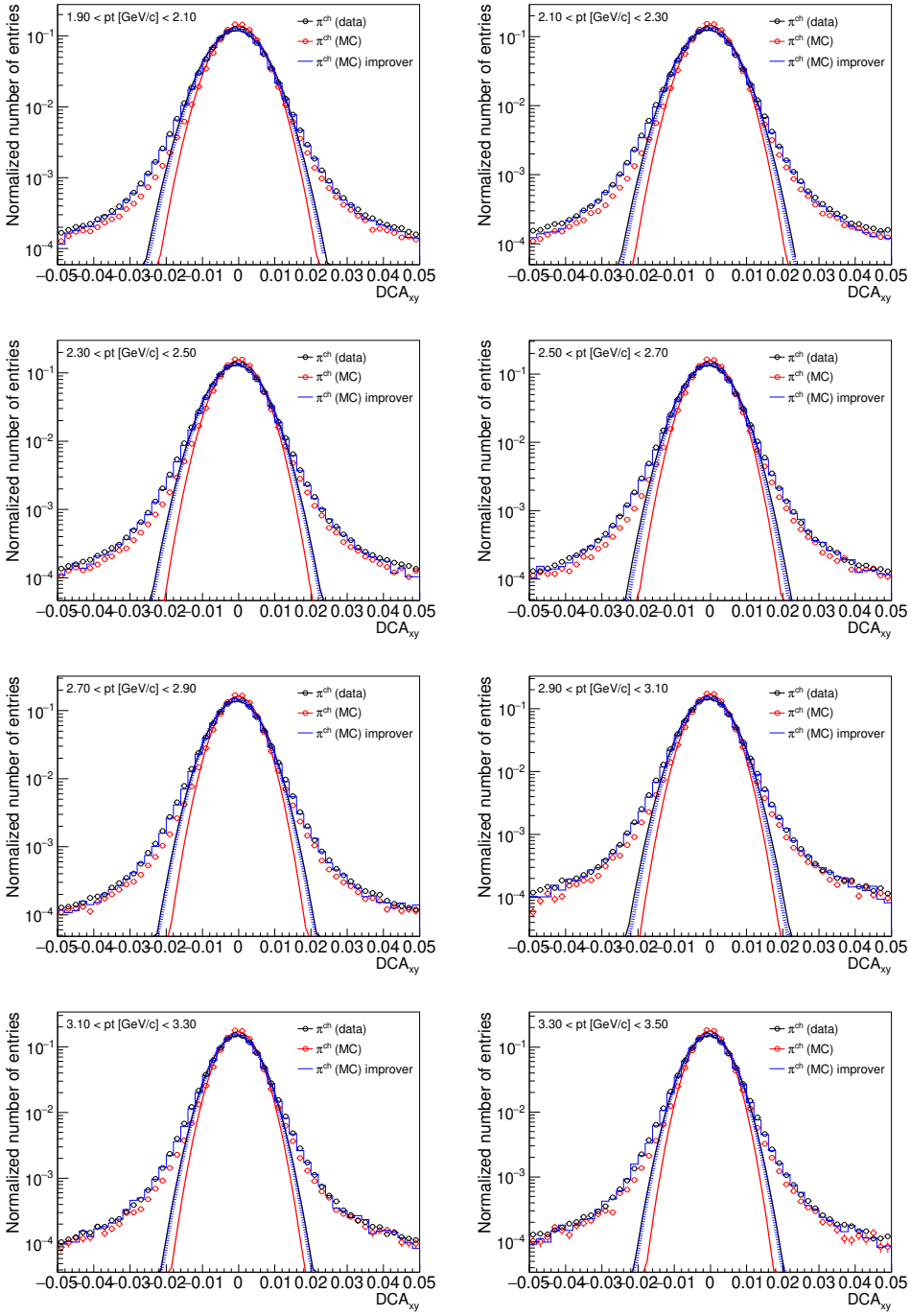

Figure 8.19. DCA distributions of charged hadrons in data (black) and MC before (red) and after (blue) the improver, and the gaussian fits performed for the extraction of the mean and sigma in different p_{T} bins.

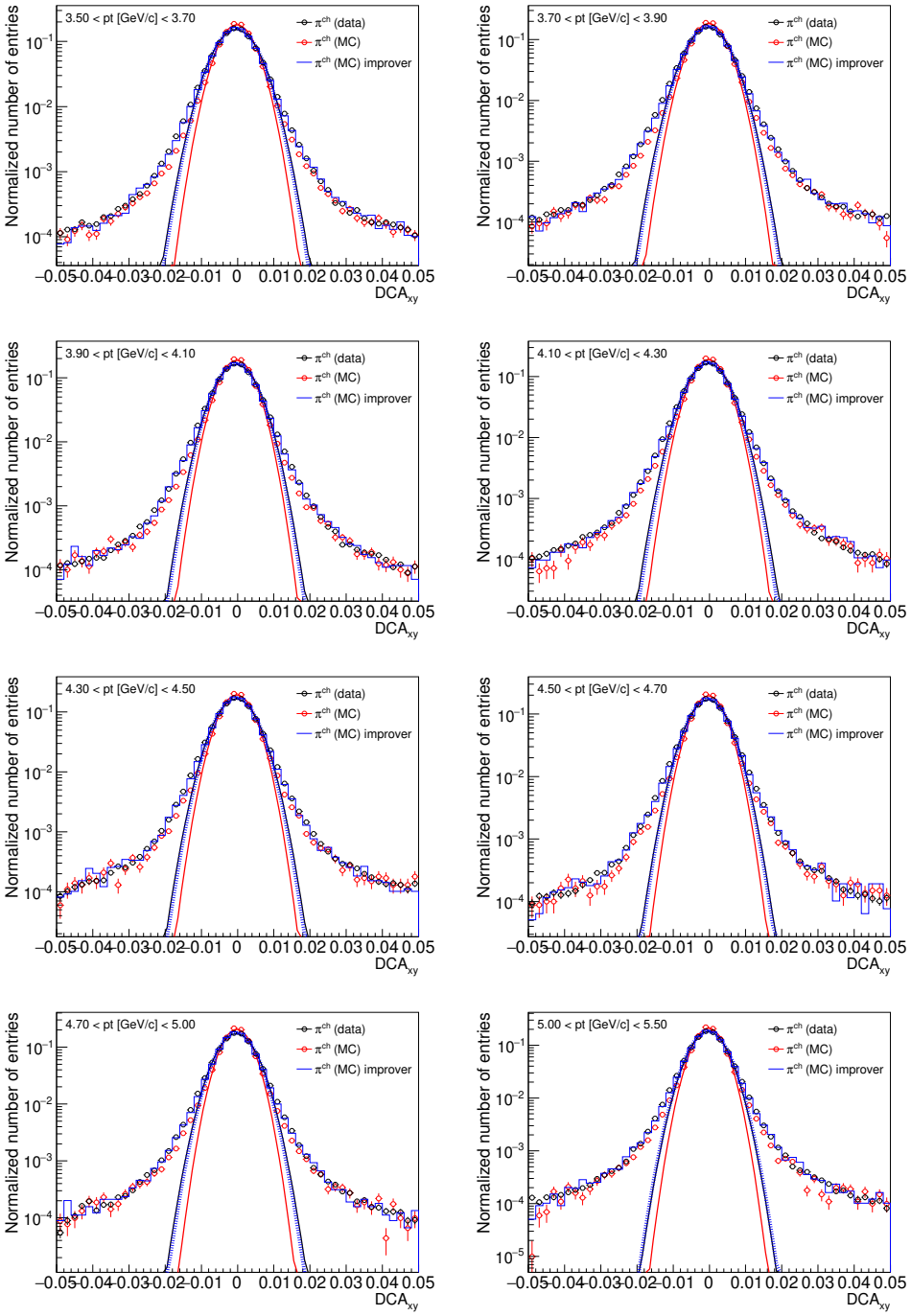

Figure 8.20. DCA distributions of charged hadrons in data (black) and MC before (red) and after (blue) the improver, and the gaussian fits performed for the extraction of the mean and sigma in different p_{T} bins.

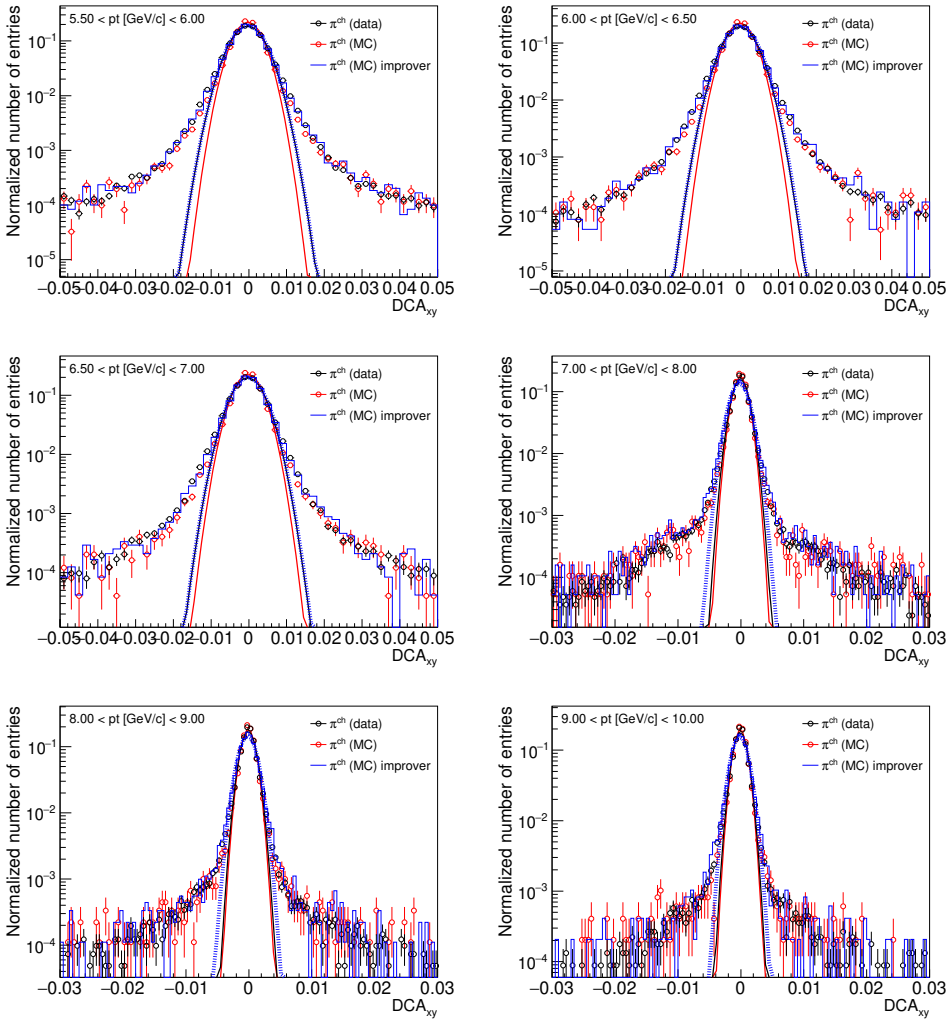

Figure 8.21. DCA distributions of charged hadrons in data (black) and MC before (red) and after (blue) the improver, and the gaussian fits performed for the extraction of the mean and sigma in different p_{T} bins.

Bibliography

[1] Y. Nambu, Phys. Rev. Lett. **4**, 380 (1960). doi:10.1103/PhysRevLett.4.380 1

[2] O. W. Greenberg, Phys. Rev. Lett. **13**, 598 (1964). doi:10.1103/PhysRevLett.13.598 1

[3] S. Chatrchyan *et al.* [CMS Collaboration], Phys. Lett. B **716**, 30 (2012) doi:10.1016/j.physletb.2012.08.021 [arXiv:1207.7235 [hep-ex]]. 2

[4] G. Aad *et al.* [ATLAS Collaboration], Phys. Lett. B **716**, 1 (2012) doi:10.1016/j.physletb.2012.08.020 [arXiv:1207.7214 [hep-ex]]. 2

[5] H. Fritzsch, M. Gell-Mann and H. Leutwyler, Phys. Lett. **47B**, 365 (1973). doi:10.1016/0370-2693(73)90625-4 2

[6] H. D. Politzer, Phys. Rev. Lett. **30**, 1346 (1973). doi:10.1103/PhysRevLett.30.1346 2

[7] D. J. Gross and F. Wilczek, Phys. Rev. Lett. **30**, 1343 (1973). doi:10.1103/PhysRevLett.30.1343 iv, 2

[8] S. Bethke, Nucl. Phys. Proc. Suppl. **121**, 74 (2003) doi:10.1016/S0920-5632(03)01817-6 [hep-ex/0211012]. xxxvi, 3

[9] Y. Aoki, G. Endrodi, Z. Fodor, S. D. Katz and K. K. Szabo, Nature **443**, 675 (2006) 3

[10] R. S. Bhalerao, doi:10.5170/CERN-2014-001.219 arXiv:1404.3294 [nucl-th]. xxxvi, 5

[11] W. Florkowski, Acta Phys. Polon. B **45**, no. 12, 2329 (2014). 4

[12] Ulrich W. Heinz, arXiv:hep-ph/0407360. 4

[13] J. Adams *et. al.* [STAR Collaboration], Nucl. Phys. A **757** (2005), 102. 4, 5

[14] K. Adcox *et. al.* [PHENIX Collaboration], Nucl. Phys. A **757** (2005), 184. 4, 5

[15] K. Aamodt *et. al.* [ALICE Collaboration], Phys. Rev. Lett. **107** (2011), 032301. 4, 5

[16] G. Aad *et. al.* [ATLAS Collaboration], Phys. Rev. C **86** (2012), 014907. 4, 5

[17] S. Chatrchyan *et. al.* [CMS Collaboration], Phys. Rev. C **89** (2014), 044906. 4, 5

[18] E. Shuryak, Rev. Mod. Phys. **89** (2017) 035001; U. Heinz, C. Shen and H. Song, AIP Conf. Proc. **1441** (2012) 766. iv, 5

[19] V. Okorokov [STAR Collaboration], EPJ Web Conf. **158**, 01004 (2017) 5

[20] G. Odyniec, PoS CPOD **2013**, 043 (2013). 5

[21] V. Kekelidze, A. Kovalenko, R. Lednicky, V. Matveev, I. Meshkov, A. Sorin and G. Trubnikov, Nucl. Phys. A **956**, 846 (2016). 5, 158

[22] T. Ablyazimov *et al.* [CBM Collaboration], Eur. Phys. J. A **53**, no. 3, 60 (2017) 5, 158

[23] C. Sturm, B. Sharkov and H. Stoecker, Nucl. Phys. A **834**, 682c (2010). 5, 158

[24] PhD Thesis: P. P. Bhaduri, "CHARMONIUM PRODUCTION AND DETECTION IN HIGH ENERGY NUCLEAR COLLISIONS AT FAIR"; xxxvi, 6

[25] J. Rafelski and B. Muller, Phys. Rev. Lett. **48**, 1066 (1982) Erratum: [Phys. Rev. Lett. **56**, 2334 (1986)]. doi:10.1103/PhysRevLett.48.1066, 10.1103/PhysRevLett.56.2334 8

[26] P. Koch, B. Muller and J. Rafelski, Phys. Rept. **142**, 167 (1986). doi:10.1016/0370-1573(86)90096-7 8

[27] L. Sandor *et al.* [NA57 Collaboration], Acta Phys. Hung. A **22**, 113 (2005) doi:10.1556/APH.22.2005.1-2.12 [nucl-ex/0404030]. 8

[28] J. Adam *et al.* [ALICE Collaboration], Nature Phys. **13**, 535 (2017) doi:10.1038/nphys4111 [arXiv:1606.07424 [nucl-ex]]. 8

[29] E. L. Feinberg, Nuovo Cim. A **34**, 391 (1976). 9

[30] J. I. Kapusta, P. Lichard and D. Seibert, Phys. Rev. D **44**, 2774 (1991) Erratum: [Phys. Rev. D **47**, 4171 (1993)]. doi:10.1103/PhysRevD.47.4171, 10.1103/PhysRevD.44.2774 9

[31] S. A. Bass, B. Muller and D. K. Srivastava, Phys. Rev. Lett. **93**, 162301 (2004) doi:10.1103/PhysRevLett.93.162301 [nucl-th/0404050]. 10

[32] S. A. Bass, B. Muller and D. K. Srivastava, Phys. Rev. Lett. **90**, 082301 (2003) doi:10.1103/PhysRevLett.90.082301 [nucl-th/0209030]. 10

[33] T. Renk, S. A. Bass and D. K. Srivastava, Phys. Lett. B **632**, 632 (2006) doi:10.1016/j.physletb.2005.11.026 [nucl-th/0505059].

[34] R. Chatterjee and D. K. Srivastava, Phys. Rev. C **79**, 021901 (2009) doi:10.1103/PhysRevC.79.021901 [arXiv:0809.0548 [nucl-th]]. 10

10

[35] R. Chatterjee, E. S. Frodermann, U. W. Heinz and D. K. Srivastava, Phys. Rev. Lett. **96**, 202302 (2006) doi:10.1103/PhysRevLett.96.202302 [nucl-th/0511079]. 10

[36] U. W. Heinz, R. Chatterjee, E. S. Frodermann, C. Gale and D. K. Srivastava, Nucl. Phys. A **783**, 379 (2007) doi:10.1016/j.nuclphysa.2006.11.090 [nucl-th/0610014]. 10

[37] K. Kajantie, J. I. Kapusta, L. D. McLerran and A. Mekjian, Phys. Rev. D **34**, 2746 (1986). doi:10.1103/PhysRevD.34.2746 10

[38] P. Mohanty, J. e. Alam and B. Mohanty, Phys. Rev. C **84**, 024903 (2011) doi:10.1103/PhysRevC.84.024903 [arXiv:1008.1112 [nucl-th]]. 10

[39] S. Chatrchyan *et al.* [CMS Collaboration], Phys. Lett. B **712**, 176 (2012) doi:10.1016/j.physletb.2012.04.058 [arXiv:1202.5022 [nucl-ex]]. 10

[40] T. Matsui and H. Satz, Phys. Lett. B **178**, 416 (1986). doi:10.1016/0370-2693(86)91404-8 11

[41] M. C. Abreu *et al.* [NA50 Collaboration], Phys. Lett. B **477**, 28 (2000). doi:10.1016/S0370-2693(00)00237-9 11

[42] A. Adare *et al.* [PHENIX Collaboration], Phys. Rev. C **84**, 054912 (2011) doi:10.1103/PhysRevC.84.054912 [arXiv:1103.6269 [nucl-ex]]. 11

[43] L. Adamczyk *et al.* [STAR], Phys. Rev. C **90** (2014) no.2, 024906 doi:10.1103/PhysRevC.90.024906 [arXiv:1310.3563 [nucl-ex]]. 11

[44] B. B. Abelev *et al.* [ALICE Collaboration], Phys. Lett. B **734**, 314 (2014) doi:10.1016/j.physletb.2014.05.064 [arXiv:1311.0214 [nucl-ex]]. 11

[45] J. Adam *et al.* [ALICE Collaboration], Phys. Lett. B **766**, 212 (2017) doi:10.1016/j.physletb.2016.12.064 [arXiv:1606.08197 [nucl-ex]]. 11

[46] K. Nakamura et al. (Particle Data Group), J. Phys. G: Nucl. Part. Phys. **37** (2010) 075021 11

[47] R. Averbeck, Prog. Part. Nucl. Phys. **70**, 159 (2013) doi:10.1016/j.ppnp.2013.01.001 [arXiv:1505.03828 [nucl-ex]]. 12

[48] M. Cacciari, M. Greco and P. Nason, JHEP **9805**, 007 (1998) viii, ix, xxxv, xxxviii, xxxix, xli, 13, 51, 68, 69, 85, 93, 94

[49] M. Cacciari, S. Frixione and P. Nason, JHEP **0103**, 006 (2001) 13

[50] M. Cacciari, S. Frixione, N. Houdeau, M. L. Mangano, P. Nason and G. Ridolfi, JHEP **1210**, 137 (2012) 13, 69

[51] M. Tanabashi *et al.* [Particle Data Group], Phys. Rev. D **98**, no. 3, 030001 (2018). doi:10.1103/PhysRevD.98.030001 xlix, 14

[52] K. Adcox *et al.* [PHENIX Collaboration], Phys. Rev. Lett. **88**, 192303 (2002) 15

[53] S. S. Adler *et al.* [PHENIX Collaboration], Phys. Rev. Lett. **94**, 082301 (2005) 15

[54] S. S. Adler *et al.* [PHENIX Collaboration], Phys. Rev. Lett. **96**, 032001 (2006) 15

[55] S. S. Adler *et al.* [PHENIX Collaboration], Phys. Rev. Lett. **96**, 032301 (2006) 15

[56] A. Adare *et al.* [PHENIX Collaboration], Phys. Rev. Lett. **97**, 252002 (2006) 15

[57] J. Adams *et al.* [STAR Collaboration], Phys. Rev. Lett. **94**, 062301 (2005) 15

[58] L. Adamczyk *et al.* [STAR Collaboration], Phys. Rev. D **86**, 072013 (2012) 15

[59] B. I. Abelev *et al.* [STAR Collaboration], Phys. Rev. D **79**, 112006 (2009) 15

[60] H. Agakishiev *et al.* [STAR Collaboration], Phys. Rev. D **83**, 052006 (2011) 15

[61] B. I. Abelev *et al.* [STAR Collaboration], Phys. Rev. Lett. **98**, 192301 (2007) Erratum: [Phys. Rev. Lett. **106**, 159902 (2011)] 15

[62] S. Acharya *et al.* [ALICE Collaboration], JHEP **1810**, 061 (2018) 15, 43

[63] S. Acharya *et al.* [ALICE], Phys. Lett. B **804** (2020), 135377 x, 15, 90, 95

[64] R. Pasechnik and M. umbera, Universe **3**, no. 1, 7 (2017) doi:10.3390/universe3010007 [arXiv:1611.01533 [hep-ph]]. xxxvi, 17

[65] S. A. Bass *et al.*, Prog. Part. Nucl. Phys. **41**, 255 (1998) 19, 130

[66] M. Bleicher *et al.*, J. Phys. G **25**, 1859 (1999) vi, 19, 130, 132

[67] L. Evans and P. Bryant, "LHC Machine," JINST **3**, S08001 (2008). xxxvi, 23, 34

[68] Mobs, Esm, "CERN-GRAPHICS-2019-002 (2019)", "https://cds.cern.ch/record/2684277", xxxvi, 24

[69] ALICE Collaboration, Tracking Technical Design Report of teh Inner Tracking System (ITS), CERN-LHCC-99-012, "http://cds.cern.ch/record/391175" xxxvi, 26, 27, 28

[70] ALICE Collaboration, Tracking Technical Design Report of the Time Projection Chamber (TPC), CERN-LHCC-2000-001, "http://cds.cern.ch/record/451098" xxxvi, 26, 28, 29, 30

[71] ALICE Collaboration, Tracking Technical Design Report of the Time of Flight (TOF), CERN-LHCC-2000-012, "http://cds.cern.ch/record/430132" xxxvi, 26, 30, 31

[72] ALICE Collaboration, Tracking Technical Design Report of the Transition Radiation Detector (TRD), CERN-LHCC-2001-021, "http://cds.cern.ch/record/519145" 26

[73] ALICE Collaboration, Tracking Technical Design Report of High Momentum Particle Identification (HMPID), CERN-LHCC-98-019, "http://cds.cern.ch/record/381431" 26

[74] ALICE Collaboration, Tracking Technical Design Report of the Photon Spectrometer (PHOS), CERN-LHCC-99-004, "http://cds.cern.ch/record/381432" 26

[75] ALICE Collaboration, Tracking Technical Design Report of Electromagnetic Calorimeter (EMCAL), CERN-LHCC-2008-014, "http://cds.cern.ch/record/1121574" 26

[76] A. Fernndez *et al.* [ACORDE Collaboration], Nucl. Instrum. Meth. A **572**, 102 (2007) 26

[77] ALICE Collaboration, Tracking Technical Design Report of the Forward Multiplicity Detector (FMD), CERN-LHCC-2004-025, "http://cds.cern.ch/record/781854" 27

[78] ALICE Collaboration, Tracking Technical Design Report of the Photon Multiplicity Detector (PMD), CERN-LHCC-99-032, "http://cds.cern.ch/record/451099" 27

[79] ALICE Collaboration, ALICE dimuon forward spectrometer: Technical Design Report, CERN-LHCC-99-022, "http://cds.cern.ch/record/401974" 27

[80] ALICE Collaboration, Tracking Technical Design Report of Zero Degree Calorimeter (ZDC), CERN-LHCC-99-005, "http://cds.cern.ch/record/381433" 27

[81] ALICE Collaboration, ALICE forward detectors: FMD, TO and VO: Technical Design Report, CERN-LHCC-2004-025, "http://cds.cern.ch/record/781854" 27, 31

[82] K. Aamodt *et al.* [ALICE Collaboration], JINST **3**, S08002 (2008). doi:10.1088/1748-0221/3/08/S08002 32

[83] S. Bagnasco *et al.*, J. Phys. Conf. Ser. **119**, 062012 (2008). doi:10.1088/1742-6596/119/6/062012 33, 78

[84] R. Brun and F. Rademakers, Nucl. Instrum. Meth. A **389**, 81 (1997). doi:10.1016/S0168-9002(97)00048-X 33

[85] H. Bethe, "Theory of the Passage of Fast Corpuscular Rays Through Matter," Annalen Phys. **5**, 325 (1930) 35

[86] B. Abelev *et al.* [ALICE Collaboration], Phys. Rev. D **86**, 112007 (2012) viii, 40, 41, 43, 46, 49, 64, 69

[87] S. Gorbunov and I. Kisel. Reconstruction of decay particles based on the Kalman filter, 2007. priv.commun. 41

[88] M. R. Ciupek, A. Dubla, S. Hornung, S. P. Rode Analysis Note: "Electrons from heavy-flavour hadron decays at mid-rapidity and low transverse momenta in pp collisions at $\sqrt{s} = 7$ TeV and $\sqrt{s} = 5.02$ TeV". https://alice-notes.web.cern.ch/node/782 42

[89] B. B. Abelev *et al.* [ALICE Collaboration], Phys. Rev. D **91**, no. 1, 012001 (2015) doi:10.1103/PhysRevD.91.012001 [arXiv:1405.4117 [nucl-ex]]. 43

[90] J. Adam *et al.* [ALICE Collaboration], Phys. Lett. B **754**, 81 (2016) 43

[91] B. Abelev *et al.* [ALICE Collaboration], Phys. Lett. B **717**, 162 (2012) doi:10.1016/j.physletb.2012.09.015 [arXiv:1205.5724 [hep-ex]]. 45

[92] L. Altenkmper, F. Bock, C. Loizides and N. Schmidt, Phys. Rev. C **96**, no. 6, 064907 (2017) doi:10.1103/PhysRevC.96.064907 [arXiv:1710.01933 [hep-ph]]. 46

[93] P. K. Khandai, P. Shukla and V. Singh, Phys. Rev. C **84**, 054904 (2011) doi:10.1103/PhysRevC.84.054904 [arXiv:1110.3929 [hep-ph]]. 46

[94] G. D'Agostini, CERN-99-03, CERN-YELLOW-99-03. 47

[95] B. Abelev *et al.* [ALICE Collaboration], Eur. Phys. J. C **73**, no. 6, 2456 (2013) doi:10.1140/epjc/s10052-013-2456-0 [arXiv:1208.4968 [hep-ex]]. 48

[96] ALICE Collaboration, ALICE luminosity determination for pp collisions at $\sqrt{s} = 13$ TeV, "ALICE-PUBLIC-2016-002" (Jun, 2016). http://cds.cern.ch/record/2160174 48

[97] R. Barlow and C. Beeston, "Fitting using finite Monte Carlo samples". http://lss.fnal.gov/archive/other/man-hep-93-1.pdf 72, 74

[98] F. James and M. Winkler, "Minuit users guide," June, 2004. http://seal.web.cern.ch/seal/documents/minuit/mnusersguide.pdf. 74

[99] M. Volkl, Thesis: “Electrons from beauty-hadron decays in central PbPb collisions at $\sqrt{s_{\rm NN}} = 2.76$ TeV”. 74

[100] S. Acharya *et al.* [ALICE Collaboration], “Measurement of $\rm D^0$, $\rm D^+$, $\rm D^{*+}$ and $\rm D_s^+$ production in pp collisions at $\sqrt{s}$ = 5.02 TeV with ALICE,” Eur. Phys. J. C **79**, no. 5, 388 (2019) 79, 81

[101] Analysis note: ”Λ_c^+ production in pp collisions at $\sqrt{s}$ = 5.02 TeV and in p–Pb collisions at $\sqrt{s_{NN}}$ = 5.02 TeV ” https://alice-publications.web.cern.ch/node/5524 81

[102] ALICE Collaboration, ALICE 2017 luminosity determination for pp collisions at $\sqrt{s}$ = 5 TeV, ”ALICE-PUBLIC-2018-014” (Nov, 2018). http://cds.cern.ch/record/2648933 84

[103] D. Baumeier, V0 Decays: Documentation of the C++ Program AliESDv0KineCuts.cxx. Bachelor thesis, Universitt Mnster, 2011 90

[104] B. Abelev *et al.* [ALICE Collaboration], Phys. Lett. B **721**, 13 (2013) Erratum: [Phys. Lett. B **763**, 507 (2016)] x, 93

[105] C. de Conti. Analysis Note: ”Electrons from beauty hadrons decays at mid-rapidity and low transverse momenta in Pb-Pb 0-10% centrality collisions at$\sqrt{s_{NN}}$ = 5.02 TeV”. https://alice-notes.web.cern.ch/node/783 95

[106] J. Park. Analysis Note: ”Measurement of electrons from beauty-hadron decays in the 30-50% centrality Pb-Pb collisions at $\sqrt{s_{NN}}$ = 5.02 TeV with ALICE detector”. https://alice-notes.web.cern.ch/node/897 95

[107] T. Ablyazimov *et al.* [CBM Collaboration], Eur. Phys. J. A **53**, no. 3, 60 (2017).

[108] N. S. Geraksiev [NICA/MPD Collaboration], J. Phys. Conf. Ser. **1390**, no. 1, 012121 (2019). 97

97

[109] J. L. Klay *et al.* [E-0895 Collaboration], Phys. Rev. C **68**, 054905 (2003) 98, 114, 117

[110] J. L. Klay *et al.* [E895 Collaboration], Phys. Rev. Lett. **88**, 102301 (2002) 98, 114

[111] L. Adamczyk *et al.* [STAR Collaboration], Phys. Rev. C **96**, no. 4, 044904 (2017) 98, 115

[112] C. Alt *et. al.* NA49 Collaboration, Phys.Rev. C77 (2008) 024903, 2008 . 98, 115

[113] S. V. Afanasiev *et. al.* NA49 Collaboration, Phys.Rev. C66 (2002) 054902, 2002 . 98, 115

[114] C. Alt *et. al.* NA49 Collaboration, Phys.Rev. C68 (2003) 034903. 98, 115

[115] C. Alt *et al.* [NA49 Collaboration], Phys. Rev. C **78**, 034918 (2008) 99, 119

[116] C. Alt *et al.* [NA49 Collaboration], Phys. Rev. Lett. **94**, 192301 (2005) 99, 119

[117] C. Alt *et al.* [NA49 Collaboration], Phys. Rev. C **78**, 044907 (2008) 99, 119

[118] S. Chatterjee, R. M. Godbole and S. Gupta, Phys. Lett. B **727**, 554 (2013); 100

[119] W. Florkowski and W. Broniowski, Acta Phys. Polon. B **35**, 2895 (2004); W. Florkowski, Nucl. Phys. A **774**, 179 (2006). 101

[120] P. J. Siemens and J. O. Rasmussen, Phys. Rev. Lett. **42** (1979) 880. 102

[121] K. S. Lee and U. Heinz, Z. Phys. C - Particles and Fields **43** (1989) 425. 102

[122] K. S. Lee, U. Heinz and E. Schnedermann, Z. Phys. C - Particles and Fields **48** (1990) 525. 102

[123] E. Schnedermann, J. Sollfrank, U. Heinz, Phys. Rev. C **48** (1993) 2462. 102, 104, 111, 113

[124] P. Huovinien *et. al.*, Phys. Lett. B **503** (2001) 58. 103

[125] C. Adler *et. al.* STAR Collaboration, Phys.Rev.Lett. 87 (2001) 182301 . 103

[126] P. Ghosh, S. Muhuri, J. K. Nayak and R. Varma, J. Phys. G **41**, 035106 (2014) doi:10.1088/0954-3899/41/3/035106 [arXiv:1402.6813 [hep-ph]]. 103

[127] D. Teaney, Phys. Rev. C **68** (2003) 034913. 103

[128] A. Jaiswal and V. Koch, J. Phys. Conf. Ser. **779**, no. 1, 012065 (2017). 103

[129] H. Dobler, J. Sollfrank and U. Heinz, Phys. Lett. B **457** (1999) 353. 104, 107, 112, 113

[130] S. P. Rode, P. P. Bhaduri, A. Jaiswal and A. Roy, Phys. Rev. C **98**, no. 2, 024907 (2018) 105

[131] S. P. Rode, P. P. Bhaduri, A. Jaiswal and A. Roy, [arXiv:2004.04703 [hep-ph]]. 106

[132] M. I. Gorenstein, K. A. Bugaev and M. Gazdzicki, Phys. Rev. Lett. **88**, 132301 (2002) 106, 120

[133] F. Cooper and G. Frye, Phys. Rev. D **10**, 186 (1974). 107, 135

[134] S. Chapman, J.R. Nix, Phys. Rev. C 54 (1996) 866; J.R. Nix, Phys. Rev. C 58 (1998) 2303. 113

[135] J. Sollfrank, P. Koch, U. W. Heniz, Phys. Lett. B**252**(1990) 256; *ibid* Z. Phys. C**52** (1991) 593. 113

[136] F. James and M. Roos, Comput. Phys. Commun. **10**, 343 (1975). 116

[137] V.5.34/32, CERN ROOT, 2015, http://root.cern.ch 116

[138] S. Chatterjee *et. al.*, Adv. High Energy Phys. 2015 (2015) 349013. 117

[139] P. K. Netrakanti and B. Mohanty, Phys. Rev. C **71**, 047901 (2005). 118

[140] J. Barrette *et al.* [E877 Collaboration], Phys. Rev. C **63**, 014902 (2001) 119

[141] B. B. Back *et al.* [E917 Collaboration], Phys. Rev. C **69**, 054901 (2004) 119

[142] J. Adam *et al.* [STAR Collaboration], arXiv:1906.03732 [nucl-ex]. 119

[143] H. Caines, STAR Collaboration, private communication. 119

[144] T. Anticic *et al.* [NA49 Collaboration], Phys. Rev. Lett. **93**, 022302 (2004) 119

[145] B. Alessandro *et al.* [NA50 Collaboration], Eur. Phys. J. **C39**, 335 (2005).

[146] M. C. Abreu *et al.* [NA50 Collaboration], Phys. Lett. B **499**, 85 (2001). 121

[147] R. Arnaldi *et al.* [NA60 Collaboration], Phys. Rev. Lett. **99**, 132302 (2007). 121

123

[148] M. Agnello *et al.* [NA60+ Collaboration], arXiv:1812.07948 [nucl-ex]. 123, 156

[149] S. Chatterjee, B. Mohanty and R. Singh, Phys. Rev. C **92**, no.2, 024917 (2015) 123

[150] D. Thakur, S. Tripathy, P. Garg, R. Sahoo and J. Cleymans, Adv. High Energy Phys. **2016**, 4149352 (2016) 123

[151] H. L. Lao, H. R. Wei, F. H. Liu and R. A. Lacey, Eur. Phys. J. A **52**, no. 7, 203 (2016) 123

[152] A. Khuntia, H. Sharma, S. Kumar Tiwari, R. Sahoo and J. Cleymans, Eur. Phys. J. A **55**, no. 1, 3 (2019) 123

[153] H. van Hecke, H. Sorge and N. Xu, Nucl. Phys. A **661** (1999), 493-496 doi:10.1016/S0375-9474(99)85073-8 124

[154] D. Biswas, K. Deka, A. Jaiswal and S. Roy, Phys. Rev. C **102** (2020) no.1, 014912 doi:10.1103/PhysRevC.102.014912 xii, 125, 156

[155] C. Y. Wong, Phys. Rev. C **78**, 054902 (2008) 125

[156] A. Bazavov *et al.* [HotQCD], Phys. Rev. D **90**, 094503 (2014). 126

[157] G. Inghirami, P. Hillmann, B. Tomik and M. Bleicher, J. Phys. G **47**, no. 2, 025104 (2020) 126

[158] K. Aamodt *et al.* [ALICE Collaboration], Phys. Rev. Lett. **105**, 252302 (2010) 129, 130

[159] K. Adcox *et al.* [PHENIX Collaboration], Nucl. Phys. A **757**, 184 (2005) 129

[160] J. Adams *et al.* [STAR Collaboration], Nucl. Phys. A **757**, 102 (2005)

[161] Y. Nara, H. Niemi, A. Ohnishi and H. Stcker, Phys. Rev. C **94**, no. 3, 034906 (2016) 129

[162] Y. Nara, N. Otuka, A. Ohnishi, K. Niita and S. Chiba, Phys. Rev. C **61**, 024901 (2000) 130

[163] V. P. Konchakovski, W. Cassing, Y. B. Ivanov and V. D. Toneev, Phys. Rev. C **90**, no. 1, 014903 (2014) 130, 131

[164] H. Liu *et al.* [E895 Collaboration], Phys. Rev. Lett. **84**, 5488 (2000) 130 xlv, 130, 137, 144, 145, 149

[165] P. Chung *et al.* [E895 Collaboration], Phys. Rev. Lett. **85**, 940 (2000) 130

[166] P. Chung *et al.*, Phys. Rev. Lett. **86**, 2533 (2001) 130

[167] H. Appelshauser *et al.* [NA49 Collaboration], Phys. Rev. Lett. **80**, 4136 (1998) 130

[168] J. Adams *et al.* [STAR Collaboration], Phys. Rev. C **72**, 014904 (2005) 130

[169] B. B. Back *et al.* [PHOBOS Collaboration], Phys. Rev. Lett. **97**, 012301 (2006)

[170] B. Alver *et al.* [PHOBOS Collaboration], Phys. Rev. Lett. **98**, 242302 (2007) 130

130

[171] P. P. Bhaduri and S. Chattopadhyay, Phys. Rev. C **81**, 034906 (2010) 130, 141

[172] S. Sarkar, P. Mali and A. Mukhopadhyay, Phys. Rev. C **95**, no. 1, 014908 (2017) 130

[173] J. Auvinen and H. Petersen, Phys. Rev. C **88** (2013) no.6, 064908 130, 131

[174] B. Andersson, G. Gustafson and B. Nilsson-Almqvist, Nucl. Phys. B **281**, 289 (1987). 132

[175] Z. W. Lin, C. M. Ko, B. A. Li, B. Zhang and S. Pal, Phys. Rev. C **72**, 064901 (2005) 130

[176] L. W. Chen, V. Greco, C. M. Ko and P. F. Kolb, Phys. Lett. B **605**, 95 (2005) 130

[177] M. Luzum, C. Gombeaud and J. Y. Ollitrault, Phys. Rev. C **81**, 054910 (2010) 130, 131, 150

[178] N. Borghini and J. Y. Ollitrault, Phys. Lett. B **642**, 227 (2006) 130, 150

[179] C. Gombeaud and J. Y. Ollitrault, Phys. Rev. C **81**, 014901 (2010) 130, 150

[180] Y. Nara, J. Steinheimer and H. Stoecker, Eur. Phys. J. A **54**, no. 11, 188 (2018) 131, 151

[181] S. P. Rode, P. P. Bhaduri and A. Roy, Eur. Phys. J. A **55** (2019) no.11, 216 doi:10.1140/epja/i2019-12921-1 [arXiv:1910.07717 [nucl-th]]. 131

[182] H. Petersen, Q. Li, X. Zhu and M. Bleicher, Phys. Rev. C **74** (2006) 064908 xlv, 131, 132, 147, 150

[183] H. Petersen and M. Bleicher, Phys. Rev. C **79** (2009) 054904 131

[184] J. Steinheimer, J. Auvinen, H. Petersen, M. Bleicher and H. Stcker, Phys. Rev. C **89** (2014) no.5, 054913 132

[185] G. Burau *et. al.*, Phys. Rev. C**71**, 054905 (2005). 132

[186] H. Petersen, J. Steinheimer, G. Burau, M. Bleicher and H. Stocker, Phys. Rev. C **78**, 044901 (2008) 133, 135

[187] P. F. Kolb, P. Huovinen, U. W. Heinz and H. Heiselberg, Phys. Lett. B **500** (2001) 232 133

[188] B. B. Back *et al.* [PHOBOS Collaboration], J. Phys. G **31** (2005) S41 133

[189] D. Zschiesche, S. Schramm, J. Schaffner-Bielich, H. Stoecker and W. Greiner, Phys. Lett. B **547**, 7 (2002)

[190] S. P. Rode, A. Roy and P. P. Bhaduri, DAE Symp. Nucl. Phys. **62**, 892 (2017). xliv, 133

[191] J. Steinheimer, S. Schramm and H. Stocker, Phys. Rev. C **84**, 045208 (2011) 135, 136

[192] P. Huovinen, P. F. Kolb, U. W. Heinz, P. V. Ruuskanen and S. A. Voloshin, Phys. Lett. B **503**, 58 (2001). 139

[193] S. Esumi [PHENIX Collaboration], Nucl. Phys. A **715**, 599 (2003) 139

[194] C. Adler *et al.* [STAR Collaboration], Phys. Rev. Lett. **87**, 182301 (2001) 140

[195] C. Adler *et al.* [STAR Collaboration], Phys. Rev. Lett. **90**, 032301 (2003) 140

[196] C. Adler *et al.* [STAR Collaboration], Phys. Rev. Lett. **89**, 132301 (2002) 140

[197] R. Abir and M. G. Mustafa, Phys. Rev. C **80**, 051903 (2009) 140

[198] R. J. Fries, B. Muller, C. Nonaka and S. A. Bass, Phys. Rev. C **68**, 044902 (2003) 140

[199] R. J. M. Snellings, H. Sorge, S. A. Voloshin, F. Q. Wang and N. Xu, Phys. Rev. Lett. **84**, 2803 (2000) 142

[200] G. Song, B. A. Li and C. M. Ko, Nucl. Phys. A **646**, 481 (1999) 144

[201] S. Pal, C. M. Ko, Z. w. Lin and B. Zhang, Phys. Rev. C **62**, 061903 (2000) 144

[202] D. B. Kaplan and A. E. Nelson, Phys. Lett. B **175**, 57 (1986). 144

[203] L. Bravina, Y. Kvasiuk, S. Sivoklokov, O. Vitiuk and E. Zabrodin, Universe **5**, no. 3, 69 (2019). 144

[204] P. Chung *et al.* [E895 Collaboration], Phys. Rev. C **66** (2002) 021901

[205] J. Adams *et al.* [STAR Collaboration], Phys. Rev. Lett. **92**, 062301 (2004) xlv, 147, 150

[206] H. Masui [PHENIX Collaboration], Nucl. Phys. A **774**, 511 (2006) 151, 158

[207] B. I. Abelev *et al.* [STAR Collaboration], Phys. Rev. C **75**, 054906 (2007) 151, 158

[208] S. Huang [PHENIX Collaboration], J. Phys. G **35**, 104105 (2008) 151, 158

[209] V. P. Konchakovski, E. L. Bratkovskaya, W. Cassing, V. D. Toneev, S. A. Voloshin and V. Voronyuk, Phys. Rev. C **85**, 044922 (2012) 151, 158

151, 158

[210] R. S. Bhalerao, J. P. Blaizot, N. Borghini and J. Y. Ollitrault, Phys. Lett. B **627**, 49 (2005) 152

[211] P. Staszel, NA61/SHINE Collaboration, Nucl. Phys. A **982** (2019) 879 157

[212] W. Broniowski and W. Florkowski, Phys. Rev. Lett. **87**, 272302 (2001) ; *ibid* Phys. Rev. C**65** (2002) 064905.

[213] I. G. Bearden *et al.* [BRAHMS Collaboration], Phys. Rev. Lett. **94**, 162301 (2005).

[214] Wikipedia: Landau Distribution, https://upload.wikimedia.org/wikipedia/commons/d/dd/Landau_Distribution_PDF.svg. xlv, 163

[215] Wikipedia: Error Function, https://upload.wikimedia.org/wikipedia/commons/2/2f/Error_Function.svg. xlv, 164